Kinetic Method for Quasi-One-Dimensional Simulation of Magnetic Nozzle Plasmadynamics

by

Frans Hendrik Ebersohn

A dissertation submitted in partial fulfillment
of the requirements for the degree of
Doctor of Philosophy
(Aerospace Engineering)
in The University of Michigan
2016

Doctoral Committee:

      Professor Alec D. Gallimore, Co-Chair
      Assistant Research Scientist J.P. Sheehan, Co-Chair
      Professor Iain D. Boyd
      Associate Professor Alexander G.R. Thomas
      John V. Shebalin, National Aeronautics and Space Association
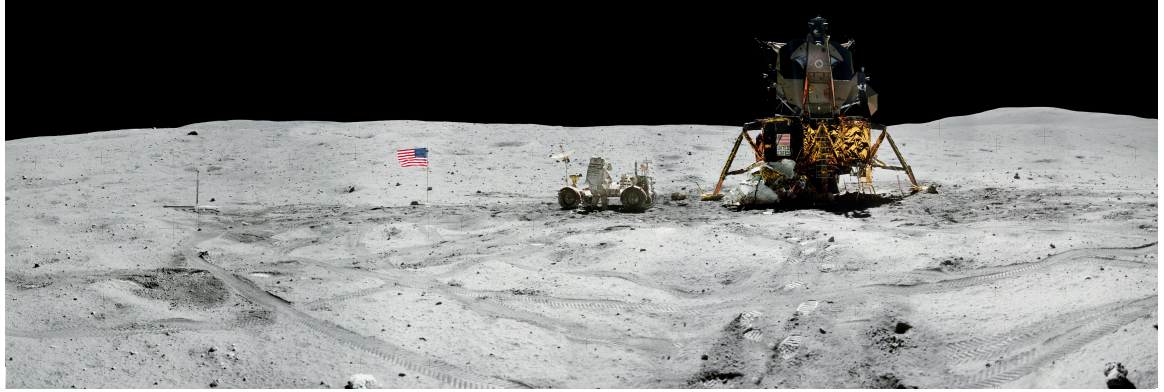
"Earth is the cradle of humanity, but one cannot live in a cradle forever." -Konstantin Tsiolkovsky [Picture Credit: NASA]

For my family. Everything here is a reflection of you. Thank you.

ACKNOWLEDGEMENTS

The path to my Ph.D. has been a long and winding road. I began down this path at Texas A&M University, took a brief detour at the University of Texas at Austin, and finally ended up at the University of Michigan. Along this road I have encountered so many people that I need to thank for making this all of this possible.

First I would like to thank my mentors and advisors at the University of Michigan. Alec Gallimore, you are a shining example of leadership in research and in life. Thank you for taking me in as a student and for your guidance along the way. Your career is something all of your students strive to emulate. My experiences at PEPL, the house that you built, have been some of the best of my life. J. P. Sheehan, your guidance and expertise have been invaluable in my research. You always asked the tough questions and gave me direction when I needed it. You have everything it takes to be a great leader in this field, and I was lucky to work with you. Thank you also to Professor Iain Boyd and Professor Alexander Thomas. Insights I gained from your courses and our discussions were extremely valuable to my research. I was lucky to have access to your world class expertise in plasma simulations.

Outside of the University of Michigan, I have also had excellent guidance. Dr. John Shebalin, my NASA mentor and guide, thank you for everything. You helped me write my proposal for this research six years ago and now, finally, you are on my dissertation committee. You were the perfect mentor and guide into this world of research. Dr. Jacques Richard, thank you for introducing me to electric propulsion. Dr. Sharath Girimaji, thank you for being my original advisor and starting me on this

journey into electric propulsion research. Finally thank you to Benjamin Longmier for bringing me to the University of Michigan and for the many adventures we had in Alaska and Europe.

To the PEPL students, my co-workers and my friends, thank you for being the best people to go through this journey with. From preliminary exams to my defense, you have always been there. Scott, Crocco's theorem and many other things will never be the same again, good luck with the biggest and baddest thruster around, get us ready for Mars. Ethan, your curiosity is infectious and keep tinkering. Tim, good luck with CAT and keep pushing magnetic nozzle research forward. Sarah, best of luck with all your thrusters, and I can't wait to see them in action. Marcel, keep laser-ing, then laser some more, and finally apply some physics. Mike, Kim, and Durot (the older generation) thank you for your guidance and direction. Thank you also to Eric for your help figuring out RPAs. The new generation, you are lucky to be where you are today. Take advantage of every minute and explore as much as you can.

There are numerous others to thank at the University of Michigan. Denise, Tom, Dave, and all the Aerospace Engineering department staff, thank you for everything. You are the glue that holds together this department and without you none of the work we do would be possible. My other fellow graduate students (Horatiu, Ken, Brandon, Maria, Astrid, and Jacob) thank you for your discussions and for sharing your research with me.

Before, during, and after graduate school I have been guided and supported by my family. Ma en Pa, julle is my inspirasie vir alles en waarlik is ek hier vandag net dankse julle harde werk en opofferings. Ek is vir ewig dankbaar. Abram, jy sal altuid my beste vriend wees broer. To my family in South Africa, my new family the Hornes, and all of my friends and family, my deepest heartfelt thank you.

Lastly and most importantly to my wife Margeaux and my son George. You are everything I am and will be. I will never be thankful enough for what you have given me. Thank you for coming on this adventure with me and I can not wait for the next one.

Frans Hendrik Ebersohn, 2016

TABLE OF CONTENTS

LIST OF FIGURES

LIST OF TABLES

LIST OF APPENDICES

Appendix

LIST OF ABBREVIATIONS

MHD magnetohydrodynamics

Q1D quasi-one-dimensional

CI cold ion

HI hot ion

1D one dimensional

2D two dimensional

PIC particle-in-cell

MN magnetic nozzle

MPI Message Passing Interface

VASIMR VAriable Specific Impulse Magnetoplasma Rocket

MPD Magnetoplasmadynamic

CAT CubeSat Ambipolar Thruster

HDLT Helicon Double Layer Thruster

ECR Electron Cyclotron Resonance

NTR Nuclear Thermal Rockets

RPA Retarding Potential Analyzers

PEPL Plasmadynamics and Electric Propulsion Laboratory

1D3V One spatial dimensions, three velocity dimensions

2D3V Two spatial dimensions, three velocity dimensions

MCC Monte Carlo Collisions

EP Electric Propulsion

DDEX Detachment Demonstration Experiment

PM-HDLT Permanent Magnetic Helicon Double Layer Thruster

ABSTRACT

Kinetic Method for Quasi-One-Dimensional Simulation of Magnetic Nozzle
Plasmadynamics

by

Frans Ebersohn

Co-Chairs: Alec D. Gallimore and J. P. Sheehan

A novel technique was developed which models two-dimensional magnetic field effects
in a one-dimensional electrostatic particle-in-cell code. This quasi-one-dimensional
formulation incorporates two-dimensional effects through the inclusion of cross-sectional
area variation and magnetic field forces. The new method is verified with a newly
formulated set of test cases of a two-particle system, magnetic mirrors, and fully two
dimensional simulations.

Magnetic nozzle physics and ion acceleration in low temperature plasmas were
investigated with a simple test problem using these kinetic simulations. The effects
of the density variation due to plasma expansion and the magnetic field forces on
ion acceleration were investigated. The density variation only weakly affected ion
acceleration. Magnetic field forces acting on the electrons were found to be responsible
for the formation of potential structures which accelerate ions. The formation of a
high energy ion beam is seen due to ion acceleration. Strongly diverging magnetic
fields drive more rapid potential drops and the length of the radio frequency heating
region was found to significantly affect the electron temperature profiles. Simulations

were performed with both argon and xenon. For the same driving current, argon simulations demonstrated higher ion velocities while xenon simulations showed higher plasma densities.

The ion acceleration physics was investigated verifying that ion acceleration occurs due to potential structures established by the magnetic field forces on the electrons. The effects of anisotropic electron pressure tensors were also found to be important for determining a simple Ohm's law used to solve for the induced electric field which accelerates the ions. Bi-Maxwellian and non-Maxwellian velocity distributions were seen for the electrons in the simulations along with the anisotropic temperatures, verifying the need for kinetic simulations. Electron thermodynamic relations (isothermal, adiabatic, polytropic, double adiabatic) were evaluated for a number of simulation results.

Results from quasi-one-dimensional simulations of magnetic nozzles were used to estimate thruster performance parameters such as specific impulse and thrust. The performance parameters were consistent with those expected in similar devices.

Simulations with parameters similar to the Helicon Double Layer Thruster were performed. Results from these simulations look encouraging for future device specific studies. Similar electron temperatures and normalized density profiles are seen in the experiments and simulations. Velocity and energy distribution functions for ions and electrons also show similar behavior to that measured in experiments.

CHAPTER I

Introduction

1.1 Problem Statement

One of the primary challenges in the field of Electric Propulsion (EP) is guaranteeing that thrusters will achieve the long lifetime needed of these devices.[1, 2, 3] Interaction of the high energy plasma with surfaces can lead to damaging these surfaces and failure of the thruster. The wear of thrusters is also particularly difficult to characterize in laboratory experiments due to the facility effects which may affect erosion rates.[4, 5] Many of the conventional thrusters (Hall thrusters, ion thrusters, and magnetoplasmadynamic thrusters) incorporate electrodes (anode, cathode, acceleration grids, etc.) which interact directly with the plasma and utilize the plasma as part of the current circuit. The electrodes often end up being some of the primary points of failure. Conventional thrusters have shown great success in both the laboratory and in flight despite these challenges with thruster lifetime.[6, 7, 8] There is inherent difficulty in scaling up these devices to higher energy density plasmas due to life-limiting surface interactions. Furthermore, scaling down of these thrusters becomes difficult because as the thruster size decreases the plasma-surface interaction becomes harder to mitigate. Plasma surface-interactions have also severely limited the operation of Magnetoplasmadynamic thrusters (MPDs). Examples of erosion mitigation techniques include the use of graphite optics in ion thrusters and the recent

advent of magnetic shielding for Hall thrusters in which a carefully shaped magnetic field is used to protect the Hall thruster channel walls. Magnetic shielding has shown great promise for increasing the lifetime of Hall thrusters by decreasing the interaction of the plasma with the thruster channel walls.[9] This use of a well designed magnetic field is a prime example of how magnetic fields can be used to improve thruster lifetime.

Electrodeless plasma thrusters seek to alleviate lifetime issues by eliminating the use of electrodes entirely. These electrodeless thrusters typically consist of a radio-frequency (RF) or microwave plasma source and an applied magnetic field known as a magnetic nozzle which directs the flow of the plasma. The magnetic field is designed so that interaction of the plasma with the walls is minimized. Thrust is generated by the plasma through the pressure forces on the walls of the plasma source and the interaction of the plasma with the magnetic nozzle. Limiting the contact of the plasma with the wall using magnetic fields allows more dense and more energetic plasmas to be used which can lead to increases in thruster performance. Furthermore, limiting the interaction of the plasma with walls by using magnetic fields allows these thrusters to be scaled down effectively. The tradeoff for these improvements is the need for addressing the new challenges of using a RF or microwave plasma source and understanding how to best design the magnetic nozzle.

The goal of this research is to improve the understanding of the fundamental plasmadynamics in magnetic nozzles which is essential to optimizing the performance of electrodeless plasma thrusters. The research herein approaches this problem from a modeling perspective and introduces a new kinetic method for studying the magnetic nozzles physics. The methods developed are particularly useful for studying the ion acceleration mechanisms in electrodeless thrusters. The model developed and insights gained from the simulations also have broader applications to astrophysical plasma jets, solar physics, and magnetic field guided plasma flows.

1.2 Research Objectives and Contributions

The major contributions of this research include:

- **A study of the operating regimes of magnetic nozzle thrusters and identification of the physical models necessary to capture important physics.** Kinetic models were shown to be necessary for the operating regimes of some currently being developed low-temperature magnetic nozzle thrusters.

- **Development of a novel kinetic quasi-one-dimensional particle-in-cell simulation technique for studying magnetized plasma jets.** This technique includes two-dimensional effects due to the magnetic field and is enabling due to the reduced computational cost compared to fully two dimensional simulations.

- **Incorporation of quasi-one-dimensional modeling technique in a general, parallelized one-dimensional particle-in-cell code with Monte Carlo collisions.** The code developed for this work will continue to be a research tool at the Plasmadynamics and Electric Propulsion Laboratory.

- **Formulation of a series of verification test cases for the quasi-one-dimensional simulation model.** These test cases include simulations of a two-particle system, magnetic mirrors, and comparisons with fully two dimensional simulations. The verification test cases illustrate the power of the model and give guidelines for verifying this technique for future implementations.

- **Simulation of a magnetic nozzle thruster test problem and thorough analysis of physics.** Magnetic nozzle test problem results identified effects of varying plasma source region, magnetic field topology, and background neutral density on ion acceleration and electron dynamics. Magnetic nozzle simulations

demonstrate ion acceleration due to potential structures which form as a result of magnetic field forces on the electrons.

- **Simulations of the Helicon Double Layer Thruster demonstrating applications of the method to large scale problems.** Results are encouraging for future device specific studies.

- **Implementation of a retarding potential analyzer for studying ion energies in magnetic nozzle thruster plume.** Includes a review of operation guidelines and critical design parameters.

1.3   Thesis Organization

The remainder of the thesis is organized as follows. Chapter II introduces the research topic and motivates its study by giving a brief background on electric propulsion, magnetic nozzles, and the previous simulation studies of magnetic nozzles. An in-depth discussion of magnetic nozzle physics is given in Chapter III. The basics of particle simulation methods and the novel techniques developed in this work are presented in Chapter IV. Chapter V discusses the implementation and verification of the one-dimensional particle-in-cell code developed as part of this work. Chapter VI presents the implementation of the quasi-one-dimensional particle simulation technique and the verification problems developed for the quasi-one-dimensional model. The magnetic nozzle test problem simulations are presented in Chapter VII followed by a detailed analysis of the physics of this problem in Chapter VIII. The simulations of the Helicon Double Layer Thruster are presented in Chapter IX and finally Chapter X summarizes this work and presents conclusions.

CHAPTER II

Background

2.1 The Case for Space Exploration

2.1.1 Scientific Need for Exploration

Science has been one of the primary drivers behind the need for space exploration. There are major scientific questions which can only be answered by looking outward from our planet. Among these questions are: "Is there life (or intelligent life) outside of our planet?"; "Where and how did life originate?"; "How was Earth, the Solar System, the Milky way, etc. formed and how do they work?". Answering these scientific questions gives deep insight on how life and the universe work and how humanity and the planet Earth are part of the bigger, universal picture.

Spaceflight is an important component in the study of the health of the planet Earth. Monitoring Earth from orbit with missions such as NASA's AQUA, GRACE, LANDSAT, and TERRA, have given tremendous insight on the Earth system as a whole as well as humanity's impacts on this.[10, 11] Characterizing the health of the planet as well as the chains of causes and effects on the planet's health will be imperative to the survival of our species on this planet.

Understanding the astrophysics of our solar system as well as the interactions of the solar system with our planet through mechanisms such as solar activity and

asteroid impacts can also have tremendous effects on our planet (ask the dinosaurs). Only by improving our scientific understanding of this system can we hope to avoid the fate of the dinosaurs.

2.1.2 Economic Need for Exploration

The expansion of humanity has been a consequence of our success and dominance of the world around us. As we continue to grow in number and develop technologically we will require more physical space and resources. Both of these are only supplied in a limited quantity on our planet. We now occupy all seven continents and harvest resources from both the land and sea to support our ever growing species. Both population and power consumption have been and are continuing to grow.[12, 13] Currently we are living like a man in a log cabin who uses wood from the structure of the home itself to fuel a fire to stay warm. Eventually he will have to venture out of his home to survive. While we are currently not in danger of consuming ourselves, as a species we should begin to look outward for resources in preparation for when we need to expand ourselves. Currently efforts are already underway through NASA and companies such as Planetary Resources to achieve this through asteroid mining. Economic reasons have led to all the major expansion of human civilization, and the time will come when we run out of room on Earth.

2.1.3 Technological Need for Exploration

Exploration of space, a place where life was never intended to survive and where resources are scarce inherently requires the development of new technologies. The high cost of space exploration also drives space technology to look for the most efficient, effective way to achieve its goals. These needs have led to the development of many spinoff technologies which NASA readily publishes to the public. These technologies include: the space blankets found in nearly every first aid kit, highly efficient solar cells

used in many alternate energy power sources, and water purification systems which produce clean water from even the most heavily contaminated water sources.[14]

In a broader sense, the modern age would not be possible without the development of space technology due to the capabilities provided by satellites. These satellites provide precise global positioning (GPS), radio and television, telecommunications, and Earth observation for monitoring weather and the state of the planet.

While technology can be developed purely for the sake of development, having a clear goal such as the exploration of space gives direction to this endeavor and will lead to further success. The development of the technology used in space exploration in particular will always have to strive for high efficiency and survivability in extremely harsh physical conditions. Making technology work the best it can in the worst conditions will naturally lead to improvements to the easier problems as well.

2.2   Cost Limitations on Space Exploration

The primary factor which inhibits further space exploration is the inherently high costs. An example of the cost restrictions is seen in the simple metric of cost per kilogram to get objects into Low Earth Orbit (LEO). The lowest cost to date was with the Saturn V with a cost of around FY2016 $4,500/kg but typically these cost are greater than $10,000/kg (FY2016). [15] These high costs result in a cascade of further costs. Access to space is expensive, which results in the developers of spacecraft requiring highly reliable and highly functional equipment to insure that the costs of access are recovered. The developers can not afford another launch, so everything has to work the first time. Development of low risk equipment with high reliability, high factor of safety, and high functionality naturally drives costs up further.

Since cost is such a limiting factor, an important current challenge is to reduce the overall cost. There are two simple ways to achieve overall cost reduction: reduce

the cost of access to space (\$/kg) or reduce the mass which must be put into space to achieve the same goals (increase functionality of spacecraft). Space Exploration Technologies (SpaceX) is a commercial company which is currently striving to reduce the cost of access to space through re-usable rockets. They have shown exciting results in flying back the rocket first stage, but time will tell if re-using the refurbished first stage will lead to significant cost reductions when all costs are considered. NASA also has an initiative with the goal of drastically decreasing launch costs to enable further exploration. Reducing the mass of the payload is another simple method for reducing cost. The best way to achieve mass reduction is to increase the functionality of equipment. In particular, this work will focus on the development of advanced spacecraft propulsion systems which reduce the overall mass (primarily due to reduced propellant) and increase the functionality of the spacecraft. The importance of the propulsion system in particular will be discussed first from the perspective of Tsiolkovsky's rocket equation.

2.3   Propulsion and the Rocket Equation

Propulsion systems are characterized by two key performance parameters: thrust (T) and specific impulse (I_{sp}). The thrust is the force exerted on the spacecraft resulting in changes of velocity. The specific impulse can be found from the thrust by the following equation:

$$I_{sp} = \frac{T}{\dot{m}g_0} \qquad (2.1)$$

in which ($\dot{m}$) is the mass flow rate and (g_0) constant acceleration due to gravity. If the thrust is determined from the flux of momentum out of the thruster, I_{sp} is a measure of the propellant exhaust velocity (v_{ex}) according to the following relation $I_{sp} = v_{ex}/g_0$. As the exit velocities increase, the energy in the propellant particles

exiting the thruster increase. The higher the energy per particle, the fewer total particles are needed to achieve the same spacecraft energy. When fewer particles are needed, less fuel is required making the specific impulse a measure of how effectively the propellant is being utilized. The decrease of required propellant is best illustrated in the Tsiolkovsky's rocket equation shown below:

$$m\frac{dv}{dt} = -\dot{m}v_{ex} = -T \tag{2.2}$$

in which m is the spacecraft mass, $\dot{m} = dm/dt$ is the propellant mass flow rate, and v is the velocity of the spacecraft. Changing a spacecraft's orbit in space (or escaping a planetary body's gravity well) requires that a certain amount of kinetic energy to be imparted to the spacecraft. This energy is gained by applying a thrust resulting in a change in velocity of the spacecraft. The typical way to quantify this necessary energy is through the change in velocity (ΔV). Manipulating Equation 2.2 leads to an expression for the propellant mass (m_p) needed by the rocket to achieve the required the ΔV for a given final mass (m_f) of the spacecraft.

$$m_p = m_f \left(e^{\frac{\Delta V}{v_{ex}}} - 1 \right) = m_f \left(e^{\frac{\Delta V}{g_0 I_{sp}}} - 1 \right) \tag{2.3}$$

The above equation shows exponential dependence in the amount of fuel necessary to deliver payloads as a function of ($\Delta V/v_{ex}$). From a cost perspective the amount of propellant should be minimized so that the total mass of the spacecraft is low. The payload mass fraction ($\zeta = m_f/m_0$) serves as a metric for determining how to minimize the fraction of propellant. The equation for the variation of the payload mass fraction is shown below:

$$\zeta = e^{-\frac{\Delta V}{v_{ex}}} = e^{-\frac{\Delta V}{g_0 I_{sp}}} \tag{2.4}$$

in which m_0 is the total initial spacecraft mass. When $v_{ex} \ll \Delta V$ the total payload
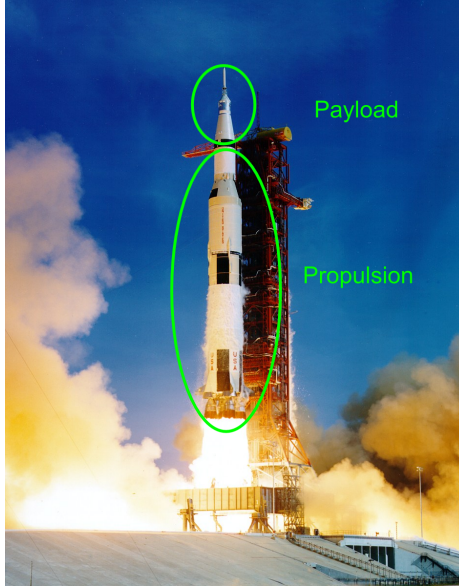
Figure 2.1: Saturn V launch. Credit:NASA

fraction approaches zero and nearly all of the spacecraft mass is dedicated to the propellant, which is non-ideal. Instead v_{ex} should be maximized to minimize the amount of propellant. The exponential nature of this expression results in dramatic changes to the payload mass fraction as the ratio $(\Delta V/g_0 I_{sp})$ varies. It also implies that for a given ΔV the specific impulse should be maximized.

A simple one way mission from the Earth to the Moon can be considered using a chemical propulsion rocket such as the RS-25 engines (Space Shuttle Main Engines) to illustrate the effects of the rocket equation. The RS-25 engines had a specific impulse ranging from $366 - 452$ seconds depending on the conditions in which they operated. For this exercise a constant value of 452 seconds is assumed. A one way mission to the Moon from the surface of the Earth requires a ΔV of approximately 12 km/s. Using RS-25 engines for this mission results in a payload mass fraction of $\zeta = 0.067$ which means that around 7% of the mass on the launch pad is delivered to the Moon while 93% of the mass is fuel. The rocket equation is clearly illustrated by looking at Figure 2.1 in which the payload delivered to the moon by the Saturn V rocket during the Apollo missions is the small section illustrated.
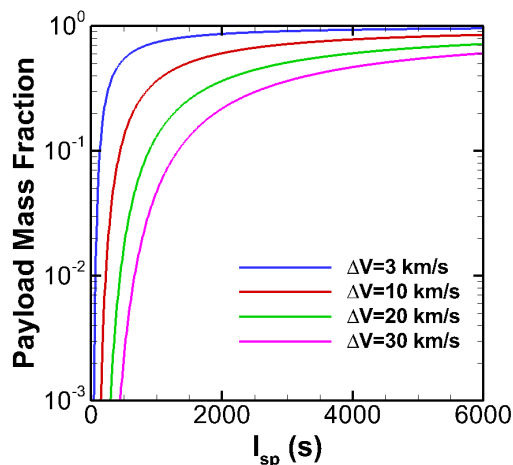
Figure 2.2: Payload mass fraction variation with specific impulse.

The effect of the rocket equation on payload mass fraction is further illustrated by Figure 2.2 which shows the payload mass fraction as a function of the specific impulse for a number of ΔV's. The lower ΔV's show a more rapid increase in the payload mass fraction as the I_{sp} is increased. The chart also illustrates that large gains in propellant mass fraction are achieved as the I_{sp} is initially increased (e.g $<$ 1000 seconds) while at high I_{sp} (e.g. $>$ 4000 seconds) there are diminishing returns. On this graph the example moon mission is nearest the red $\Delta V = 10$ km/s line which has a payload mass fraction of less that 0.1. These plots illustrate the "tyranny" of the rocket equation as well as the drastic improvements in system mass that can be achieved by choosing highly efficient, high I_{sp} propulsion systems. Decreasing system mass can then significantly decrease costs of spacecraft and improve the capabilities for further exploring space.

2.4   Propulsion Methods

Propulsion systems must do one thing, impart a force on the spacecraft to change its velocity. Typically the force is applied by expelling a working gas one direction while the spacecraft is accelerated in the opposite direction. Current in-space propul-

sion technology includes cold gas thrusters, chemical rockets, nuclear thermal rockets, and electric propulsion devices.

Cold gas thrusters are the simplest method to produce thrust in which a high pressure gas is expanded out of a nozzle. Typical cold gas thrusters have very low specific impulse (< 100 seconds) but are the simplest to design. Thrust is generated in the device due to the pressure forces on the walls of the thruster and nozzle. Figure 2.3 demonstrates how thrust is generated in these simple devices by illustrating the pressures inside the nozzle (p_{int}) and the flow out of the nozzle. Ignoring external pressures, the high internal pressure forces on the left walls of the nozzle are not balanced by any pressure forces on the right. This creates a net force, the thrust, which pushes the rocket to the left. This net force can be found by integrating all the pressure forces on the walls, but a simpler method finds this force by considering the fluid control volume and integrating the momentum equation. The resulting relation is shown below which relates the thrust to the internal pressures (p_{int}), the mass flow rate ($\dot{m}$), and the exit velocity.

$$T = \oiint p_{int} dA = \dot{m} v_{ex} \tag{2.5}$$

The maximum efficiencies of cold gas thrusters can be estimated from thermodynamics. If the nozzle is working perfectly, all of the thermal energy of the working gas is converted into a directed kinetic energy and expelled out of the nozzle. A simple one dimensional energy equation can be used to estimate this ideal operation and predict the propellant exit velocity and specific impulse. The resulting expression for the maximum specific impulse is shown in Equation 2.6.

$$I_{sp,max} = \frac{\sqrt{2c_p T_0}}{g_0} \tag{2.6}$$

In this equation c_p is the constant pressure specific heat and T_0 is the stagnation tem-
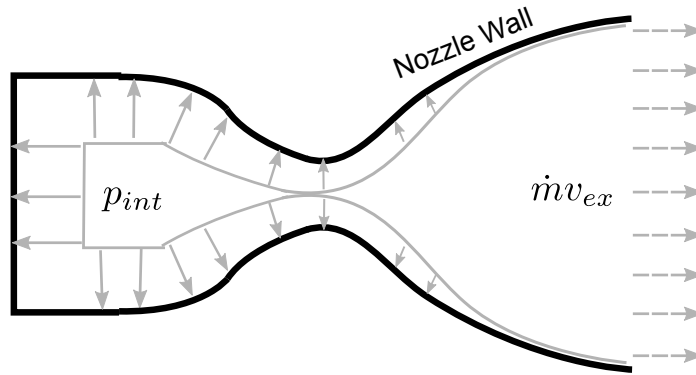
Figure 2.3: Schematic of thrust generation in a nozzle.

perature in the pressure vessel. A cold gas thruster using nitrogen at a temperature of 300 K has an exit velocity of around 775 m/s and a specific impulse of around 79 seconds. These are low performance parameters but the simplicity and reliability of these systems insures that they are still used.

Chemical rockets differ from cold gas thrusters by first heating the gas though chemical reactions which occur in a combustion chamber. The high energy gas leads to much higher performance and specific impulse for these types of devices as illustrated by Equation 2.6. Similar to cold gas devices, thrust is primarily generated by pressure forces on the walls of the rocket. These devices however are limited to combustion chamber temperatures of around 3500 K due to material constraints for temperature and pressure. Furthermore, chemical rockets are limited in specific impulse performance to the energy that is in the chemical bonds of the fuel. The Space Shuttle main engines (RS-25 engines) mentioned in the previous section are some of the best performing engines ever made operating at a maximum specific impulse of around 452 seconds. The chemical rockets show a significant improvement over cold gas thrusters which occurs due to the heating of the propellant by chemical reactions. Chemical rockets are also very versatile and can be used for a broad range of thrust

applications from milli-newtons to mega-newtons. These rockets are currently the work-horse of modern rocket propulsion.

Nuclear Thermal Rockets (NTR) heat gas by flowing it through a heat exchanger attached to a nuclear reactor and then passing the gas through a rocket nozzle. Energy is imparted to the gas through a heat exchanger instead of a chemical reaction. Similar to cold gas and chemical rockets, thrust is generated due to the pressure forces on the thruster and nozzle walls. Generally NTR have higher specific impulse than chemical rockets. This performance improvement is primarily attributed due to the fact that NTR's are able to heat the working gas to temperatures similar to chemical rockets and use hydrogen as a fuel which has a much higher specific heat (almost an order of magnitude) than the typical gases (water vapor for RS-25) in chemical rockets. Specific impulses for the Nuclear Engine for Rocket Vehicle Application (NERVA) program were reported to be around 850 seconds with a reported thrust of 333.6 kN. [16, 17] While NTR has shown good performance these rockets have not been extensively developed since the 1970's when NERVA was canceled due to budgetary concerns. Currently efforts are underway to resurrect the NTR program at NASA.

2.5 Electric Propulsion

EP is unique compared to all the other propulsion methods because the amount of energy which can be put into the fluid is no longer limited by chemical reactions or the ability to exchange heat between the nuclear reactor and the fluid. Instead the energy is limited only by the available power. The ability to add more energy to the gas/plasma particles results in higher specific impulse and performance. Material constraints which limit the design of combustion systems are also alleviated because the plasma can interact with the spacecraft through the long-range electromagnetic forces to create thrust keeping the plasma away from the walls. There are three basic

types of EP devices that use different mechanisms to produce thrust.

The simplest type of electric propulsion devices are electrothermal devices. These include resistojets in which a gas is heated by passing over a heated surface and arcjets in which the gas is heated by passing through an arc discharge. Electrothermal devices produce thrust in the same way as cold gas, chemical, and nuclear thermal rockets due to pressure forces. The only difference is that in electrothermal devices the gas is heated by an electrical power source through a heater or a plasma arc.

Electrostatic propulsion devices generate a plasma and then accelerate the constituent charged particles using an imposed or induced electric field. These devices are classified as electrostatic because they use the electric field component of the Lorentz force equation, shown below, to accelerate the charged particles.

$$\boldsymbol{F} = q(\boldsymbol{E} + \boldsymbol{v} \times \boldsymbol{B}) \tag{2.7}$$

In this equation q is the particle charge, E is the electric field, and B is the magnetic field. Examples of electrostatic propulsion include gridded ion thrusters.

Electromagnetic propulsion devices accelerate the plasma through interactions between applied or induced magnetic fields and currents induced in the plasma. Forces are generated here by the second term in the Lorentz force equation due to currents flowing across magnetic fields. Examples of electromagnetic thrusters include Magnetoplasmadynamic (MPD)'s and magnetic nozzle thrusters.

The typical performance of the propulsion methods introduced in this chapter are shown in Figure 2.4 as well as the power required. The operational regimes shown include areas where these devices are predicted to operate in the future. Electric propulsion systems are high specific impulse, low thrust devices, while chemical rockets are low specific impulse, high thrust devices. Electric propulsion devices often operate for months at a time to deliver the desired ΔV while chemical propulsion devices operate at most for minutes at a time. Electric propulsion will deliver a
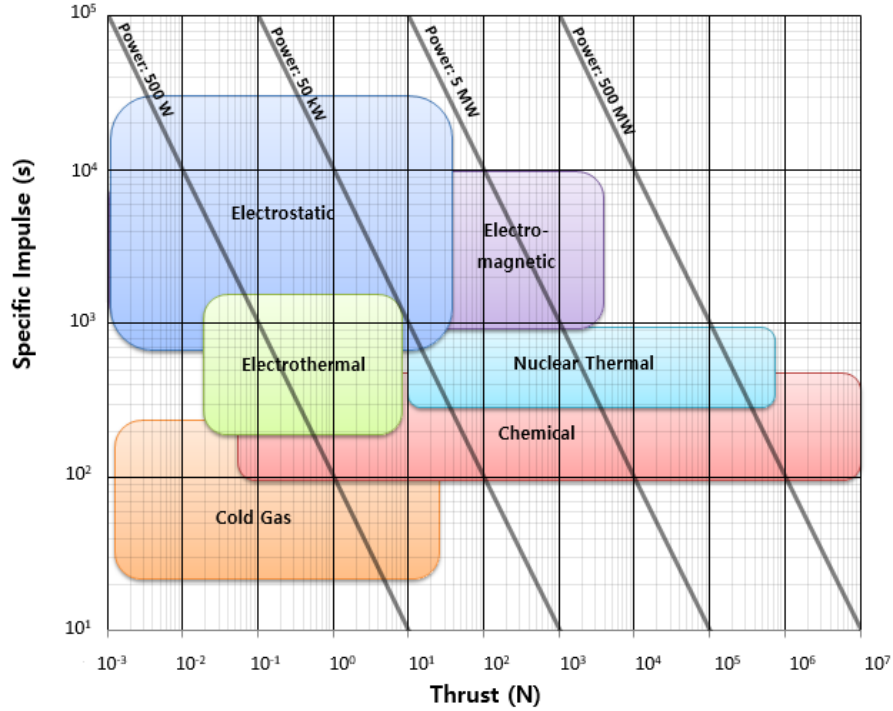
Figure 2.4: Specific impulse versus thrust for common propulsion methods.

payload very efficiently (less propellant, less mass cost) but slowly, while chemical propulsion will get a payload somewhere quickly but inefficiently. In other words, electric propulsion maximizes payload mass fraction while chemical propulsion maximizes thrust thereby minimizing time of flight. Each of these propulsion types has important applications in modern mission architectures.

2.6 Electric Propulsion and the Rocket Equation

The conclusions drawn from the Rocket Equation section suggest that propulsion systems strive for high specific impulse to maximize the payload mass fraction. However, for electric propulsion the power system needed to run these devices should be taken into account to truly consider performance. The simplest way to illustrate the effects of the power system on design is to use the thruster beam power to determine the required power. The power in the beam of the thruster is defined as $P_{beam} = T v_{ex}$.

In an ideal thruster all of the power provided by the power supply would go into the thruster beam, (e.g $P_{supply} = P_{beam}$). However, there are inherent losses in the system which result in the beam power being less than the input power from the power supply. To account for this a general efficiency, η_T, is defined so that $\eta_T P_{supply} = P_{beam}$.

The scaling of the power sub-systems is often defined according to a parameter α which is the mass of the power system needed to produce the desired power with units of kg/W. Combining all of these expressions leads to a relationship for the scaling of the mass of the power sub-system (m_{ps}) which is a function of the power required by the thruster and the performance characteristics.

$$m_{ps} = \alpha T v_{ex}/\eta \tag{2.8}$$

The correct way to approach this problem for the full system is to consider both the mass of the payload and the mass of the power system in the calculation of the final mass. The following expression for the payload mass fraction is found from this treatment:

$$\Gamma = e^{-\frac{\Delta V}{v_{ex}}} \left(1 - \frac{v_{ex}/v^*}{1 + v_{ex}/v^*}\right) \tag{2.9}$$

in which $v^* = (\eta m_{pl})/(\alpha T)$ is a parameter which normalizes the velocity and is a function of the payload mass (m_{pl}). The expression for the payload mass fraction was plotted for several values of v^* and Δv in Figure 2.5 illustrating a more realistic trade space for choosing the specific impulse necessary for a particular mission. This plot shows that a maximum for the payload mass fraction exists which depends on the mission and thruster parameters. Each mission has an ideal specific impulse which is set by ΔV, payload mass, thruster efficiency, and α. The maximum exists because increasing specific impulse leads to an increase in the required power. Eventually,
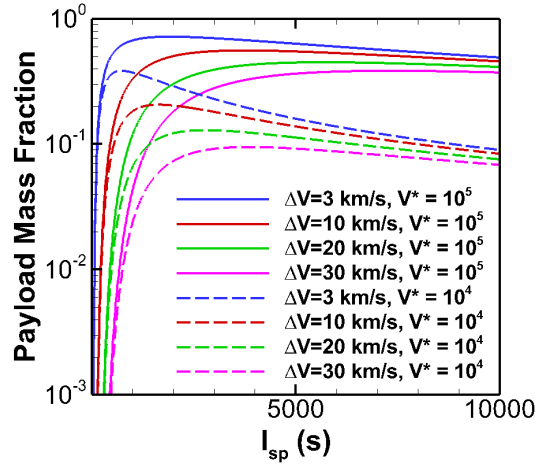
Figure 2.5: Payload mass fraction variation with specific impulse considering power system mass and payload mass for electric propulsion system.

further increasing the specific impulse to lower the spacecraft mass does not offset the increases in power supply mass required.

2.7 Magnetic Nozzles as Electromagnetic Propulsion

The applications of the techniques developed in this dissertations are focused on the study of magnetic nozzles which are a particular type of electromagnetic propulsion. Magnetic nozzles are strong magnetic fields used to guide the flow of plasma to generate thrust. The magnetic field effectively replaces the physical wall of conventional rocket (de Laval) nozzles and guides the flow with a "magnetic wall" that is created by electromagnetic forces on the plasma. A comparison between magnetic nozzles and de Laval nozzles is shown in Figure 2.6 illustrating this difference.

One of the earliest studies of magnetic nozzles was performed by Andersen as a means to create a supersonic plasma to be used for experiments. [18] Andersen's work demonstrated a way to produce a directed beam of energetic plasma, which naturally found applications in space propulsion methods. A number of thruster concepts have been developed since Andersen's work. These thrusters include electrodeless radio

18

De Laval Nozzle

Magnetic Nozzle

Combustion Chamber

Physical Wall

B

I

Plasma Source

Physical Wall

Plasma-Vacuum Boundary
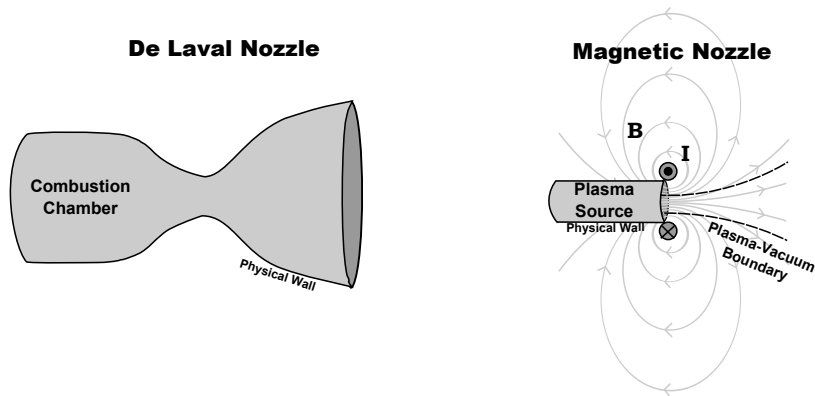
Figure 2.6: Magnetic nozzle comparison with de Laval nozzle.

frequency thrusters, MPD's, and high energy fusion plasma rockets. [19, 20, 21, 3, 22, 23, 24, 25] Even before the work of Andersen, devices were considered at NASA which operate on the same principles as magnetic nozzles, although not explicitly called magnetic nozzle devices. [23]

Electrodeless thrusters use magnetic nozzles as the primary means for accelerating a plasma which is typically produced by an RF source. No electrodes are exposed to the plasma and the plasma is guided by a strong magnetic field. These devices strive to minimize the interaction of plasma with surfaces which should increase thruster lifetime. Minimizing contact with walls should also enable these devices to scale to higher particle and energy densities, which is necessary to push electric propulsion devices into higher thrust density regimes. The improved plasma confinement should also enable scaling to smaller sizes where plasma confinement is more difficult. These are the promises of magnetic nozzle technology and are the goal of current research and thruster development.

Magnetic nozzle thrusters in development span a broad range of powers and sizes. Small, low power ($< 300\ W$) thrusters in development include the Helicon Double Layer Thruster (HDLT), CubeSat Ambipolar Thruster (CAT), and Electron Cyclotron Resonance (ECR) thrusters. [25, 3, 22] These thrusters show promise for

future small satellite (CubeSats, microsattellite) missions in power ranges between 1-300 W. Currently, these low-power thrusters are an important part of this research and have significantly improved the understanding of magnetic nozzle physics in the last few years.[3, 26, 27, 28, 29, 30] Higher power radio frequency (e.g. helicon) sources ($> 500 \ W, < 1 \ MW$) are also being used in magnetic nozzle propulsion devices.[25, 31] An example of this is the VAriable Specific Impulse Magnetoplasma Rocket (VASIMR) which generates plasma by a high power helicon source and then further heats the plasma by an ion cyclotron resonance heating stage.[32, 25] The plasma then undergoes a directed expansion by a magnetic nozzle. The VASIMR experiment currently operates at 200 kW producing approximately 6 N of thrust.[33] Scaling to much higher powers(> 1 MW) is feasible, making VASIMR a candidate for a number of missions including station keeping, lunar tug, and manned missions. Many future fusion-based propulsion systems also incorporate magnetic nozzles.[34, 35] In these theoretical devices the energetic plasma generated by the fusion process is expanded by a magnetic nozzle. It is predicted that these devices would operate at 1 GW generating 4.6 kN of thrust.[36] Fusion devices are not included in Figure 2.4 and would significantly extend the regime of electromagnetic propulsion.

Lastly, MPD research has also suggested that incorporation of magnetic nozzles could improve performance by continuing to accelerate the plasma as it leaves the exit of the thruster.[19, 20, 21] Strong axial guiding fields are anticipated to increase lifetime of these thrusters by limiting the transport of energetic plasma to the walls.

2.8 Past Magnetic Nozzle Theory and Simulations

Magnetic nozzle thrusters operate in a broad range of regimes requiring that different physical models be used. One of the important parameters for determining these regimes is the Knudsen number ($Kn = \lambda_{mfp}/L$) which is a ratio of the mean

free path between collisions (λ_{mfp}) to a characteristic length of the system (L). Small Knudsen numbers ($Kn < 0.01$) imply that frequent collisions occur, locally the plasma is in equilibrium, and thus the fluid description can be used. Fluid models treat the plasma as a continuum from the macroscopic viewpoint. Individual particles are not considered, the plasma is assumed to be in local equilibrium. Conservation equations are solved for quantities such as for density, mean velocity, and temperature.

Large Knudsen numbers ($Kn > 1.0$) imply that collisions are infrequent and that the plasma is experiencing free molecular flow. The plasma can be treated as individual particles which follow trajectories only affected by electromagnetic fields. Kinetic methods can still be used in this regime, but collisions are so infrequent that they need not be considered.

A region known as the transitional regime ($0.01 < Kn < 1.0$) exists between continuum and free molecular flows where fully kinetic methods should be used. The plasma can no longer be assumed to be in equilibrium and must be treated more generally. Insight can still be gained with fluid approaches, but the most accurate results require a kinetic description to capture non-equilibrium effects. Kinetic methods treat the plasma either as individual particles or as a statistical distribution of particles which is affected by electromagnetic fields and collisions. This regime is the most challenging to model.

2.8.1 Fluid Models

One of the simplest ways to describe a plasma is to use a magnetohydrodynamics (MHD) approach. In this model the plasma is treated as a single fluid by combining the conservation equations for the ions and electrons and assuming quasi-neutrality.[37, 38] The electron motion is assumed to be fast, which leads to the simplification of the electron equations of motion to an Ohm's law which is used to solve for the time evolution of the magnetic field. The type of Ohm's law (ideal,

Ideal MHD	Resistive MHD	Hall MHD	Generalized Ohm's Law MHD
$\mathbf{E} + \mathbf{U} \times \mathbf{B} = 0$	$\mathbf{E} + \mathbf{U} \times \mathbf{B} = \eta\mathbf{J}$ $\eta = constant$	$\mathbf{E} + \mathbf{U} \times \mathbf{B} + \dfrac{1}{n_e e}\mathbf{J} \times \mathbf{B} = \eta\mathbf{J}$	$\mathbf{E} + \mathbf{U} \times \mathbf{B} + \dfrac{1}{n_e e}\mathbf{J} \times \mathbf{B} + \dfrac{1}{n_e e}\nabla(n_e k T_e) = \eta\mathbf{J}$

Increased Complexity

→

Incorporate Additional Physics

Figure 2.7: MHD model heirarchy. $\mathbf{E}$ is the electric field, $\mathbf{U}$ is the mean flow velocity, $\mathbf{B}$ is the magnetic field, η is the resistivity, n_e is the electron number density, e is the elementary charge, $\mathbf{J}$ is the current density, and T_e is the electron temperature.

resistive, Hall, generalized) has large implications on the physics captured by this model. Figure 2.7 illustrates the hierarchy of these MHD methods. MHD models have been used in a number of studies, particularly for high density plasmas where the MHD assumptions may hold. [39, 40, 41, 42, 39, 40, 43] Previous parametric studies have suggested that a generalized Ohm's law MHD model should be used to capture the important physical mechanisms of the thrust generation process in many current magnetic nozzle experiments such as the HDLT and VASIMR. [44, 45] A generalized Ohm's law method includes two fluid effects through incorporation of the Hall term and electron pressure effects. The plasmadynamics in magnetic nozzles has also been described by models which treat the electrons and ions as separate fluids. [46, 47, 31, 48, 49] Quasi-neutrality is no longer assumed and the full electron conservation equations are solved. Historically, studies of magnetic nozzles with these models use steady-state approximations and include assumptions (e.g. isothermal or isotropic electrons) that make the solutions computationally tractable. [46, 47, 31]

These fluid models are most appropriate for studying high density plasmas in devices such as MPD's and fusion based propulsion systems. They are not as applicable to lower density devices such as many of the lower power electrodeless magnetic nozzle thrusters which have Knudsen numbers in the transitional regime. [44] Knudsen numbers become particularly low in the plasma plume, where the density decreases

rapidly and few particle collisions occur. The plasmadynamics in these low-density devices may include important non-equilibrium effects, making kinetic modeling necessary for the most accurate solution. There are however important insights which can be gained from using fluid models to study these devices, but some non-equilibrium effects which may be important will be missed.

2.8.2   Kinetic Models

A plasma can be studied kinetically by modeling the individual particle dynamics. Treating the plasma as a collection of particles is the most general way of studying the system but also the most complex. Particle methods have been utilized to study important physical phenomena such as ion acceleration and plasma detachment in magnetic nozzles. [50, 35, 51, 52, 53, 23] In particular, the particle-in-cell (PIC) technique was used to study the formation of double layers in magnetic nozzle plasmas. [52, 51, 54] PIC simulations have typically been limited in scope to one dimensional [51, 54] simulations or very truncated multi-dimensional simulations [55] due to the inherent computational costs associated with particle methods. Simulations which include two- and three- dimensional effects of these systems are still necessary to fully characterize many of the important physical processes. Free-molecular, particle trajectory codes have also been used to study the detachment process. [50, 56, 57] These codes ignore the coupling between the particles which could be very important to the detachment process. Fully kinetic simulations using Boltzmann and Vlasov solvers have yet to be used for studying magnetic nozzles. However, there codes have shown great promise in other devices such as Hall thrusters. [58, 59]

CHAPTER III

Magnetic Nozzle Physics

3.1 Introduction

Magnetic nozzles are functionally similar to de Laval nozzles by achieving thrust through conversion of internal energy or non-directional kinetic energy of the plasma to directed kinetic energy. A comparison between de Laval nozzles and magnetic nozzles is shown in Figure 3.1. The virtue of magnetic nozzles lies in minimizing contact between the high temperature plasma and surfaces while also providing mechanisms for thrust generation by plasma-field interaction. Magnetic field topology and thereby the magnetic nozzle configuration is also variable, enabling versatility in nozzle shape and thrust vectoring without gimbals.

The magnetic fields in a magnetic nozzle must initially confine the plasma plume to a configuration which produces directed kinetic energy. Thrust is generated by the forces that result from the interaction between the magnetic fields and the induced currents. Ion acceleration occurs and non-directed energy is converted into directed kinetic energy. Confinement must eventually be broken to ensure efficient detachment from the closed applied magnetic field lines which may pull the plasma back to the spacecraft. This reflects the requirements of both initial confinement and eventual detachment. The transition from plasma containment to detachment must be understood to optimize magnetic nozzles.
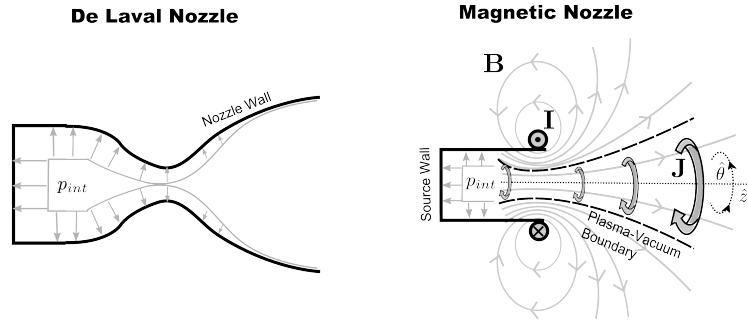
Figure 3.1: Thrust generation mechanism comparison between magnetic nozzle and de Laval nozzle.

This chapter presents an in-depth survey of the important physics of plasma flow in magnetic nozzles. Previous literature reviews and discussions on the topic will be further extended.[46, 60, 61] Findings and advances in magnetic nozzle physics are consolidated, summarized, and analyzed to define the current status of magnetic nozzle theory. The relevant regimes of the different magnetic nozzle physical mechanisms are defined with results from prominent experiments briefly summarized.

3.2 Ion Acceleration and Energy Conversion Physics

Magnetic nozzle ion acceleration mechanisms considered in this review include: A) magnetic dipole force; B) induced electric fields; C) generalized Hall, thermoelectric, and swirl acceleration; and D) directionalizing fluid thermal energy. Many of the physical mechanisms discussed are intimately coupled but are considered separately in the following sections.

3.2.1 Magnetic Dipole Force

Physical Description

Particles in strong magnetic fields will orbit around those field lines. The orbiting particles can be imagined as small current loops centered around the magnetic field
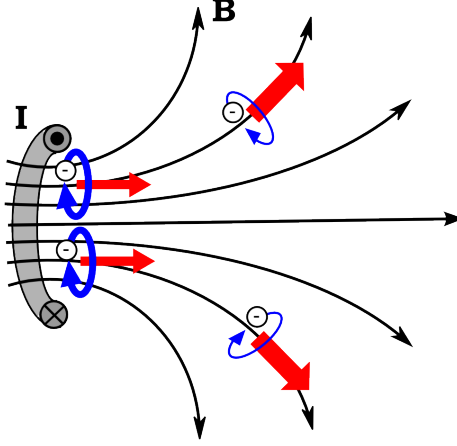
Figure 3.2: Sketch of magnetic dipole force in a magnetic field generated by a current loop (I). Blue arrows are perpendicular velocities while red arrows are parallel velocities. Thickness of the arrows represents the magnitude of the velocity.

lines. The particle orbits are diamagnetic so that the current direction is such that the magnetic field that would be produced by the particle orbit opposes the applied field. The interaction of localized current distribution with the applied magnetic field results in a force.[62] A simple sketch of the effects of this force on the velocities is shown in Figure 3.2. Blue lines illustrate the gyration velocities while red arrows show the velocity along the field line. The thickness of the arrows is meant to represent the magnitude of the velocity. Velocities along the field line increase at the expense of the gyration velocities as the particles are accelerated along the field line.

An expression for this force is shown in Equation 3.1.

$$\boldsymbol{F_\mu} = \nabla\left(\boldsymbol{\mu}_m \cdot \boldsymbol{B}\right) \tag{3.1}$$

where $\boldsymbol{\mu}_m$ is the vector magnetic moment. The general force in Equation 3.1 can be simplified by assuming a constant, anti-parallel scalar magnetic moment.

$$\boldsymbol{F_\mu} = (\boldsymbol{\mu_m} \cdot \nabla)\boldsymbol{B} = -(\mu_m \hat{\boldsymbol{B}} \cdot \nabla)\boldsymbol{B} \tag{3.2}$$

The scalar magnetic moment for these orbiting particles has the form shown below:

$$\mu_m = \frac{mv_\perp^2}{2B} \tag{3.3}$$

where m is the particle mass, v is the particle velocity, and B is the magnetic field strength. The parallel and perpendicular directions are defined with respect to the magnetic field unless stated otherwise.

The general force in Equation 3.1 can be simplified by assuming a constant, anti-parallel magnetic moment.

$$\boldsymbol{F_\mu} = (\boldsymbol{\mu_m} \cdot \nabla)\boldsymbol{B} = -(\mu_m \hat{\boldsymbol{B}} \cdot \nabla)\boldsymbol{B} \tag{3.4}$$

The above description may also be represented by a potential energy $\Phi_\mu = \boldsymbol{\mu_m} \cdot \boldsymbol{B}$.

The magnetic moment of a particle in the above equations is an adiabatic constant of motion if the variation of the magnetic field is small over a single period of cyclotron motion, $\delta B \ll B$. This condition may be represented by the relations shown in Equation 3.5.

$$\frac{dB}{dt} \ll B\omega_c \;\; or \;\; \nabla_\parallel B \ll B\frac{v_\parallel}{\omega_c} \;\; or \;\; r_L \left|\frac{\nabla B}{B}\right| \ll 1 \tag{3.5}$$

In these equations $\omega_c = qB/m$ is the cyclotron frequency of the particle. The first condition implies that the temporal variation of the magnetic field is small during a cyclotron orbit. The second condition implies that the spatial variation of the magnetic field along the magnetic field direction is small over the distance traveled by the particle during a cyclotron orbit. The last condition is the most often used and describes the ratio of the Larmor radius, $r_L = mv_\perp/(qB)$, to the characteristic length over which the magnetic field changes, $1/|\frac{\nabla B}{B}|$. Particles satisfying these conditions are said to be magnetized.

The condition for maintaining magnetization must be considered more generally when collisional effects are included. A highly collisional species may experience

collisions on the same timescale as its cyclotron motion causing the particles to violate adiabaticity. The ratio of the cyclotron frequency of a particle to the collision frequency is defined as the Hall parameter. The Hall parameter (Ω_{col}) is shown in Equation 3.6 and gives an additional necessary condition for maintaining adiabaticity.

$$\Omega_{col} = \omega_c/\nu \gg 1 \tag{3.6}$$

in this equation ν represents the collision frequency.

Energy Exchange

To describe adiabatic energy exchange the conservation of total kinetic energy, K_{total}, of a particle is used, shown in Equation 3.7.

$$K_{total} = K_\perp + K_\parallel = \frac{mv_\perp^2}{2} + \frac{mv_\parallel^2}{2} = constant \tag{3.7}$$

When the magnetic moment of a particle is an adiabatic invariant and the total kinetic energy of a particle is conserved the velocity parallel to the magnetic field increases as the magnetic field strength decreases. Combining these equations results in the following relationship for the velocity parallel to the magnetic field.

$$v_\parallel = \sqrt{v_{total}^2 - 2\mu_m B/m} \tag{3.8}$$

In this expression both the magnetic moment and the total velocity are constant.

Electron-ion Coupling

For certain parameter regimes the heavy ions may become demagnetized while electrons remain magnetized. Electrons maintain adiabaticity while they are magnetized and are accelerated from high magnetic field to weak magnetic field regions. The ions are not magnetized and do not feel the magnetic dipole force. Acceleration

of the electrons and not the ions leads to a charge imbalance which then leads to the formation of a field-parallel electric field which accelerates the ions out along with the electrons.[63, 23]

Previous Work

The behavior of magnetized particles described in this section is similar to the well known physics of magnetic mirrors.[64] Magnetic mirrors confine particles through a converging magnetic field while magnetic nozzles accelerate particles through a diverging magnetic field. Insights can be gained by comparing with magnetic mirror studies.

Experimental thrusters have suggested this mechanism as the primary means to produce ion acceleration. The VASIMR propulsion system operating with ion cyclotron resonance heating has shown significant ion acceleration which it attributes primarily to this force.[25, 65, 32, 50, 33, 66] Other theoretical, computational, and experimental efforts have also studied and demonstrated the thrust production capabilities of this mechanism. [67, 23, 24] The body of work thus far has shown that this is an effective method for acceleration, but further study is necessary, particularly to understand the coupling between electrons and ions as well as the conditions where particles become demagnetized and this treatment is no longer valid.

It is important to note that this acceleration mechanism was derived primarily from a particle or kinetic standpoint. The manifestation of this mechanism from a fluid perspective has also been considered. A particularly important result from the continuum treatment is that this force appears explicitly in the equations of motion when anisotropic pressures are present in the plasma. [68]

3.2.2   Induced Electric Fields

Physical Description
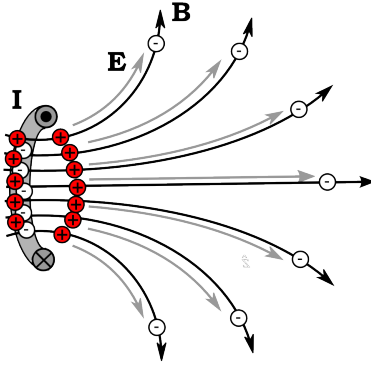
Figure 3.3: Sketch of electron driven acceleration in a magnetic field generated by a current loop (I). The electric field is shown with gray lines while the magnetic field is shown with black lines.

Electric fields form to strive to maintain quasi-neutrality in a plasma. Imbalances of charge fluxes due to boundaries (e.g. sheaths), ambipolar , and forces on the particles can drive the formation of these electric fields.

An example of an electric field that forms due to an initial imbalance of fluxes is shown in Figure 3.3. A plasma produced in a plasma source is exposed to a vacuum. The light electrons, which have a much higher thermal velocity ($v_{th} = \sqrt{k_B T/m}$) than the heavy ions, expand rapidly into the vacuum leaving the ions behind. The expansion leads to an imbalance of charge and establishes an electric field which accelerates the ions out with the electrons. The electric fields driving this acceleration mechanism have shown characteristics of double layers[69, 30, 3] or ambipolar fields [66] which will be discussed in the sections below.

Energy Exchange

Induced field ion acceleration occurs due to an exchange of energy between the electron energy and the field aligned ion directed kinetic energy. The thermal expansion of the electrons leads the formation of a potential drop which accelerates the ions. Considering only the induced electric fields however does not lead to net additional

production of thrust beyond the pressure of the plasma on the walls. [70] If only one-dimensional effects are considered no net energy is added to the axial direction. Energy gains in the axial direction by the ions are balanced by energy losses in the axial direction from the electron. In other words, there is no net gain of energy in the axial direction when considering electron-ion pairs. Additional multi-dimensional effects due to the magnetic field, induced currents, or instabilities are necessary to explain the full energy exchange process. A mechanism must exist to couple energies from other dimensions to the acceleration direction to generate a force which results in directed kinetic energy. Furthermore, Fruchtman showed with a simple one dimensional analysis that the requirement of zero electric fields at the boundaries of a one dimensional treatment of the plasma require that no net momentum be imparted on the plasma if only electric field effects are considered.

Previous Work

Double layers are sharp potential drops that occur between two regions of opposing charge. The sharp potential accelerates the ions leading to the formation of an ion beam. The double layer region is short ($\approx 10 - 100\lambda_D$)s.[71] The debye length λ_D is the characteristic length in a plasma over which short range electric fields are shielded out. The essential requirements for a double layer are that the electric field inside the double layer is much stronger than the field surrounding it and that a region exists which violates quasi-neutrality. [26] The current-free double layer is a particular type of double layer through which no net current flows.[72, 73] Recently, current free double layers have been created in expanding plasmas which are guided by magnetic nozzles. [26, 30] These double-layers are current-free because there are no electrodes driving a current. Acceleration due to double layers in magnetic nozzles has been shown experimentally [30, 69] and by PIC simulations.[51, 54]

A number of theories exist on what drives the formation of these current free

double layers. One theory uses a one-dimensional four species approach including diffusive transport to explain the formation. [74] This theory predicted that double layers exist over a particular range of background pressures which depends on the plasma properties. Another theory uses a quasi-one-dimensional treatment of the plasma with three species (two electron species) to describe the double layer formation. [75] This theory predicts double layer formation when the ratio of the two electron temperatures is greater than 10. A free-standing sheath theory also exists which suggests that a sheath forms when plasma radius expands by 28% due to the magnetic field. [76] There is no clear consensus yet as to which theory is the most correct and this remains an open question. Also note that all of these theories assume that the constituent species are isothermal.

Ambipolar ion acceleration has been observed in experiments [19, 66] and simulations.[65] Ambipolar electric fields can reach lengths of 10, 000's of Debye lengths making them much longer than double layers. [66] The plasma is also no longer isothermal with the temperature decreasing as the plasma expands.

Several models have been used to study ambipolar acceleration. One model assumes a quasineutral paraxial plasma expansion along the magnetic field.[65] A species of electrons trapped between the magnetic nozzle throat and a time-dependent rarefaction wave was included in this study and modeled with kinetic theory. Ions are treated with fluid theory. The importance of adiabatic cooling of electrons is shown in relation to the ion acceleration. Another model uses one-dimensional, steady-state, magnetized plasma theory ignoring collisions to analyze experimental data. [66] Ions are treated using a one dimensional energy conservation equation while electrons are treated as a fluid. Results with this treatment verified the ambipolar acceleration mechanism in experiments. Finally, an adiabatic theory is proposed which is combined with field aligned momentum equations and the assumption of Maxwellian plasma. [77] A simple linear relationship is found relating the variation of the electron

temperature to the potential in the plasma.

3.2.3 Magnetic Stresses on a Fluid

Physical Description

Forces on a plasma from a fluid perspective can be found by considering the interaction of the applied magnetic field and the induced plasma currents. The fluid form of the Lorentz force arises from the fluid momentum equations and has the following form for the magnetic field term $\boldsymbol{J} \times \boldsymbol{B}$. Assuming non-relativistic flows in Ampere's law gives a description for the current density in terms of the magnetic field, $\boldsymbol{J} = \nabla \times \boldsymbol{B}/\mu_0$. Combining these equations results in two terms which illustrate the forces on the plasma due to the magnetic field. These are shown on the right hand side of Equation 3.9 as the magnetic pressure (first term) and the magnetic field convection (second term).

$$\boldsymbol{J} \times \boldsymbol{B} = -\nabla\left(\frac{\boldsymbol{B}^2}{2\mu_0}\right) + \frac{1}{\mu_0}(\boldsymbol{B} \cdot \nabla)\boldsymbol{B} = -\frac{1}{\mu_0}\nabla \cdot \left(I\frac{\boldsymbol{B}^2}{2} - \boldsymbol{B} \otimes \boldsymbol{B}\right) \tag{3.9}$$

In this equation $\boldsymbol{B}^2 = \boldsymbol{B} \cdot \boldsymbol{B}$. Returning to Figure 3.1, the thrust generated by de Laval nozzles is typically derived from a steady state control volume analysis of the pressure on the walls of the nozzle. Assuming operation in a vacuum, this analysis leads to an expression for the thrust not in terms of the internal pressure forces on the nozzle wall, but in terms of the mass flow rate, the exit velocity of the fluid, and the pressure at the nozzle exit. The overall effect of the internal pressure on the walls is thus represented by the momentum flux out of the nozzle exit and the pressure at the nozzle exit. This description is necessary because measurement of the internal pressures on the nozzle wall is not possible.

Magnetic nozzle thrust may also be determined by a steady state control volume

analysis if a well defined plasma-vacuum boundary is present. The force imparted on the spacecraft can be found by determining the total $\boldsymbol{J} \times \boldsymbol{B}$ force on the plasma. The effects of this force are significantly simplified in a control volume approach by representing the force as the Maxwell stress tensor $\left(I\frac{\boldsymbol{B}^2}{2} - \boldsymbol{B} \otimes \boldsymbol{B}\right)$ just derived. Integrating the Lorentz force over a control volume leads to the following simplified representation of the stresses on the walls of the control volume.

$$\iiint\limits_{V} \boldsymbol{J} \times \boldsymbol{B} dV = \frac{1}{\mu_0} \oint_S \left(\boldsymbol{B} \otimes \boldsymbol{B} - I\frac{\boldsymbol{B}^2}{2}\right) \cdot \hat{\boldsymbol{n}} dS \qquad (3.10)$$

This simplification allows the total force to be determined by the surface magnetic field forces on the control volume, similar to the description in de Laval nozzles. Thus the total force on the plasma can be described in multiple ways: i) determine the magnetic stress tensor terms at the surface of the control volume; ii) integrate the $\boldsymbol{J} \times \boldsymbol{B}$ over the the entire volume, iii) measure velocity and mass flow rate at the nozzle exit. If the electric field is also taken into account the total force can more generally be described by Equation 3.11 which is the full Maxwell stress tensor.

$$\iiint\limits_{V} \left(\rho_e \boldsymbol{E} + \boldsymbol{J} \times \boldsymbol{B}\right) dV = \oint_S \left[\epsilon_0 \left(\boldsymbol{E} \otimes \boldsymbol{E} - I\frac{\boldsymbol{E}^2}{2}\right)\right.$$
$$\left. + \frac{1}{\mu_0} \left(\boldsymbol{B} \otimes \boldsymbol{B} - I\frac{\boldsymbol{B}^2}{2}\right)\right] \cdot \hat{\boldsymbol{n}} dS \qquad (3.11)$$

In this equation ρ_e is the charge density. The full Maxwell stress tensor completely describes the effects of the magnetic and electric field forces on a conductive material such as a plasma. Evaluation of the right-hand side of this equations will lead to an expression for the total force based on the surface magnetic and electric fields.

Confinement

Confinement of the plasma must occur in order for a magnetic wall to establish. Confinement in relation to thermal forces is characterized by the ratio of the fluid pressure to the magnetic pressure shown in Equation 3.12.

$$\beta_p = \frac{nk_BT}{B^2/2\mu_0} < 1 \tag{3.12}$$

If this relation is satisfied the magnetic pressure is stronger than the thermal pressure and confinement is possible but not guaranteed. Formation of a current layer which shields the internal plasma requires large induced fields which are diamagnetic in character. The diamagnetic behavior of the plasmas is also quantified by β_p. For confinement this ratio must be less than one and for the plasma to be diamagnetic in character it must not be much less than one. For $\beta_p \ll 1$ the plasma is confined by the magnetic pressure but the internal fields may not be entirely canceled out. In this high magnetic field strength regime directionalizing of thermal energy and conservation of the magnetic moment adiabatic invariant may become intimately coupled because the magnetic fields are not canceled out in the internal plasma.

The influence of induced fields is also characterized by the magnetic Reynolds number (R_m) defined in Equation 3.13.

$$R_m = UL/\eta = UL\sigma\mu_0 \tag{3.13}$$

In this equation η and σ are the plasma resistivity and conductivity respectively. For large R_m the plasma is highly conductive and the induced magnetic field may be large. Large R_m implies that the plasma is confined and significant diffusion of the plasma across the magnetic field lines does not occur. Diffusive processes become important as R_m is decreased and may degrade the current layer which shields the inner core of the plasma. [35] Diffusion of the plasma must be understood to characterize the losses due to non-ideal confinement.

Another important parameter to insure confinement of the plasma is found by comparing the advection along the field line to the cross field diffusion using the Peclet number. [48]

$$Pe = \frac{c_s/L}{D_\perp/R^2} \tag{3.14}$$

In this equation c_s is the ion acoustic speed, L a characteristic length, $D_\perp$ is the perpendicular diffusion coefficient, and R is the characteristic radius of the plasma. $Pe \geq 1$ is required for plasma to limit the diffusion of the plasma across the magnetic field lines. This parameter can be an important consideration for detachment by cross-field diffusion as well, discussed later in this chapter.

Energy exchange

The energy exchange in this mechanism occurs between the random thermal energy of the plasma and the directed kinetic energy. Nozzles accelerate a fluid to supersonic velocities through converging-diverging configurations which achieve sonic velocity at the throat. This acceleration is driven by a pressure gradient and involves the conversion of thermal energy into directed kinetic energy. De Laval nozzles direct thermal motion into the axial direction with a physical wall. Magnetic nozzles can direct thermal energy by confining the plasma to a desired geometry with a strong guiding field. Interaction of the guiding field with the plasma can create a magnetic wall characterized by a current layer at the plasma-vacuum boundary, as seen in Figure 3.4. If the plasma is sufficiently conductive this current layer may shield the inner plasma from the applied field. [35, 40, 42] The function of the externally applied field is to form this current layer which acts as a confining wall to the internal plasma. The forces acting in this current layer replace the forces acting on the wall of a de Laval nozzle.

The physics of energy conversion in this mechanism are based on hydrodynamics
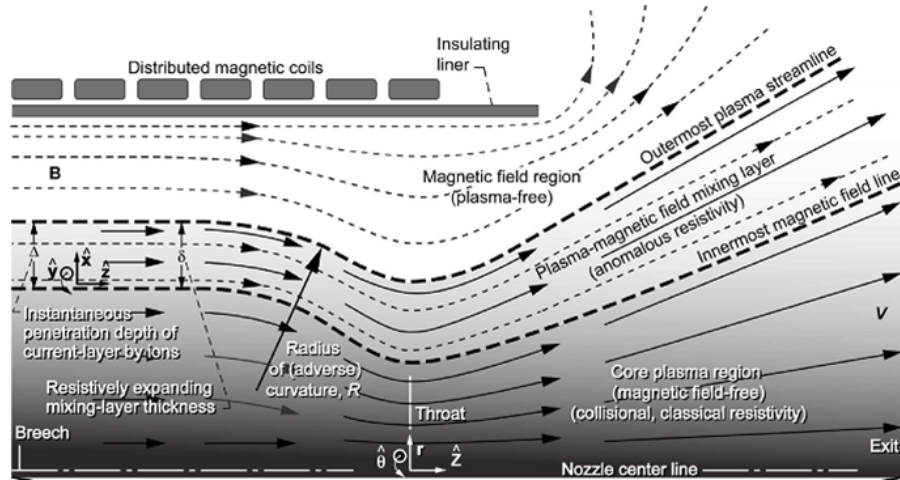
Figure 3.4: Magnetic nozzle configuration for directionalizing of thermal energy in a high density, highly conductive plasma.

while the geometry of the magnetic nozzle is determined by plasma-field interaction. Relationships based on hydrodynamics similar to those in de Laval nozzle analysis may be used to analyze energy conversion if negligible losses occur in establishing the magnetic wall.

Previous Work

Thrust analysis with the magnetic stress tensor was first suggested for MPD's.[1] Calculations using the magnetic stress tensor or similar methods to determine thrust show agreement when compared with experimental measurements.[78, 20, 79] The physics of converting thermal energy to kinetic energy through the use of a magnetic nozzle has been demonstrated experimentally and computationally. [67, 19, 80, 41] Experiments with high density plasmas have showed nozzle expansion results which matched more closely with isentropic expansion models than with a magnetic moment conservation model. [19]

3.3 Momentum Transfer and the Plasma Currents

The momentum imparted on the plasma due to ion acceleration must be transferred to the spacecraft to produce thrust. The electric field alone is not enough to transfer momentum to the spacecraft, particularly since there are no electrodes. Magnetic nozzles transfer momentum from the plasma to the spacecraft through a mutual Lorentz force between the source of the applied magnetic field (permanent magnet, solenoid, etc) and the plasma. The force on the applied field source results from the interaction of the induced magnetic field and the currents which generate the applied field. Similarly, the force on the plasma results from the interaction between the magnetic field in the plasma plume and the induced currents. The forces on the magnetic field source and the plasma are equal and opposite. Net thrust is produced when the plasma and the source of the applied magnetic field generate a mutual repelling force in the section downstream of the nozzle throat.

3.3.1 Plasma Currents

Induced currents are created throughout the magnetic nozzle plume due to the motion of the plasma and are primarily azimuthal. The resulting currents can be either diamagnetic, opposing the applied field, or paramagnetic, amplifying the applied field. Diamagnetic currents create a repulsive force in the diverging section which is desirable for thrust production while paramagnetic currents create an attractive force resulting in drag on the plasma. Diamagnetic currents also result in the cancellation and divergence of magnetic field lines while paramagnetic currents amplify and focus the field lines. The ion acceleration mechanisms discussed in the previous section primarily induce diamagnetic currents.

Previous studies have confirmed that the forces between the currents induced in the plasma plume and currents which generate the applied field of the magnetic nozzle are the primary mechanisms by which momentum is transfered between the spacecraft

and the plasma. [81, 82, 83, 47, 46] Diamagnetic currents for thrust generation have been studied in numerous experiments and have been directly measured in the diverging section of magnetic nozzle plasma plumes.[84, 85] Paramagnetic and diamagnetic currents may exist simultaneously in a plasma due to diamagnetic surface currents and paramagnetic volumetric currents. [82, 83, 47, 46] To produce thrust under these conditions the force per unit length due to the diamagnetic surface currents must exceed that of the paramagnetic volumetric currents.[83]

As an additional note, for a magnetic nozzle with both a converging and diverging section the physics becomes more complex. For the plasma to be continually accelerated by the Lorentz force the currents should be paramagnetic in the converging section and diamagnetic in the diverging section. However, if the currents are paramagnetic in the converging section the fields do not produce a confining force on the plasma. An analog may again be drawn to de Laval nozzles in which the pressures on the converging wall are not in the direction which actually generates positive thrust thus being equivalent to diamagnetic currents in the converging section of the magnetic nozzle. This initial convergence is necessary to effectively accelerate the fluid to sonic or supersonic velocities.

3.3.2   Hall and thermoelectric effects on current

To describe Hall and thermoelectric currents which may be generated in the plasma the fluid form of the electron momentum equation is simplified by assuming the characteristic frequency for electron motion is much faster than the characteristic frequency for the motion of the plasma as a whole ($\omega_{ce} \gg \omega_f$). The assumption about the time scales, combined with the fact that the ion mass is much greater than the electron mass ($m_{ion} \gg m_e$), and treatment of the plasma as a single fluid leads to the generalized Ohm's law shown in Equation 3.15.

$$\boldsymbol{E} = -\boldsymbol{U} \times \boldsymbol{B} + \frac{1}{n_e q}\boldsymbol{J} \times \boldsymbol{B} - \frac{1}{n_e e}\nabla(n_e k T_e) + \eta\boldsymbol{J} \qquad (3.15)$$

In this equation $\boldsymbol{U}$ is the center of mass velocity of the ions and electrons, n is the number density, T is the temperature, and k is the Boltzmann constant. The terms on the right side of Equation 3.15 will be referred to as the convective, Hall, electron pressure, and resistive terms, respectively.

An order of magnitude analysis shows that the importance of the Hall term is characterized by the following two ratios: ω_f/ω_{ci} and ω_{ce}/ν_e. In these relations ν_e is the collision frequency of the electrons. The first condition compares the Hall term to the convective term while the latter compares the Hall term to the resistive term. The larger the value of these terms the more important the Hall term becomes. The first ratio implies that the Hall term is important when ions are effectively demagnetized in the domain. The second ratio combined with the original assumptions made in deriving the generalized Ohm's law imply that the electrons must be magnetized.

Characterizing the effects of the Hall term are non-trivial due to its non-linearity. Studies have shown that the Hall effect can generate azimuthal currents which interact with the applied field and produce an accelerating force on the plasma.[86, 87, 88, 88] The Hall effect describes the $\boldsymbol{E} \times \boldsymbol{B}$ drift of electrons which ultimately results in current due to the lack of a equivalent $\boldsymbol{E} \times \boldsymbol{B}$ drift of the demagnetized ions. It has also been suggested that the Hall effect can produce azimuthal rotation of plasma due to interaction between the applied field and induced radial and axial currents. [34, 35, 44] The azimuthal velocity due to this force results in a swirl kinetic energy of the plasma. This input of swirl kinetic energy can be a loss mechanisms or result in the further generation of axial kinetic energy due to the conservation of the kinetic energy and the angular momentum of the plasma as it expands. [86, 88, 87, 89] The swirl acceleration mechanism can be considered separately, but may be strongly coupled to the Hall acceleration mechanism. [89]

As discussed in the previous section, in expanding magnetic nozzles the mobile electrons establish an electron pressure gradient ahead of the slow ions. To maintain quasineutrality an electric field is formed which accelerates ions and slows down the fast expanding electrons. The electron pressure gradient and the resulting electric field are represented by the electron pressure term in the generalized Ohm's law. Diamagnetic azimuthal currents are produced due to this thermoelectric effect which result in an accelerating force on the plasma. [90, 88, 87, 84] Comparison of the theory for fluid Hall and thermoelectric acceleration with experimental data has shown agreement. [90, 88, 87, 84]

3.4   Plasma Detachment

For magnetic nozzles to produce thrust the directed kinetic energy must detach from the applied field. Detachment is a complex problem because it is may not be a binary phenomenon with different portions of the plume being either attached or detached. Plasma detachment mechanisms are central to magnetic nozzle design because losses due to electromagnetic drag forces and divergence of the plasma plume must be minimized. Detachment methods can be grouped into three categories: collisionless, collisional, and magnetic reconnection detachment.

3.4.1   Collisionless Detachment

The primary means for achieving collisionless detachment are due to loss of magnetization, electron inertial effects, [50, 53, 91, 92, 82, 47, 46, 93, 94] and induced magnetic field effects.[39, 95, 96, 97, 81, 31, 98, 94, 82, 46, 83]

3.4.1.1   Loss of Magnetization

Detachment due to the loss of magnetization occurs when the conditions of Equation 3.5 are violated and the plasma effectively becomes demagnetized. The third

41

condition relating the Larmor radius of the particle to the characteristic length of magnetic field changes is the most often used of these to quantify detachment. Demagnetization implies that particles are no longer bound to single field lines. The particle inertia becomes too much for the magnetic field force to confine it to a field line. This behavior can best be visualized by imagining a particle which starts an orbit around one field line but then during this orbit encounters a different magnetic field which alters the previous orbit.

Loss of magnetization is specific to each species with electrons remaining magnetized at weaker magnetic fields than the heavy ions. The ions are more likely to separate from the field lines because their large mass gives them more inertia and makes them harder to confine. Some theory predicts that the demagnetization of ions alone does not ensure detachment of the plasma as a whole due to the formation of electric fields between the bound electrons and the detached ions. [57, 47, 46, 82, 93, 91, 53] Detachment in this particular complex scenario is referred to as inertial detachment and will be discussed in the next section. Lagrangian invariants may also be used to define distinct regions in which charged particles may be found. [56] These invariants give conserved quantities for the particle dynamics which along with a magnetic field structure define distinct regions that particles with known properties can reach (mass, momentum, energy).

3.4.1.2 Particle drifts

Particle detachment can occur due to single particle drifts across curved magnetic field lines. The following discussion is shown pictorially in Figure 3.5. When particles enter regions with curved magnetic field lines they experience both curvature and $\nabla \boldsymbol{B}$ drifts defined in Equations 3.16 and 3.17.

$$\boldsymbol{v}_R = \frac{mv_\parallel^2}{qB} \frac{\boldsymbol{R_c} \times \boldsymbol{B}}{R_c^2 B} \tag{3.16}$$
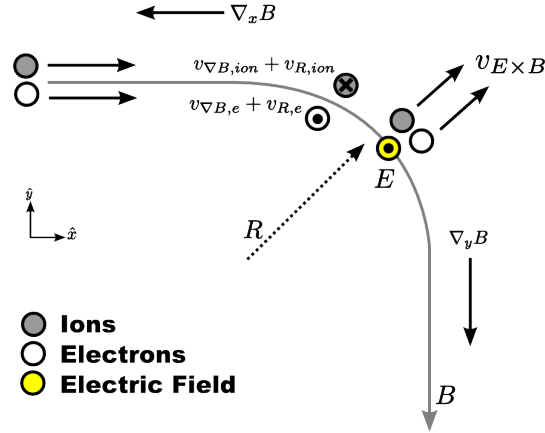
Figure 3.5: Particle drifts in a curved magnetic field. Ions and ion drifts denoted in grey while electrons and electron drifts are denoted in white. The induced electric field is shown in yellow. Vectors for the magnetic field gradients, particle drift velocities, radius of curvature, and magnetic field are shown.

$$\boldsymbol{v}_{\nabla B} = \frac{mv_\perp^2}{2qB} \frac{\boldsymbol{B} \times \nabla \boldsymbol{B}}{B^2} \tag{3.17}$$

Figure 3.5 shows the flow of ion and electron particles entering a curved magnetic field region. The resulting curvature and $\nabla \boldsymbol{B}$ drift for the ions in this configuration is in the same direction into the page. The electrons curvature and $\nabla \boldsymbol{B}$ drifts are in the same direction as well, coming out of the page. Therefore, direction of ion and electron drifts are in opposite directions resulting in a net current and the formation of an electric fields out of the page. The formation of an electric field then leads to an $\boldsymbol{E} \times \boldsymbol{B}$ drift shown in Equation 3.18.

$$\boldsymbol{v}_{E \times B} = \frac{\boldsymbol{E} \times \boldsymbol{B}}{B^2} \tag{3.18}$$

Ions and electrons drift together for the $\boldsymbol{E} \times \boldsymbol{B}$ drift resulting in a net drift of the plasma. This drift is in the direction of the radius of curvature and perpendicular to $\boldsymbol{B}$ which enables the plasma to flow across the magnetic field.

The theoretical framework behind this drift behavior was established by Schmidt and found that a non-dimensional number defined as the polarization characterizes this drift.[99] The polarization (κ) and the necessary condition for this drift are shown in Equation 3.19.

$$\kappa \equiv \frac{mn}{\epsilon_0 B^2} \gg 1 \tag{3.19}$$

This equation relates the rest energy of the plasma to the magnetic energy.

Experimental studies have verified this drift behavior and validated the importance of the polarization parameter. [100, 101, 99] The experimental studies also noted the importance of establishing and maintaining the necessary current structure to drive this detachment. Currents were measured along the magnetic field lines and conducting surface upstream of the plasma were able to short out the plasma. This inhibits formation of the electric fields necessary for the $\boldsymbol{E} \times \boldsymbol{B}$ drifts which lead to detachment. [100, 101, 99]

3.4.1.3 Inertial Detachment

Inertial detachment concerns the scenario when only a single species becomes demagnetized and an electric field is established to maintain quasineutrality. Figure 3.6 shows this resultant electric field which attracts the magnetized and demagnetized particles.

Detachment of the plasma may still be achieved by the system of particles having enough inertia to overcome the confining magnetic field forces. A hybrid Larmor radius is introduced to better examine this behavior. Detachment in this scenario can be imagined as the drift of a hybrid electron-ion particles. The ratio of the magnetic inertia to the flow inertia is characterized by the non-dimensional parameter shown in Equation 3.20. [53, 91, 82]
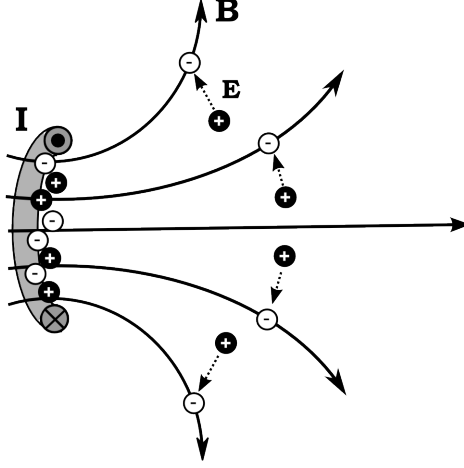
Figure 3.6: Sketch of inertial detachment in a magnetic field generated by a current loop (I). Induced electric fields are illustrated by dotted lines while magnetic field lines are illustrated by solid lines.

$$G \approx \frac{eB}{m_e} \frac{eB}{m_i} \frac{r_0^2}{u_0^2} \tag{3.20}$$

In this equation m_i is the ion mass, m_e is the electron mass, r_0 is a characteristic dimension of the system, and u_0 is the plasma mean velocity. The condition for the detachment of the hybrid Larmor radius particle has been suggested to be $G^{-1/2}|\frac{\nabla B}{B}| \geq 0.5$. [83] It has also been shown that imposing an initial azimuthal velocity will increase detachment efficiency and decrease nozzle divergence. [92] The analysis based on the parameter G suggest by Hooper et al. [53] has been criticized by Ahedo et al. [47, 94] due to the simplifying assumptions made, particularly that of current ambipolarity. Significant theoretical and computational study has been done to characterize the effectiveness of inertial detachment with some suggesting demagnetization based on the hybrid Larmor radius as an effective means for detachment [53, 91, 99] and others suggesting only demagnetization of electrons effectively achieves detachment.[47, 46]

An alternate approach to the hybrid particle method is to consider the inertia of the two-particle system and the confining force to define a new inertial Larmor radius. Assume that the two particles are constrained to move together by the electric field. Next assume that the two particle system is bound to a magnetic field line. A force balance between the confining force and centrifugal inertia leads to the following equation.

$$\frac{m_{ion}v_{\perp,ion}^2 + m_e v_{\perp,e}^2}{r_{L,h}} = qv_{\perp,e}B \tag{3.21}$$

Both the ion and electron inertial are considered, but for simplicity only the electron Lorentz force is included due to the fact that $v_{\perp,e} \gg v_{\perp,ion}$. This equation can be solved for the new, inertial Larmor radius $r_{L,inertial}$.

$$r_{L,inertial} = r_{L,e} + \frac{v_{\perp,ion}}{v_{\perp,e}}r_{L,ion} \tag{3.22}$$

This inertial Larmor radius can also be used to determine magnetization by comparing with length scales of the system and magnetic field gradient length scales.

Contrary to the predictions of the inertial detachment mechanism, recent experiments have shown that some degree of detachment may occur even with only ion demagnetization.[102, 30] Numerical simulations related to VASIMR have also shown detachment occurring due to solely ion demagnetization.[50] Further study is required to verify this behavior. Detachment by inertial means is often referred to as the "lower limit" of detachment which can be enhanced by other detachment mechanisms.

3.4.1.4 Induced field detachment

Detachment via induced magnetic fields is possible by either stretching the magnetic field lines to infinity or by canceling out the applied fields and thereby demagnetizing the plasma. Induced field detachment effectiveness can be studied by the

currents which create these fields and is an inherently fluid phenomenon.

Magnetic field stretching occurs when the plasma kinetic energy exceeds the magnetic energy or equivalently when the plasma fluid velocity exceeds the Alfvén velocity. This is characterized by the non-dimensional parameters shown in Equation 3.23.

$$M_A^2 = \beta_f = \frac{\rho u^2/2}{(B^2/2\mu_0)} > 1 \qquad (3.23)$$

When this condition is satisfied the fluid is considered to be super-Alfvénic ($M_A > 1$) and is traveling faster than the rate at which perturbations in the magnetic field affect the flow. As a result of this behavior, magnetic field lines get dragged to infinity. [39, 101] The currents required to produce super-Alfvénic detachment are paramagnetic which results in convergent detachment but produce thrust losses due to attractive forces between the applied field and induced field currents.[39, 95, 46] Studies have shown that sub- to super-Alfvénic transition can minimize detachment losses with a slowly diverging magnetic field. An experimental study has suggested detachment behavior due to $\beta_f > 1$ rather than ion demagnetization and shows agreement with computational results.[96, 98, 97] Field line stretching, a condition necessary for this detachment method, was not measured. Other experimental and computational results have also demonstrated super-Alfvénic detachment and have identified a mechanism for self-collimation of the plasma plume.[31]

The cancellation of the applied field by the induced field is referred to as self-demagnetization and occurs due to the formation of diamagnetic currents in the plasma. These currents create an axial accelerating force and a radial confining force which are favorable for momentum transfer to the spacecraft.[93] Self-demagnetization detachment has been demonstrated computationally.[93, 46] Strong diamagnetic currents which effectively cancel out the applied field on the magnetic nozzle axis have been measured in experiments.[85]

3.4.2 Collisional Detachment

Collisional detachment may be achieved through resistive diffusion across magnetic field lines [103, 41, 104], recombination and charge exchange collisions[105, 106], and current closure.

3.4.2.1 Diffusion

Resistive diffusion has been suggested as a means to achieve detachment and is governed by the cross field diffusion of plasma due to collisions.[103] Resistive detachment exhibits conflicting requirements of initial confinement necessary for the correct nozzle geometry and eventual cross field diffusion to ensure detachment. The resistive drag must also be minimized. Conditions to ensure this duality is satisfied for resistive detachment in an adiabatically cooling plasma plume have been defined.[103] In general, a gradually diverging magnetic field is preferred to ensure efficient resistive detachment.

The magnetic Reynolds number (R_m) defined earlier can be used to quantify the confinement of a plasma in a magnetic nozzle. For high values, resistive diffusion is negligible compared to convective effects and confinement is achieved. For intermediate and low values diffusion is important and the plasma may move across magnetic field lines. Therefore, high values of R_m are required for confinement while intermediate to low numbers are required for detachment.[107, 104] The difficulty with determining the magnetic Reynolds number is correctly quantifying the plasma resistivity, which may contain anomalous contributions.

The cross field plasma diffusion can have a number of implications on magnetic nozzle design. Cross-field diffusion is typically characterized by the flux of particles perpendicular to the magnetic field lines, $\Gamma_\perp$. This flux is shown in Equation 3.24 below in which D is known as the diffusion coefficient.

$$\Gamma_\perp = n v_\perp = D_\perp \nabla n \tag{3.24}$$

The diffusion coefficient may take very different forms for different types of plasmas. Classical diffusion is described by Equation 3.25 while Bohm diffusion is described by Equation 3.26.[64]

$$D_{\perp,classical} = \frac{\eta_\perp n \sum kT}{B^2} \tag{3.25}$$

$$D_{\perp,Bohm} = \frac{1}{16} \frac{kT_e}{eB} \tag{3.26}$$

It is important to note also that the resistivity for classical diffusion η is proportional to $(kT_e)^{-3/2}$. Thus, classical diffusion scales as $(kT)^{-1/2}/B^2$ while Bohm diffusion scales as kT/B. For classical diffusion, the cross field flux increases more quickly as the magnetic field strength decreases than for Bohm diffusion. This increasing flux governs the transition from a confined plasma to a detached plasma and suggests that a plasma exhibiting classical diffusion will transition more quickly from a confined state to a detached state. As the plasma expands the temperature also decreases. Using the previously shown scaling with temperature, it is found that the cross-field flux due to classical diffusion increases even more due to the temperature decreases while the cross field flux due to Bohm diffusion has competing effects between the temperature and magnetic field decreases.

Additionally, the Bohm diffusion coefficient is typically greater than the classical diffusion coefficient by several orders of magnitude thereby hindering confinement and facilitating detachment.[64] It is also possible that the diffusion characteristics change during the expansion, behaving classically for a portion of the expansion and Bohm for the rest.

The significantly different behavior of classical and Bohm diffusion show that

knowing the diffusive character of the plasma is important in determining not only the extent of cross field fluxes, but also the transition from a confined plasma to a detached plasma. Predicting the extent at which plasma diffuses across a magnetic barrier has been extensively studied and has shown that plasma may exhibit anomalous resistivity several orders of magnitude greater than predicted by classical plasma theory and Bohm diffusion.[101, 41, 103] Anomalous diffusion may be be caused by micro-instabilities which are driven by field gradients and field line curvature.[103, 42] The problem of anomalous turbulent transport is an active topic in Hall thrusters and cathode plumes. These micro-turbulent fluctuations are three-dimensional in nature and are difficult to describe physically.

As a means to achieve detachment, resistive diffusion has been largely considered as ineffective due to the adverse affects it would have on thrust production and likely divergent detachment that would occur.[46] Resistive effects however can not be ignored as they may still be important experimentally. Far-field detachment due to resistive effects may also be attractive particularly near the nozzle centerline where the travel time for particle confinement may be large compared to the collision time. Detachment may be facilitated by the presence of turbulent fluctuations which grow as they convect out of the plasma into the plume.

3.4.2.2 Recombination and Charge Exchange Collisions

Recombination achieves detachment by the formation of neutral particles which are no longer affected by the magnetic fields. Creation of neutrals is driven primarily by three body recombination and requires sufficiently high electron-ion collision frequency to be considered an effective means of detachment. Although initial analysis of recombination as a means for detachment are not encouraging, recombination rates can be increased by sharply decreasing magnetic field configurations or rapid cooling of electrons in the expanding nozzle. [105, 106] However, a sharply falling magnetic

field requires a very divergent magnetic field which may result in large plume divergence thrust losses.

Collisions between ions and neutrals can also cause detachment through charge exchange or backscattering collisions. During these collisions electrons are transferred between neutrals and ions. This transfer of charge can facilitate detachment by enabling cross field mobility and exchanging energy between the high energy ion species and lower energy neutral species. This however may not be an effective means of detachment due to the low energy charged species which remain after the collisions which are more likely to remain attached to the field lines. Furthermore, charge exchange and recombination mean free paths are typically long compared to the system dimension and will only increase in space. [66] Generally charge exchange represents a loss mechanism in the plasma plume because directed beam energy is lost to neutral gas heating.

3.4.2.3 Current Closure

Demagnetized ions and magnetized electrons lead to the formation of an electric field across the magnetic field lines which strives to achieve quasineutrality. The motion of electrons across the magnetic field is inhibited due to their magnetization. Inertial detachment deals with the mutual separation of the electrons and ions while assuming that the ions and electrons have the same velocity. This assumption is known as current ambipolarity. An additional detachment method is possible if this assumption is not made and the species are allowed to have different velocities which produce a net current.

For this detachment scenario it can be imagined that electrons travel back into the high density plume where the plasma is more collisional, cross magnetic field lines, and travel out along new magnetic field lines to supply electrons to the regions of streaming demagnetized ions. A net current forms which supplies electrons to the

51

regions of positive charge accumulation that occur due to ion demagnetization. An example of the net current produced is seen in Figure 3.7.
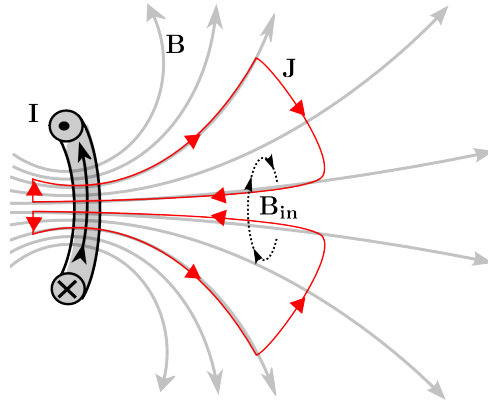
Figure 3.7: Examples of currents for current closure in a magnetic nozzle generated by a current loop (I).

This mechanism has only been sparsely studied [46], but radial and axial currents which would characterize this type of detachment have been measured in magnetic nozzle devices.[85] These radial and axial currents should also produce azimuthal magnetic fields.

3.4.3 Magnetic Reconnection

Magnetic reconnection is a widely studied topic in plasma physics but has not been sufficiently studied when relating to plasma propulsion detachment scenarios. Phenomenon exhibiting magnetic reconnection physics relevant to plasma detachment are evident in coronal mass ejections and magnetic confinement fusion experiments.[108]

The most elementary description of magnetic reconnection is shown in Figure 3.8. An initial configuration of two magnetic field lines, (1), has a finite diffusion across the magnetic field lines, (2), which eventually leads the magnetic field lines to tear and reconnect into a new configuration (3) of lower energy.[38, 109] The reconfiguration of the magnetic field lines allows plasma flows which under the previous configuration were not possible. This characteristic of magnetic reconnection is particularly attrac-

tive for magnetic nozzle detachment because it allows magnetic islands to form which separate from the applied field. Magnetic reconnection is an inherently transient phenomenon.
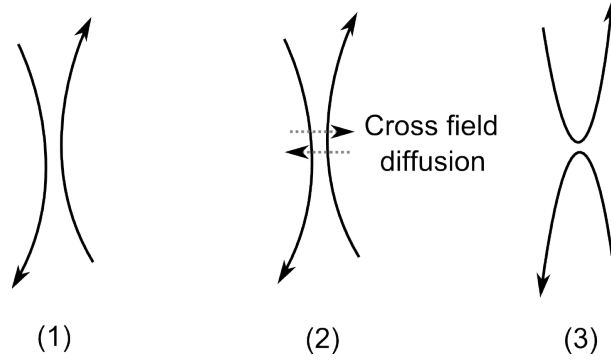
Figure 3.8: Simple schematic of magnetic reconnection. Magnetic fields are solid lines while cross field diffusion is denoted by dotted lines.

The parameters typically used to characterize magnetic reconnection behavior are the magnetic Reynolds number and the Lundquist number. The Lundquist number is defined in Equation 3.27. As both of the magnetic Reynolds number and the Lundquist number decrease the diffusive behavior of the plasma increases and reconnection becomes more likely.

$$S = v_A L/\eta = \frac{BL}{\eta\sqrt{\mu_0\rho}} \tag{3.27}$$

In this equation $v_A = B/\sqrt{\mu_0\rho}$ is the Alfvén velocity.

3.5 Summary of Parameters and Experiments

Numerous physical mechanisms in the thrust generation process have been presented based on a review of magnetic nozzle physics literature. Summaries of the parameters which characterize these physical processes are shown in Appendix A. A summary of the experiments which were mentioned in the discussion above is also given.

CHAPTER IV

Particle Simulation and the
Quasi-One-Dimensional Formulation

4.1 Introduction

Many magnetic nozzle devices operate at the edge of the continuum regime and into regimes where kinetic treatment of the physics is necessary. Kinetic methods using particle, Boltzmann, or Vlasov techniques are essential to studying the important non-equilibrium effects. Particle simulations treat the plasma or fluid as a collection of particles or macro-particles (group of particles treated as a single particle) and solve the equations of motion for each of the particles. Boltzmann and Vlasov simulations solve for the probability distribution function using the Boltzmann or Vlasov equations.

Particle simulations treat the plasma most generally and require few assumptions about the behavior of the plasma. However, these simulations are inherently very expensive and are prone to numerical noise and instabilities when an insufficient number of particles are used or when stability criteria are not met. Boltmann and Vlasov simulations require more assumptions about the plasma behavior than particle simulations, but are much less prone to numerical noise and are generally less expensive numerically.

The goal of this research is to treat the plasmadynamics in a magnetic nozzle from the most fundamental perspective, that of the particles. Therefore, particle simulations were chosen to study the ion acceleration mechanisms in a magnetic nozzle. The method chosen is the particle-in-cell (PIC) method which is discussed in detail in the next section.

This chapter will first introduce electrostatic PIC simulations and the theory behind these. This will be followed by a discussion of the previous use of PIC simulations to study magnetic nozzles. A novel PIC method will then be introduced which resolves one dimension spatially and includes two-dimensional effects associated with the magnetic field effects and the plasma compression and expansion.

4.2 Particle-In-Cell Simulations

Particle-In-Cell simulations treat the plasma as a collection of macroparticles which are free to move over a mesh or grid while the fields are solved for on the grid. This simplification reduces the computational cost from N^2 for a full particle method to $Nln(N)$ for PIC. Particles within a cell do not affect one another. Therefore, only long range effects of the particles are captured on one another and effects such as Coulomb collisions are not captured unless they are explicitly modeled by another algorithm (Monte Carlo method, grid based collision method). Figure 4.1 shows a diagram and a flowchart of electrostatic PIC simulations. The steps that are part of this flow chart are outlined below:

1. The location of the particles is used to weight the charge onto the grid and the volume of each cell used to calculate a charge density (ρ).

2. The charge density and the imposed boundary conditions are then used to calculate the potential (ϕ) on the grid using Poisson's equation ($\nabla^2\phi = -\rho_c/\epsilon_0$).

3. This potential is then used to calculate an electric field ($\boldsymbol{E}$) on the grid.
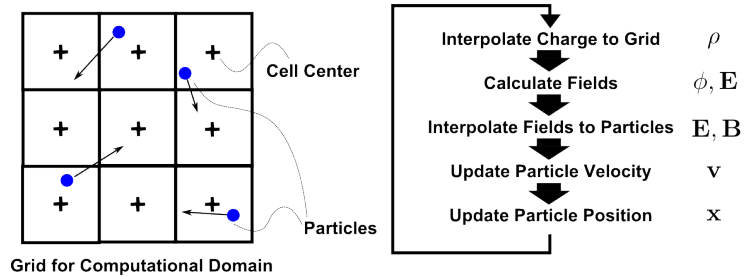
Figure 4.1: Particle-in-cell domain and flowchart.

4. The electric field and applied magnetic field ($\boldsymbol{B}$) are weighted from the grid to the particles.

5. The Lorentz force, $\boldsymbol{F} = q(\boldsymbol{E} + \boldsymbol{v} \times \boldsymbol{B})$, is then used to update the particle velocity ($\boldsymbol{v}$).

6. The new velocity is used to calculate an updated position ($\boldsymbol{x}$).

7. Additional steps can be added next such as collisions, heating, or boundary effects.

8. Repeat.

Specific methods and the resulting stability requirements will be discussed in the next chapter as they pertain to the code developed for this research.

4.3 Previous Kinetic Simulations of Magnetic Nozzles

Previous studies with kinetic methods have focused primarily on one-dimensional PIC [51, 54], multi-dimensional PIC simulations with unrealistic mass ratios or with small truncated domains, [110, 52, 55] and multi-dimensional hybrid PIC.[50]

The one-dimensional PIC simulations by Meige et al and Baalrud et al studied the formation of double layers and the ion acceleration associated with them. [51, 54] These simulations mimicked the expansion process in the magnetic nozzle by imposing

a particle loss frequency to the portion of the domain in which the magnetic field is diverging. The results of these simulations showed that the formation of the double layer was dependent on the chosen loss frequency. For sufficiently high loss frequencies a double layer structure appeared which accelerated the ions. Distinct groups of electrons were also seen with different temperatures.

Multi-dimensional PIC simulations have been used to study the formation of double-layers in magnetic nozzles as well as the detachment process. The simulations of Sefkow et al used a full 3D3V PIC-MCC code to study the flow of the MNX plasma flow through a mechanical aperture.[52] The simulation domain focused only on the flow near the aperture in order to cut down on computational costs. Double layers where shown to form as a result of the flux imbalance that occurs as the unmagnetized ions are lost to the aperture wall. The double layer attempts to balance this flux loss. Electron temperatures of the bulk, aperture size, Larmor radii, and neutral background pressure all were shown to affect the strength of the double layer. Simulations by Rao et al use a 2D3V planar PIC code with a truncated simulation domain to study the formation of double layers. [55] The simulation domain only captures a small section of the plasma expansion and does not consider collisions. Some of the two-dimensional characteristics of current free double layers seen in experiments are replicated due to the radial electric field which develop in the plume. These radial electric field are shown to be important to the overall structure of the plume. A 2D3V PIC axisymmetric code was used to study detachment in magnetic nozzles. [110] The mass ratio between the ions and electrons is decreased to make these simulations tractable. Detachment was demonstrated, but these simulations have been limited to qualitative comparisons with experiments.

Hybrid PIC simulations have been performed primarily to study detachment. These simulations typically treat the ions as particles and the electrons as a fluid. Simulations by Ilin et al [50] used a hybrid PIC code which treated the ions as particles

and assumed Boltzmann electrons. These simulations illustrated plasma detachment in the VASIMR plume, but the assumption of Boltmann electrons may be invalid due to the changing temperatures of the electrons in the VASIMR plume.

As shown in this section, kinetic codes have primarily been used for two types of studies. The first of these is to study the formation of double layers.[51, 54, 55] These studies have been limited to one dimensional or truncated two-dimensional domain. Other studies have focused on detachment but must either use a hybrid approach or simplify the problem by changing the plasma properties. [50, 110] The work presented herein more generally strives to model the plasma expansion along a magnetic field. The introduced methods can not capture effects like detachment because of the assumptions of magnetization which were made in deriving the model. Details are presented in the next section.

4.4   Quasi-One-Dimensional Particle-In-Cell Simulations

To further advance the kinetic study of magnetic nozzles with PIC simulations a new method was developed for the Quasi-one-dimensional quasi-one-dimensional (Q1D) PIC simulation of magnetic nozzles through the inclusion of two-dimensional effects in one-dimensional full PIC simulations. The effects included are: the cross-sectional area variation of the domain and magnetic field forces. These effects are discussed in detail below. These simulations include two-dimensional effects without the cost of scaling to full two-dimensional simulations by making simplifying assumptions about the physics. This type of simulations can be referred to as quasi-one-dimensional, $1\frac{1}{2} - D$, or flux-tube simulations.

4.4.1   Cross-sectional Area Variation

The cross-section of the one-dimensional domain was varied to include the effects of the plasma expansion. As a simplification the plasma properties were assumed to be

constant over the cross-section, allowing a one-dimensional domain to be used while capturing the two-dimensional effects of the plasma compression and expansion by the magnetic field. The area at each cell is determined by assuming that the plasma follows the magnetic field lines enclosing the plasma in a magnetic flux surface as shown in Figure 4.2. Knowing the structure of the magnetic flux surface then defines the variation of the plasma cross-section. It is further assumed that a flux-tube near the axis is chosen such the radial component of the magnetic field (B_r) is much smaller that the axial component (B_z). Integrating Gauss' Law of Magnetism and assuming that the radial flux is negligible leads to an expression for the cross-sectional area as a function of the axial magnetic field along the centerline axis, as shown in Equation 4.1.

$$A = \frac{B_{z,in}}{B_z} A_{in} \tag{4.1}$$

The variation of the cross-sectional area models the compression and expansion of the plasma due to the magnetic field forces. The area variation couples to the rest of the governing equations through the calculation of the density of the particles, which in turn affects the solution of Poisson's equation.
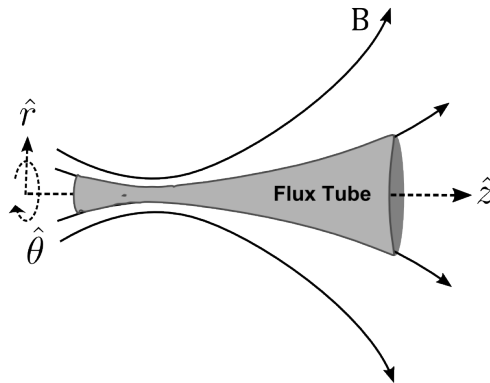
Figure 4.2: Flux-tube used for calculating cross sectional area variation.

4.4.2 Magnetic Field Force

Particles feel a force along the magnetic field line similar to the magnetic dipole force on a localized current density.[62] To capture this force, magnetized particles are assumed to be displaced from the axis by their Larmor radii. Using Gauss' Law of Magnetism and assuming that the axial magnetic field does not vary significantly over the orbit leads to an expression for an average radial magnetic field over the particle orbit

$$B_r = -\frac{r_L}{2}\frac{dB_z}{dz} \tag{4.2}$$

In this equation $r_L = \frac{mv_\perp}{qB}$ is the Larmor radius, $v_\perp$ is the perpendicular velocity, and q is the charge of the particle. The combination of the radial magnetic field and the perpendicular velocities results in forces along the axis of symmetry. The assumptions made in this derivation are very similar to those made in examining magnetic mirror physics. [64]

The force on the particles was derived in a cylindrical coordinate system. In cylindrical coordinate systems inertial forces due to the coordinate system must be included, as shown in Equation 4.3.

$$\frac{d\mathbf{v}}{dt} = \frac{q}{m}(\mathbf{v} \times \mathbf{B}) + \mathbf{a}_{coord} \tag{4.3}$$

In which the acceleration due to inertial effects, $\mathbf{a}_{coord}$, is:

$$\mathbf{a}_{coord} = \frac{v_\theta^2}{r_L}\hat{r} - \frac{v_\theta v_r}{r_L}\hat{\theta}. \tag{4.4}$$

Substituting Equation 4.2 into Equation 4.3 leads to a significant simplification as the inertial forces cancel some of the magnetic field forces. Physically, this cancellation occurs due to the assumption of magnetization of the particles. The magnetic field

forces confine the particles to following the axis, which is a magnetic field line. The remaining terms are shown below in Equations 4.5 - 4.7 and represent the magnetic dipole force on a magnetized particle as well as the kinetic energy conserving force.

$$\frac{dv_z}{dt} = -\frac{1}{2B_z}\frac{dB_z}{dz}v_\theta^2 \tag{4.5}$$

$$\frac{dv_\theta}{dt} = \frac{1}{2B_z}\frac{dB_z}{dz}v_\theta v_z \tag{4.6}$$

$$\frac{dv_r}{dt} = 0 \tag{4.7}$$

Implicit in this derivation is the assumption of changing to a frame of reference along the field line in which the azimuthal velocity (v_θ) is in fact the velocity perpendicular to the field line ($v_\perp$) which defines the particle orbit. The velocity used in the dipole force calculations can therefore be simplified to two dimensions, one along the magnetic field line and one perpendicular to the magnetic field line. These simplified equations are shown below in which s is the direction along the magnetic field line:

$$\frac{dv_\parallel}{dt} = -\frac{1}{2B}\frac{dB}{ds}v_\perp^2 \tag{4.8}$$

$$\frac{dv_\perp}{dt} = \frac{1}{2B}\frac{dB}{ds}v_\perp v_\parallel \tag{4.9}$$

The simplification to two-dimensions can be explained using Figure 4.3. In this figure the magnetic field is along the $\hat{z}$ direction and the velocity of the particle perpendicular to the field line shown by the dotted lines. The particles can be imagined first in a Cartesian coordinate system in which they have velocities in the $\hat{x}$ and $\hat{y}$ directions. These coordinates can be transformed to a cylindrical coordinate system where they now have velocities in the $\hat{r}$ and $\hat{\theta}$ directions. A final transformation can
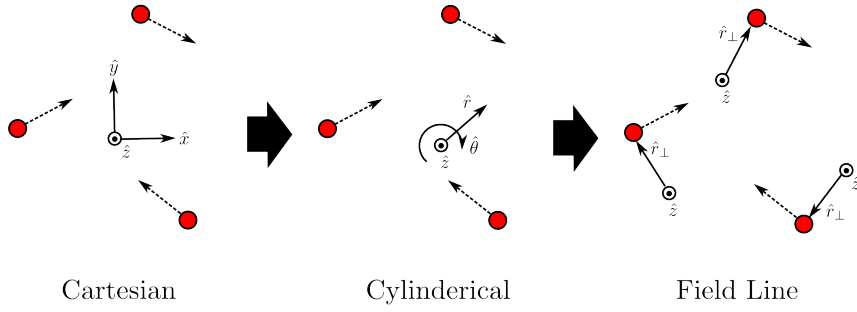
Figure 4.3: Illustration of changing to magnetic field line reference for Q1D simulations.

be made to a local field line coordinate system in which each particle has only a perpendicular gyro-velocity. The $\hat{z}$ direction is the same for each particle. Furthermore it is assumed that the magnetic field does not change significantly in the direction perpendicular to the field line $\left(r_\perp \frac{dB}{dx_\perp}/B \ll 1 \right)$, which implies that the magnetic field variation in the $r - \theta$ plane is small and the particles are bound to similar field lines.

In summary, each particle experiencing gyro-motion around a magnetic field can be moved to a cylindrical coordinate system around a chosen magnetic field line. In this coordinate system the particle only has a velocity along the field line (formerly $\hat{z}$) and around the field line (formerly $\hat{\theta}$). Each particle can be assigned its own coordinate system along that magnetic field line around which is it bound. If the variation of the magnetic field is small then the particles are assigned to similar field lines and the entire group of particles can be treated by the equations derived.

CHAPTER V

One Dimensional Model Implementation and Verification

The development and verification of the one dimensional code which serves as the framework on which the Q1D model was implemented is presented in this chapter. The one-dimensional algorithms are presented as well as the verification of these algorithms. Implementation and verification of the collisional algorithms are presented next. The code used in this work was developed from scratch and the paralellization with Message Passing Interface (MPI) is discussed. The code was written as generally as possible to be used beyond the current problem.

5.1 One-dimensional Algorithms

The one dimensional (1D) code was developed based on the work of Birdsall [111, 112], Verbonceuor [113, 114, 115], and Hutchinson[116] among many others.[117, 118] A basic flowchart of the code is shown in Figure 5.1. Particles are free to move throughout the domain while the potential, electric field, and continuum properties are solved for on the grid. The plasma continuum properties are found by weighing the particle properties such as mass, charge, and momentum to the grid. The charge density on the grid is then used to solve Poisson's equation and obtain the potential

and electric field on the grid. Finally the electric and magnetic fields are weighed to the particles in order to calculate the forces on the particles and move the particles. Additional algorithms are also included to model Monte Carlo Collisions[111, 117], RF heating[51], and Coulomb collisions.[119] The domain, particle mover, weighing algorithms, Poisson solver, boundary conditions, and particle loading are each discussed in greater detail in the following sections.

5.1.1 Domain

The domain used in these simulations was a uniform one dimensional grid. The addition of two-dimensional effects did not change the grid structure. The number of grid points used in the simulation was NP. Cell centers were also defined between each point and are used in some of the algorithms. The grid points were referred to as X_i where X_0 was the first point which was on the left boundary and X_{NP-1} was the final point at the right boundary (note that indexes start at 0). The total number of cell centers including ghost cells (cells outside the solution domain) was $NC = NP + 1$. The length of the domain was defined as: $(L = (NP - 1) * \Delta x)$. A schematic of the domain is shown in Figure 5.2.

For the results presented herein the potential, electric field, density, velocity, energy, and the magnetic field are all calculated at the grid points. The code also contains functionality to weight or calculate the potential, density, and energy at the cell centers while calculating or setting the electric and magnetic fields at the grid points.

5.1.2 Particle Mover

Particles are moved according to the standard leap frog algorithm shown below in which x is the particle location, n is the time step, and v is the particle velocity. [112] The position and velocity are offset by half steps in time.
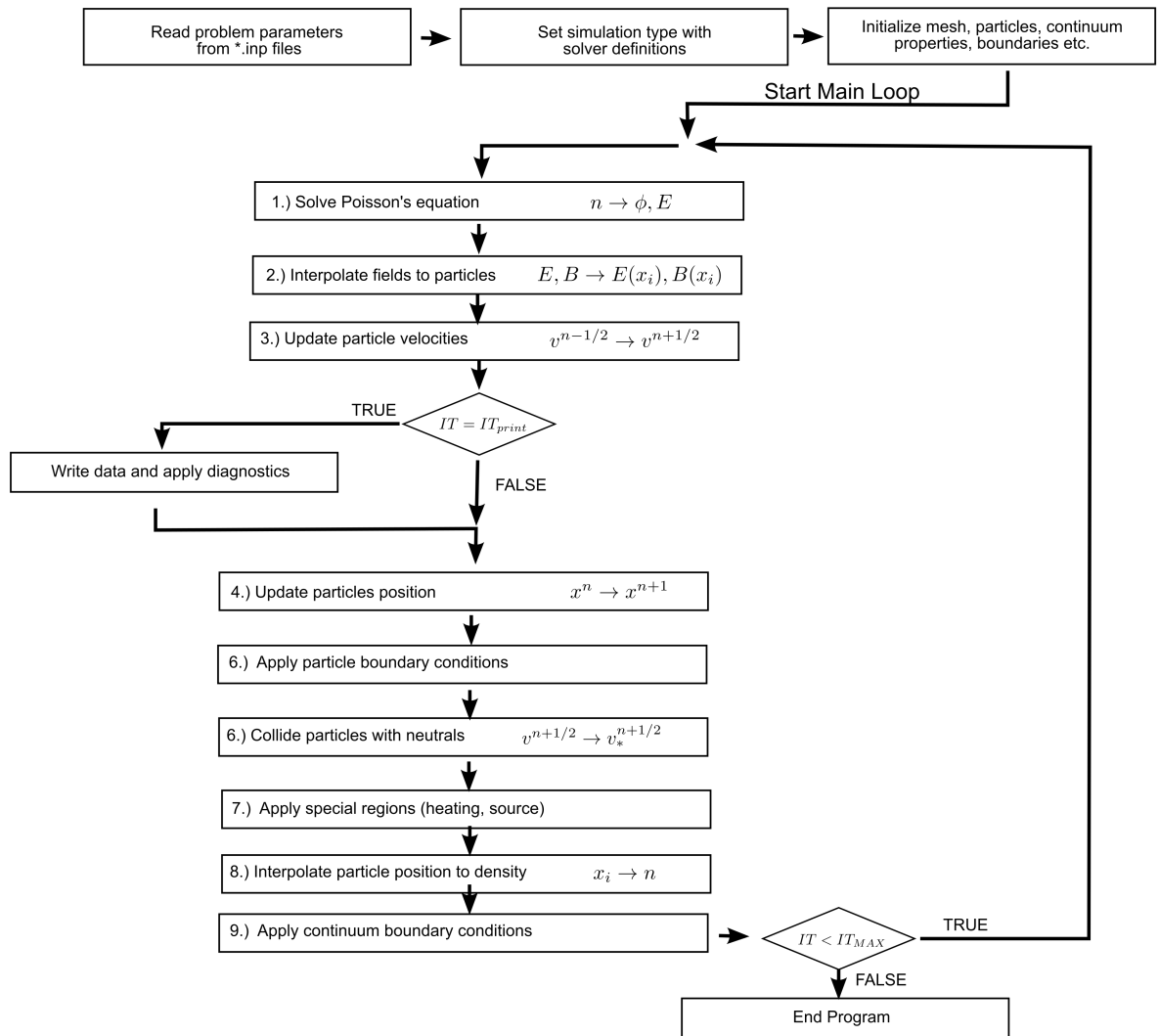
Figure 5.1: Flowchart of PIC code.

The flowchart contains the following boxes and decision nodes:

- Read problem parameters from *.inp files
- Set simulation type with solver definitions
- Initialize mesh, particles, continuum properties, boundaries etc.

Start Main Loop

- 1.) Solve Poisson's equation $\qquad n \to \phi, E$
- 2.) Interpolate fields to particles $\qquad E, B \to E(x_i), B(x_i)$
- 3.) Update particle velocities $\qquad v^{n-1/2} \to v^{n+1/2}$

Decision: $IT = IT_{print}$
- TRUE → Write data and apply diagnostics
- FALSE ↓

- 4.) Update particles position $\qquad x^n \to x^{n+1}$
- 6.) Apply particle boundary conditions
- 6.) Collide particles with neutrals $\qquad v^{n+1/2} \to v_*^{n+1/2}$
- 7.) Apply special regions (heating, source)
- 8.) Interpolate particle position to density $\qquad x_i \to n$
- 9.) Apply continuum boundary conditions

Decision: $IT < IT_{MAX}$
- TRUE → (loop back to Start Main Loop)
- FALSE → End Program

Figure 5.2: One-dimensional domain used in simulations. Index i is used for grid points.

$$\vec{x}^{n+1} = \vec{x}^n + \vec{v}^{n+1/2}\Delta t \tag{5.1}$$

$$\vec{v}^{n+1/2} = \vec{v}^{n-1/2} + \vec{a}\Delta t \tag{5.2}$$

The acceleration term depends on the type of forces incorporated in the model. For a simple model which only considers the electric field this becomes:

$$\vec{v}^{n+1/2} = v^{n-1/2} + \frac{q\vec{E}^n}{m}\Delta t \tag{5.3}$$

In this equation E^n is the electric field which has been interpolated to the particles. The electric field is found by solving Poisson's equation at the nth time step. Stability requires a time step of $\omega_p \Delta t < 2.0$ but typically the time step is restricted to be $\omega_p \Delta t < 0.2$ to compromise between phase error and computational cost. [112] Phase error decreases as $1/\Delta t^3$.

The Boris algorithm was also incorporated for test cases which include a conventional applied magnetic field.[120] It is important to note that the Boris method is not used in any of the quasi-one-dimensional simulations, but is discussed because it is modified in the new implementation. The Boris algorithm is decomposed into three separate velocity pushes: an initial half push by the electric field, followed by an implicit magnetic field rotation, and a final half push by the electric field. These three separate pushes are shown below.

66

$$\vec{v}^- = \vec{v}^{n+1/2} + \Delta t \left[\frac{q}{2m} \vec{E}^n \right] \tag{5.4}$$

$$\vec{v}^+ = \vec{v}^- + \Delta t \frac{q}{2m} (\vec{v}^+ + \vec{v}^-) \times \vec{B} \tag{5.5}$$

$$\vec{v}^{n+3/2} = \vec{v}^+ + \Delta t \left[\frac{q}{2m} \vec{E}^n \right] \tag{5.6}$$

In these equations $\vec{v}^+$ and $\vec{v}^-$ are the intermediate velocities in the velocity push. The optimal method for performing implicit rotation is outlined in the literature. [112, 120] Typically the time step is restricted to $\omega_c \Delta t < 0.35$ to guarantee an error of less than one percent in the rotation angle for the particle orbit.

5.1.3 Weighting Algorithm

Zeroth order and first order weighting schemes were incorporated in the code. Zeroth order weighting assigns a particle's charge to the nearest grid point and imposes the nearest point's electric field on the particle. First order weighting imposes a linear weighting to and from the particle using the two nearest grid points. In linear weighting, each macro-particle can be imagined as a cloud of particles spanning the width of a cell and each grid point has a sphere of influence that is a cell width wide. The fraction of the particle cloud which falls within each grid point's sphere of influence is weighted to that cell.

The weighing scheme selected was applied to both the grid to particle and particle to grid weighting to guarantee consistency. For all simulations shown first order weighting was used. First order weighting smooths the density and potential fluctuations in the simulations (compared to zeroth order simulations), thereby reducing the noise. Higher order weighting schemes also exist, but are not included due to the additional computational costs associated with them. [111]

5.1.4 Poisson Solver

The charge densities (ρ) at the grid points are used to solve Poisson's equation ($\nabla^2 \phi = -\rho/\epsilon_0$) for the potential ($\phi$) at the grid points. A simple central difference discretization of Poisson's equation is used:

$$\frac{\phi_{i+1} - 2\phi_i + \phi_{i-1}}{\Delta x^2} = -\frac{\rho_i}{\epsilon_0} \tag{5.7}$$

This equation can be written out for the entire domain forming the matrix equation $AX = B$ where A is a tridiagonal matrix of coefficients, X is composed of ϕ's, and B depends on the densities and grid. The selected boundary conditions affect the first and last row of this matrix and will be discussed later in this section because they relate to the boundary conditions applied in the code. The tri-diagonal matrix is solved using Gaussian elimination with partial pivoting with the Linear Algebra PACKage (LAPACK) included in the Intel Math Kernel Libraries.

The electric field ($\boldsymbol{E} = -\nabla\phi$) is found at the grid points using a central difference scheme. The boundary conditions applied for the electric field will be discussed in the next section.

$$E_i = -\frac{\phi_{i+1} - \phi_{i-1}}{2\Delta x} \tag{5.8}$$

5.1.5 General Boundary Conditions

A variety of boundary conditions are applied to the one dimensional domain. These boundary conditions include periodic, Dirichlet, and Neumann conditions. Although these general boundary conditions can be used, they require more careful handling for devices which are discussed in the next section.

5.1.5.1 Periodic

Periodic boundary conditions imply that the grid points with index $i = 0$ and $i = NP - 1$ are the same grid point. The continuum boundary conditions for properties such as potential are applied such that:

$$\phi_0 = \phi_{NP-1} \tag{5.9}$$

On the particle side, this type of boundary is applied by injecting particles which exit the domain at one boundary at the other boundary. The continuum quantities (densities, etc.) found by weighting the particle properties to the grid points $i = 0$ and $i = NG - 1$ must be summed with one another to capture the effects from both sides of each of these points.

5.1.5.2 Dirichlet

Dirichlet boundary conditions directly impose a particular parameter at the boundary. For example, potentials can be imposed at the boundary points:

$$\phi_0 = \phi_{applied,0} \tag{5.10}$$

$$\phi_{NG-1} = \phi_{applied,NP-1} \tag{5.11}$$

Weighting for continuum properties at the boundary grid points ($i = 0, NP - 1$) can be done either by doubling the weighting (more like a Neumann condition) to the boundary cell, calculating the density based on the characteristics of the boundary (device specific), or including the effects of an imposed density in the ghost cell to account for particles that would be outside the domain.

5.1.5.3 Neumann

Neumann boundary conditions impose a gradient at the grid point. In the case of the potential this imposes an electric field at the boundary. On the particle side, a Neumann condition implies that the charge densities in the final grid points ($i = 0, NP-1$) can be found by doubling the weighting to account for particles that would be outside the domain.

5.1.6 Device Boundary Conditions

Boundary conditions can be applied so that the simulation represents a device by incorporation of a grounded plate, floating collector, grounded plate, driving current, or capacitor. Potentials or electric fields are imposed at the boundary based on the type of device while the unspecified quantities are chosen to guarantee consistency. For example, the electric field at the boundary (E_0) is found by manipulating the following equations:

$$E_0 = -\frac{\phi_1 - \phi_{-1}}{2\Delta x} \tag{5.12}$$

$$\frac{\rho_0}{\epsilon_0} = -\frac{\phi_1 - 2\phi_0 + \phi_{-1}}{\Delta x^2} \tag{5.13}$$

This system of equations typically has two unknowns which depend on the type of boundary condition applied. The potential ϕ_{-1} is always an unknown and serves primarily as a means to ensure consistency. When imposing Dirichlet boundary conditions on the electromagnetic field a quantity for ϕ_0 is imposed while ϕ_{-1} and E_0 are solved for with the known other quantities (ρ_0, ϕ_1). Note that ρ_0 is found by doubling the weighting of the charges to the $i = 0$, which is actually similar to a Neumann boundary condition on the density.

When Electric field boundary conditions are applied a surface charge density (σ)

is often used. The surface charge density is related to the electric field by solving Poisson's equation over a Gaussian pill box to get the following form for the electric field at the left boundary.

$$E_0 = \frac{\sigma_0}{\epsilon_0} \tag{5.14}$$

Similar equations are solved for the right boundary, but care must be taken with the signs.

Grounded plate

When a boundary is grounded the potential is fixed at $\phi = 0$. Typically the continuum properties like the density are found by doubling the value weighted to the point to account for the lack of weighting from the other side where no particles are present. This is a Dirichlet boundary condition, so the Equations 5.12 and 5.13 are solved for E_{bound} using $\phi_{bound} = 0$.

Driving Voltage

The boundary can be treated as an electrode with a voltage (ϕ_{bound}) which is driving the device. This is a Dirichlet boundary condition which is applied just like the grounded electrode except with a non-zero voltage.

Floating collector

This boundary is treated as a floating collector at which charge is collected. The charge passing through the boundary is recorded and used as a charge density (σ). Therefore, a Neumann boundary condition is applied and equations 5.13 and 5.12 are solved for ϕ_{bound} using σ to find the electric field at the boundary.

Driving current

A current can also be used to drive a boundary. In this case a boundary condition similar to the floating collector is applied, but with an additional source for current. The equation is shown below in which A is the domain cross section and N_{ex} is the number of particles which left the domain through that boundary.

$$\frac{d\sigma}{dt} = \frac{I}{A} + \frac{\sum_0^{N_{ex}} q}{A \Delta t} \tag{5.15}$$

This equation is used to track the surface charge density. The same procedure as in the floating collector was then followed once the updated surface charge density is calculated.

Capacitor

The device can also be treated as if a capacitor is connected to the boundary. The capacitance (C) of the circuit is related to the voltage through the following equation in which Q is the charge on the capacitor plate.

$$V = Q/C \tag{5.16}$$

The charge on the capacitor is found by multiplying the surface charge density σ by the electrode area A. This charge and the specified capacitance is used to calculate the voltage on the electrode. This voltage is then applied as a typical Dirichlet boundary condition and is relative to the potential at the other side of the capacitor, which may be the other side of the domain.

General RLC circuits

Expressions also exist for general RLC circuits, but are not presented here because they are not used in the simulations presented. [115] These expressions can become fairly complex and require special treatment.

Note for staggered meshes

For staggered meshes in which the potential (cell-centers) and electric field (grid-points) are on the different meshes this method becomes more complex. It is important to also keep in mind where the boundary condition is applied, whether it is at the cell center or the cell boundaries (which are the grid points). Application of boundary conditions is similar to the standard boundary conditions used in finite-volume computational fluid dynamics.

5.1.7 Particle Loading

Loading and injection of particles into the simulation involves sampling particle velocities from a probability distribution function. Particles velocities can be loaded according to any distribution function, but the focus here will be on Maxwellian or drifting Maxwellian velocity distributions.[121, 122] The equations used for determining the velocities of loaded particles are found by mapping the velocities in the velocity distribution function to a set of random numbers. This is achieved by integrating the velocity distribution function to the desired velocity and normalizing by the distribution integrated over all space. For a Maxwellian distribution this has an analytical solution. An expression is found for the velocity,

$$v^* = \mathrm{erf}^{-1}(R\,\mathrm{erf}(v_{cu}^*) + (1 - R)\,\mathrm{erf}(v_{cl}^*)) \tag{5.17}$$

in which v_{cl}^*, v_{cu}^*, and v^* are the lower cut-off velocity, the upper cut-off velocity, and particle velocity respectively. The velocities here are normalized by $\sqrt{2kT/m}$. The parameter R is a random number between 0 and 1. Each direction is found independently and drifting Maxwellians are seeded by adding a mean velocity to each of the velocities selected by Equation 5.17. Figure 5.3 below shows the Maxwellian distributions produced using this seeding algorithm. The black line represents the analytical distribution while the histogram shows the calculated distribution. The normalized

(by mean) root mean square error found for a one hundred point Maxwellian distribution is shown as the number of particles used to resolve it is increased.

(a) Velocity Maxwellian distribution. Comparison of analytical to calculated distribution.

(b) Speed (or energy) Maxwellian. Comparison between analytical (black line) and calculated(blue histogram).

(c) RMS error normalized by mean as the number of particles to resolve the velocity and speed Maxwellian is increased.
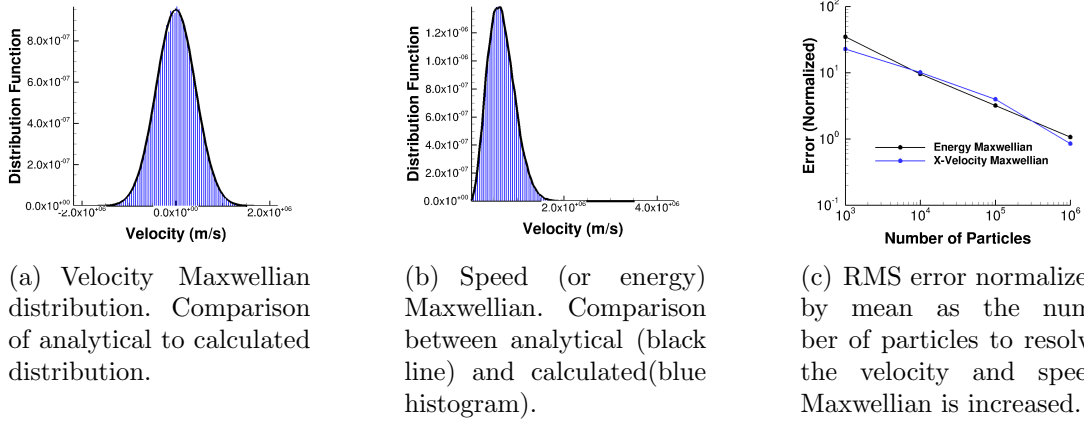
Figure 5.3: Results from loading of Maxwellian distributions.

Algorithms for the injection of Maxwellian fluxes at the boundaries have also been implemented. Flux loading requires the integration of a flux biased, stationary Maxwellian to map the distribution to random numbers and results in the expression below for the velocity.

$$v^* = \sqrt{v_{cl}^{*2} + v_{cu}^{*2} - \ln(R\exp(v^{*2}) + (1-R)\exp(v_{cu}^{*2}))} \tag{5.18}$$

This equation is used along with random number to correctly load the distribution of particles originating from a Maxwellian source.

The integration required to map the velocity distribution to random numbers for the flux of a drifting Maxwellian (as opposed to a stationary Maxwellian) does not lead to an analytical solution. Instead numerical solutions are required to find the particle velocities and is not currently incorporated.

Figure 5.4 shows the analytical and calculated flux-biased distributions used for injection of non-drifting Maxwellian using the above algorithms. The black line shows the analytical distribution while the histogram shows the calculated distribution. The root mean square error for a one hundred point Maxwellian is also shown in Figure

74

5.4 as the number of particles used for the seeding is increased.
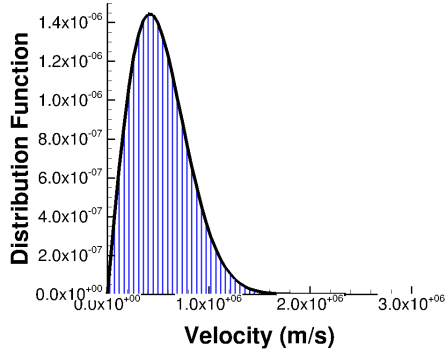
(a) Flux biased Maxwellian distribution for injection. Comparison of analytical to calculated distribution.
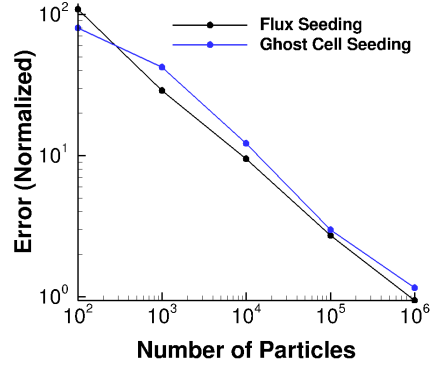
(b) Normalized (by mean value) RMS error for flux biased Maxwellian with increasing number of particles.

Figure 5.4: Results from loading of flux-biased Maxwellian distributions for particle injection.

A method for injection of particles at the boundaries using ghost particles in a ghost cell was also tested. Particles were loaded in the ghost cell according to a Maxwellian or drifting Maxwellian and then allowed to flux naturally into the domain during the particle push. Particles that do not enter the domain were deleted and a new set of ghost particles was loaded during the next time step. Initial testing reproduced the flux biased Maxwellian used in the conventional flux source approach shown above. The error reduction with increasing number of particles is shown in Figure 5.4 for the ghost cell seeding method. The ghost cell seeding method does not require a numerical solution for integrating the drifting, flux-biased Maxwellian which makes it attractive. However, this method can be inefficient due to the number of particles that need to be seeded and deleted every time step.

Another important consideration for the loading and injection of particles is time centering of the velocities. Time centering of velocities requires that an initial half step backwards in time is performed with the grid properties so that the particle velocity and position are off-set initially according to the leap-frog algorithm. While not explicitly done in these simulations, it should be taken into consideration to

75

improve accuracy and is necessary in some types of simulations.[121]

Loading and injection of general distributions can also be done using acceptance-rejection sampling. This is not currently incorporated in the code, but should be considered in the future. Acceptance-rejection sampling can be expensive computationally for an ill-chosen sampling function.

5.1.8 Heating Region

The particles were heated in the heating region according to the mechanism developed by Meige for an RF plasma. [51] The perpendicular electric field was calculated according to:

$$J_{y,tot} = \epsilon_0 \frac{\partial E_y}{\partial t} + J_{y,conv} \tag{5.19}$$

in which E_y is the electric field in the $\hat{y}$-direction and J_y is the current density in the $\hat{y}$-direction. The $\hat{y}$-direction is in the $\hat{r} - \hat{\theta}$ plane which will be used in the Q1D simulations and is perpendicular to the axial, magnetic field direction($\hat{z}$) which is spatially resolved. The $\hat{y}$ notation is maintained because this heating scheme does not translate well to axisymmetric coordinates. For an axisymmetric scheme currents would be applied to the perpendicular direction, in which velocities are always positive definite and could not respond correctly to the oscillating currents. The perpendicular direction is also a quantity that is relative to each field line and a net current from all field lines is not recoverable because the gyro-phase is not considered. Therefore, cartesian coordinates are necessary for the heating scheme.

The plasma convective current ($J_{y,conv}$) is found by summing the current (qv) contribution of the particles (both ions and electrons) in the heating zone, while the total applied current is varied as desired. For the simulation presented later the applied current was of the form $J_{y,tot} = J_0 sin(\omega t)$. Simulation using this heating region are started by initially seeding the domain with a small number of electrons and

ions. The varying electric field resulting from this method heats the initially seeded electrons which can then collide with the neutral background to produce additional ions and electrons.

5.2 One-dimensional Verification

5.2.1 Two-stream Instability

Two opposing streams of charged particles with a perturbation in their density (and thereby electric field) can be unstable for a chosen ratio of the plasma frequency (ω_p) to the wave freque ncy (kv_0). [112] The characteristic frequency for this plasma is shown below in which each stream has a velocity of $\pm v_0$ and the perturbation has a wave number k.

$$\omega = \pm \left(k^2 v_0^2 + \omega_p^2 \pm \omega_p \sqrt{4k^2 v_0^2 + \omega_p^2} \right)^{1/2} \tag{5.20}$$

The characteristic frequency has imaginary roots when $kv_0/\omega_p < \sqrt{2}$ which implies that the system is unstable and the perturbation to the density (and electric field) will grow. This behavior was tested with the 1D PIC code by seeding two streams of particles with velocities $v_0 = \pm 1$, a small sinusoidal perturbation ($k = 2\pi$) in their density, and a plasma frequency $\omega_p = 1$. The parameters were chosen to be the same as those used by Birdsall et al[112] and the domain is periodic.

The results in position-velocity phase space are shown in Figure 5.5. As the counter-flowing streams interact the grows perturbation grows, destroying the uniform structure of the streams. In this figure the time is non-dimensionalized by the plasma frequency. Birdsall's results for the same test case have been digitized and are shown for comparison. The comparison illustrates the qualitative agreement between these results. Quantitative comparisons were not made due to errors which are inherent in the digitization.

(a) $t = 16\omega_p$

(b) $t = 17\omega_p$

(c) $t = 18\omega_p$

(d) $t = 34\omega_p$

(e) $t = 60\omega_p$
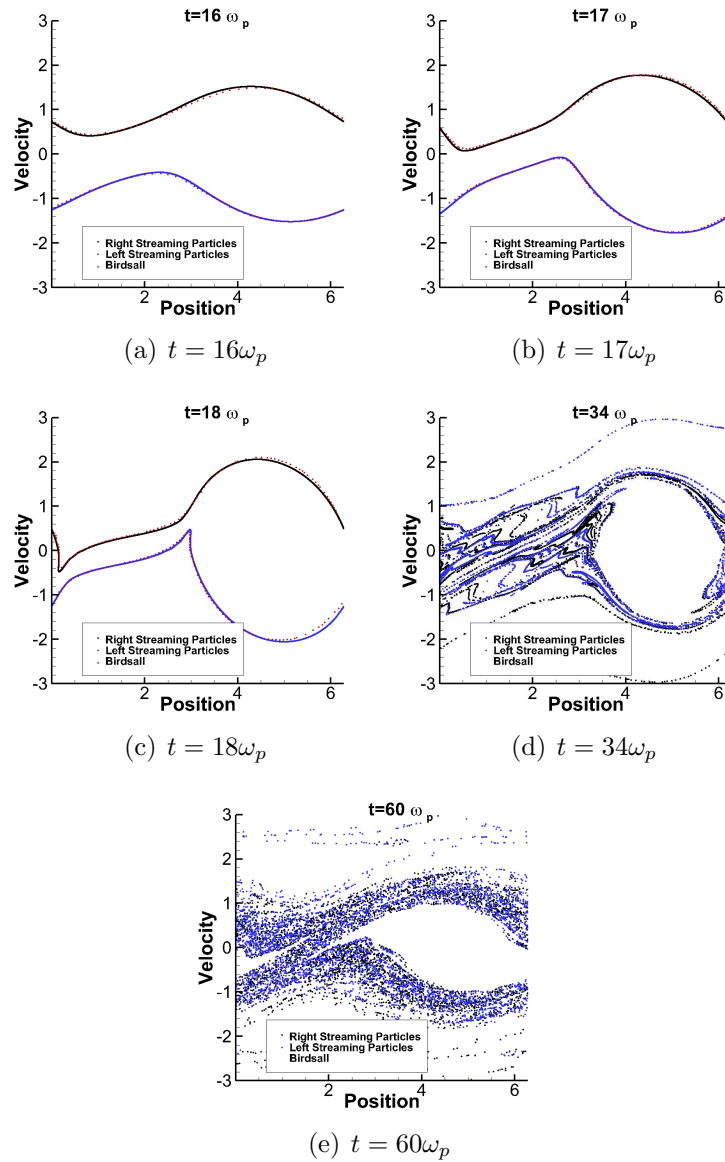
Figure 5.5: Two stream instability velocity space evolution in time. The time was normalized by the plasma frequency. Comparisons with digitized results from Birdsall are shown.
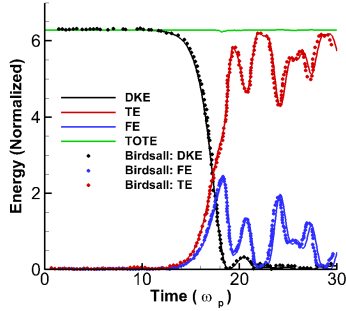
(a) Figure A: Energy history in time of directed kinetic energy (DKE), thermal energy (TKE), field energy (FE), and total energy (TOTE).
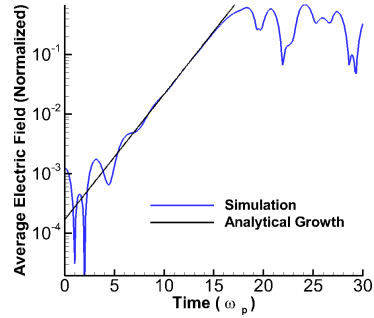
(b) Figure B: Growth of average electric field due to instability compared to linear analytical growth rate.

Figure 5.6: Energy history and instability growth in two stream instability simulations. Times are shown as cycles of the plasma frequency (ω_p).

The energy history of the simulation is shown in Figure 5.6. The instability causes the perturbation to grow and transfers energy from the uniform, directed kinetic energy to thermal and electrostatic modes. The growth of the average electric field is also shown in comparison to that predicted by theory. Equation 5.20 predicts a frequency of $\omega = 0.481i$ which implies a growth of the electric field as $e^{0.481t}$. This growth rate is plotted in Figure 5.6 and shows good agreement in the region where linear effects dominate.

The results from these simulations show good agreement with those from Birdsall as well as with the predicted theory. This simulation verified the electrostatic particle mover, weighting/interpolation algorithms, and the periodic boundary conditions. The ability of the solver to correctly capture instabilities and instability growth rates was also demonstrated. Test cases of the oppositely charged two stream instability, warm two stream instability, and beam instability have also been simulated and show good agreement with additional results presented by Birdsall. These cases are not shown here for the sake of brevity.

5.2.2 Landau Damping

Damping of electrostatic waves occurs in a plasma even without the presence of collisions. [112, 122] This phenomenon is called Landau damping and occurs due to the energy exchanged between an electrostatic wave and particles traveling near the phase velocity, $v_{ph} = \omega/k$, of the wave. Particles with velocities less than the phase velocity of the wave gain energy from the wave while particles with velocities greater than the wave phase velocity give energy to the wave. In the case of a Maxwellian distribution, there are more particles with velocities less than the wave, resulting in a net transfer of energy from the wave to the particles. The transfer of energy from the wave leads to damping of the wave.

Simulations of the Landau damping phenomenon were performed for further verification of the code. The domain chosen was one dimensional with periodic boundary conditions. A quiet start algorithm was used for loading particle velocities according to a Maxwellian velocity distribution.[111] If particle velocities were loaded randomly, no damping would be seen because the velocity distribution is not as well defined. The particle density was slightly perturbed to generate an electrostatic wave. Simulation parameters are chosen to match those of Birdsall et al [112] and Denavit et al[122]. The number of particles was 10^5 and 10^6 which is different from that of Denavit who used 17711 particles. The reason for the use of more particles was because the quiet start implemented in our simulations is not as complex as that of Denavit and required additional particles to resolve the Landau damping. The charge and mass (ratio q/m remains the same) of the particles was changed so that all other parameters remain the same.

The damping rate (ω_i) can be determined from linear analysis and is found to be:[111]

$$\omega = \omega_p \sqrt{\frac{\pi}{8}} \left(\frac{\omega_p}{kv_{th}}\right)^3 \exp\left(\frac{-\omega_{th}^2}{2(kv_{th})^2}\right) \tag{5.21}$$

80
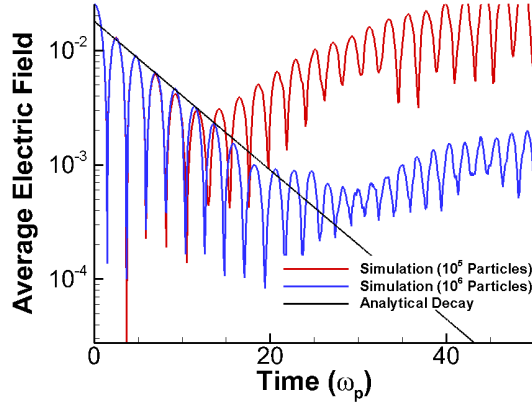
Figure 5.7: Landau damping as the number of particles is increased as well as the analytical damping rate.

where $\omega_{th} = \sqrt{\omega_p^2 + 3k^2 v_{th}^2}$. For the parameters used in this simulation a damping rate of $\omega_i = -0.15$ is expected resulting in an exponential damping $\propto e^{-0.15t}$. The average electric field from the simulations as well as the analytical damping solution are shown in Figure 5.2.2. The solutions found by Denavit et al are also shown in Figure 5.8 for comparison.

The results from Figure 5.2.2 show that the code correctly reproduces the analytic damping rate expected for a wave traveling in a Maxwellian plasma. The periodic oscillations of the electric field are due to the plasma frequency while the overall decrease is due to the effects of Landau damping. The mean electrostatic energy is damped for a finite amount of time after which growth in the average electric field occurs. Ideally, the damping would continue indefinitely, however, the finite number of particles used in these simulations limits the amount of damping due to the depletion of particles from the velocity space in which damping occurs. Increasing the number of particles allows the simulation to damp further, as illustrated. The simulation results presented here also show good qualitative agreement with those of Denavit. These results verify the algorithms used to load particles for a Maxwellian quiet start, which is essential to capturing thermal instabilities in PIC simulations.
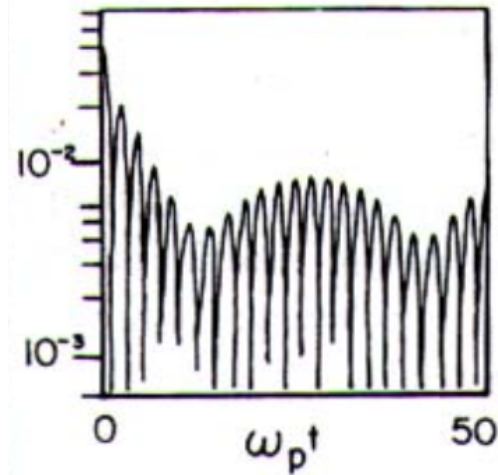
Figure 5.8: Landua damping in simulations by Denavit.

5.2.3 Source and Collector Sheath

This solver was further verified by simulating conditions which lead to the formation of source and collector sheaths. Source sheaths form to balance particle fluxes which occurs at the boundary of a Maxwellian plasma source. Collector sheaths form due to an imbalance of fluxes at a physical boundary.

The region between a Maxwellian plasma source and a collecting surface was simulated with the one dimensional PIC code and compared with the results of Schwager et al. [123] The left boundary of the domain was a Maxwellian plasma source injecting a flux of particles into the domain. Particles which are reflected back to this boundary from the domain were thermalized according to the source and then re-injected into the domain. No net charge builds up at the injection boundary. The right boundary was an electrically floating collector and net charge accumulation can occur.

The results presented herein were compared to a selected case of Schwager in which the ion-electron mass ratio (m_i/m_e) is 40, the electrons and ions have the same temperature $(T_e = T_i)$, and the domain length is 44 Debye lengths $(L = 44\lambda_D)$. The remaining parameters, grid size, and time step are chosen to match those of presented
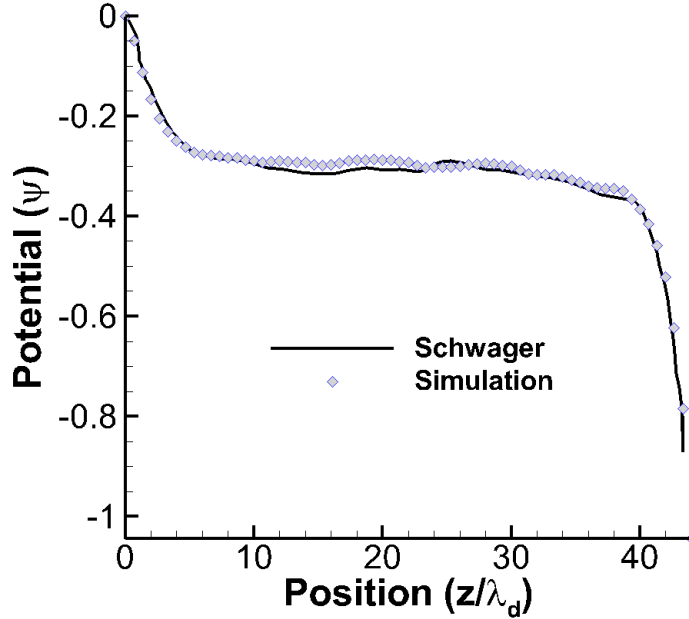
Figure 5.9: Normalized potential comparison with results of Schwager.

in detail by Schwager. Time-steps were set to $0.05/\omega_p$ and six grid points were used per Debye length. Macroparticle weights were chosen so that there were at least 400 particles per cell.[123]

Figure 5.9 shows a comparison of the non-dimensionalized potential, $\psi = e\phi/kT$, simulation results from the two codes.[123] The position in the figures are shown in terms of Debye lengths to give context for the sheath structures and compare with Schwager et al. The code developed herein correctly captured the formation of both the source and collector sheath. Both the magnitude of the potential drop and the length of the sheaths are well reproduced.

The normalized (by mid-point value) electron number densities from both simulations is shown in Figure 5.10. Again the two codes showed good agreement. Figure 5.11 shows the ion and electron densities together for comparison. Both our simulations and those of Schwager showed that the ion density is on average higher than the electron density in sheath regions. This is especially true at the collector sheath.

83
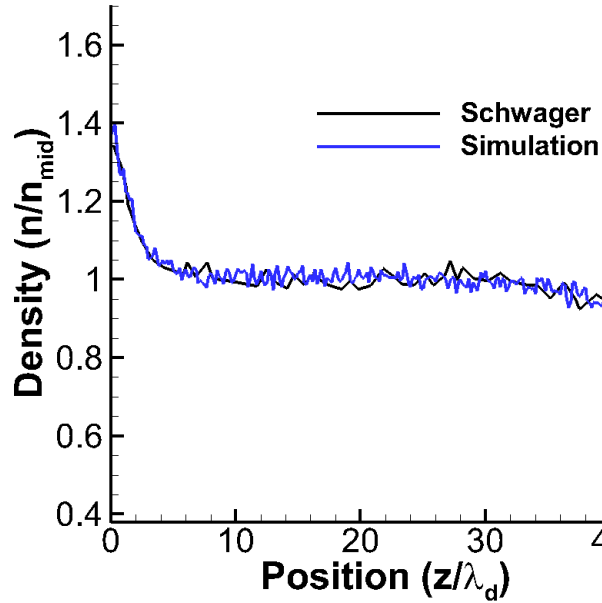
Figure 5.10: Normalized electron density results comparison for source-collector sheath simulation.

The same oscillatory behavior of the density is also seen in both simulations.

Further comparisons can be made with the temperatures and mean ion velocities reported by Schwager et al. These results are shown in Figures 5.12 and 5.13 below. Again good agreement is seen between the two codes.

Finally the velocity phase space at the end of the simulation for ions and electrons is shown in Figures 5.14 and 5.15 respectively. These contour plots show the evolution of the velocity distribution function in space. This again agrees well with the results of Schwager et al and illustrates the effects of the sheath on velocity space. Certain regions of velocity space become inaccessible by the particles due to the induced potentials.

Sheath simulations verified the code with more complex boundary conditions which include a flux source and collector. These results also illustrate the ability of the code correctly capture complex potential structures.
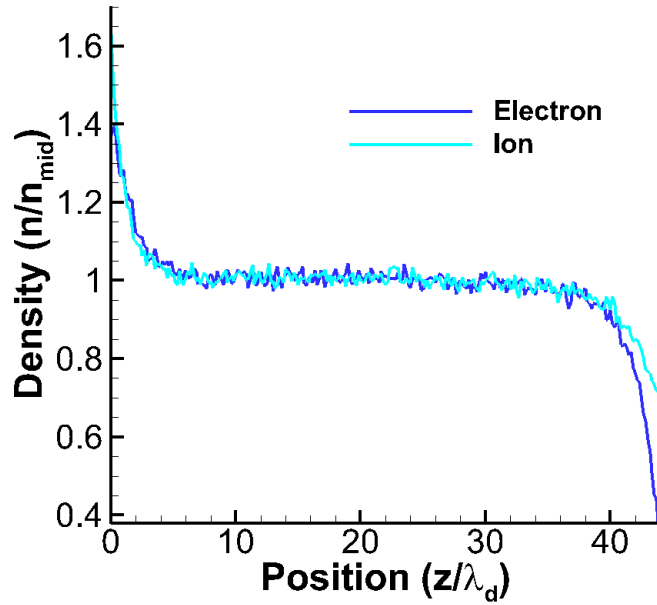
Figure 5.11: Normalized ion and electron densities for simulation for source-collector sheath simulation.
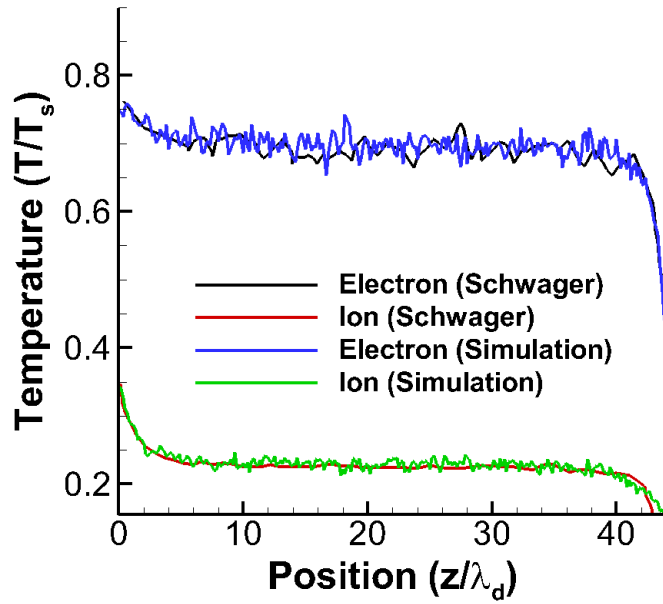
Figure 5.12: Normalized (by source temperature T_s) ion and electron temperature profile comparisons for for source-collector sheath simulation.
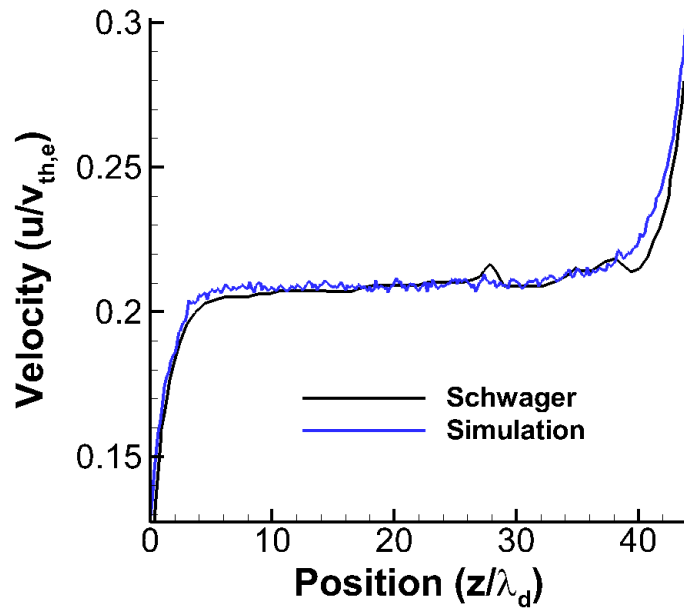
Figure 5.13: Normalized (by electron thermal velocity) mean ion velocity comparisons for source-collector sheath simulation.
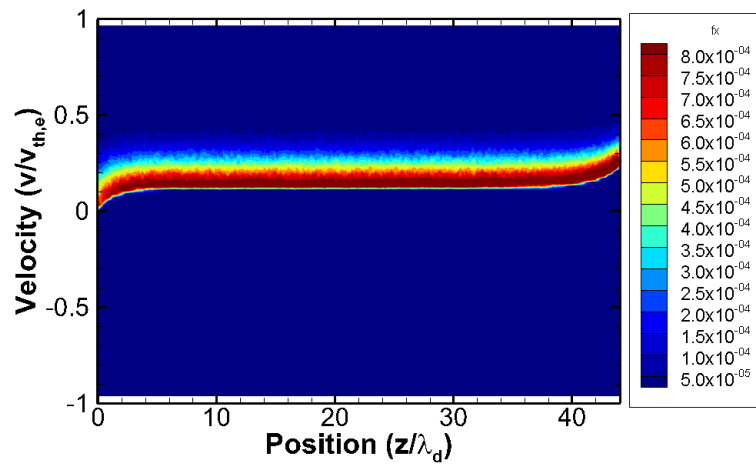
Figure 5.14: Velocity phase space for ions in source-collector sheath simulation. Velocity is normalized by electron thermal velocity.
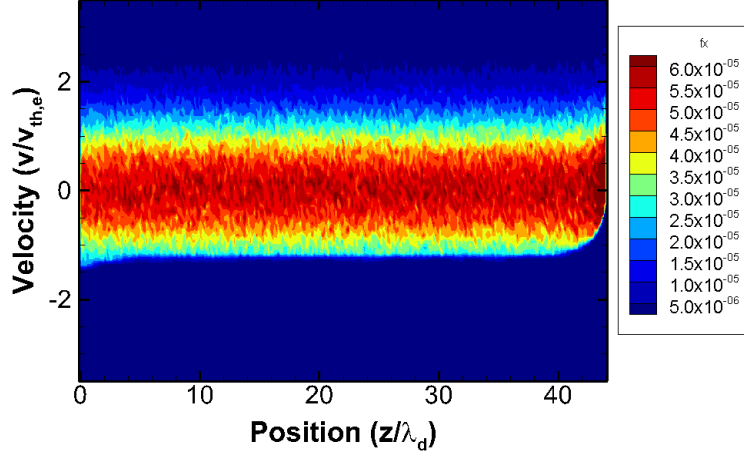
Figure 5.15: Velocity phase space for electrons in source-collector sheath simulation. Velocity is normalized by electron thermal velocity.

5.3 Neutral Collision Algorithms

Electron-neutral elastic, inelastic, and ionization collisions were included in these simulations as well as ion-neutral elastic and charge exchange collisions. These collisions were incorporated using a PIC Monte-Carlo Collision model with the null collision algorithm. [117]

The probability of a particle undergoing a collision can be found by first calculating a total collision cross-section for all the different types of collisions the particle could undergo:

$$\sigma(g)_{tot} = \sum \sigma_i(g) \tag{5.22}$$

The probability of a particle undergoing any collision (P) can then be found with the following equation in which g is the relative speed between the colliding particles:

$$P = 1 - \exp(-g\sigma(g)_{tot}n_n\Delta t) \tag{5.23}$$

The collision frequency ($\nu = g\sigma(g)n_n$) is dependent of the types of collisions, the

energy of the particle, and the background density of neutrals (n_n). The probability of a collision occurring is compared with a random number generator to determine if a collision occurs. The type of collision is then determined by using another random number generator and the relative fraction of each type of collision cross-section.

Typically the collision probability is determined particle by particle which is very expensive computationally. The null algorithm was used to significantly decrease the computational cost.[117] This algorithm imposes a constant collision frequency (ν_{tot}) for all particles that is greater than the maximum collision frequency of all the collision types combined over the entire domain of the simulation. The probability using this frequency is given below:

$$P_{null} = 1 - e^{-\nu_{tot}\Delta t} \tag{5.24}$$

This over-predicted collision frequency is used to select the number of particles which undergo a "collision" ($N_{col} = P_{null}N_{tot}$). These particles are then randomly chosen from the simulation domain.

The type of collision each of the potential colliding particles undergoes is then determined. Collision frequencies for each type of collision are calculated using the particle properties and are normalized by the total collision frequency which was used to select the particles. These normalized quantities are the probability the particle has of undergoing a specific kind of collision. Random numbers are used to select which kind of collision. A range of the random number space corresponding to the probability of each collision is determined which illustrated below in which R is a random number from $[0:1]$.

$$\begin{aligned} \text{Collision } 1 : 0 < R \le P_1 &= \frac{\nu_1}{\nu_{tot}} \\ \text{Collision } n : P_{n-1} < R \le P_n &\frac{\sum^n \nu_i}{\nu_{tot}} \end{aligned} \tag{5.25}$$

The range of probabilities used will never reach a value of one due to the fact that some of the total collision frequency is due to the arbitrary null collision frequency added to simplify the selection of particles. Random numbers that fall outside of the range of probabilities undergo a null collision, implying no collision occurs at all. The null collision frequency provides a means for reducing the number of particles analyzed by including a fictitious collision. By over-predicting the number of particles that undergo collisions this method simultaneously reduces the overall number of particles analyzed and captures the probabilities of all other possible collisions.

The cross-section data used in this code was incorporated in tabulated form based on literature and collected from the LXCat database. [124, 125, 126]

5.3.1 Electron-Neutral Collisions

The types of electron-neutral collisions considered include elastic, inelastic, and ionization. Detailed discussion of these types of collisions can be found in the work of Vahedi et al. [117] The following sections provide a very brief summary of the equations used in this model.

5.3.1.1 Elastic

Elastic electron-neutral collisions are the first type of collision considered. For these collisions the neutral background is assumed to be stationary to simplify the calculations. This assumption is possible because the electron velocity is much greater than that of the neutral background.

Kinetic energy is conserved in elastic collisions, although the energy of the neutrals is not tracked. The scattering angle (χ) for the electron is determined by integrating over a differential cross-section model leading to the expression below for the distribution of the scattering angles in terms of the incident energy in eV ($\mathcal{E}_i$) and a random number (R) between 0 and 1.

$$\chi = \cos^{-1}\left(\frac{1 + \mathcal{E}_i - 2(1 + \mathcal{E}_i)^R}{\mathcal{E}_i}\right) \tag{5.26}$$

The azimuthal angle (ϕ) is chosen randomly between 0 and 2π. Using these angles the scattered velocity can be found using the following equation:[118]

$$\mathbf{v_{scat,i}} = \mathbf{v_{inc,i}}\cos(\chi) + \frac{\mathbf{v_{inc}} \times \hat{k}}{|v|\sin(\theta)} + |v|\sin(\chi)\sin(\phi) + \frac{\mathbf{v_{inc}} \times (\mathbf{v_{inc}} \times \hat{k})}{|v|^2\sin(\theta)}|v|\sin(\chi)\cos(\phi) \tag{5.27}$$

In this equation θ is the angle between the unit vector $\hat{k}$ and the incident velocity. This scattered velocity must be scaled to account for the energy which is exchanged with the neutral background (the energy lost by the electron, $\Delta\mathcal{E}$) and is found by the expression below.

$$\Delta\mathcal{E} = \frac{2m_e}{m_n}(1 - \cos(\chi))\mathcal{E}_i \tag{5.28}$$

This change in energy is used to scale the scattered velocities by the factor α below:

$$\alpha = \sqrt{1 - \frac{\Delta\mathcal{E}}{\mathcal{E}_i}} \tag{5.29}$$

The energy loss per collisions is typically very small because it scales as m_e/m_n. These collisions are important to creating isotropic distributions for the electrons at low energies ($< 100\ eV$) and result in primarily small angle collisions at high energies ($> 100\ eV$).

5.3.1.2 Excitation

Excitation collisions do not conserve the kinetic energy of the colliding particles. Energy is lost to the internal modes of the electron and then emitted as radiation.

There are a number of different inelastic energy modes to consider and for these simulations only a single inelastic mode (the highest cross-section) was considered. The final energy of the electron undergoing an excitation collision is found by subtracting the excitation energy $(\mathcal{E}_{ex})$ from the incident energy. The velocity scaling factor is determined using Equation 5.29 with $\Delta\mathcal{E} = \mathcal{E}_{ex}$. The scatting angle is obtained from Equation 5.26 using the final energy of the particle and a random number. The azimuthal angle is again chosen randomly. The scattering velocity (Equation 5.27) and final scaled velocity can then be calculated using the same methods used in elastic collisions. These excitation collision only occur for electron energies greater than $\mathcal{E}_{ex}$.

5.3.1.3 Ionization

In ionization collisions a high energy electron creates an additional ion-electron pair by colliding with a background neutral. For simplicity the newly created ion is assumed to have the same energy as the neutral background. The initial energy of the incident electron is then divided between the energy needed for ionization $(\mathcal{E}_{ion})$, the final energy of the incident electron, and the energy of the newly ejected electron $\mathcal{E}_{ej}$. The energy of the ejected particle is found using Equation 5.30.

$$\mathcal{E}_{ej} = B \tan \left(R \tan^{-1} \left(\frac{\mathcal{E}_{in} - \mathcal{E}_{ion}}{2B} \right) \right) \tag{5.30}$$

In this equation B is an experimentally determined parameter which for argon is $B_{Ar} = 10 \ eV$ and for xenon is $B_{Xe} = 8.7 \ eV$.[118, 127] The energy of the scattered particle can now be determined, or equivalently the change in energy of the incident particle is found to be $\Delta\mathcal{E} = \mathcal{E}_{ion} + \mathcal{E}_{ej}$. The energy of the scattered and ejected particles are used in Equation 5.26 to determine the scattering angle of each. An azimuthal angle is then chosen randomly for each. The scattering velocity (Equation 5.27) and final scaled velocity are calculated using these scattering angles. The initial velocity of the incident particle is the velocity transformed for both electrons. The

energy change undergone relative to the incident electron is used to scale the final velocities using Equation 5.29. Ionization collisions only occur for incident electrons with energies greater than $\mathcal{E}_{ion}$.

5.3.2   Ion-Neutral Collisions

Both elastic and charge-exchange (or backscattering) collisions are considered for ion-neutral collisions. The primary difference between ion-neutral and electron-neutral collisions is that the neutral species dynamics must be taken into account and the background can no longer be assumed as stationary. The heavy mass of the ions means that they will move at lower velocities, which could be on the order of the background neutral velocity.

5.3.2.1   Elastic

Elastic collisions conserve the kinetic energy during a collision. The first step in the elastic collision is to create a neutral particle based on the neutral background temperature with which the incoming ion can collide. The colliding ion is then transferred from the lab frame to a frame in which the neutral is stationary. The collisions are treated as hard sphere collisions between particles of the same mass which results in the following scattered energy .

$$\mathcal{E}_{scat} = \mathcal{E}_i cos^2(\chi) \tag{5.31}$$

The angle χ is the scattering angle in the laboratory frame. This angle is found by assuming a uniform, isotropic scattering in the center of mass frame to give the following equation in which R is a random number from $[0:1]$.

$$\chi = \cos^{-1}(\sqrt{1-R}) \tag{5.32}$$

The azimuthal angle used in scattering is determined by another random number between $[0 : 2\pi]$. The scattering of the ion is performed in the stationary neutral frame and the resulting velocities are then transferred back to the laboratory frame.

5.3.2.2 Charge-Exchange

In charge-exchange (or backscattering) collisions the high energy ion gives its charge to the the slow neutral particles. In effect, a new slow ion is produced along with a hot neutral while destroying the original ion and neutral. This type of collision is the simplest to handle because the velocity of the colliding ion is just replaced with a velocity representative of the neutral background temperature.

5.4 Collision Algorithm Verification

The verification of the null-collisional algorithm is presented in this section. Verification is shown for collisions with a neutral argon background density, but the code is implemented so that an arbitrary gas can be used as long as cross-sections and collision data are available. The code has been tested with xenon as well, but is not presented here.

Verification of the collision algorithms was done in two steps.[118] First the scattering algorithm was tested to make sure particles are scattered correctly and then the collision selecting algorithm was tested to show that algorithm produces the correct collision frequencies.

5.4.1 Electron-Neutral Collisions

Analytical velocity distributions can be derived for a beam of particles undergoing an isotropic collision process. Each particle undergoes a collision at every timestep. The velocity distribution in the streaming and perpendicular directions can be determined analytically after each collision occurs as shown by Sydorenko.[118] Figure 5.16

(a) Initial velocity distribution.

(b) Velocity distribution after 1 collision.

(c) Figure C: Velocity distribution after 6 collisions.
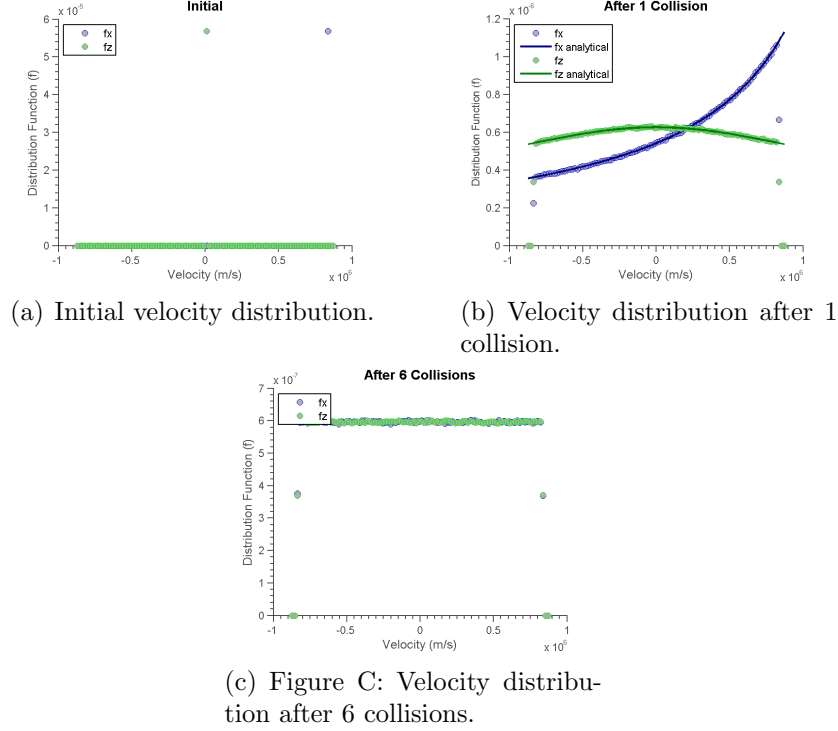
Figure 5.16: Evolution of velocity distribution for electrons due to collisions.

shows the analytical and simulation velocity distribution functions. The simulations agree well with the analytically predicted distributions and after six collisions the velocity distribution of the electrons has become isotropic.

The ability of the algorithm to produce the correct collision frequency was also tested. This simulation was performed by injecting a beam of particles with a known energy into a the neutral background and counting the number of each type of collision. The number of collisions was used along with the total time to calculate the collision frequency. Figure 5.17 shows the result of these test simulations and demonstrates the reproduction of the correct analytical collision frequencies. A neutral background density of $n_n = 10^{18} \; \frac{\#}{m^3}$ was used in these simulations.

5.4.2 Ion-Neutral Collisions

An analytical solution was not derived for the response of a beam of ions colliding with the neutral background, but a simple test case was still studied to insure that

94
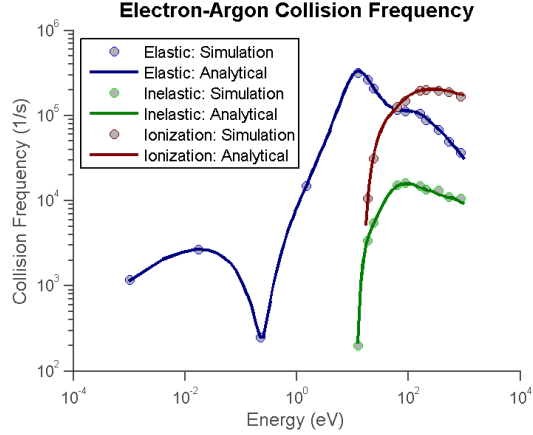
Figure 5.17: Collision frequencies for electron-neutral collisions based on simulations and calculations.

these types of collision produce the correct behavior over time. This solution is more complex because the ion mass is essentially the same as the background neutral mass, which no longer allows for simplifying assumptions to be made in the analysis. Figures 5.18 and 5.19 show how an initial beam of ions approaches the ion velocity and speed distribution function of the background neutrals. After fifty collisions the beam has lost all of its energy to the neutral background and has equilibrated to the distribution of the background.

Verification of null collision frequency algorithm was also performed by injecting beams of ions with varying energies into a neutral background. The ion-neutral collision frequency was then calculated in a manner similar to that done for the electron-neutral frequencies where the number of collisions are counted over a known simulation time. Figure 5.20 shows the result of these test cases in which the correct collision frequencies are captured for the ion-neutral elastic and charge exchange collisions. A neutral background with a density $n_n = 10^{18} \frac{\#}{m^3}$ and a temperature of $T_n = 10\ K$ was used for these simulations.
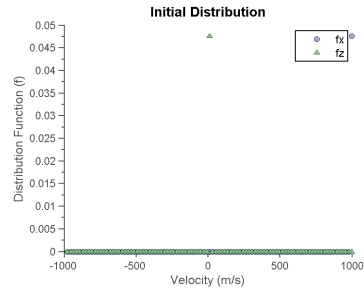
(a) Initial velocity distribution.
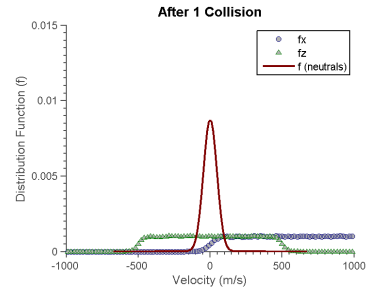
(b) Velocity distribution after 1 collision.
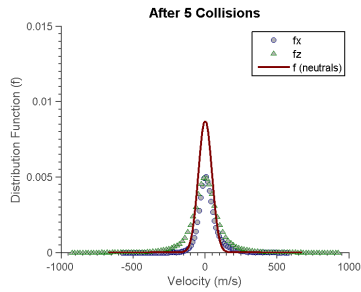
(c) Velocity distribution after 5 collisions.
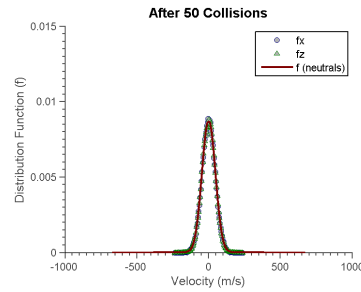
(d) Velocity distribution after 50 collisions.

Figure 5.18: Ion velocity distribution variation due to collisions.
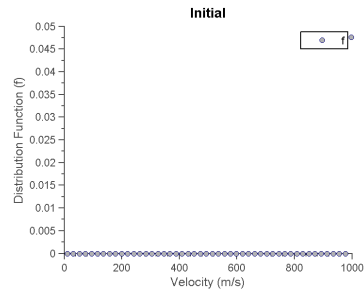
(a) Initial speed distribution.
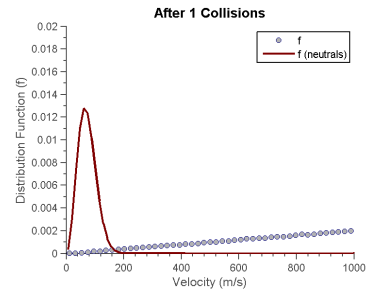
(b) Speed distribution after 1 collision.
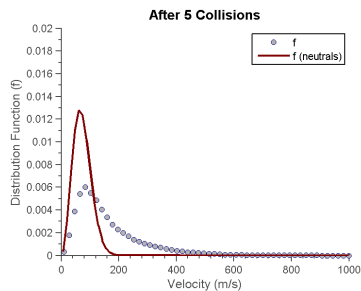
(c) Speed distribution after 5 collisions.
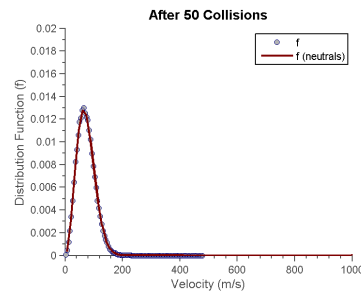
(d) Speed distribution after 50 collisions.

Figure 5.19: Ion speed/energy distribution variation due to collisions.
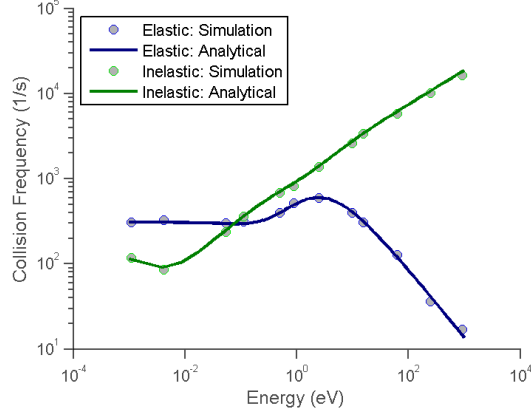
Figure 5.20: Ion-neutral collision frequencies based on simulations and calculations.

5.5 Radio-frequency Plasma Simulation

The most rigorous verification of the 1D algorithms was performed by simulating one-dimensional voltage-driven and current-driven radio-frequency plasma discharges. Results for these simulations are compared with the XPDP1 (X-Windows Plasma Device Planar Planar 1D) one dimensional PIC code [115] as well as with other simulations and experiments.[128, 127] XPDP1 is an object-oriented plasma device code with planar electrodes. The code includes external circuit components, Monte Carlo collisions with neutrals, and a number of more advanced numerical schemes such as implicit particle movers, smoothing, and second order particle loading. For comparisons with XPDP1 the cross-section data used was obtained from the code instead of using the cross-sections from the LxCat database in order to better compare results.

5.5.1 Voltage-Driven Discharge

The parameters chosen for the voltage-driven discharge are summarized in Table 5.1 and are taken from a test case for XPDP1. The domain is initially seeded with density of 10^{15} $\#/m^3$ ions and electrons at $T = 1$ eV. The left boundary of the domain was a sinusoidally varying applied voltage while the right boundary was a

grounded electrode. Identical simulations were performed with the Q1D code and XPDP1 to further verify the correct implementation of the 1D algorithms. Some algorithms (e.g. time centered loading, etc.) and the implementation of algorithms (e.g. tabular cross-section data, etc.) used in each code are different, but simulation parameters are chosen to be the same. Note that no two dimensional effects are included, the code is just referred to as Q1D for ease of comparison.

Table 5.1: Parameters for RF voltage driven plasma simulation.

Parameter	Value
Length	5 cm
Grid Points	301
Time Step	3.8×10^{-11} s
Voltage Amplitude	500 V
Heating Frequency	13.56 MHz
Macroparticle Weight	1×10^8 Particles/Macroparticle
Neutral Pressure	50 mTorr
Neutral Temperature	300 K
Gas	Argon

The results from both codes are shown in the Figures 5.21(a) - 5.21(d) below. All results are compared at $t = 2.88072 \times 10^{-4}$ seconds. Good qualitative and quantitative agreement is shown for the argon density in Figure 5.21(a). A difference is seen in the maximum density with XPDP1 predicting a value around $n_{Ar,max} = 1.2 \times 10^{16}$ $\#/m^3$ and the Q1D code predicting a value of around $n_{Ar,max} = 1.15 \times 10^{16}$ $\#/m^3$. This difference can be attributed to a number of nuanced differences between the implemented numerical methods (e.g. cross-sections in tabular versus functional form, different particle loading schemes, etc.) in the codes. The electron density, Figure 5.21(b), shows similar agreement. More noise is seen in the electrons due to their propensity to respond rapidly to any changes in the plasma. The potential shown in Figure 5.21(c) is nearly identical between the two codes.

Finally, the electron kinetic energy is shown in Figure 5.21(d). Electron temperature is an inherently fluctuating parameter in these PIC simulations due to the
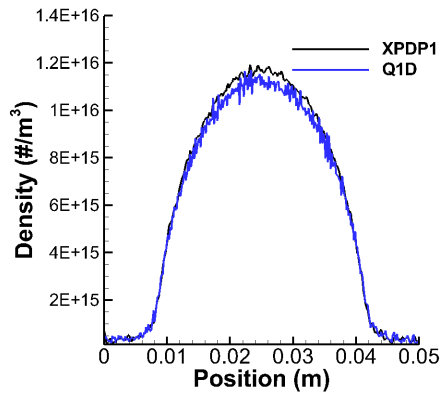
(a) Argon number density variation
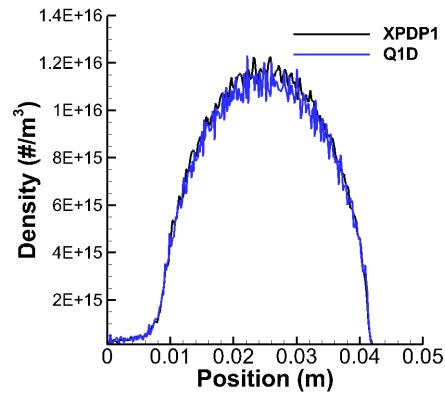
(b) Electron number density variation
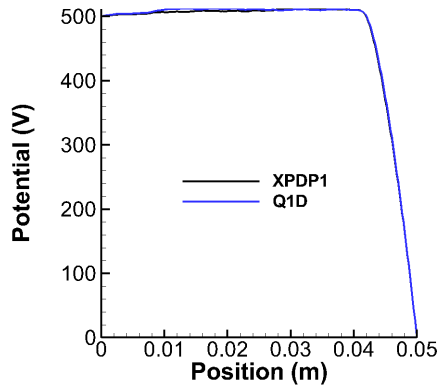
(c) Potential
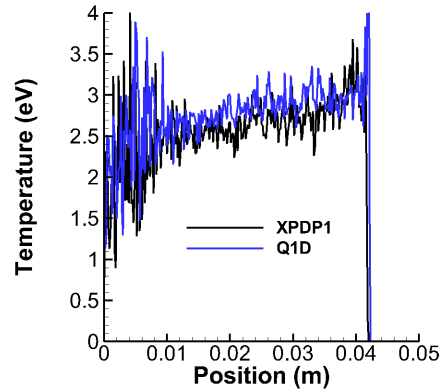
(d) Electron Temperature

Figure 5.21: Voltage driven discharge results comparing XPDP1 and Q1D results.

rapid response of the electrons to the changing applied field. The two codes produce very similar electron energy profiles in the domain, but some differences are seen. In particular the Q1D code predicts slightly higher temperatures. This may again be attributed to the different algorithms incorporated in the two codes. XPDP1 is a much more mature code and incorporates more sophisticated schemes than some of those currently implemented in the Q1D code.

The RMS errors between the simulations is shown in Table 5.2. Errors are found by treating the XPDP1 results as the predicted value and are normalized by the maximum value. The density errors are below 4% while the errors in the potential are less than a percent. Errors in the electron temperature are higher, mostly due to

the fluctuating nature of the data.

Table 5.2: Root mean square errors for voltage-driven discharge simulations.

Parameter	Error
Argon Density	3.09 %
Electron Density	3.92 %
Potential	0.48 %
Electron Temperature	15.4 %

5.5.2 Current-driven RF Discharge

The simulation parameters for the current-driven discharge are chosen to match those of Vahedi et al. [129] These simulations were designed to model an experiment by Godyak[128] for which the chosen parameters are summarized in the table below.

Table 5.3: Parameters for RF current-driven plasma simulation.

Parameter	Value
Length	2 cm
Grid Points	401
Time Step	3.8×10^{-11} s
Heating Current	25.6 A/m^2
Heating Frequency	13.56 MHz
Macroparticle Weight	1×10^9 Particles/Macroparticle
Neutral Pressure	100 mTorr
Neutral Temperature	300 K
Gas	Argon

The domain is initially seeded with density of 10^{15} #/m^3 ions and electrons at $T = 1$ eV. The left boundary imposes a sinusoidally varying applied current while the right boundary is grounded. The resulting densities produced by XPDP1 and the newly developed Q1D code are shown in Figures 5.22(a) and 5.22(b). All results are compared at $t = 1.14 \times 10^{-4}$ seconds. Both the electron densities, Figure 5.22(b), and the ion densities, Figure 5.22(a) show very similar densities. The slight differences in densities can easily be attributed to slightly different numerical schemes or

(a) Argon number density variation

(b) Electron number density variation

(c) Potential variation

(d) Electron kinetic energy variation
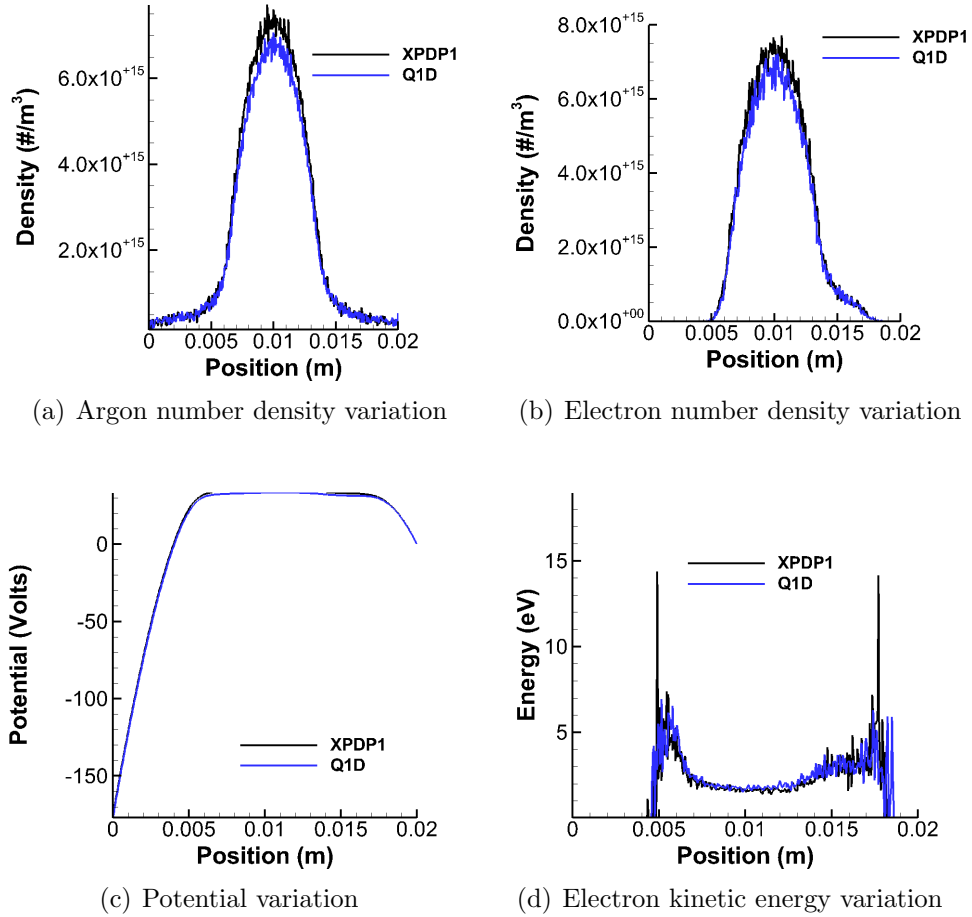
Figure 5.22: Current-driven discharge results comparing XPDP1 and Q1D simulations.

implementations. The potential and electron kinetic energy found in both codes also shows good agreement.

The RMS errors are shown in Table 5.4. Errors are found by treating the XPDP1 results as the predicted value and are normalized by the maximum value in the domain. The density errors are below 5% while the errors in the potential are less than a percent. Errors in the electron temperature are higher, mostly due to the fluctuating nature of the data.

The velocity distribution of the Q1D simulations was analyzed to compare with the results of Vahedi et al.[127] The resulting axial velocity distribution is shown in Figure 5.23 along with Maxwellian distributions for comparison. The y-axis is on a log

Table 5.4: Root mean square errors for current-driven discharge simulations.

Parameter	Error
Argon Density	4.23 %
Electron Density	4.71 %
Potential	0.85 %
Electron Temperature	8.76 %
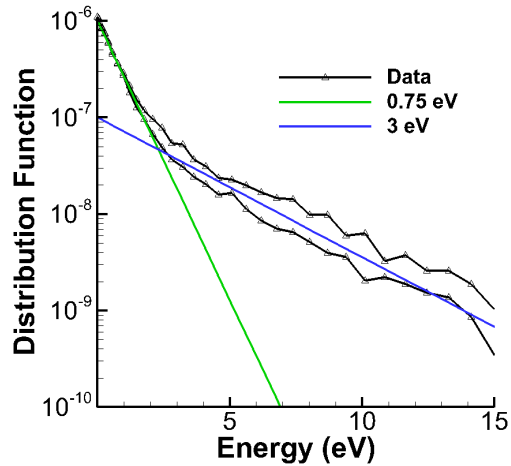
Figure 5.23: Electron axial velocity distribution function.

scale and the velocity is put in energy units (eV). On this type of plot a Maxwellian distribution is a straight line with a slope equal to $1/T$. The data from simulations shows two lines, one for each side of the velocity distribution function. Both sides are positive because this is plotted on an energy scale for ease of comparison with the Maxwellian distribution.

The velocity distribution of Figure 5.23 shows that the distribution has two characteristic temperatures. Low energy particles have the characteristics of a plasma at $0.75\ eV$ while the high energy particles have the characteristics of a plasma at $3\ eV$.

Finally simulations were performed using the cross-section data which will be used in the bulk of the thesis instead of used in the XPDP1 code. This data was obtained from the LXCat database.[124, 125, 126] Results of these simulations are shown in Figure 5.24. These LxCat cross-section results show an overall higher density with a maximum around $1.5 \times 10^{15}\ \#/m^3$. The velocity distribution results are also shown

(a) Argon number density variation   (b) Electron number density variation
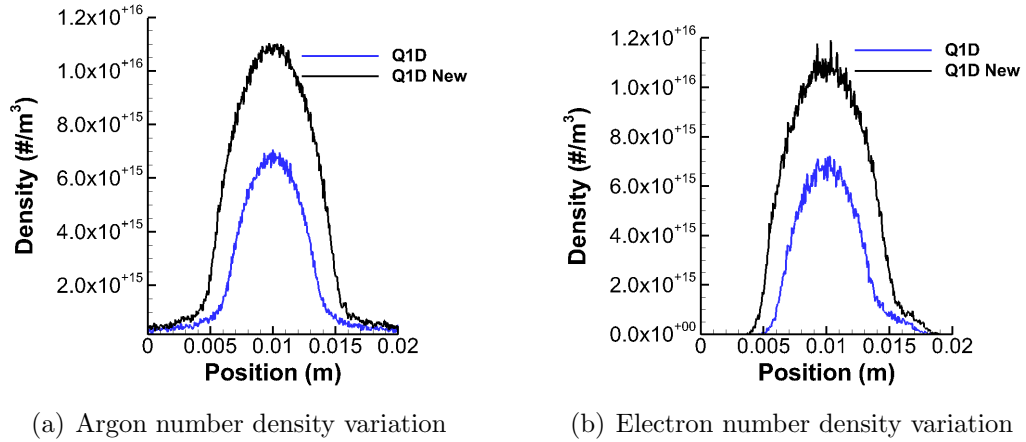
Figure 5.24: Simulation results with LxCat cross-section data (Q1D New) compared to results using cross-section data from in XPDP1 (Q1D).

in Figure 5.25. Two temperatures are seen again, with a hot group of electrons at 3 eV and a cold group of electrons at around 0.6 eV.

These simulations results compare favorably with the previous simulation results of Vahedi et al as well as the experiment they compared against.[129, 127] The simulation results of Vahedi predicted a maximum density of $n_{max} = 8 \times 10^{15}$ $\#/m^3$, hot electrons at 3 eV, and cold electrons at .5 eV. The experiment results measured a maximum density of $n_{max} = 1.5 \times 10^{16}$ $\#/m^3$, hot electrons at 3 eV, and cold electrons at .4 eV. Therefore, the code developed herein was able to very closely match the maximum number density when the LxCat cross-sections were implemented. It also showed the two temperature characteristics for the electrons, with slightly higher temperatures for the cold electrons than those in Vahedi's simulations and in the experiments.

5.6 Coulomb Collision Algorithms

The effects of Coulomb collisions were also modeled using a grid-based collision model. [119] Inter-species forces on the particle are found using properties determined from moments of the distribution function and reproduce the fluid transport
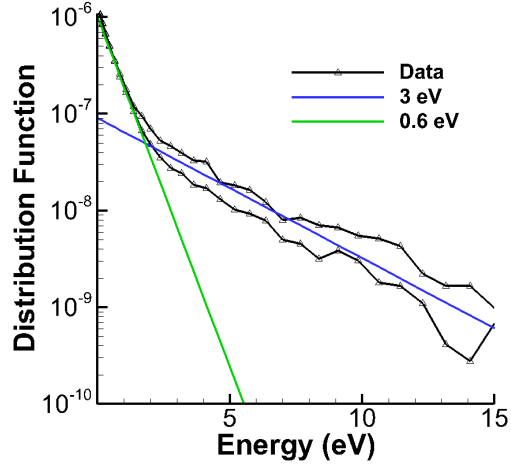
Figure 5.25: Electron axial velocity distribution using LxCat database cross-section data.

equations. Intra-species collisions are modeled based on the Langevin equation and incorporate scattering similar to that in Monte-Carlo collisions.[119] Each method is discussed below.

5.6.1 Inter-species Collisions

Inter-species collisions occur between particles of different species α and β. Momentum transfer $(\nu_{\alpha\beta})$ and energy equilibration $(\nu_{\alpha\beta}^{\mathcal{E}})$ collision frequencies are defined as part of these equations and are shown below.

$$\nu_{\alpha\beta} = \frac{8\sqrt{\pi}q_\alpha^2 q_\beta^2 n_\beta ln\Lambda_{\alpha\beta}}{m_{\alpha\beta}^2 \Delta v^3 (4\pi\epsilon_0)^2} \left(\frac{\sqrt{\pi}}{2} \mathrm{erf}\left(\frac{\Delta v}{v_{th}}\right) - \frac{\Delta v}{v_{th,\alpha\beta}} \exp\left(-\frac{\Delta v^2}{v_{th,\alpha\beta}^2}\right) \right) \tag{5.33}$$

$$\nu_{\alpha\beta}^{\mathcal{E}} = \frac{16\sqrt{\pi}q_\alpha^2 q_\beta^2 n_\beta ln\Lambda_{\alpha\beta}}{m_\alpha m_\beta v_{th,\alpha\beta}^3 (4\pi\epsilon_0)^2} \left(-\exp\left(-\frac{\Delta v^2}{v_{th,\alpha\beta}^2}\right) \right) \tag{5.34}$$

These equations include the Coulomb logarithm $(\ln\Lambda_{\alpha\beta})$, the reduced thermal velocity $(v_{vth,\alpha\beta} = \sqrt{2(k_b T_\alpha/m_\alpha + k_b T_\beta/m_\beta)})$, the magnitude of the mean velocity

difference ($\Delta v = |\boldsymbol{u}_\alpha - \boldsymbol{u}_\beta|$), the reduced mass ($m_{\alpha\beta} = m_\alpha m_\beta/(m_\alpha + m_\beta)$), and the permittivity of free space (ϵ_0). The mean velocity $\boldsymbol{u}_\alpha$ is found by averaging the velocity of all the particles $\langle \boldsymbol{v}_\alpha \rangle$. The Coulomb logarithm is a factor which scales the collision frequency when including the effects of multiple small angle collisions and typically ranges from 5 to 15. These equations give rates similar to those found both in the Naval Research Lab Plasma Formulary[130] and the work of Decoster [119] and Rambo [131].

These collision frequencies were used in the following expression for the force each particle feels due to inter-species Coulomb collisions.

$$
\begin{aligned}
\mathbf{F}_{\alpha\beta} = \nu_{\alpha\beta} m_{\alpha\beta}(\boldsymbol{u}_\beta - \boldsymbol{u}_\alpha) &- \nu_{\alpha\beta}\frac{m_{\alpha\beta}^2}{m_\alpha}\frac{(\boldsymbol{u}_\alpha - \boldsymbol{u}_\beta)^2}{\langle\mathbf{v}^2\rangle_\alpha - \langle\mathbf{v}_\alpha\rangle^2}(\boldsymbol{u}_\alpha - \mathbf{v}_\alpha) \\
&+ \nu_{\alpha\beta}^{\mathcal{E}}\frac{(k_b T_\alpha - k_b T_\beta)}{\sum^\alpha\left(\langle\mathbf{v}^2\rangle_\alpha - \langle\mathbf{v}_\alpha\rangle^2\right)}(\boldsymbol{u}_\alpha - \mathbf{v}_\alpha)
\end{aligned}
\tag{5.35}
$$

This form for the force was chosen because it satisfies both momentum and energy conservation between the species and reduces to the fluid transport equations when averaged. The form of Equation 5.35 is slightly different from that presented in Jones et al [119]. The third term includes a sum in the denominator for the equations to simplify to the correct fluid equations and produce the correct relaxation behavior.

5.6.2   Intra-species Collisions

Intra-species collisions occur between particles of the same species and must be treated differently. These collisions are modeled using the Langevin equation with the form:

$$
\mathbf{F}_{\alpha\alpha} = -m_\alpha \nu_\alpha(\mathbf{v}_\alpha - \mathbf{u}_\alpha) + m_\alpha\mathbf{A}
\tag{5.36}
$$

In this equation $\mathbf{A}$ is a random vector and ν_α is a friction coefficient. The friction

coefficient is chosen to be the same as that derived by Spitzer[37]. The collision frequency is shown below for singly charged ions:

$$\nu = \frac{ne^4 \ln \Lambda}{12\sqrt{m}\epsilon_0^2 (k_b \pi T)^{3/2}} \tag{5.37}$$

The form of Equation 5.36 conserves momentum as long as a statistically significant number of particles is used so that $\langle \mathbf{A} \rangle = 0$. The random vector $\mathbf{A}$ is chosen so that the energy is conserved and so that the distribution approaches a Maxwellian. These requirements are achieved by randomly selecting the components of $\mathbf{A}$ from the Maxwellian distribution shown below:

$$f_A = \left(\frac{1}{2\pi v_{th,A}^2} \right)^{3/2} \exp \left(-\frac{\mathbf{A} \cdot \mathbf{A}}{2v_{th,A}^2} \right) \tag{5.38}$$

The typical thermal velocity of a Maxwellian distribution $(v_{th} = \sqrt{kT/m})$ is replaced by $v_{th,A}$ of the form below:

$$v_{th,A} = \sqrt{\frac{3\nu_\alpha \Delta t k_b T_\alpha}{m_\alpha}} \tag{5.39}$$

This choice of the distribution and thermal velocity results in the Langevin equation modeling the relaxation to a Maxwellian distribution while conserving both momentum and energy. The vector $\mathbf{A}$ is chosen by sampling from this Maxwellian distribution using the methods outlined in the previous section using the newly defined thermal velocity.

5.6.3 Implementation

The Coulomb collision forces are incorporated by using a first order, Euler discretization in time. This method is chosen due to the simplicity of implementation, requiring only information from the current time step such as the rest of the code. The macroscopic quantities needed for these calculations (e.g. $\langle v \rangle$, $\langle v^2 \rangle$,etc) are weighted

to the grid and are used to determine the forces on the particles. For the Coulomb collision algorithm all weighting is done with a the nearest cell scheme to insure momentum is conserved within the Coulomb collision algorithm and no self-force is present. The nearest cell weighting is used for simplicity because linear weighting becomes complex when using all the continuum properties required by Equations 5.35 and 5.36. Note that the weighting in the Coulomb algorithm may be different than that used by the rest of the code but is consistent within itself. Future work should incorporate a linear weighting of the properties needed to calculate these forces.

As suggested by Jones et al [119], when both collision types are implemented the intra-species collisions are performed first, after which the inter-species collisions are performed. This is intended to alleviate the drifting of the temperature of the distribution which may occur over time for large collision frequencies. The macroscopic properties are re-weighted after the intra-species collisions and then used in the inter-species collisions.

5.7 Coulomb Collision Verification

5.7.1 Intra-Species Collisions

Intra-species collisions are verified by investigating the relaxation of a non-Maxwellian distribution to a Maxwellian distribution. [118, 132] A distribution is seeded randomly with a maximum energy in each direction to 2 eV. This distribution is then allowed to relax to equilibrium. At equilibrium the random distribution should relax to a Maxwellian distribution with $T = 1.33$ eV because the initial random distribution has a mean energy $\langle mv^2 \rangle = 1.33$ eV. The relaxation results will be compared with a different scheme developed by Manheimer which incorporates a different Coulomb collision algorithm also based on the Langevin equation but which does not explicitly assume isotropic scattering as is done in the grid-based model.[132] The difference be-
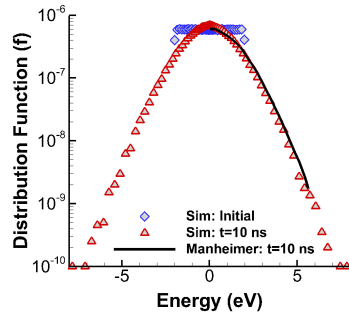
(a) Velocity distribution at t=10 ns.
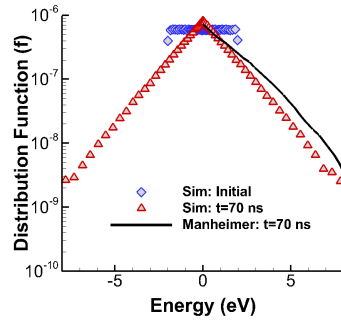
(b) Velocity distribution at t=70 ns.
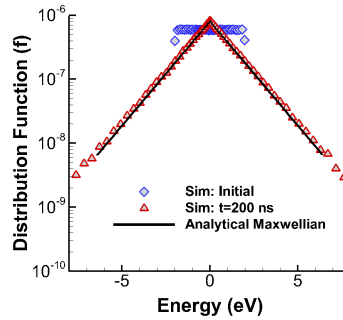
(c) Velocity distribution at t=200 ns.

Figure 5.26: Velocity distribution relaxation comparison with Manheimer.

tween these schemes is particularly important for resolving the high energy tail. The method implemented here over predicts the cooling in the tail, while Manheimer's technique better treats the cooling of the high energy particles.

The results of the velocity distribution relaxation are shown in Figure 5.7.1 and is compared with the results of Manheimer [132]. Results show good agreement and the distribution relaxes to the correct distribution. The grid-based collision algorithm relaxes faster than that of Manheimer and some difference is seen at 70 ns. This differences is due to the over prediction of cooling of high energy particles in the implemented scheme.

Figure 5.27 also shows the particles in velocity space. The initial block distribution relaxes to the circular Maxwellian distribution over time.

(a) Initial velocity space.

(b) Final velocity space.
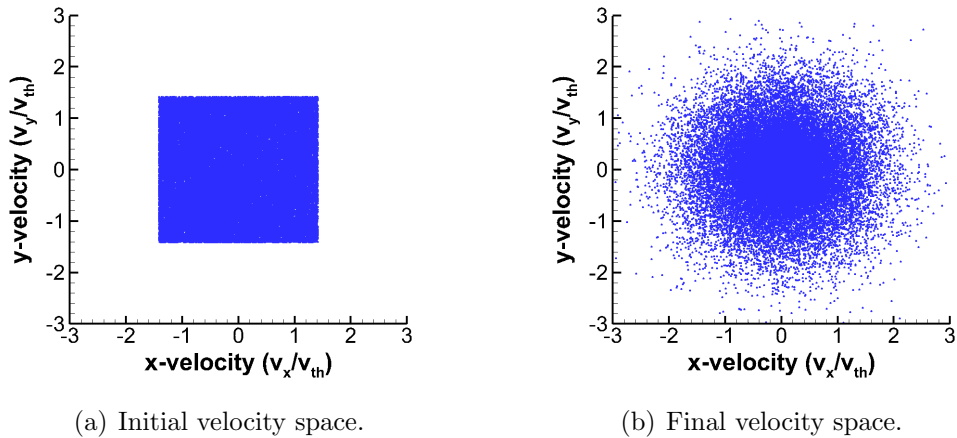
Figure 5.27: Velocity phase space variation for Coulomb intra-species collisions.

5.7.2 Inter-Species Collisions

Two test cases were tested to verify the implementation of the inter-species Coulomb collisions. The test cases were taken from Rambo et al [131] in which the relaxation processes in a plasma were modeled with both multi-fluid and kinetic simulations.

5.7.2.1 Temperature equilibration

The first test case involves the relaxation to equilibrium of two groups of particles with different temperatures. The parameters for the simulation are summarized in Table 5.5. The particles are fully stripped Carbon ions. The first group of particles is at a low density and high temperature, while the second is at a higher density and a lower temperature.

The temperature equilibration of the warm group of particles using the grid-based collision algorithm implemented in the code is compared to the multi-fluid simulation results of Rambo et al in Figure 5.28. The grid-based collision algorithm reproduces the multi-fluid results and excellent agreement is shown. Rambo also compares results with a Monte-Carlo collision algorithm which shows similar relaxation behavior. The RMS error normalized by the maximum temperature for this simulation is 0.38 %.

Table 5.5: Parameters for temperature equilibrium test.

Group 1	
Species	Carbon
Charge	9.6×10^{-19} C
Mass	2.0×10^{-26} kg
Density	10^{19} #/cm^3
Temperature	1 keV
Group 2	
Species	Carbon
Charge	9.6×10^{-19} C
Mass	2.0×10^{-26} kg
Density	10^{20} #/cm^3
Temperature	250 eV

5.7.2.2 Beam Slowing

The next test case simulates a beam slowing down due to Coulomb collisions with a background of stationary plasma. The particles are again fully stripped Carbon ions. The directed energy of the beam is much greater than the temperature of the beam and the temperature of the background. The beam is also at a lower density than the stationary background.

Table 5.6: Parameters for beam relaxation test.

Group 1	
Species	Carbon
Charge	9.6×10^{-19} C
Mass	2.0×10^{-26} kg
Density	10^{19} #/cm^3
Temperature	500 eV
Beam Velocity	6.55×10^5 m/s
Group 2	
Species	Carbon
Charge	9.6×10^{-19} C
Mass	2.0×10^{-26} kg
Density	10^{20} #/cm^3
Temperature	500 eV
Beam Velocity	0 m/s
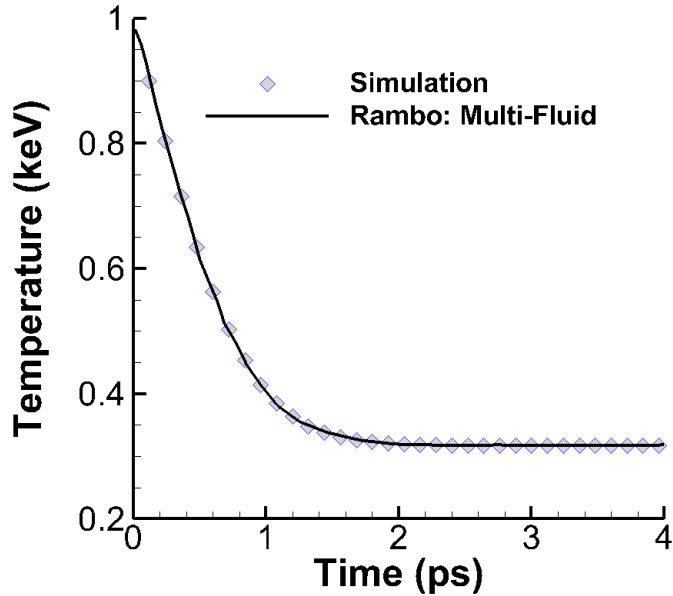
Figure 5.28: Temperature relaxation due to inter-species collisions.

The slowing down of the beam is shown in Figure 5.29(a) and is compared with the multi-fluid results of Rambo. Results are also shown for the simulation including the intra-species collisions, which does not change the beam relaxation much in the times shown. Again the simulations results agree well with the multi-fluid results, which Rambo showed agrees well with fully kinetic collisions.

The effects of beam slowing down on the beam temperature is shown in Figure 5.29(b). The temperature initially increases to around 6 eV and then relaxes to a temperature above 2 eV. The simulation considering only the inter-species collision agrees well with the multi-fluid simulation results. Inclusion of the intraspecies collisions changes the relaxation behavior slightly as expected due to the additional collisions distributing energy internal to each species and driving these distributions to a Maxwellian in all directions. The normalized RMS error for the velocity and temperature are 0.25 % and 1 % respectively, showing good agreement.
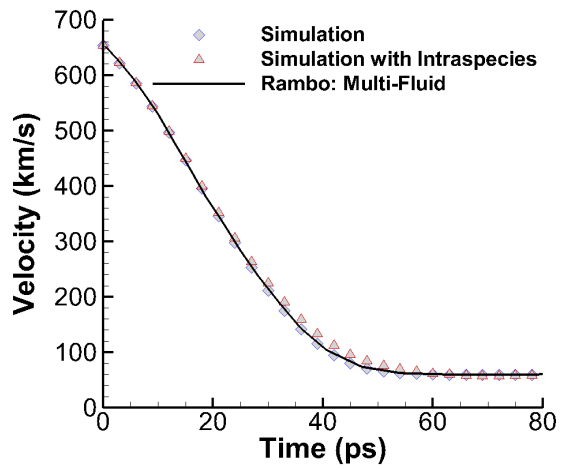
(a) Beam velocity.
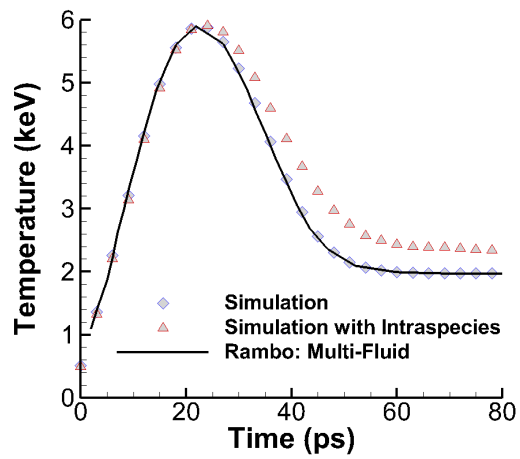
(b) Beam temperatures.

Figure 5.29: Relaxation of beam due to inter-species collisions.

5.7.3 Discussion

These simulation results agreed well with the multi-fluid results of Rambo. The work of Rambo illustrated that the multi-fluid relaxation results also show good agreement with fully kinetic Monte-Carlo collision models. However, there are limitations to the implemented model. This method relaxes faster than the kinetic simulations, particularly for the high energy particles in the tail of the Maxwellian. The interspecies collision also does not consider some multi-dimensional effects. Specifically, in the beam slowing case all of the beam energy goes into the random kinetic energy in the same direction of the beam. This leads to the correct overall temperature, but there is no mechanism to equilibrate the temperature between the directions using only the interspecies collisions. This is the reason intraspecies were also included, to capture some of this redistribution of energy among the different directions.

Overall this method was implemented due to compromise between the ease of implementation, speed, and accuracy. Fully kinetic, Monte-Carlo methods are more robust, but are more expensive computationally and are not compatible with the currently implemented parallel schemes.[131, 133] Other grid based methods are more robust, but again are more expensive computationally and not compatible with the currently implemented parallel schemes. [132]

5.8 Parallelization

A simple parallelization scheme was implemented in the code to allow for simulations to be run on multiple processors and decrease the simulation run time. This section outlines this simple parallelization scheme and shows some characteristics of the code's parallel efficiency. The code is parallelized using Message Passing Interface (MPI). This was chosen over other options such as OpenMP and GPU parallelization so the code is not limited to shared memory machines. MPI parallelized codes can

be run on an arbitrary number of processors each with its own memory.

5.8.1 Implementation

At the most fundamental level, parallelization is achieved by distributing the particles between the processors. Particles are arbitrarily divided between the processors. Processors are not assigned to a particular set of cells and particles are not passed between cells. This was done in hope of alleviating some of the communication overhead with sharing this data and checking the position of the particle data. Load balancing is insured by redistributing the particles between the processors at a designated time step.

Particle velocity pushes, position pushes, neutral collisions, and Coulomb collisions are performed independently on each processor with each particle. Individual particle pushes are independent of the other particles except through properties on the grid, enabling this type of parallelization. The independence of particles from one another is also reliant on the choice of a grid-based Coulomb collision algorithm instead of an algorithm which pairs collision partners in a cell. Continuum properties are weighted to the grid by each processor and then combined by summing or averaging the continuum properties from each processor to find the total continuum properties. The total continuum properties are shared between all the processors to be used when updating the properties on each processor.

The parallel efficiency (Speed up/Ideal Speed up) was tested using the radio-frequency source test problem. The macroparticle weight was changed to vary the numbers of particles which were used in the simulation since this method is based on dividing the particles between processors. The results of this study are shown in Figure 5.30. The efficiency increases as the number of particles is increased. Eventually each of the curves reaches a maximum speedup where the benefits of adding additional processors is outweighed by the communication costs between processors.

114
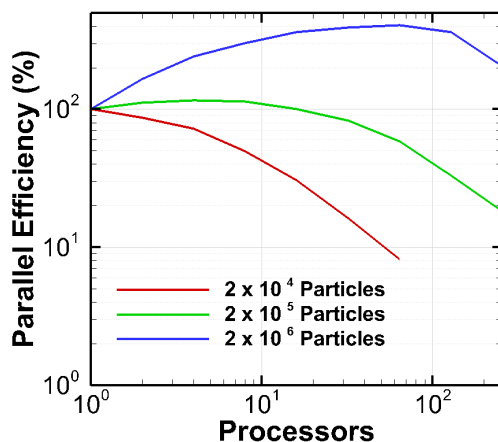
Figure 5.30: Parallel efficiency variation with increasing number of particles.

The codes shows greater than ideal scaling ($\propto N_{processors}$) as the number of processors is initially increased for the simulations with a large number of processors. This super-scaling is likely due to the fact that a greater fraction of the particle data (if not all of it) is able to fit in the cache of the processor.

Figure 5.31 shows the time per iteration as it varies with the number of particles per processor. All of the test cases have nearly the same time taken per iteration for the same number of particles per processor. This is an indicator of good scaling with increasing number of particles. Each of the test cases begins to diverge from the overall curve with larger numbers of particles diverging at higher particles per processor. This diverging occurs when the communication costs begin to become significant. Furthermore, communication costs are greater as the number of processors are increased and the number of particles per processor is increased. The fraction of communication cost increases with decreasing particles per processors.

Another important parameter to be considered in the parallel scaling is how the number of grid cells affects the speed up. Increasing the number of grid points increases the size of the arrays passed when MPI communication is used to sum the weighted continuum properties. For very large grids, it was found that MPI commu-
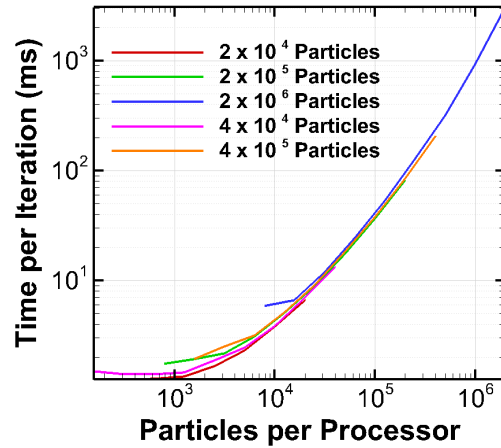
Figure 5.31: Time per iteration variation with number of particles per processor.

nication can account for almost 10% of the computational cost adversely affecting the speed up. For example, if the MPI communication cost is 10%, the maximum speed up for an ideal simulation is around ten times. A thorough study of the effects of the grid was not performed, but these effects were seen during simulations and profiling of the code.

CHAPTER VI

Quasi-One-Dimensional Model Implementation and Verification

The previous section outlined the development, testing, and verification of the one-dimensional PIC code which served as the framework to implement the new quasi-1D (Q1D) effects discussed in Chapter IV. In this chapter the numerical implementation, testing, and verification of the quasi-1D effects are presented.

6.1 Quasi-1D Algorithms

6.1.1 Area Variation

The area variation algorithm incorporates the effects of the magnetic field expansion and compression on the plasma. The cross sectional area throughout the domain is calculated by imposing an applied magnetic field on the domain and setting an inlet area for the flux tube ($A_{i=0}$) at the start of the domain ($i = 0$) where the magnetic field strength is $B_{i=0}$. The cross sectional area throughout the rest of the domain is calculated according to Equation 6.1.

$$A_i = \frac{B_{i=0}}{B_i} A_{i=0} \tag{6.1}$$

The cross-sectional area at each point was used along with the cell width to

calculate a cell volume ($\Delta V_i = A_i \Delta x_i$) to calculate the number density at each grid point. Conventional PIC methods typically assume a constant cross-section which is often set to $A_i = 1$.

An alternate approach to this method would be to change the macro-particle size (M) depending on the particle position on the grid. The macro-particles can be thought of as charge sheets with units $\#/m^2$. The local weight of the particle is then found according to the following Equation 6.2. This weight is used when the particle properties are weighted to the grid points.

$$M_i = \frac{B_{i=0}}{B_i} M_{i=0} \tag{6.2}$$

The area variation method was selected and used throughout this work. This was chosen due to the fact that the cross sectional area is more like a grid value than a particle value. The varying particle weight is also a viable solution, but was not tested.

6.1.2 Magnetic Field Force

The new magnetic field forces were implemented in a means similar to the Boris method [120] which was discussed in the previous chapter. An initial half push was performed with the electric field. This is followed by including the magnetic field force described in Equations 4.8 and 4.9. A last half-push is then applied by the electric field. The methods to incorporate the new magnetic field push are described below.

The magnetic field force has been included using two numerical methods. The first of these involves an implicit push of Equations 4.8 and 4.9. The equations for this implicit push are shown below:

$$v_{\parallel}^+ = v_{\parallel}^- - \frac{\Delta t}{8B} \frac{dB}{ds} \left(v_{\perp}^+ + v_{\perp}^- \right)^2 \tag{6.3}$$

$$v_\perp^+ = v_\perp^- + \frac{\Delta t}{8B}\frac{dB}{ds}\left(v_\perp^+ + v_\perp^-\right)\left(v_\parallel^+ + v_\parallel^-\right) \tag{6.4}$$

The v^+ values are found by using a predictor-corrector method until the solution converges. This method demonstrated good results, but a more simple and less expensive method was investigated.

Analytical expressions can be derived for the differential Equations 4.8 and 4.9. The first of these expressions is shown below (with no assumptions about the physics), which is a direct result of energy conservation and the fact that the magnetic field does no work:

$$(v_\parallel^n)^2 + (v_\perp^n)^2 = (v_\parallel^{n+1})^2 + (v_\perp^{n+1})^2 = C \tag{6.5}$$

in which C is a constant. This leads to a simple expression relating both velocities to one another. If it is further assumed that the quantity $\zeta = \frac{1}{2B}\frac{dB}{ds}$ is constant of the time step (Δt). The following expression is then found for the parallel velocity at time step $n + 1$.

$$v_\parallel^{n+1} = \sqrt{C}\tanh\left[\tanh^{-1}\left(\frac{v_\parallel^n}{\sqrt{C}}\right) - \zeta\sqrt{C}\Delta t\right] \tag{6.6}$$

This expression contains the variables ζ and C which were just defined and gives a result for the parallel velocity in time if ζ is constant. The corresponding perpendicular velocity can be found with Equation 6.5. These expressions are used to find the velocities during the magnetic field velocity push over which ζ is assumed to be constant. The quantity ζ changes once the particle position changes and is weighted from the nearby grid points. This is the reason for the use of Δt in Equation 6.6 and not t since this equation is only valid over a small time step in which $\zeta \approx$ constant. The analytical solution enforces energy conservation and is implicit through its analytical nature.

119

The predictor-corrector and analytical methods were compared with one another with both showing accurate results for the verification test cases which will be outlined below. However, the analytical methods showed superior computational performance and was selected and implemented in the simulation results shown.

6.1.3   Implementation in a 1D3V Code

An important note should be made about the implementation of this method, which relies on perpendicular and parallel velocities, into a fully 1D3V code which incorporates three velocities in Cartesian space. First, a 1D3V code is essential to the problem because it is necessary to resolve three velocity dimensions when self-consistently modeling a plasma source which includes both neutral and Coulomb collisions. The collision processes are inherently three velocity processes.

The quasi-1D effects are incorporated by assigning one of these velocities to be the parallel direction $(\hat{z})$ while the other velocities $(\hat{x}, \hat{y})$ are combined to be the perpendicular direction $(v_\perp = \sqrt{v_x^2 + v_y^2})$. The three dimensional nature of the problem is preserved for use in the collision algorithms while also incorporating the quasi-1D effects associated with modeling a magnetic flux tube of particles. Changes in the perpendicular velocity are scaled equally to both the perpendicular directions.

6.2   Two Particle Motion

The two-particle verification test case solves for the motion of two like-charged particles. This test verifies the two-dimensional effects due to the cross-section variation and the magnetic field force on the particle mover.

6.2.1   Theory

Two like-charged particles will repel one another until both exit the domain.[118] The one-dimensional domain treats the plasma as a sheet of particles symmetric in

the perpendicular, $\hat{x}$ and $\hat{y}$, directions. An expression can be derived for the electric field outside of the charge sheets by using Gauss' law and assuming contributions perpendicular to the flux tube are negligible ($E_z \gg E_\perp$).

$$E_z = \frac{Q}{2A\epsilon_0}\hat{n} \tag{6.7}$$

In this equation A is the cross sectional area of the charge sheet, Q is the charge, and $\hat{n}$ is the direction normal to the charge sheet. For the two particle system this leads to an electric field that cancels out in the region between the particles and sums in the rest of the domain. Each particle sheet feels the electric field of the other, leading to each of the particles feeling the forces shown in Equation 6.8.

$$F_z^\pm = \pm\frac{Q^2}{2A\epsilon_0} \tag{6.8}$$

In this equation and those following, the plus sign in the exponent refers to quantities for the particle on the right side of the domain while the minus sign refers to the quantities for the particle on the left side of the domain. When the cross-sectional area is constant the particles exert a constant force on one another, giving a simple expression for the motion of the particles.

$$z^\pm = \pm\frac{Q^2}{2mA\epsilon_0}t^2 + v_0^\pm t + z_0^\pm \tag{6.9}$$

in which $v_0^\pm$ is the initial velocity and $z_0^\pm$ is the initial position.

Variation of the cross-sectional area results in a force that is no longer constant as is illustrated by Figure 6.1. As the particle sheets approach one another the magnetic field magnitude increases and the flux-tube shrinks. The number of particles each sheet represents is constant, implying that the density is now greater due to the decrease in cross-section. This leads to a larger force between the particles. The cross-section varies with the magnetic field as shown in Equation 6.1. This leads to

121
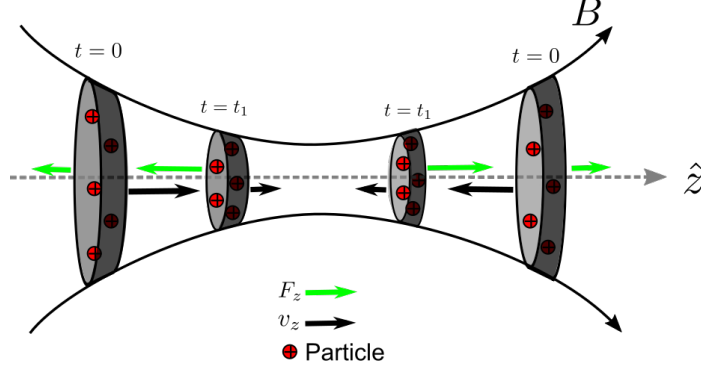
Figure 6.1: Illustration of cross-sectional area variation effects for a moving sheet of charticles.

the electric field outside each charge sheet varying as below:

$$E_z = \frac{QB}{2B_0 A_0 \epsilon_0} \hat{n} \tag{6.10}$$

Resulting in the force varying as:

$$F_z^{\pm} = \frac{Q^2 B^{\mp}}{2B_0 A_0 \epsilon_0} \tag{6.11}$$

Note that in this equation the plus/minus is flipped on the right hand side because the force each particle experiences is due to the other charge sheet.

This problem has a simple analytical solution when choosing a magnetic field which varies as $B = B^* + \alpha_{\pm} z$ and using particles which are initially equidistant from $z = 0$ traveling toward each other with the same velocity. The magnetic field is a piecewise function for which α_- is the slope for $z < 0$ and α_+ is the slope for $z > 0$. The general solution is shown below:

$$z^{\pm} = \left(\frac{v_0^{\pm}}{\gamma}\right) \sin(\gamma t) \pm \left(\frac{B_0}{\alpha}\right) \cos(\gamma t) + z_0^{\pm} - \frac{B_0}{\alpha} \tag{6.12}$$

In this equation $\gamma = \sqrt{\beta\alpha}$ with $\beta = Q^2/(2m\epsilon_0 B_0 A_0)$.

An analytical solution can also be found for the case with the magnetic field force incorporated since the magnetic field imposed is linear and the magnetic moment is approximately constant. The total axial force in this case is shown below.

$$F_z^{\pm} = \left(\frac{Q^2 B^{\mp}}{2 B_0 A_0 \epsilon_0}\right) - \mu \nabla B^{\pm} = \left(\frac{Q^2 B^{\pm}}{2 B_0 A_0 \epsilon_0}\right) - \frac{m v_{\perp_0}^2}{2 B_0} \nabla B^{\pm} \tag{6.13}$$

The perpendicular velocity is a free parameter in this equation and is set according to the Equation 6.14.

$$v_{\perp} = \sqrt{\frac{Q^2 B^*}{\epsilon_0 A_0 m \alpha}} \tag{6.14}$$

Using the above perpendicular velocity and a piece-wise linear magnetic field leads to a cancellation of the constant part of the force in Equation 6.13 and a simple analytical solution shown below.

$$z^{\pm} = \left(\frac{v_0^{\pm}}{\gamma}\right) \sin(\gamma t) \pm \left(\frac{B_0 + B^*}{\alpha}\right) \cos(\gamma t) + z_0^{\pm} - \frac{B_0 + B^*}{\alpha} \tag{6.15}$$

These analytical solutions can be significantly simplified by using particles with $Q = m = 1$ while setting $\epsilon_0 = 1$ and $A_0 = 1$. Further selecting initial conditions where the two particles start at $z_0^{\pm} = \pm 1$ with velocities in opposite directions $v_0^{\pm} = \mp\sqrt{3}/2$ leads to the following solutions for the constant area case:

$$z^{\pm} = \pm\frac{1}{4}t^2 \mp \frac{\sqrt{3}}{2}t \pm 1 \tag{6.16}$$

$$v^{\pm} = \pm\frac{1}{2}t \mp \frac{\sqrt{3}}{2} \tag{6.17}$$

The varying area solution:

$$z^{\pm} = \mp\sqrt{\frac{3B_0}{2\alpha}}\sin\left(\sqrt{\frac{\alpha}{2B_0}}t\right) \mp \frac{B_0}{\alpha}\cos\left(\sqrt{\frac{\alpha}{2B_0}}t\right) \pm \left(1 + \frac{B_0}{\alpha}\right) \tag{6.18}$$

$$z^{\pm} = \mp\sqrt{\frac{3}{2}}\cos\left(\sqrt{\frac{\alpha}{2B_0}}t\right) \pm \sqrt{\frac{B_0}{2\alpha}}\sin\left(\sqrt{\frac{\alpha}{2B_0}}t\right) \tag{6.19}$$

The varying area solution with the magnetic field force:

$$z^{\pm} = \mp\sqrt{\frac{3B_0}{2\alpha}}\sin\left(\sqrt{\frac{\alpha}{2B_0}}t\right) \mp \frac{B_0}{\alpha}\cos\left(\sqrt{\frac{\alpha}{2B_0}}t\right) \pm \left(1 + \frac{B_0}{\alpha}\right) \tag{6.20}$$

$$v^{\pm} = \mp\sqrt{\frac{3}{2}}\cos\left(\sqrt{\frac{\alpha}{2B_0}}t\right) \pm \sqrt{\frac{B_0}{2\alpha}}\sin\left(\sqrt{\frac{\alpha}{2B_0}}t\right) \tag{6.21}$$

In these equations the + solution is for the particle traveling through $z > 0$ while the - solution is for the particle traveling through $z < 0$.

6.2.2 Results

The analytical solution and the simulation results for the position and velocity of the particles is shown in Figure 6.2. The constant area (C), area variation (AV), and area variation with magnetic field force (AVB) test cases are all shown. The constant area shows a linear change in the velocity as expected due to the constant force while the varying area shows a non-linear change in the velocity. The magnetic field force included adds an additional strong repelling force which rapidly repels the particle. The non-linear effects of the area variation are not shown as much due to the strong magnetic field force.

The root-mean-square (RMS) error between the computed and analytical solution are summarized in Table 6.1. The error in each of these cases is small (less
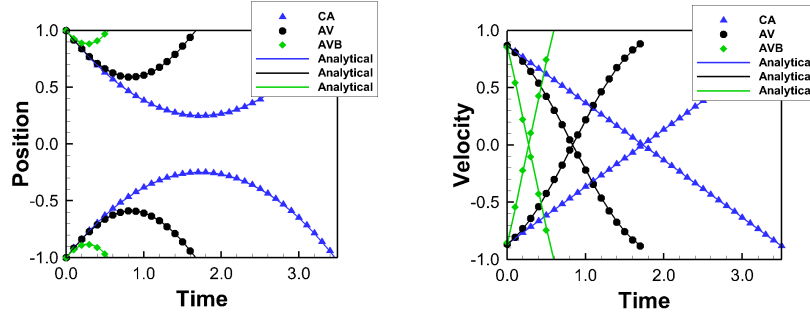
(a) Particle position in time.

(b) Particle velocity in time.
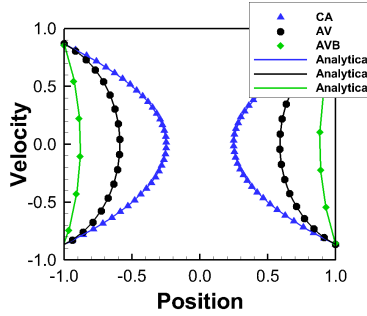
(c) Particle velocity and position.

Figure 6.2: Two-particle motion simulation results compared to analytic solutions. Constant area (CA), Area Varying (AV), and Area Varying with magnetic field force (AVB) results are shown.

than a percent) verifying that the method agrees well with the analytically predicted behavior.

The results of these simulations show that the two-dimensional effects are correctly incorporated in the code, reproducing simple analytical solutions for two-particle motion. The particle mover, interpolation, Poisson solver, and the algorithms incorporated to capture two dimensional effects are all verified.

Table 6.1: RMS error for quasi-one-dimensional verification simulations.

Simulation	Position	Velocity	Position Normalized	Velocity Normalized
Constant Area	2.6×10^{-3}	1.3×10^{-3}	0.23%	0.14%
Varying Area	1.0×10^{-3}	1.8×10^{-3}	0.091%	0.20%
Varying Area and Magnetic Force	3.9×10^{-3}	1.2×10^{-2}	0.12%	1.1%

6.3 Magnetic Mirror

Additional simulations were performed to further verify the magnetic field force incorporation. The theory and simulations in this section do not solve Poisson's equation and the only two-dimensional effect considered is that of magnetic field force.

6.3.1 Theory

Magnetic mirrors are devices where particles are generated in a magnetic field well with increasing magnetic field strength in all directions. As magnetized particles move from the weak to the strong magnetic field region they are acted on by a force which repels them back into the weak field region. This repelling force can result in the particles being reflected back into the well under certain conditions. The theory applied in this section considers two identical magnetic mirrors adjacent to one another with a weak magnetic field region between them. This creates a magnetic bottle (or magnetic mirror machine) which can trap particles in the weak field region between the two mirrors.

An analytic solution exists describing the velocity space of particles which are trapped for a given minimum and maximum magnetic field:

$$\frac{v_{\perp,0}^2}{v_{\parallel,0}^2 + v_{\perp,0}^2} > \frac{1}{R} \tag{6.22}$$

In this equation $R = \frac{B_{max}}{B_{min}}$ is the mirror ratio of the magnetic confinement device. Particles satisfying the above condition are trapped by the magnetic field, while those that do not are in the loss cone. The loss cone is a cone shape in velocity space which contains particles that are not trapped by the magnetic mirror device. This cone is defined by an angle $\theta_{loss} = \sin^{-1}(\sqrt{1/R})$ which is relative to the field parallel direction.

Equation 6.22 can be rewritten in the following form:

$$v_{\perp,0} = v_{\parallel,0}\sqrt{R-1} \tag{6.23}$$

The number or fraction of particles trapped in the mirror can be found by integrating the velocity distribution of the particles present in the mirror using the conditions which define the loss cone. A detailed discussion of this is found in Appendix B. For an isotropic distribution without an applied electric field the equation for the trapped fraction, Γ, is shown below.

$$\Gamma = \sqrt{1 - \frac{1}{R}} \tag{6.24}$$

A solution can also be derived if a constant electric field is imposed on the particles. The resulting relation for the trapped particles is shown below:

$$v_\perp > \sqrt{\frac{v_\parallel^2 - \frac{2q}{m}\Delta\phi}{R-1}} \tag{6.25}$$

in which $\Delta\phi$ is the potential drop the particles experience. Imposing an electric field leads to a non-trivial solution for the fraction of trapped particles due to the non-linear nature of Equation 6.25. The solution strongly depends on the velocity distribution chosen, even if it is isotropic. The fraction of trapped particles can still be found by integrating this distribution over the trapped particle velocity space, but either a simple velocity distribution must be chosen or it must be done numerically to obtain an analytical solution.

The trapped particles in the magnetic mirror will oscillate back and forth in the device due to the magnetic field forces. An analytic expression can be derived for the oscillation frequency of these trapped particles using Equations 4.8 and 4.9, assuming a constant magnetic moment, and knowing the magnetic field profile. The form of this frequency is affected by the magnetic field profile which was chosen to be

$B_z = A_1 z^2 + C_1$. The resulting frequency when no electric field is imposed is shown below:

$$\omega_{trap} = \sqrt{\frac{2\mu}{m} A_1} = \sqrt{\frac{v_{\perp,0}^2 A_1}{B_0}} \tag{6.26}$$

An analytical solution can also be found for the case when a potential of the form $\phi = A_2 z^2 + C_2$ is imposed. The frequency for this case is shown below. If the potential applied is confining, the oscillation frequency is increased due to the addition of another restoring force.

$$\omega_{trap} = \sqrt{\frac{2}{m}(\mu A_1 + q A_2)} = \sqrt{\frac{v_{\perp,0}^2 A_1}{B_0} + \frac{2q}{m} A_2} \tag{6.27}$$

The solution for the motion of each particle in both these cases differs only by the initial perpendicular velocity of these particles if all particles are created at the same location at the minimum of the magnetic field strength (as is done for the simulations in the next section). The trapped frequency of the particles implies that particles with the same magnetic moment (μ) oscillate with the same frequency. This solution can be used to predict when a group of particles with the same magnetic moment (initial perpendicular velocity) will cross the center of the domain where the particles were seeded.

6.3.2 Results

The magnetic field force effects were verified with the simulation of particles in a magnetic mirror. Poisson's equation was not solved in these simulation to focus on the effects of the magnetic field force only. Therefore, these simulations study the uncoupled single particle motion of a distribution of particles. Particles were seeded at the center of the magnetic mirror where the magnetic field is a minimum. The domain extends from $z = ([-0.5, 0.5]$ and particles that reach the edge of the domain

Table 6.2: Magnetic mirror simulation parameters.

Simulation	Particles	Charge	Mass	Temperature	A_1	C_1	A_2	C_2
Case 1	10^4	-1	1	10^{-4}	4	1	0	0
Case 2 (Confining)	10^4	-1	1	10^{-4}	4	1	4×10^{-4}	0
Case 3 (Non-confining)	10^4	-1	1	10^{-4}	4	1	-4×10^{-4}	0

Table 6.3: Number of trapped particles for magnetic mirror simulations.

	Simulation	Analytical	Error
Case 1	7121	7071	0.7%
Case 2	2613	2601	0.5%
Case 3	9291	9302	0.1%

are removed. A grid with 100 cells is used along with a time step of 0.5 seconds. The simulation parameters used are summarized in Table 6.2. The magnetic field is applied according to the equation $B = A_1 z^2 + C_1$ and the potential according to $\phi = A_2 z^2 + C_2$.

For the parameters chosen the magnetic mirror ratio ($R = B_{max}/B_{min}$) is 2.0. Particles are initially seeded according to a Maxwellian velocity distribution using the temperatures shown in Table 6.2 and with a Boltzmann constant (k_b) of 1.

Figure 6.3 shows the initial and final velocity space of a magnetic mirror as well as the analytic loss cone for the cases tested. The results from this simulation show clearly that the magnetic dipole force effects are captured and produces accurate results.

For these simulation 10^4 particles were used. The analytical and simulation number of trapped particles is shown in Table 6.3. While these errors might seem unusually low for a PIC simulation, this is the error only from the particle pusher since there is no solving Poisson's equation and no weighting the charge to the grid. These errors are not statistically averaged over a number of simulations and only represent a single simulation. Contributions for error may come from the particle mover or the seeding algorithms.

(a) Case 1: Initial distribution   (b) Case 1: Final distribution

(c) Case 2: Initial distribution   (d) Case 2: Final distribution

(e) Case 3: Initial distribution   (f) Case 3: Final distribution
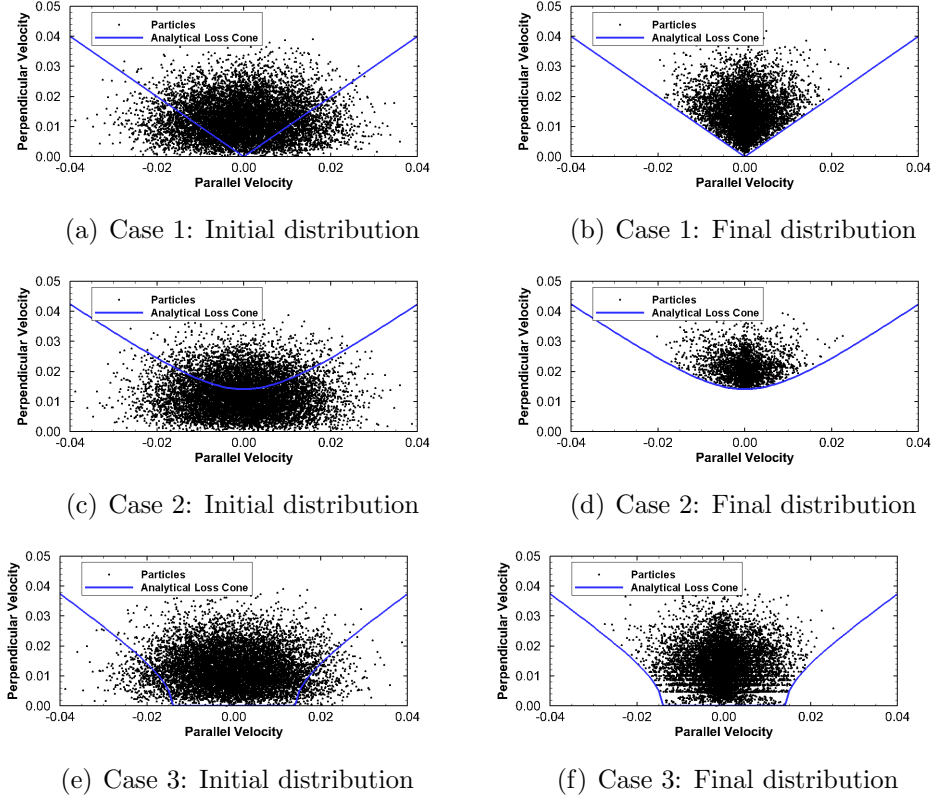
Figure 6.3: Velocity phase space distributions for magnetic mirror simulations illustrating the capture of the analytical loss cone behavior.

A more dynamic test of the method is to compare with the analytical oscillations derived in the previous section. The best diagnostic for examining these oscillations is the particle $v_\perp - z$ space. Particles with the same initial magnetic moment will cross the $z = 0$ line in $v_\perp - z$ space at the same time resulting in a high density at that perpendicular velocity and collapse to a single point in $v_\perp - z$ space. Figures 6.4 shows the $v_\perp - z$ space for the particles at a given time along with the analytically predicted time when a group of particles with the same magnetic moment will return to the center of the domain for the first time. The results agree well with the theory. The oscillation frequency is seen to decrease for the non-confining case (Case 2) and increase for the confining case (Case 3).

130
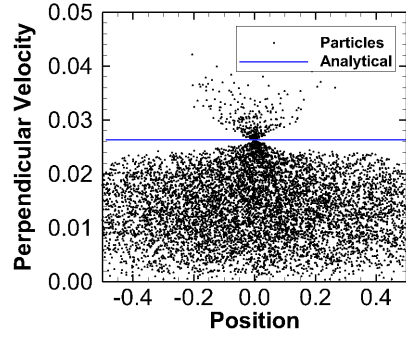
(a) Case 1, t=60
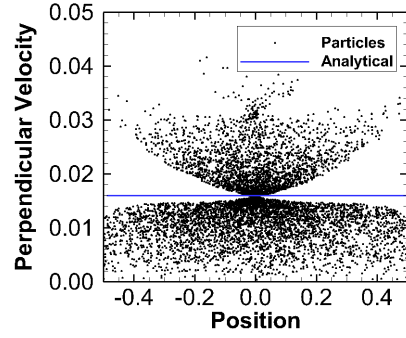
(b) Case 1, t=100
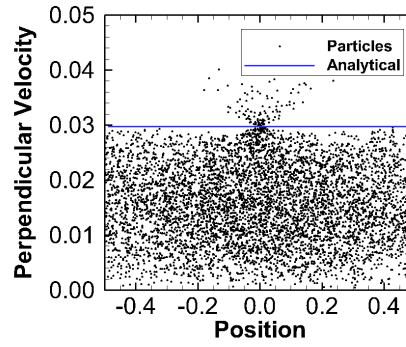
(c) Case 2, t=60
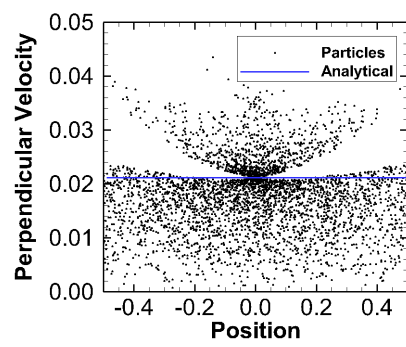
(d) Case 2, t=100
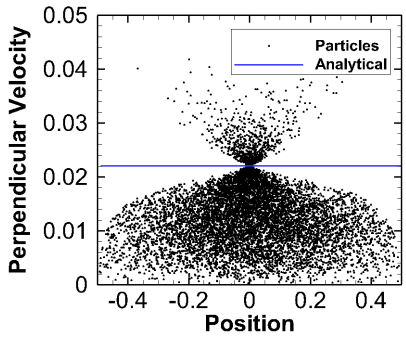
(e) Case 3, t=60
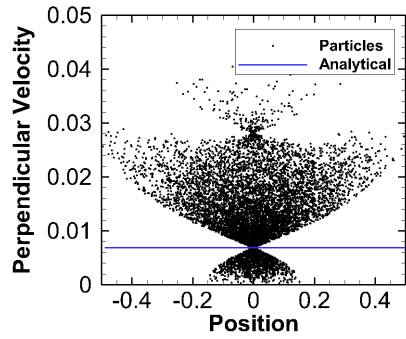
(f) Case 3: t=100

Figure 6.4: Magnetic mirror oscillations illustrating the prediction of particles crossing the center of the domain.

6.4 Maxwellian Source in Diverging Magnetic Field

The Q1D method was also verified by comparing with two-dimensional full PIC simulations which include solving Poisson's equation and the particle motion. Two-dimensional simulations were performed using XOOPIC (X11-based Object Oriented PIC). [113] XOOPIC is a fully two-dimensional (Cartesian and cylindrical) PIC code with electrostatic and electromagnetic field solvers. The code was initially developed at the University of California Plasma Theory and Simulation Group. XOOPIC has applications for solving a wide variety of plasma problems and includes features such as Monte-Carlo collisions, device boundary conditions, implicit particle movers to name a few. For the simulations presented herein only the electrostatic, cylindrically symmetric solver was used.

The first of the fully two-dimensional test cases was adapted from the source-collector sheath problem of Schwager [123] studied in the previous chapter. This problem was made two-dimensional by including a guiding, diverging magnetic field which directs the flow of a Maxwellian source of particles into a collector boundary. A schematic of the two-dimensional grid used is showed in Figure 6.5. Particles are injected at the Maxwellian source boundary and then flow through the domain toward the collecting, dielectric boundary. A conducting boundary is necessary at the left boundary adjacent to the inlet in order for potential solutions to be found. The XOOPIC grid was comprised of 200 cells in the axial direction and 75 cells in the radial direction. The length of the domain is 0.2 meters and the height 0.075 meters. The Maxwellian source region extends for 15 cells radially at the left boundary from r=[0,0.015] m. The Q1D grid is 200 cells and the initial inlet area is set equal to the equivalent inlet area of the XOOPIC grid. The timestep used in both simulations is $\Delta t = 10^{-10}$ seconds.

The magnetic field topology used for these simulations is shown in Figure 6.6 and 6.7 for the 2D and Q1D simulations respectively. The magnetic field is created by a
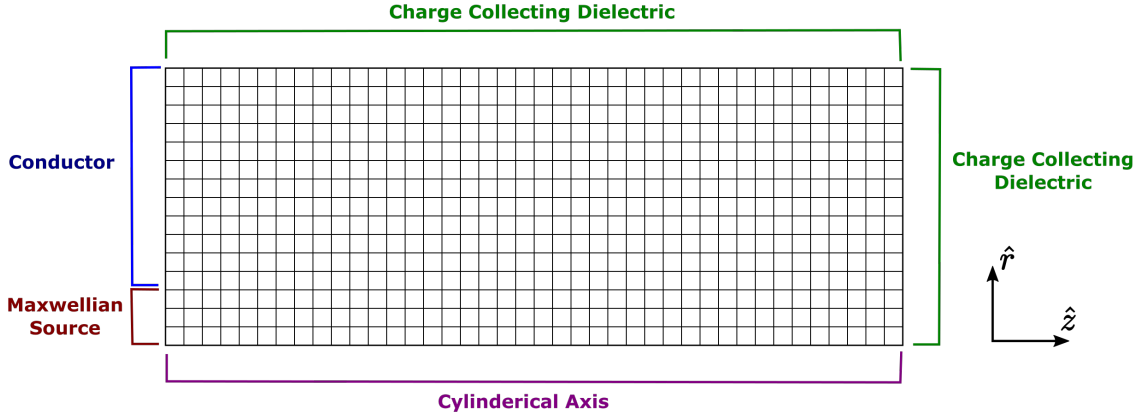
Figure 6.5: Grid for XOOPIC simulations of Maxwellian source in a diverging magnetic field.
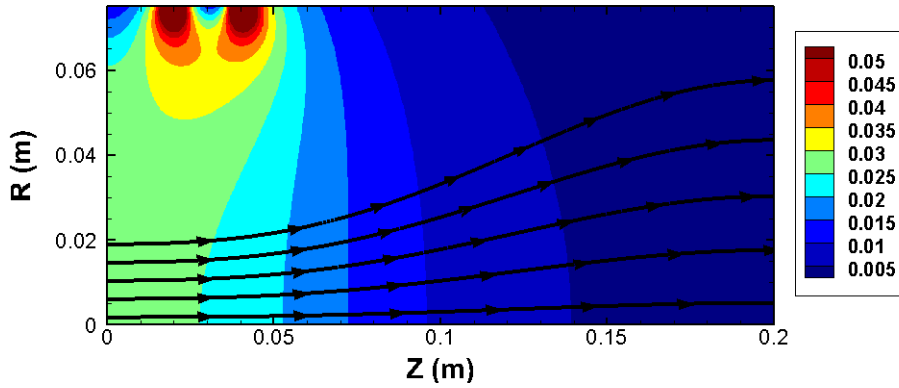
Figure 6.6: Magnetic field strength contours and streamlines for XOOPIC simulations of Maxwellian source in a diverging magnetic field.

series of 8 current loops each with a current of 1000 A and a radius of 0.075 m. The current loops were positioned at the following axial locations: -0.04 m, -0.02 m, 0.02 m, 0.04 m, 0.36 m, 0.38 m, 0.42 m, and 0.44 m.

The properties of the Maxwellian source $(n_{ion}, n_e, T_i, T_e, etc)$ were varied to test and compare a variety of conditions and determine the regimes in which the Q1D model is valid. The magnitude of magnetic field strength was also varied and the entire domain shrunk. A table of all the tested conditions is give in Appendix C. There will be two cases in particular which are highlighted. The source parameters

133
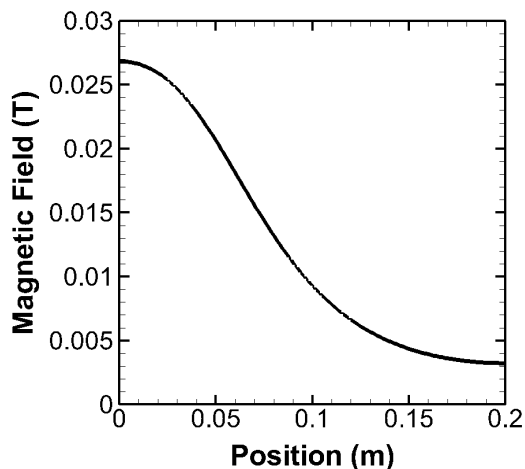
Figure 6.7: Magnetic field for Q1D simulations of Maxwellian source in a diverging magnetic field.

for these cases are: $n_i = n_e = 10^{15}$ $\#/m^3$ and $T_e = 5$ eV. The ions have the same mass as hydrogen and the only difference between these cases is the ion temperature which is $T_i = 300$ K and $T_i = 5$ eV. They will be referred to as the cold ion (CI) and hot ion (HI) cases from here on.

This section is divided into multiple sub-sections discussing different facets of this problem. First, the effects of the Q1D model compared to a 1D model will be presented. Then the XOOPIC results will be presented. The Q1D and XOOPIC results will then be compared. Finally a discussion of the difference between the models will be presented.

6.4.1 Quasi-one-dimensional effects

The effects of the Q1D model was first compared with purely one-dimensional simulations. Simulation were performed with the one dimensional code (1D), a code with only area variation effects and no magnetic field force (NBF), a code with no magnetic field force on the ions (IDM), and then full Q1D simulations (Full). The case with no magnetic field force on the ions would be equivalent to a simulation where the ions are demagnetized do not feel the magnetic field force, but are still bound to

(a) Electron density

(b) Ion density

(c) Ion mean velocity
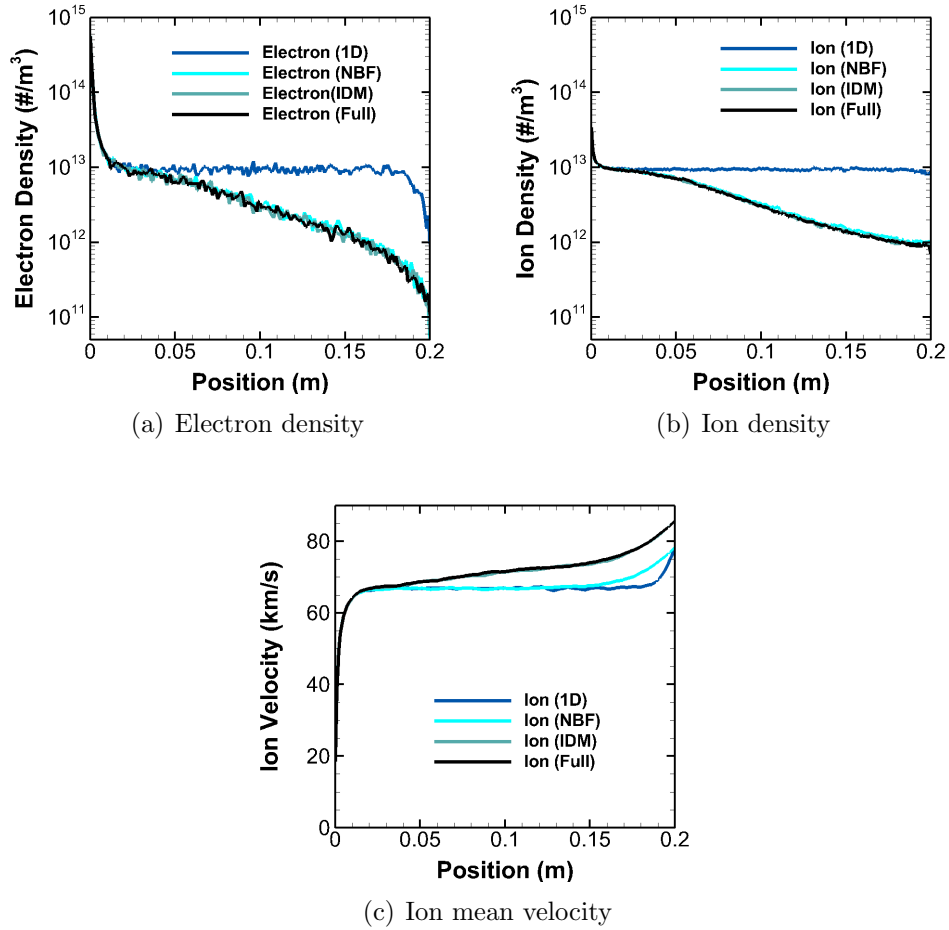
Figure 6.8: Results for the cold ion case illustrating the effects of the Q1D solver.

the magnetic field lines through the electrons. The results of these simulations are shown in Figure 6.8 for the CI case and in Figure 6.9 for the HI case.

Figure 6.8 shows the electron density, ion density, and mean ion velocity. The electron and ion density profiles show very different results between the 1D and Q1D simulations. After the source sheath the 1D simulations maintains a constant density until the collector sheath. The Q1D simulations all show a decreasing density as the plasma expands, as expected. This density decrease is captured by the inclusion of the area variation which is in NBF, IDM, and the Full simulation.

The ion velocity results shows distinct differences between the 1D and Q1D simulations as well. The 1D case shows acceleration occurring due to the sheaths, but no

acceleration between them. Inclusion of area effects in NBF does not show additional acceleration. The difference in ion velocity compared to the 1D case occurs due to the slightly longer sheath which forms due to the lower density (increase in λ_D). Inclusion of the magnetic field forces on the electrons in the IDM and Full simulations show additional ion acceleration after the source sheath. This acceleration occurs even in the IDM case where the magnetic field force directly on the ions is ignored.

The magnetic field forces on the ions is unimportant in this case because the ions are cold. The energy in the ions which can be directed along the axis is small compared to the electron energy. The highly energetic electrons are rapidly accelerated by the diverging magnetic field. The resulting charge imbalance sets up an electric field which draws the ions out with the electrons. This ambipolar force is much greater than the magnetic field force on the cold ions.

Figure 6.9 contains the results for the HI test case. Similar trends are seen for the electron and ion densities where the inclusion of the area variation captures most of the effects with the density decrease. However, a difference is also seen between the NBF, IDM, and Full simulations. This difference was also present in the CI test cases but was not as prevalent. The reason for this difference is best described from the standpoint of the mean ion velocity. It is clear that each one of the simulations has a different results for the velocity. The NBF source just shows a slightly extended sheath. The IDM case captures additional acceleration, but does include the effects of the ion forces. Finally the Full simulation captures the full acceleration of the ions due to the magnetic field forces. The reason for the density differences stems from these velocity differences and the need for mass flux to be conserved. As the velocities are increased, the density must decrease, which now shows up in the densities for the different methods. This did not show up in the CI case because the velocities for the NBF and the IDM cases were the same. Inclusion of the ion magnetic field force in this case is important because now the amount of energy in the ions themselves
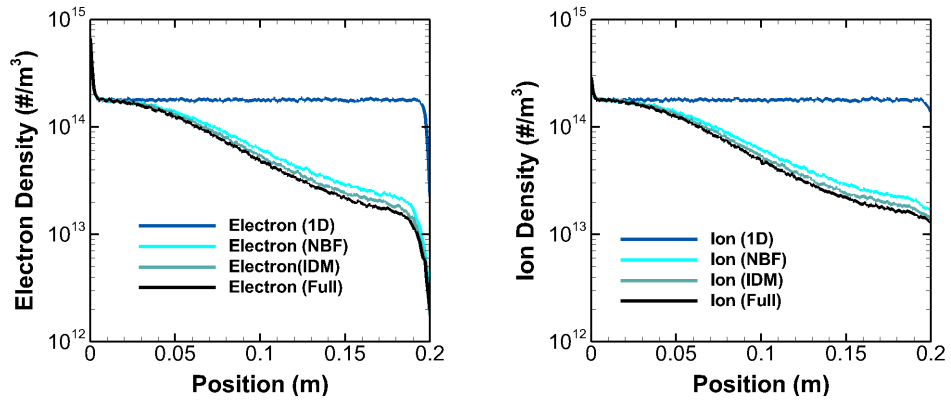
(a) Electron density

(b) Ion density
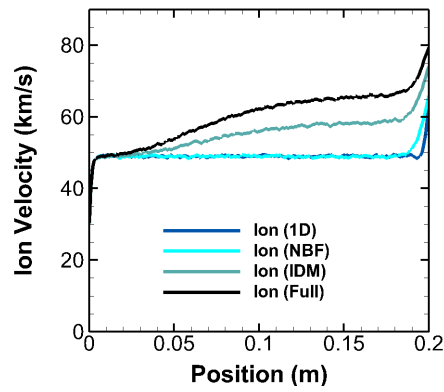
(c) Ion mean velocity

Figure 6.9: Results for hot ion case illustrating the effects of the Q1D solver.

which can be directed along the axis is the same as the electron energy. In this case the ambipolar force between the electrons and the magnetic field force on the ions are both essential for capturing the ion acceleration.

6.4.2 Comparison between Q1D and XOOPIC Results

The results from the XOOPIC simulations of the CI and HI cases are shown in Figure 6.10. The electron density, ion density, and potential are shown on contour plots of the domain. These results show how the parameters vary radially over the plasma cross section. The CI case shows that both the electrons and ions are well confined by the magnetic field lines. The HI case still shows a bulk of the ions trapped by the magnetic field, but also shows a more divergent density profile. The divergent profile occurs due to the higher energy of the ions making them more difficult to confine by the magnetic field. The potential also show an interesting structure. Sharp decreases in the potential are seen at the inlet boundary, but a continued potential drop is seen as the plasma expands.

The results from the Q1D and XOOPIC simulations for the CI case are compared in Figure 6.11 In these Figures an additional XOOPIC simulation was performed with a stronger magnetic field (XOOPIC (S)) to check that the Q1D results approach the XOOPIC results in the strong magnetic field limit. Note that additional Q1D simulations did not have to be performed because these simulations are independent of the magnetic field strength, they depend only on the magnetic field topology. XOOPIC simulation results are averaged radially over the plasma cross-section (defined by the location of the electrons) so that they can be compared with the Q1D simulations

The results from Figure 6.11 show that in general the Q1D and the XOOPIC results agree well with one another qualitatively. The ion density and velocity plots also show that increasing the magnetic field strength in the XOOPIC simulations causes the Q1D results to agree more closely with the XOOPIC simulations. Both
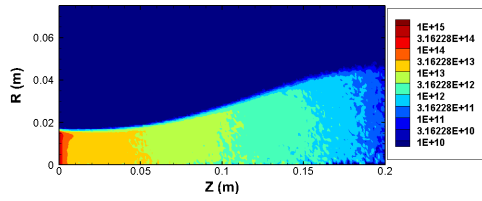
(a) CI: Electron density contours ($\#/m^3$)
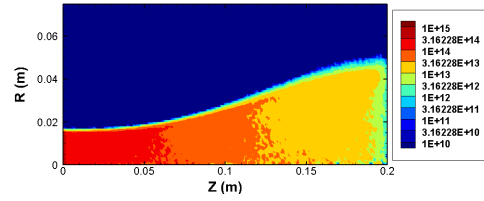
(b) HI: Electron density contours ($\#/m^3$)
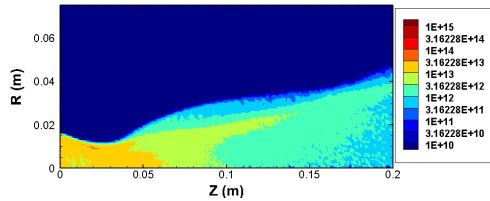
(c) CI: Ion density contours ($\#/m^3$)
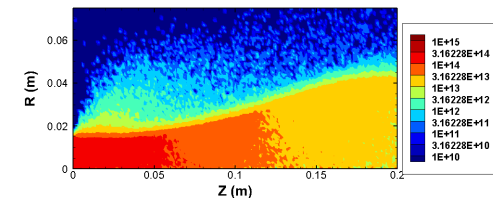
(d) HI: Ion density contours ($\#/m^3$)
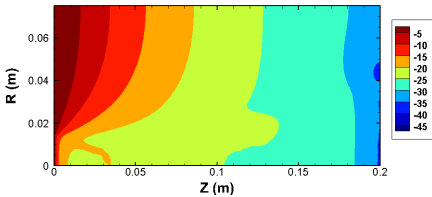
(e) CI: Potential contours (V)
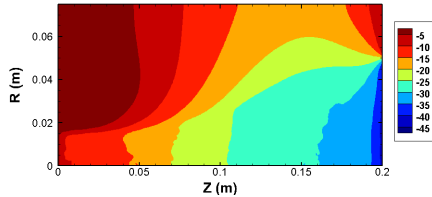
(f) HI: Potential contours (V)

Figure 6.10: XOOPIC simulation results for Maxwellian source in a diverging magnetic field.
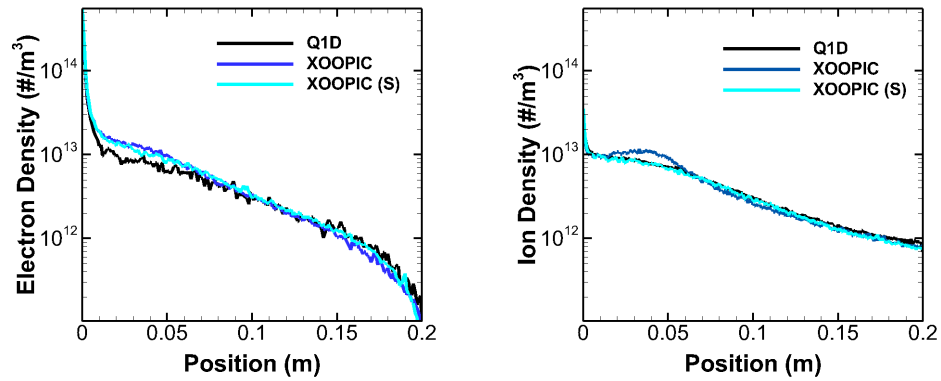
(a) Electron density
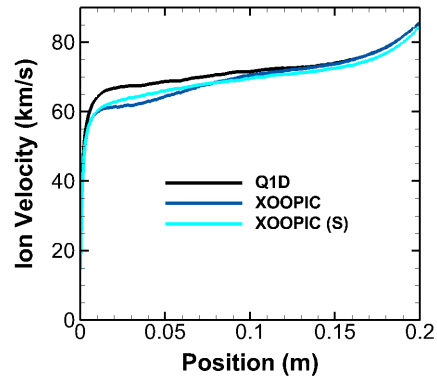
(b) Ion density

(c) Ion mean velocity

Figure 6.11: Comparison of CI results for Maxwellian source in a diverging magnetic field.

codes shows a rapid decrease in density due to the sheath, followed by further decrease due to the magnetic field guided expansion. The ion velocity results agree well also, showing an initial acceleration due to the source sheath, followed by an continued ambipolar acceleration. The major differences in the ion velocity are caused by the two codes treating the source sheath differently. After the source sheath region the two code results begin to approach another more closely. This difference is most likely due to the 2D structures in the sheath region which are evident in the XOOPIC contour plots. The stronger magnetic field simulations with XOOPIC also shows closer agreement with the Q1D simulations, as expected.

The results from the Q1D and XOOPIC simulations for the HI case are compared in Figure 6.12. Here no strong magnetic test case was simulated. The Q1D ion and electron density profiles again show good agreement with the XOOPIC results in Figure 6.12. The Q1D code captures the initial density decrease due to the sheath as well as the continued expansion along the magnetic field. The ion velocity also shows good agreement capturing the sheath acceleration as well as the continued acceleration of the ions due to the combined ambipolar effects and the magnetic field forces.

This sub-section showed that there is good qualitative agreement between the Q1D and XOOPIC results. The ion and electron densities demonstrate very similar behavior between the two simulations. The ions velocity results show the ability of the Q1D code to capture the 2D effects associated with the magnetic field forces as well as the ambipolar acceleration without having to perform a fully-2D simulation which is more computationally expensive.

The capturing of 2D effects by the Q1D model is an important result because while XOOPIC was able to simulate the problems presented in this section, scaling up to the higher densities and the larger domains required to simulate magnetic nozzle devices becomes extremely cost prohibitive. The Q1D method alleviates these costs by
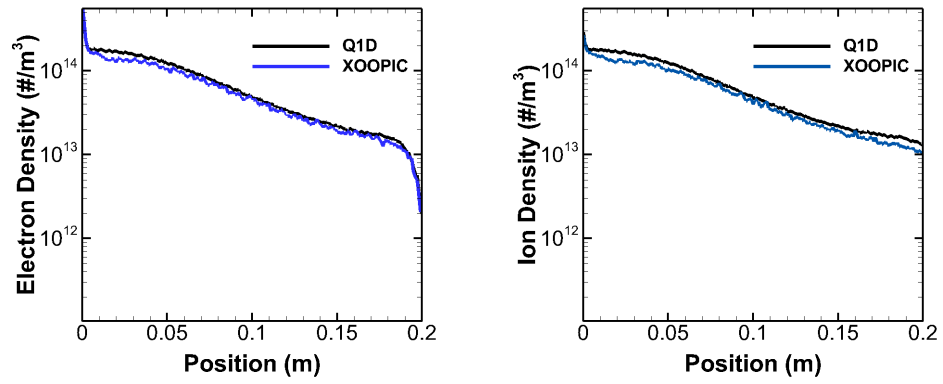
(a) Electron density

(b) Ion density
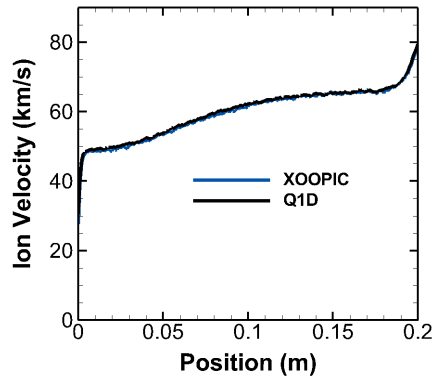
(c) Ion mean velocity

Figure 6.12: Comparison of HI results for Maxwellian source in a diverging magnetic field.

significantly reducing the number of cells (no resolving the radial dimension) thereby also reducing the total number of particles needed. The number of particles is reduced because each cell requires a minimum number of particles to avoid random noise and produce statistically significant results. For the simulations in this section the total number of particles required in the Q1D simulations is reduced by a factor of 75 to reproduce the XOOPIC simulations with similar statistical noise. The Q1D method is enabling for modeling higher density plasmas by simplifying the problem and reducing computational costs. Quantitative comparisons and a rigorous discussion of errors is presented in Section 7.6.1.

6.5   Particle Source in Converging-Diverging Magnetic Field

An additional two dimensional test case was performed in XOOPIC to compare with the Q1D method. This simulation was performed by seeding particles according to a Maxwellian source in the center of a domain with a converging-diverging magnetic field. The grid used for the XOOPIC simulations is shown in Figure 6.13. For the test cases presented in this section, the domain is 0.1 meters in the axial direction and 0.05 meters in the radial direction. The axial direction used 100 cells while the radial direction used 50 cells. Particles are seeded at the center of the domain according to a Maxwellian particle source which extends from $z = [0.049, 0.051]$ and $r = [0.0, 0.02]$. Symmetry boundary conditions are applied on the cylindrical axis, equipotential conductor boundaries at the left and right boundary, and exit port boundary conditions at the radial boundary.

The magnetic field topology used in the XOOPIC simulations is shown in Figure 6.14. The magnetic fields are produced by four current loops each with a current of $I = 10^3$ A and radius of 0.025 m. The positions of the current loops are: -0.03 m, 0.03 m, 0.07 m, 0.13 m. The equivalent magnetic field in the Q1D model is shown in Figure 6.15.
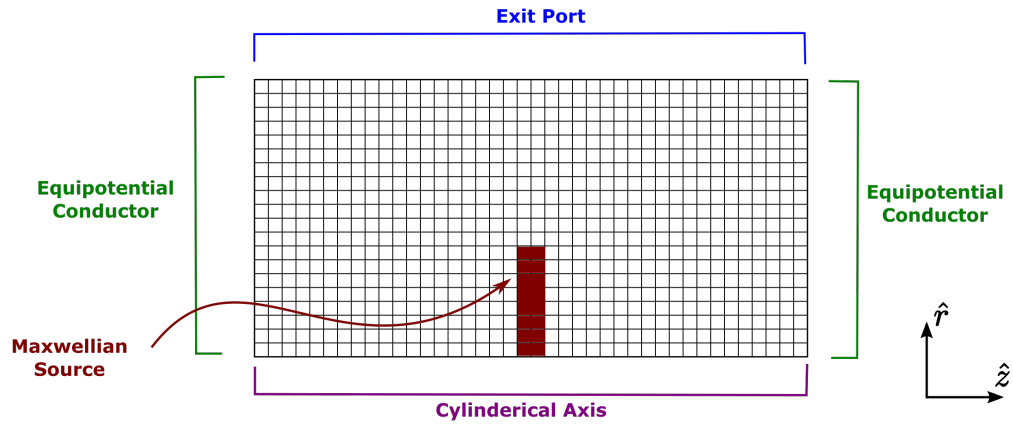
Figure 6.13: Grid for XOOPIC simulations of a particle source in a converging-diverging magnetic field.
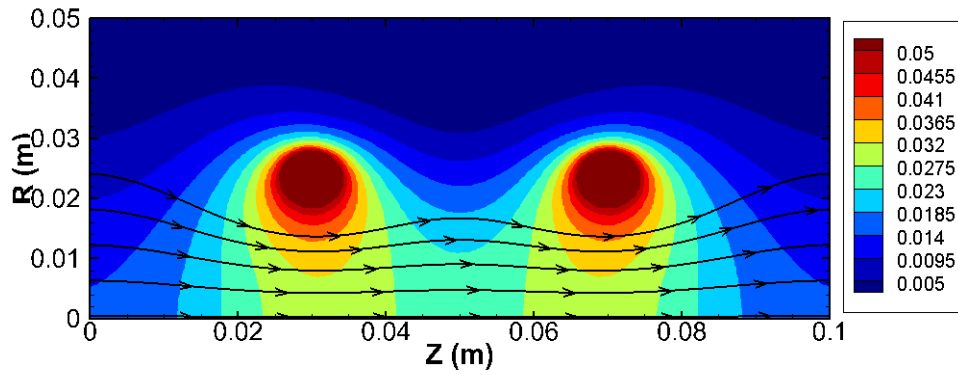
Figure 6.14: Contours of magnetic field strength (T) and magnetic field lines for XOOPIC simulations of a particle source in a converging-diverging magnetic field.
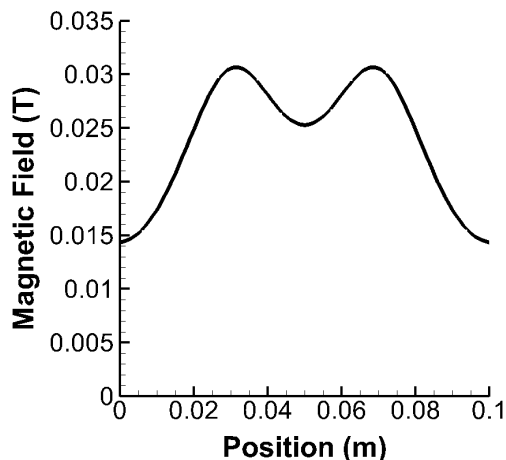
Figure 6.15: Magnetic field for Q1D simulations of a particle source in a converging-
diverging magnetic field.

A number of different simulations were performed with this setup by varying the
characteristics of the plasma source. A summary of all the parameters tested can
be found in Appendix D. The parameters varied include the flux rate of particles,
the mass of the ions, and the temperatures of both species. This enables control
of parameters which can test the validity of this Q1D model, such as the ion and
electron Larmor radii. Two cases in particular will be highlighted here. These cases
have a source rate of 10^{20} $\#/(m^3 s)$ and electron temperatures of $T_e = 5$ eV. The
only parameter varied is the ion temperature which is $T_i = 300$ K for the cold ion
case (CI) and $T_i = 5$ eV for the hot ion case (HI).

6.5.1 XOOPIC Results

The XOOPIC results for the CI simulation are shown in Figure 6.16. The electron
and ion density contours are shown. The electrons are well confined by the magnetic
field while the ions show some losses occurring near the center of the domain. Ions
with large radial velocities can be lost because the magnetic forces are not enough
to confine them in the radial direction. These losses are especially prevalent at the
center of the domain, where the magnetic field is monotonically decreasing in the

145

(a) Electron Density Contours ($\#/m^3$) (b) Ion Density Contours ($\#/m^3$)
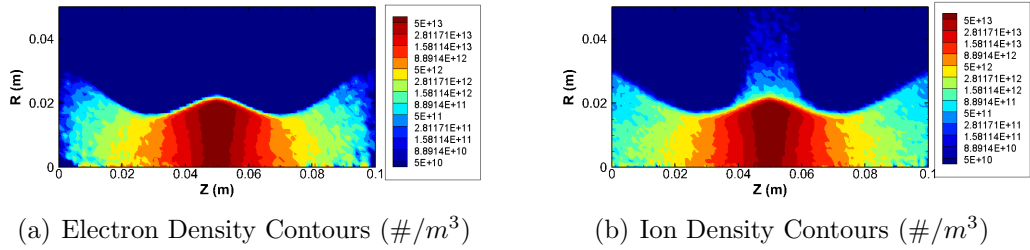
Figure 6.16: XOOPIC results for particle source simulation with cold ions.

(a) Electron density contours ($\#/m^3$). (b) Electron density contours ($\#/m^3$) for stronger magnetic field.

(c) Ion density contours ($\#/m^3$) (d) Ion density contours ($\#/m^3$) for stronger magnetic field.
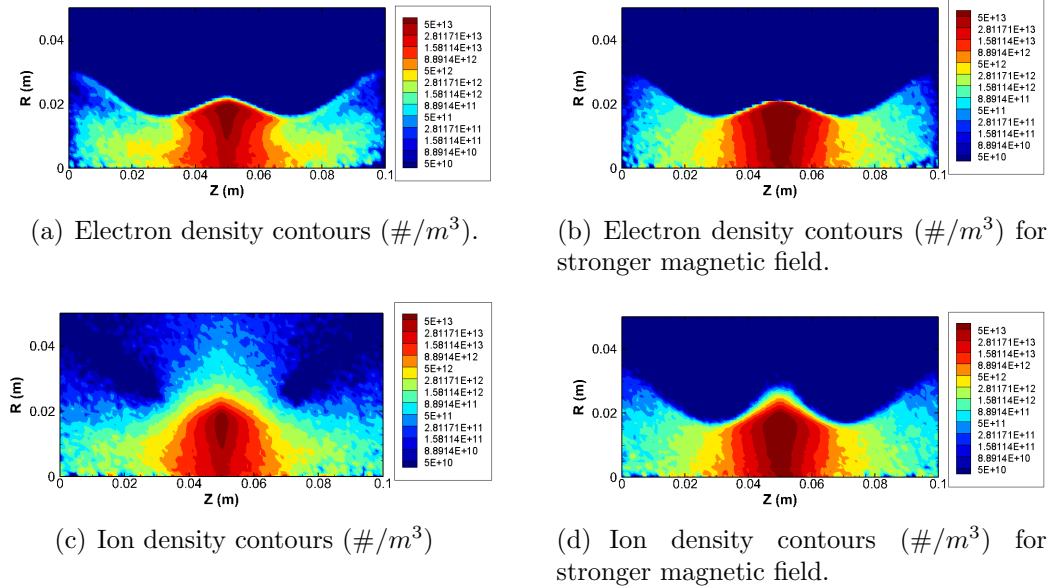
Figure 6.17: XOOPIC results for particle source simulation with hot ions.

radial direction. Ions with large radial velocities will have large Larmor radii and will move into regions of lower magnetic field (decreases radially).

The HI results are shown in Figure 6.17. Two simulations were performed here, one with the default magnetic field and one with a magnetic field that was ten times stronger. The electrons are well confined in both, however the weaker field simulations has slightly lower densities and shows more variation in the radial direction. The ions densities show very different results with the strong field simulation showing much more confinement of the plasma. The weaker field simulation still shows a majority of the ions are confined, but a significant portion of ions are no longer confined to the field lines.

These XOOPIC simulations will be compared with the Q1D simulations by taking radial averages of the XOOPIC data. The average is taken of the region where the plasma is present, which has been defined as the cells in which electrons are present.

6.5.2 Comparison between Q1D and XOOPIC simulations

The comparison of the Q1D results with those of the plasma cross-section averaged XOOPIC results for the CI case is shown in Figure 6.18. The results for the electron and ion densities show good agreement near the center of the domain. The results start to differ more after the converging section. Part of the reason for this difference may come from the lack of particles in the region for the XOOPIC simulations. The XOOPIC result clearly shows some noise which occurs because some of the cells have few, if any particles in them. An inherent difficulty with the 2D simulation compared to the Q1D simulation is highlighted here: 2D simulations need many more particles to eliminate noise and this is particularly challenging for a simulation where the density varies by three orders of magnitude. More particles leads to cascade of greater simulation costs and limits the 2D solver to studying low density plasmas.

The results for the mean ion velocity show good agreement. The ions are slightly accelerated in the converging section, and then are rapidly accelerated in the diverging section. The results obtained with the XOOPIC and the Q1D codes show the same behavior and the ion velocities are very near one another.

Results from the HI case are shown in Figure 6.19. In these simulations the Q1D and XOOPIC simulation results for the ion and electron density show a much more significant difference for the default magnetic field strength simulations. Increasing the magnetic field strength causes the simulations to agree much more closely with one another. Differences are still seen in the expansion region where few particles are present in the XOOPIC simulations. The ion velocity results however still show good agreement between the Q1D and XOOPIC results even for the default magnetic
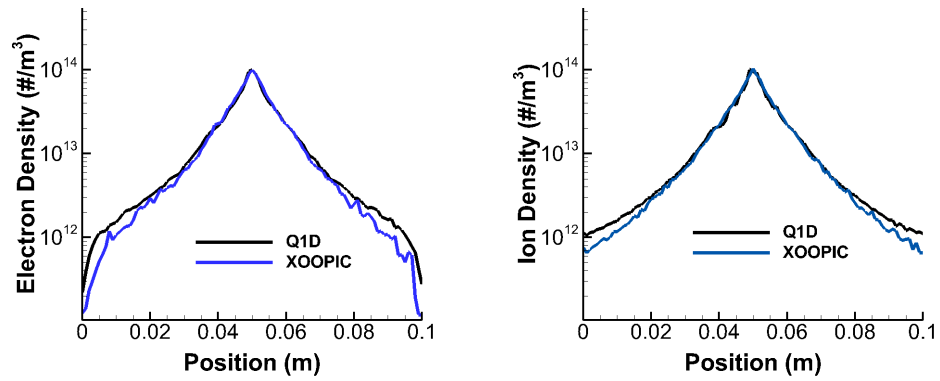
(a) Electron density

(b) Ion density
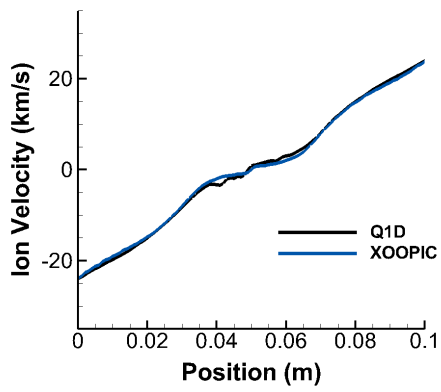
(c) Ion mean velocity

Figure 6.18: Comparison Q1D and XOOPIC cold ion results.

(a) Electron density

(b) Ion density

(c) Ion mean velocity
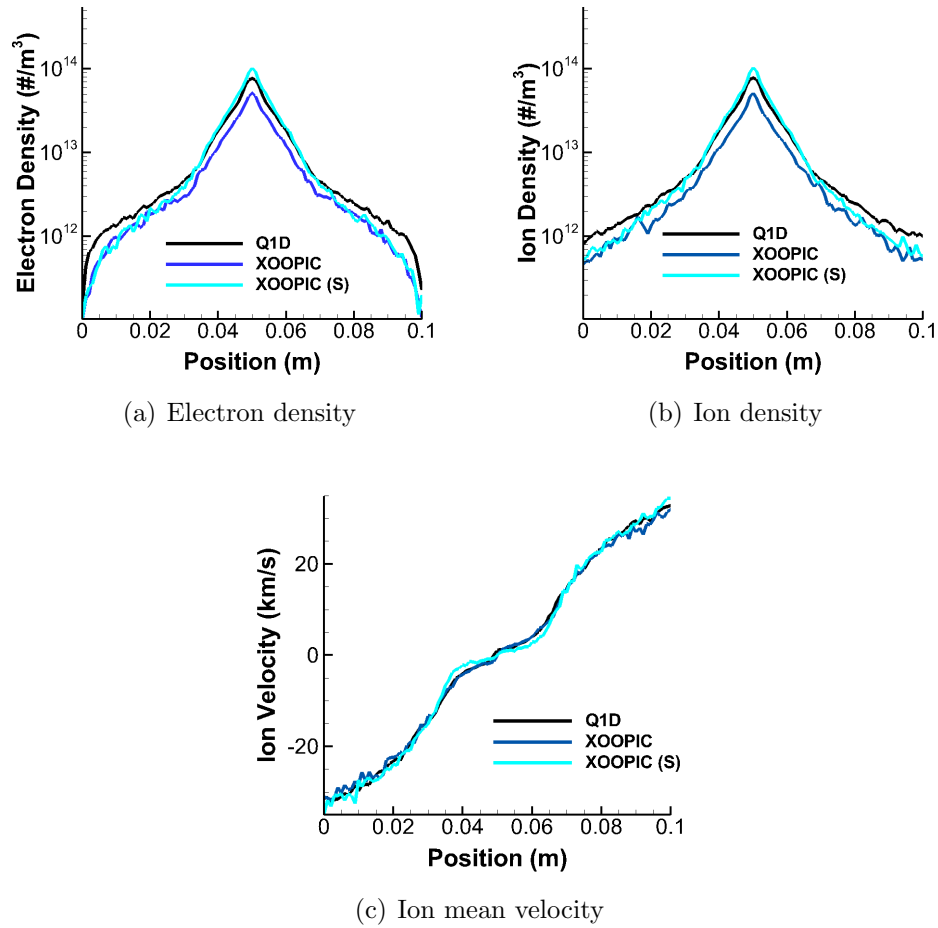
Figure 6.19: Comparison Q1D and XOOPIC hot ion results.

field strength case. The HI case also shows greater ion acceleration compared to the CI case. The ions accelerate more rapidly in the expansion region and have a higher final velocity.

Overall these simulations have demonstrated that the Q1D code qualitatively captures the two dimensional effects in a fully two-dimensional simulations. A quantitative comparison is made in the next section to determine in which regimes the Q1D simulations reproduce the 1D simulation results.

6.6 Discussion of Diverging Magnetic Field and Source Simulations

In this section a quantitative comparison of the errors between the XOOPIC and Q1D simulations is made for both the diverging magnetic field and the converging-diverging particle source test problems. All the test cases studied are outlined in Appendix C and Appendix D. The simulation parameters were varied so that the limits of accuracy for the Q1D model could be tested. The Q1D method was derived by assuming the particles were magnetized, this is tested here by varying the magnetic field strength and particle energies. As the magnetic field strength is decreased the Q1D assumptions should fail. Increasing the particle energies also increases the inertia of the particles making it less likely for the particles to remain magnetized at a given magnetic field strength. Therefore it is expected that as the energy is increased the Q1D assumptions should begin to fail and the error should increase.

The error shown in this section is found by finding the root mean square error between the Q1D and XOOPIC simulation results for the ion density, electron density, and ion velocity. This error is normalized to the maximum value to give a percent error to be compared across the different simulations.

Scaling of the error with characteristic parameters was performed to see which parameters serve as the best metric to evaluate the validity and/or accuracy of the Q1D model for a problem. The parameters include the ion Larmor raduis, electron Larmor radius, and plasma beta, to name a few. The parameters which showed the best scaling were an inertial Larmor radius ($r_{L,inertial}$) and the hybrid Larmor radius ($r_{l,H}$) defined in Equations 6.28 and 6.29.

$$r_{L,inertial} = r_{L,e} + r_{L,i} \frac{v_i}{v_e} \tag{6.28}$$

$$r_{L,H} = \sqrt{r_{L,e} r_{L,i}} \tag{6.29}$$

Both these Larmor radii are derived by treating the ions and electrons as a two-particle system and comparing the inertia of this system with the confining force of the magnetic field. They are both derived in the magnetic nozzle theory section in Equations 3.20 and 3.22.

6.6.1 Source in a Diverging Magnetic Field

The results for the diverging magnetic field simulations are shown in Figure 6.20. Error scaling for the ion density, electron density, and mean ion velocity are shown with respect to the inertial and hybrid Larmor radii which were normalized by the gradient magnetic field length scale ($L_B = |B|/|\nabla B|$). The x-axis of the charts is on a logarithmic scale so the broad range of parameters can be seen. The density errors are shown for all the test cases. Velocity errors are only shown for test cases which had the same ratio of electron to ion temperatures, which is the driving parameter for the sheath characteristics. Comparing velocity errors across simulations with different temperature ratios was inconclusive due to the overwhelming importance of the sheath on the velocity. Differences in how the codes captured these sheaths overwhelmed any other velocity errors.

Over all simulations the source parameters were selected so that the ratio of the Debye length to the domain length was the same. This is necessary so that the source sheath remains small compared to the domain. This is achieved by keeping the ratio of the source density and the electron temperature the same. Simulations were also performed with a domain one tenth the size to test that the non-dimensional properties hold at a different length scale. To keep this simulation consistent with the larger simulations the ratio of Debye length to the system dimension had to be kept the same. For a domain $1/10^{th}$ the size the Maxwellian source density was increased
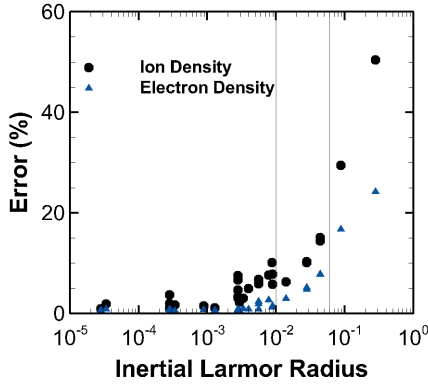
(a) Density Errors for Inertial Larmor Radius
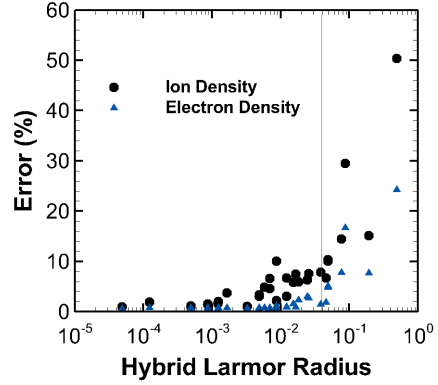
(b) Density Errors for Hybrid Larmor Radius
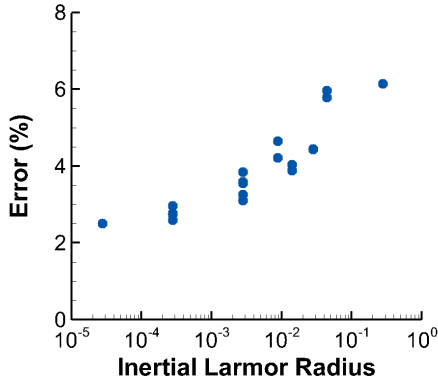
(c) Velocity errors for Inertial Larmor radius
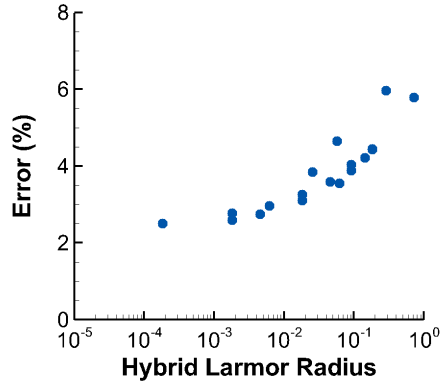
(d) Velocity for Hybrid Larmor Radius variation

Figure 6.20: Scaling of errors for Maxwellian source in a diverging magnetic field.

by a factor of 100 to keep the simulations consistent.

The scaling of the error with the Larmor radii shows a trend of increasing error as both the inertial and hybrid are increased. The error in the ion density stays approximately below 10% for inertial Larmor radii less than 10^{-2} and below 20% for inertial Larmor radii less than 10^{-1}. Similarly, the electron density error stays approximately below 5% for inertial Larmor radii less than 10^{-2} and below 10% for inertial Larmor radii less than 10^{-1}. The electron error is generally less because they are more well confined than the ions, both show the same trends with the inertial radius. The ion velocity also shows a general trend of increasing error with the
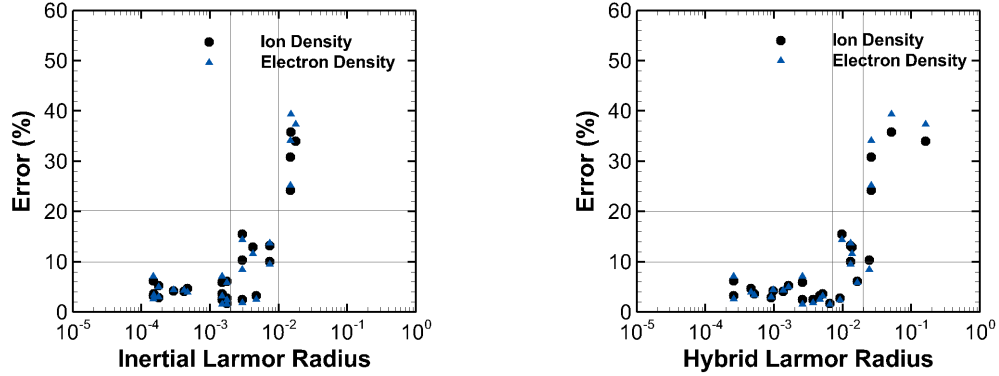
(a) Density errors with inertial Larmor radius

(b) Density errors with hybrid Larmor radius

Figure 6.21: Scaling of errors for particle source in a converging-diverging magnetic field simulations.

inertial Larmor radius. These errors remain fairly low because the source sheath is the dominating feature affecting the ion velocity and this does not change significantly between simulations by design. Changing the magnetic field also does not significantly alter the sheath structure near the inlet.

The error in the ion density stays approximately below 10% for hybrid Larmor radii less than 3×10^{-2} Similarly, the electron density error stays approximately below 5% for inertial Larmor radii less than 3×10^{-2}. Similar trends of increasing ion velocity error are seen in the case of the hybrid radius with the error increasing as the hybrid Larmor radius increases.

6.6.2 Particle Source in a Converging-Diverging Field

Results from the error analysis for the particle source in a converging-diverging magnetic field is shown in Figure 6.21. The density errors are shown scaling with the inertial and hybrid Larmor radii.

Figure 6.21 shows a trend of increasing error as both the inertial and hybrid Larmor radius is increased. The inertial radius scaling shows that an error of less than 10% is achieved for $r_{L_{inertial}} \leq 2 \times 10^{-3}$ and an error of less than 20% for

$r_{L_i inertial} \leq 10^{-2}$. Hybrid Larmor radius scaling shows a error of less than 10% for $r_{L_H} \leq 7 \times 10^{-3}$ and an error less than 20% for $r_{L_H} \leq 2 \times 10^{-2}$. After the error reaches 20% the errors begin to rapidly increase.

In these simulations the ion and electron densities scale with one another, contrary to the source in the diverging field where the ions showed a larger error. The reason for this may be that there is no sheath present in these simulations which immediately puts a lot of energy into the ions. The high ion energies imply that they have a lot of inertia, which makes them more difficult to confine. For the plasma source simulations there is no sheath, resulting in the ions maintaining a low energy until they are accelerated due to the ambipolar and magnetic field forces.

6.6.3 Discussion

The error analysis comparing with XOOPIC results yields two important results:

1. The Q1D model reproduces two-dimensional results in the correct regimes.

2. The error between the Q1D model and the 2D results scales with intuitive parameters based on the non-dimensional Larmor radii of the constituent species.

These results are significant because they show that the Q1D model works as an approximation for the 2D plasma physics within the right regimes and that it consistently scales with physically relevant parameters.

Some important points must be made however. The length scales used in this analysis were non-dimensionalized by the gradient magnetic field length scale, which is the most physically relevant for determining if quasi-1D assumptions hold for a collisionless, boundary-less plasma. However, in other problems more relevant length scales may be the system dimensions or mean free path. The assumption of magnetization may no longer be valid if particles are colliding frequently with other particles or the device boundaries. For example, ion Larmor radii can readily be larger than

the device boundaries, while electrons may undergo frequent collisions. These regimes however does not preclude the use of the Q1D model. Instead different variants of the solver (e.g. with and without magnetic field forces on ions) can be compared with experimental results to determine the best suited variant of the model.

The motivation for the development of the Q1D model is to enable the simulation of two-dimensional effects in a magnetic field guided plasma expansion without the inherent computational costs of a fully two-dimensional system. For particle simulations cost is tied directly to the number of particles required in a simulation. PIC code computational costs typical scale as $Nlog(N)$ where N is the number of particles used. The required number of particles is set by the number of cells in the simulation and is chosen such that the noise is reduced and a statistically significant number of particles is used. Two-dimensional simulations have more cells because they resolve an additional dimension and therefore require more particles. For instance, the two-dimensional simulations in this chapter typically have 50 to 75 cells in the radial direction, which implies that 50 to 75 times as many particles should be used resulting in a cost increase. This cost increase factor can be quantified as $(I_R N \log(I_R N)/N \log(N))$ where I_R is the number of cells in the radial direction. This can be simplified to just I_R in the case of simulations with a large number of particles.

The Q1D method removes the I_R factor cost increase. The additional operations in the Q1D method due to the magnetic field forces and area variation only slightly change the overall computational cost compared to a one dimensional simulation. In fact, the overall cost should be comparable to a one-dimensional code which includes the Boris magnetic field push because the Q1D algorithms have effectively replaced this step.

A direct comparison of compute times was not made because the only fair comparison would be between identical codes. The code developed for this work is currently

not nearly as efficient as the much more mature XPDP1 and XOOPIC codes. Cursory comparisons were made, which show the Q1D method implemented in the code developed for this work being approximately an order of magnitude faster for some of the serial, 2D XOOPIC simulations performed in this chapter. The code developed herein however does have the additional advantage of being fully parallelized with MPI instead of only using shared memory machines. This is particularly important for large simulations.

CHAPTER VII

Test Problem

7.1 Introduction

Previous kinetic studies of magnetic nozzles have focused on simulations with one-dimensional PIC codes.[51, 54] Kinetic simulation of magnetic nozzles is difficult because it is an inherently multi-dimensional problem. Simulation with higher dimensions becomes prohibitively expensive for the already computationally taxing problem of simulating a plasma kinetically. The one-dimensional simulations of Meige [51] and Baalrud[54] investigated the conditions which lead to the formation of a double layer in a configuration similar to the HDLT. [3] The expansion process was mimicked by including a loss frequency for removing particles from the simulation over a portion of the domain. Formation of double layers was found to be dependent on this loss frequency, with double layers appearing for sufficiently high loss frequencies. The dependence on loss frequency implies that double layers form when the plasma rapidly expands. These simulations also showed the formation of an accelerated ion beam due to this potential structure. Meige and Baalrud both acknowledge the limitations of this model and suggest future work which includes the effects of the magnetic field to better capture of the plume expansion. The work presented herein further investigates this problem by modeling the two dimensional effects of the magnetic nozzle on the plasma. This work addresses the need for a more robust simulation which

includes two-dimensional effects without prohibitively increasing the computational cost. This chapter presents results from the magnetic nozzle test problem simulations while the next chapter will delve in more detail into the physics.

7.2 Simulation Parameters

Simulation parameters for the magnetic nozzle test problem are chosen to compare with previous one-dimensional simulations by Meige[51] and Baalrud[54] in regimes of operation similar to the HDLT.[3] The goal of these simulations is to further study this problem by including the two-dimensional effects without assuming a loss frequency for the particles. The simulation domain consists of a heating region from $x = [0.0, 0.05]$ m which is followed by an expansion region from $x = [0.05, 0.1]$ m. The left boundary is a floating collector while the right boundary is grounded. The simulation parameters are shown in Table 7.1.

Table 7.1: Parameters for magnetic nozzle test problem simulations.

Parameter	Value
Length	10 cm
Grid Cells	250
Time Step	5×10^{-11} s
Total Time	25 μs
Heating Current	100 A/m^2
Heating Frequency	10 MHz
Macroparticle Weight	2×10^8 Particles/Macroparticle
Neutral Pressure	1.23 mTorr
Neutral Temperature	293 K
Gas	Argon
Magnetic Field (B_0)	300 G

The effects of the cross-sectional area variation and the magnetic field forces on the simulation results were investigated individually and collectively. The effects of ion magnetization were also investigated by including or neglecting the magnetic field forces on the ions. The magnetic field is constant in the heating region and then
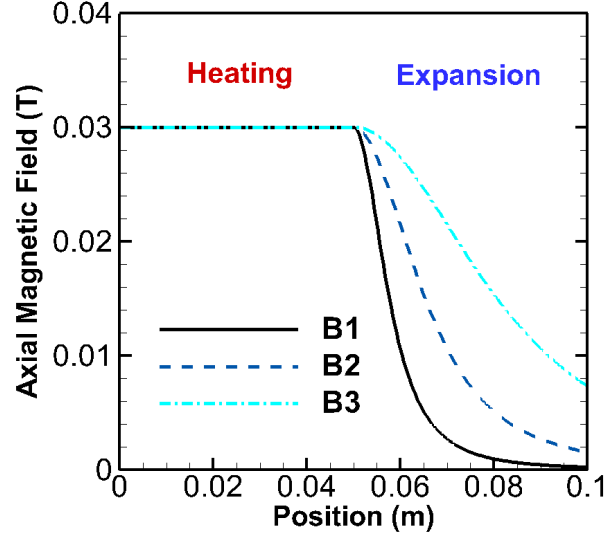
Figure 7.1: Magnetic field topologies used in test problem simulations.

decreases in the expansion region. The magnetic field profile along the axis is chosen to take a form similar to that for the magnetic field along the centerline of a current loop. [54] Equation 7.1 shows this relation.

$$B_z = \frac{B_0}{\left(1 + \frac{(z-0.05)^2}{C^2}\right)^{3/2}} \tag{7.1}$$

The constant C in this equation is varied to change how rapidly the magnetic field diverges. Figure 7.1 shows the magnetic field topologies tested in these simulations. The one dimensional simulation includes no magnetic field expansion ($B(z) = B_0$) while B3 is the strongest expansion. The C values for Cases B1,B2, and B3 are 0.04, 0.02, and 0.01 respectively.

The influence of the two-dimensional effects was first investigated by adding two-dimensional effects to the Meige and Baalrud simulations. The parameter space was then further investigated by varying the profile of the magnetic field topology, the background neutral density profile, the gas used, and the length of the heating region.

7.3 Quasi-One-Dimensional Effects

Four different types of simulations were performed adding various of the Q1D effects. The first simulation was purely one dimensional (1D) and includes no 2D effects. The second simulation type (AR) investigated the effects of varying the cross-sectional area. The third simulation is the full quasi-1D simulation (Q1D) including both the area variation and magnetic field forces. The final simulation type (NoIon) includes the effects of the cross-sectional area variation and only includes magnetic field forces on the electrons corresponding to a condition in which the ions are not magnetized but still follow the field lines. The results shown for all simulations were averaged over the last heating cycle. The results of these different simulation types is shown in Figure 7.2 and will be discussed in detail. The electron density, ion density, potential, and ion axial velocity are shown.

One-Dimensional Simulation (1D)

The 1D simulation corresponds to the case where the magnetic field is constant, resulting in no two-dimensional effects in the quasi-1D model. Simulation parameters for this case are similar to the case presented by Meige for a discharge with zero loss frequency and a background neutral pressure of $P_{neut} = 1$ mTorr.[51] The simulation results of this paper and those of Meige show similar behavior, although they are not identical due to the slightly different neutral pressure used, differences in collision cross-section data, and the difference in the heating scheme. In our simulations the ion current is also included in calculating the plasma conduction current (J_{cond}).

These results show the formation of a sheath at the left floating boundary as well as a sheath at the right grounded boundary. The density is nearly uniform through the rest of the domain. A source sheath is not seen at the edge of the heating region because charged particles are created not only in the heating region, but throughout the domain due to electron-neutral ionization collisions of heated electrons from the

160

(a) Electron density

(b) Ion density

(c) Potential

(d) Mean ion velocity
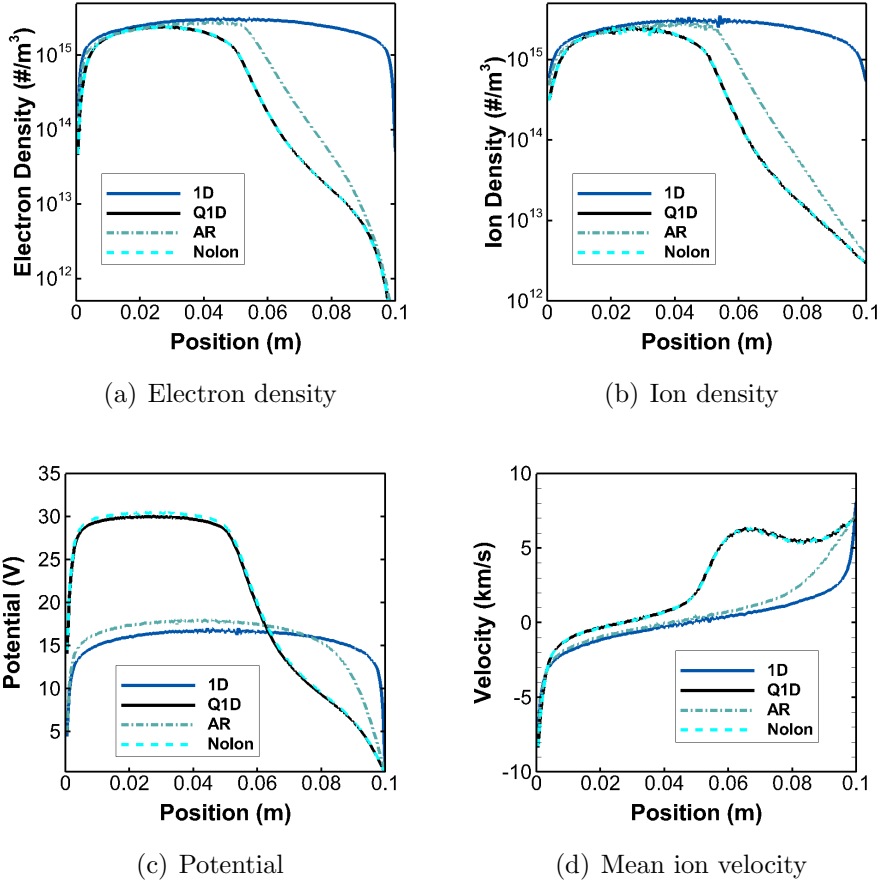
Figure 7.2: Illustration of quasi-1D effects in magnetic nozzle simulations.

heating region. The mean free path for ionization collisions is long enough so that ionization is not confined to areas close to the heating region. This is an important phenomenon which effectively stretches the source region beyond where heating occurs and eliminates the source sheath. The creation of particles outside the heating region inhibits the formation of the potential structures which may occur due to the rapid thermal expansion of electrons from a finite source.

The electron temperature in these simulations is found to be around 4.3 eV and increases near the edges of the domain. The temperature in the $\hat{y}$-direction is slightly higher than the other directions due to the heating in this direction.

Area Ratio Effects (AR)

This simulation type only included the effects of the cross-sectional area variation on the jet expansion. These simulations capture the decreases in density that occur due to the plasma expanding along the magnetic field lines. Both the electron (a) and the argon ion (b) densities decrease as the plasma expands. The plasma potential (c) is not significantly affected by the expansion region. A slight decrease in the overall potential is seen and no rapid potential drops similar to a double layer are present at the beginning of the expansion. An extended sheath region is seen at the right boundary which is due to the decrease in density and the resulting increase in Debye length. The ion mean velocities also do not change significantly showing only a slight acceleration due to the extended sheath region.

These results indicate that the effects of the density decrease resulting from the plasma expansion do not by themselves result in the formation of sharp, ion-accelerating potential structures in the Q1D formulation. A reason for the lack of acceleration is that the variation of density alone does not have a mechanism which would drive the plasma to establish these structures. As illustrated in Case 1, no source sheath is established at the edge of the heating region because the collisions of the electrons with the background neutrals throughout the domain generates plasma outside the heating region. These collisions effectively stretch the source region beyond where the plasma is heated into the expansion region. The decrease of the electron and ion densities in the expansion region does not affect this source stretching behavior because the collisionality of the ions and electrons with the background neutrals is not a function of the ion or electron densities. The collision frequency of the particles is given by $\nu = n_{neut}\sigma v_{rel}$ in which n_{neut} is the background density, σ is the collision cross-section, and v_{rel} is the relative velocity of the particles. The neutral density is constant in the domain and neither the collision cross-section nor the relative velocity are a function of the plasma density. Simulations presented later in this section investigate varying the neutral background pressure and neutral density,

which affect the region over which plasma is generated.

Full Quasi-1D Simulation (Q1D)

Test cases with both the area variation and the magnetic field force were simulated. Electron (a) and ion (b) densities show the characteristics a drop in density due to a combination of the cross-sectional area variation and magnetic field force acceleration. The potential (c) undergoes a rapid drop as the plasma expands and a lengthened sheath is seen at the right boundary due to the decreased plasma density and increased Debye length. The mean ion velocity (d) rapidly increases as the plasma expands. The acceleration of the ions does not continue through the entire potential drop due to a balance between the accelerating potential and the collisions with the neutral background.

The effects of the magnetic field force on the plasma lead to the formation of a potential structure which accelerates the ions. The magnetic field force rapidly accelerates the electrons outwards ahead of the ions. The magnetized ions are also accelerated by the magnetic field forces, but the magnitude of this force is much less for the cold ions. This is due to the fact that the magnetic field forces are a function of the perpendicular velocity ($v_\perp$) which is much smaller for the ions. Therefore, the ions lag behind the electrons, leading to the formation of the potential structure that also accelerates the ions. This hypothesis is further investigated in the final set of simulations which remove the magnetic force effects on the ions while still including the magnetic field forces on the electrons.

Full Simulation with Demagnetized Ions (NoIon)

Finally simulations were performed with the effects of the magnetic field forces on the ions neglected while including the cross-sectional area variation effects and the electron magnetic field forces. This simulates conditions in which the ions would be demagnetized, but still, on average, follow the magnetic field lines. The results

of these simulations is shown in Figure 7.2. These plots show that the results are very similar to the results of the full simulation which includes the ion magnetic field forces. This suggests that the effects of the magnetic field forces on the ions is negligible for these conditions with cold ions in comparison to the other forces. Therefore, these simulation results validate the arguments that the ion acceleration is not caused directly by the magnetic field forces on the ions. The ion acceleration is instead caused by potential structure which establishes as a result of the magnetic field forces on the electrons.

Electron Temperature and Velocity Distribution

The electron temperatures in the simulations show interesting behavior as Q1D effects are included. Temperatures are calculated using the formula shown below and represent the mean random energy of the particles.

$$T_i = \frac{m}{k_b} \frac{\sum_0^{j=N} (v_{i,j} - u_i)^2}{N} \tag{7.2}$$

In this equation N is the number of particles, the i index the direction, j the particle index, and u the mean velocity.

Figure 7.3 shows how the electron temperature in the domain varies as Q1D effects are included. The temperature remains nearly constant in the domain (except near the sheaths) for the 1D and AR simulations. Once the magnetic field forces are incorporated sharp peaks in the temperature appear at the edges of the heating region.

Further insight is gained by examining the electron distribution function for the full Q1D simulations. Plots of the electron velocity distribution for the axial direction at $t = 5 \times 10^{-5}$ seconds are shown in Figure 7.4 and are not averaged over an RF cycle. The distribution functions are plotted on an a log scale with respect to the kinetic energy in that direction. On this type of plot a Maxwellian distribution will appear

164
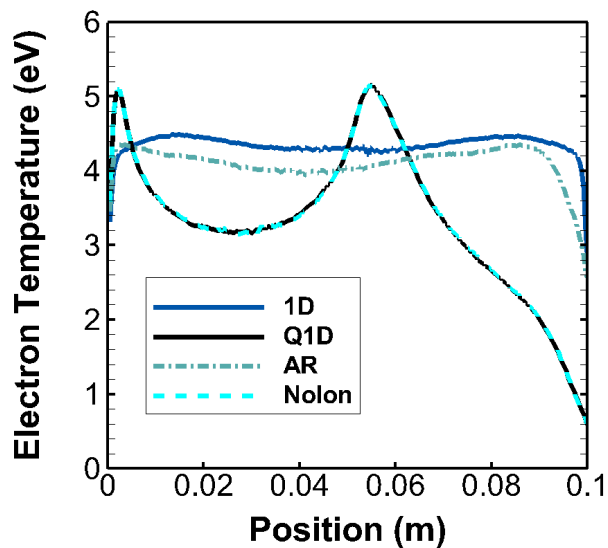
Figure 7.3: Temperatures in the quasi-one-dimensional simulations with inclusion of Q1D effects.

as a straight line with a slope equal to the inverse of a Maxwellian temperature. The simulation results also have two lines, one for each side of the velocity distribution function. Use of the energy leads to a positive value for both and makes comparison with the Maxwellian distribution easy.

Figure 7.4 shows the electron axial velocity distributions at three locations as well as the slopes for some Maxwellian distributions. Velocity distributions are not averaged over an RF cycle. The distribution at (a) in the heating region shows characteristics of a bi-Maxwellian. Low energy particles have the characteristics of Maxwellian distribution at $T_e = 2\ eV$ while the high energy particles have the characteristics of a distribution at $T_e = 5\ eV$. This multi temperature plasma in a source is not uncharacteristic of RF discharges as was shown in earlier simulations of voltage and current driven discharges. At the center of the domain (b) the distribution is primarily characteristic of a $T = 5\ eV$ Maxwellian. Here the distribution has settled to a single temperature before the electrons begin the expansion. In the expansion region (c) the distribution changes significantly, appearing to be non-Maxwellian. The
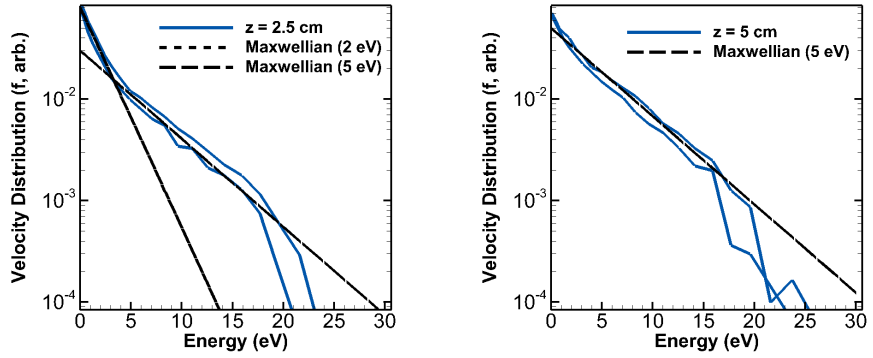
165

(a) Center of heating region($z = 2.5$ cm)   (b) Center of domain($z = 5$ cm)
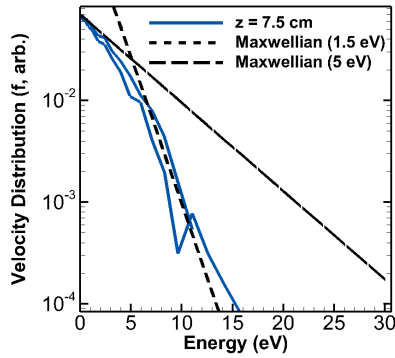
(c) Center of expansion region($z = 7.5$ cm)

Figure 7.4: Axial velocity distribution function variation in space. Simulation results have two lines, one for each side of the distribution.

distribution may be slightly bi-Maxwellian, in this case with the low energy particles appearing to be characteristic of a distribution at $T = 5\ eV$ and the high energy particles as a $T = 1.5\ eV$ Maxwellian. This reversal of Maxwellian compared to heating region may be a reflection of the effects of the potential structure on the distribution function. This decrease in temperature occurs as the plasma expands and electron energy is passed to the ions.

The results in this section illustrate the needs for a kinetic description of this problem through the appearance of bi-Maxwellian distributions or even non-Maxwellian distributions. Distributions in the other directions are not shown for this particular case because the behavior is approximately the same. The electron distribution

functions are slightly different in the heating direction since these are not averaged results, but the behavior remains the same due to the collisions.

Discussion

Previous simulations have investigated ion accelerating potential structures by using one-dimensional PIC codes and a loss frequency in the expansion region of the domain. [51, 54] Those simulations showed similar results to those found in this thesis, but with a very different model to examine the expansion region. The loss frequency method was implemented in a way similar to a collision frequency and removed particles from the domain to mimic the density decrease as the plasma expands. These simulations showed that a sharp drop in potential similar to a double layer occurs when the loss frequency of particles is large enough. This double layer then accelerates the ions.

Based on those results, it was hypothesized that including the effects of the density variation (cross-section variation) in the plasma expansion using the quasi-1D model of this thesis would produce similar results. However, the results of the previous section suggest that the density variation due to the expansion does not result in the formation of any ion accelerating potential structures and that instead these structures form due to the magnetic field forces which act on the electrons. The magnetic field forces accelerate both the electrons and ions along the field line. The high energy electrons are more greatly affected by the accelerating magnetic field forces which are a function of $v_\perp^2$. The ions have much lower perpendicular velocity which results in a much weaker accelerating force. Rapid acceleration of the electrons relative to the ions leads to the formation of a potential structure that accelerates the ions to keep up with the electrons. Ion acceleration is governed by the potential structure established by the magnetic field force driven electron acceleration. This mechanism is further confirmed by the simulations which remove the effects of the

167

magnetic field force on the ions which still show acceleration of the ions due to the formation of a potential structure.

These results suggest that the effects of the density on the expansion alone are not sufficient to establish these potential structures, which may seem contrary to the previous results in literature. As pointed out by Baalrud, the loss frequency method has an inherent bias for removing slow particles from the domain more frequently. [54] Slow particles are in the domain longer, so there is a higher probability that they are removed for an isotropic loss frequency. Preferential removal of slow particles in the domain then leads to a higher than expected ratio of high energy particles to low energy particles. Furthermore, the ions are much slower than the electrons, implying that on average the slow ions are more likely to be removed than the fast electrons leading to a higher density of electrons than expected. The higher ratio of energetic, negatively charged particles may result in the formation of a potential structure which accelerates the slow, positively charged ions. A possible way to test this theory would be to add a weighting factor to the loss frequency.

7.4   Varying Heating Region Length

The heating profile used in the simulation was varied to illustrate the effects on the plasma properties, particularly the electron temperature. In the original simulations the heating region stretched from $x = 0$ to $x = 0.05$. An additional simulation was performed with a shorter heating region which from $x = 0.015$ to $x = 0.035$. The results from the shorter region are labeled with a J in the plots comparing with the full Q1D simulations shown in Figure 7.5.

Results from Figure 7.5 show that there are differences in the results due to the heating region length, although the qualitative behavior stays the same. The ion density, potential, and ion axial velocity all show the same structure in the two simulations. The longer region has a higher potential in the heating region and

(a) Ion density

(b) Potential

(c) Mean ion velocity
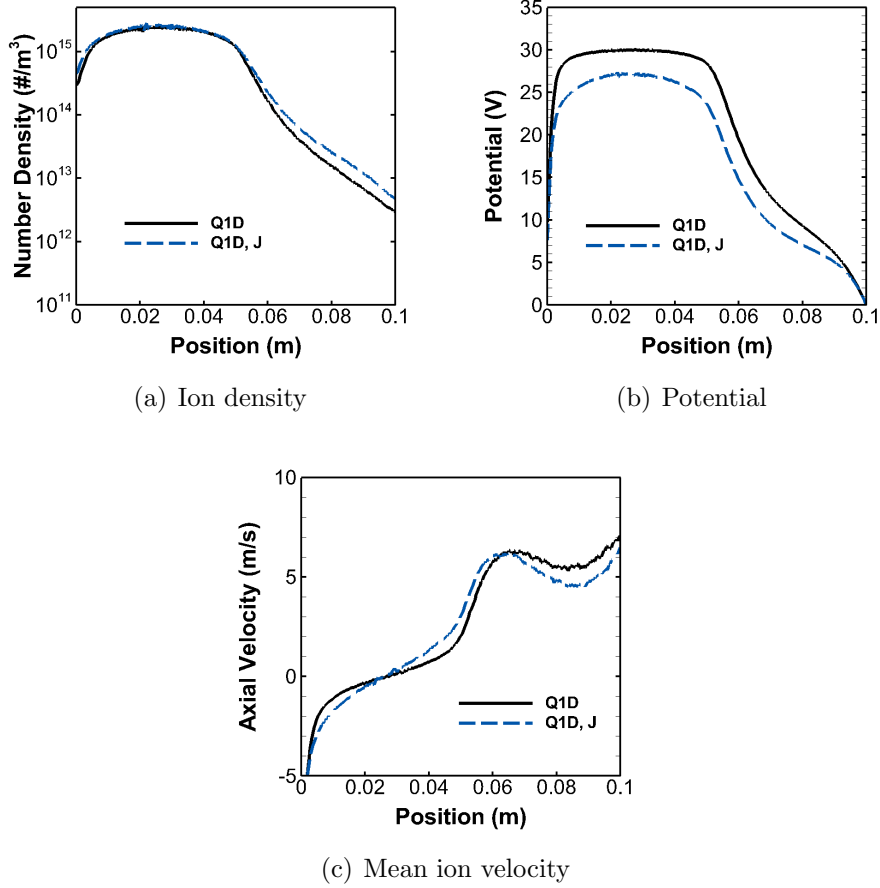
Figure 7.5: Illustration of effects of varying heating region length. Normal heating region (Q1D), short heating region (Q1D J).

slightly lower ion densities in the expansion region. The short heating region shows a more rounded potential structure and as a result the ions begin being accelerated earlier in the heating region. The earlier acceleration leads to a maximum in the velocity at a position closer to the beginning of the expansion region. This gives more time for the ion-neutral collisions to remove energy from the mean velocity resulting in a lower dip and lower final velocity for the shortened heating region case.

7.4.1 Effects on Electron Temperature and Electron Distribution

The differences in these results can be further highlighted by the temperature profiles in each shown in Figure 7.6. Here clear differences are seen between the two

169

simulations which drive the difference in the other parameters. The long heating region in the original simulations results in a temperature profile with sharp peaks at the edges of the domain while the short heating region results in a nearly flat temperature profile in the heating region. The interesting point here is not that the peaks form when the heating region is long, but instead that a trough forms in the middle of the heating region instead of a uniform temperature profile. This is an important distinction because the maximum temperature of both simulations match and is close to the maximum of the 1D simulations. The formation of a trough occurs when there is a sharp potential structure coinciding with the edge of the heating region. A possible explanation for this is that the potential structure combined with the sheath at the other edge of the domain act as a potential well which will more readily confine the lower temperature electrons in the heating zone. This confinement is less pronounced if there is a region between the heating region and the potential structures over which the electrons experience collisions or other dynamical processes.
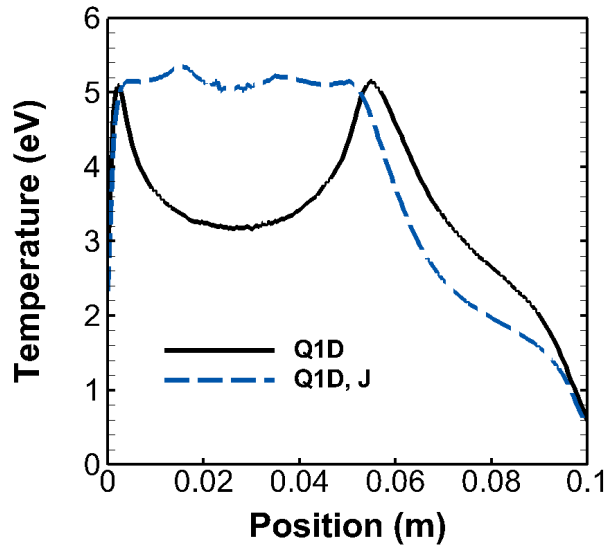
Figure 7.6: Temperatures in the quasi-one-dimensional simulations with different lengths for the heating region. Normal length heating region (Q1D), shortened heating region (Q1D,J).

170

The resulting electron velocity distributions in the axial direction are shown in Figure 7.7 for three positions. As shown in (a) and (b), the shorter heating region results in a single temperature plasma in the heating region. This agrees with the results shown in Figure 7.6 where the temperature is constant until the beginning of the expansion region. This is different from the longer heating region which also showed a large population of lower temperature gas. The expansion region shows similar behavior for the longer and shorter heating region simulations where the distribution is no longer Maxwellian and does not have a characteristic Maxwellian temperature or temperatures. Maxwellian distributions are shown in (c) give a general idea of the slopes.
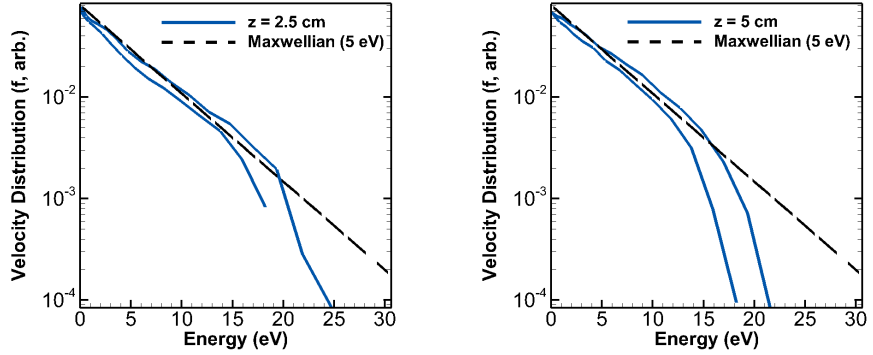
(a) Center of heating region($z = 2.5$ cm)   (b) Center of domain($z = 5$ cm)
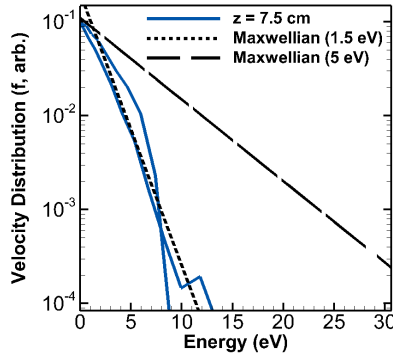
(c) Center of expansion region($z = 7.5$ cm)

Figure 7.7: Axial velocity distribution variation in space for shorter heating region (Q1D,J).

7.4.2 Discussion

Varying the heating region length shows pronounced effects on the electron temperature in the heating region while the other plasma properties stay approximately the same aside from variations driven by changes in the electron temperature. Shortening the heating region produces the same amount of plasma despite the fact that the total current into the plasma is decreased. This implies that the shorter heating region is more efficient at coupling the energy from the driving current to the plasma. The optimal length for the heating region will be a function of the current magnitude (which is related to the energy input into the plasma) and the neutral background density which both affect the average ionization mean free path, which is the relevant length scale.

7.5 Varying Neutral Density Profile

The background neutral density was varied to examine the effects on the simulation results. This is intended to simulate the case in which there is a initially a high neutral density which decreases rapidly as ions are created and the neutral gas expands into the vacuum chamber.

The results from simulations with varying the neutral density are shows in Figure 7.8. In these simulations the neutral density outside the heating region ($x = [0.05, 0.1]$ m)is abruptly reduced to $n = 1 \times 10^{17}$ $\#/m^3$. Simulation results are shown for both the 1D and Q1D simulations as well as the simulations with decreased neutral densities(1D,DD and Q1D,DD).

In the 1D simulations the decrease in neutral density leads to the formation of a source sheath and corresponding drop in density. This occurs due to the abrupt change in regions where plasma is created and the plasma balancing the fluxes of particles. The potential drop is around 3.5 V which is greater than the minimum electron

(a) Electron density

(b) Ion density

(c) Potential

(d) Mean ion velocity
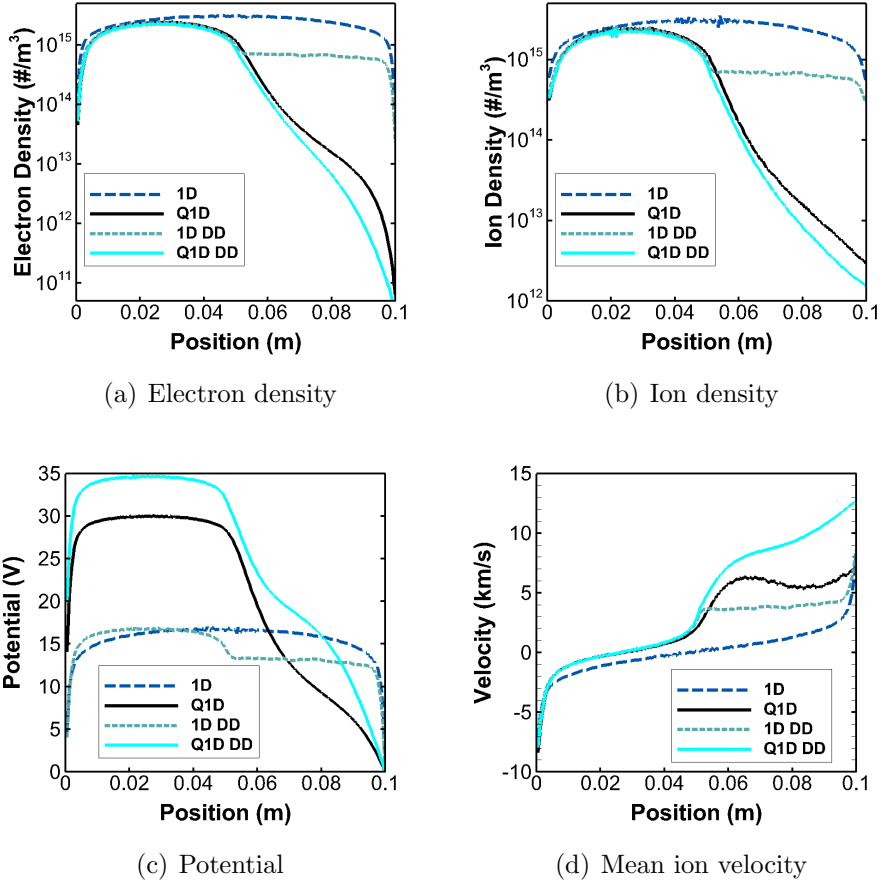
Figure 7.8: Results for simulations with decreased neutral background density in plume.

temperature in the heating region ($T_{e,min} \approx 3.1$ eV) and less than the temperature at the edge of the heating region ($T_{e,max} \approx 4.25$ eV).

Incorporation of the decreasing neutral density into the Q1D simulations shows similar results to the previous simulations. The major difference is that ion charge-exchange and elastic collisions become less likely in the ion beam, resulting in a continued acceleration of the ion particles and no slowing due to collisions. The ion and electron densities do not show major changes, they are slightly lower in the expansion region due to the continued acceleration of the ions. The potential structure stays approximately the same, except for an increase in the overall potential due to a change in the sheath at the right boundary.

7.5.1 Effects on Temperature and Electron Distribution for 1D Simulation

The decreased neutral density (DD) outside of the heating region had profound effects on the temperature profile. These temperature profiles are shown in Figure 7.9. The parallel temperature is along the field line while the perpendicular temperature is the average of the perpendicular directions. The perpendicular temperature is higher due to the heating that occurs in this direction.
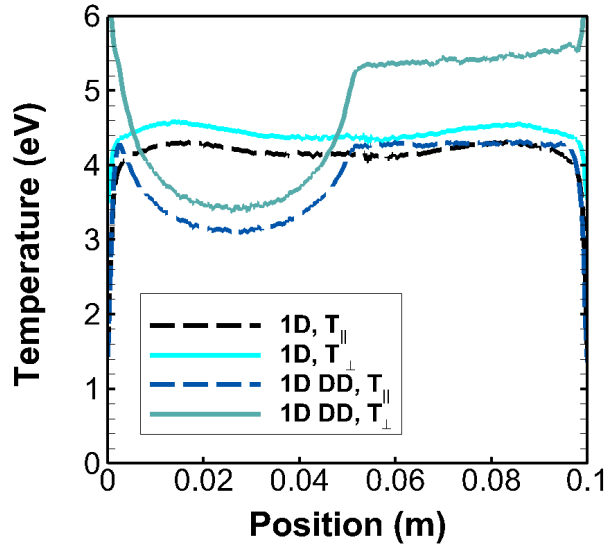
Figure 7.9: Temperatures in the one-dimensional simulations with lower neutral density in the expansion region.

The decreased neutral density outside the heating region leads to the formation of a temperature profile similar to that seen when the magnetic field effects are incorporated in the Q1D simulation. A minimum for both the parallel and perpendicular temperature appears in the heating region. At the edge of the heating region and in the remainder of the decreased density region the temperatures remain approximately constant. This decreased temperature profile occurs due to the interaction between the heating region and the source sheath due to the decreased density outside this region.

174

Further insight is again gained by looking at the electron velocity distribution functions. The velocity distribution in the axial direction is shown in Figure 7.10. The distribution in the heating region (a) shows the same two temperature behavior seen in some of the Q1D simulations, explaining the temperature drop seen. At the edge of the heating region the distribution is mostly Maxwellian with a temperature near $T_e = 5$ eV It appears that there may be a depleted tail as well, but this is hard to quantify because there are far fewer particles in the tail. Depletion in the tail may occur due to the higher energy particles being able to traverse the wall sheaths and then be lost to the wall.[54] The profile in the expansion region remains the same as that at the edge of the expansion region, implying that the temperature is largely unaffected by the presence of the source sheath.

The distribution in the x-direction (not the heating direction and not the axial direction) is shown in Figure 7.11. The distribution in the heating region shows the same two temperature behavior. At the edge of the heating region and beyond the temperature remains constant at nearly $T_e = 5 \ eV$. These velocity distributions also do not show a depleted tail because there are mechanisms for losses in the perpendicular direction.

The behavior of the distribution function and the temperature show that even in the case of the one-dimensional simulation effects such as a rapid decrease in density can lead to the formation of electron distributions with bi-Maxwellian shapes. The interaction of the heating region with a potential structure at the edge of the heating domain also produces this two-temperature behavior and results in a lower temperature in the center of the heating region.
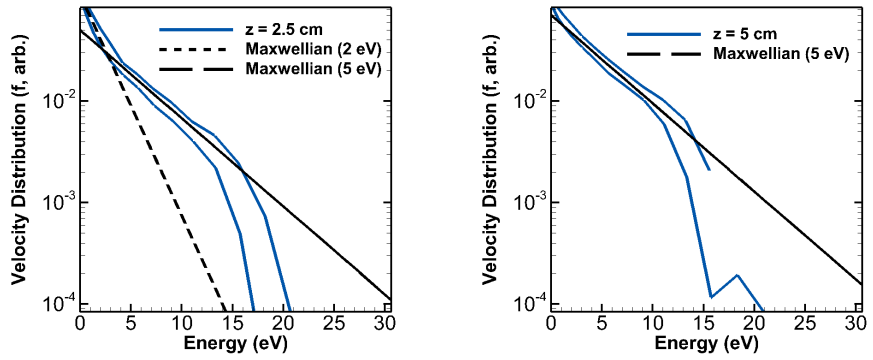
(a) Center of heating region($z = 2.5$ cm)   (b) Center of domain($z = 5$ cm)
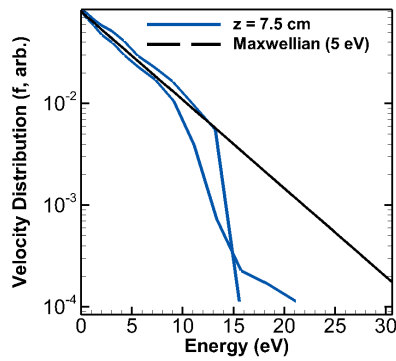
(c) Center of expansion region($z = 7.5$ cm)

Figure 7.10: Axial velocity distribution variation in space for 1D simulations with neutral density decrease in plume.

7.5.2 Effects on Temperature and Electron Distribution for Q1D Simulation

Temperature profiles for the Q1D simulations with a decreased neutral density in the expansion region are shown in Figure 7.12. The plots illustrate the anisotropy in the temperature when there is not a sufficiently high density of neutral gas in the expansion region for collisions to create an isotropic distribution. The parallel temperature in the expansion begins by slightly varying and then starts to decrease near more rapidly near the extended sheath region and the perpendicular temperature decreases as the magnetic field forces remove energy from this mode. This same
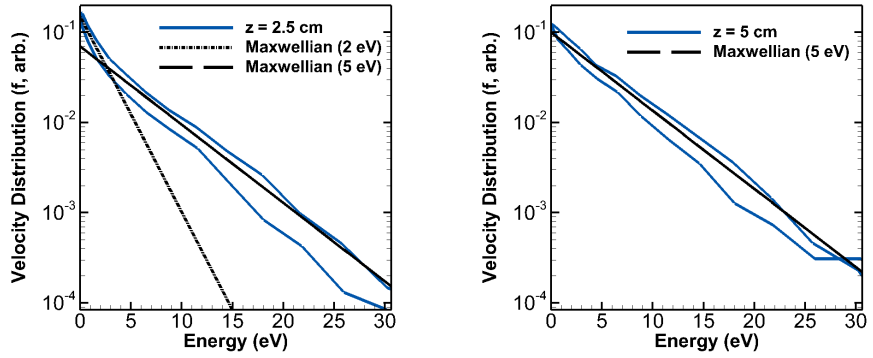
(a) Center of heating region($z = 2.5$ cm)   (b) Center of domain($z = 5$ cm)
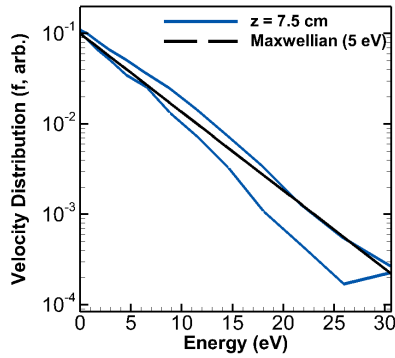
(c) Center of expansion region($z = 7.5$ cm)

Figure 7.11: Transverse ($\hat{x}$) velocity distribution variation in space for 1D simulation with decreased neutral density in plume.

physical process occurs in the simulations with a high background density in the expansion, except that the inclusion of electron-neutral collisions results in the parallel and perpendicular energy approaching equilibrium with one another.

The electron velocity distribution in the z-direction (axial) is shown at three locations in Figure 7.13. In the heating region (a) characteristics are seen of a two-temperature distribution as seen in previous simulations. At the edge of the heating region (b) the distribution is primarily Maxwellian with a temperature of $T_e = 5$ eV. In the plume (c) the distribution remains near $T_e = 5$ eV, implying that in the z-direction the bulk of the distribution does not change significantly.

The variation of the x velocity distribution in space is shown in Figure 7.14. This
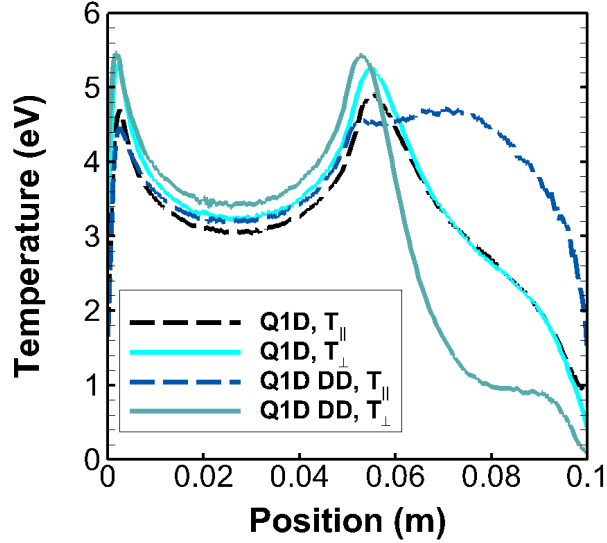
Figure 7.12: Temperatures in the quasi-one-dimensional simulations with lower neutral density in expansion region.

direction is perpendicular to the axial direction and not in the heating direction. Again a two temperature Maxwellian is seen in the heating region (a) while at the edge of the heating region a single Maxwellian is seen with a temperature of $T_e = 5\ eV$. Similar to the results for the 1D case, there appears to be no depletion of the high energy tails in the perpendicular directions. In the plume the velocity distribution in the transverse direction is significantly different from the axial direction. The temperatures have dropped significantly and it can no longer be approximated with a single Maxwellian distribution. The distribution shows characteristics of a Maxwellian at $T_e = 0.5\ eV$ for the low energy particles and a Maxwellian at $T_e = 2\ eV$ for the high energy particles.

These simulations again illustrate that the electron dynamics drive the ion acceleration and that the perpendicular electron energy is transferred elsewhere to the ions. Furthermore, the importance of kinetic effects are illustrated by both the anisotropic temperatures and the multiple temperature Maxwellians which can be seen in the expansion.
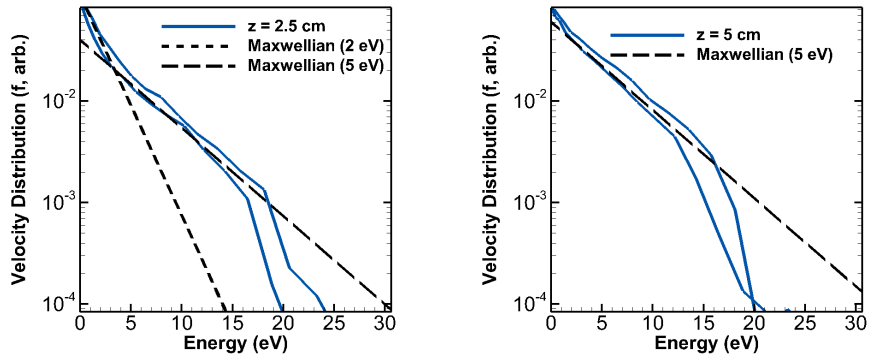
(a) Center of heating region($z = 2.5$ cm)

(b) Center of domain($z = 5$ cm)
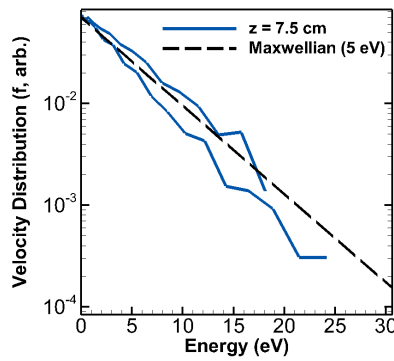
(c) Center of expansion region($z = 7.5$ cm)

Figure 7.13: Variation of axial velocity distribution in space for Q1D simulations with reduced neutral density in plume.

7.5.3 Ion Beam Formation

Figure 7.15 shows the ion axial velocity distribution functions for the high and low plume neutral density simulations. The ion velocity distribution shows the development of a sharp peak corresponding to the accelerated beam of ions created as the plasma expands. Charge-exchange collisions create the broad velocity distribution at lower energies. The ions are not accelerated indefinitely due to the collisions with the neutral background. The average velocity reached occurs as a balance between the accelerating potential and the ion-neutral collisions. The charge exchange mean free path for the beam ions is approximately 0.06-0.08 m, which is less than the length of
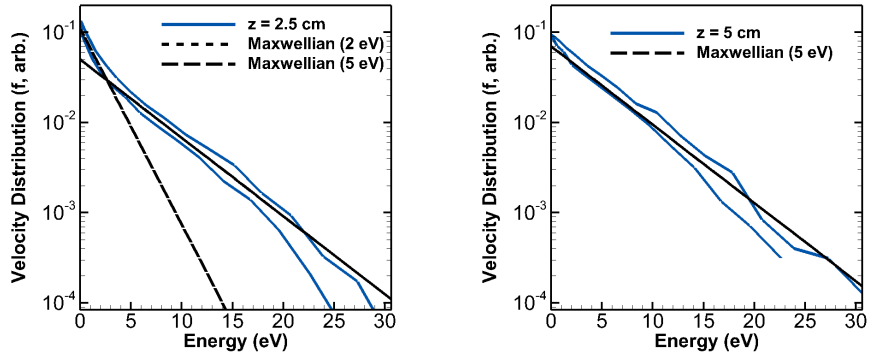
179

(a) Center of heating region($z = 2.5$ cm)

(b) Center of domain($z = 5$ cm)
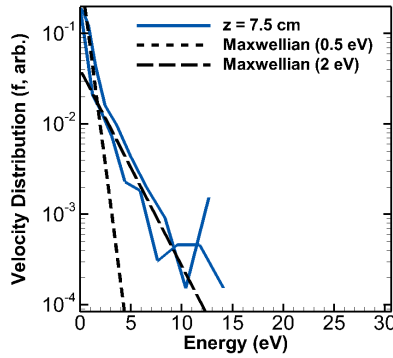
(c) Center of expansion region($z = 7.5$ cm)

Figure 7.14: Variation of transverse ($\hat{x}$) velocity distribution in space for Q1D simulations with reduced neutral density in plume.

the domain and explains the formation of the low energy peak. Removal of neutrals in the plume removes the low energy particles created due to collisions and shows a sharper beam.

Further development of the beams is shown in the velocity phase space contours for both cases in Figure 7.16. These plots show spatially the evolution of the distribution function. The case with a low background density clearly shows no low velocity ions in the expansion. The high background density case shows these low energy ions being created and then partially accelerated by the remainder of the potential drop. Some of the intermediate velocities are a result of the acceleration of ions which are created in the expansion region and do not experience the entire potential drop.
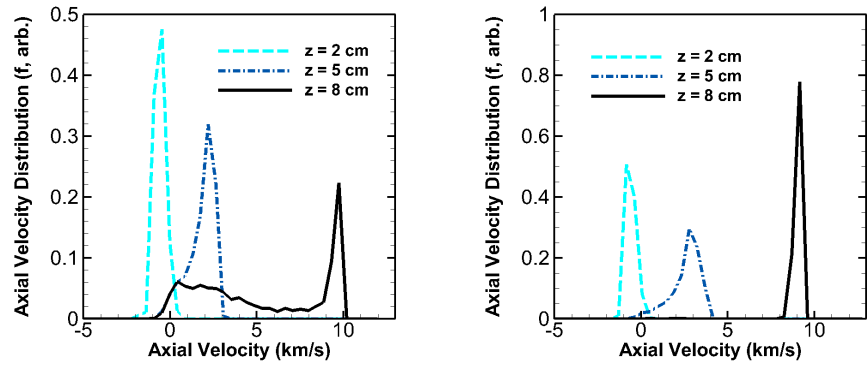
(a) Constant neutral density   (b) Low neutral density in plume

Figure 7.15: Ion axial velocity distribution showing development of beam.
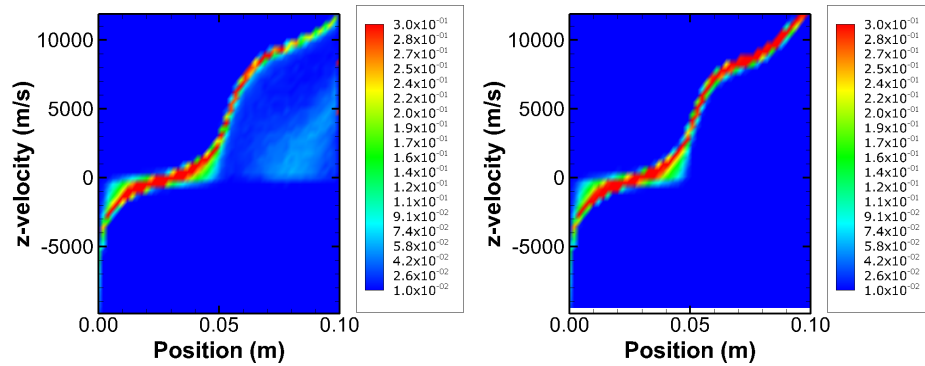
(a) Constant neutral background density. density

(b) Decreased neutral background density in expansion region.

Figure 7.16: Ion axial velocity phase space.

The simulation data for the ion energy distribution function can readily be compared with experimental results from diagnostics such as a retarding potential analyzer. Appendix E discusses retarding potential analyzers and the implementation of this diagnostic in the CubeSat Ambipolar Thruster. Future work at PEPL will compare simulation results with RPA results.

7.6 Magnetic Field Topology Simulations

The effects of varying the magnetic field divergence were tested in the Q1D simulations. The results of these simulations are shown in Figure 7.6. The ion and electron densities decrease more rapidly as the magnetic field expands more rapidly, as expected. This is due to the fact that the flux tubes are larger for the lower magnetic field strengths. The magnitude of this potential (c) drop increased as the magnetic field divergence increased. The increased potential drop resulted in the mean ion velocity (d) showing more significant ion acceleration in the rapidly diverging magnetic field test cases. This increased acceleration is due to the larger gradients of the magnetic field resulting in stronger forces on the electrons. An important point must be made here that although the larger gradients result in faster acceleration, these larger gradients can also result in a violation of the assumption that the magnetic field does not vary rapidly over an electron orbit.

As mentioned in the magnetic nozzle theory section, the acceleration due to the dipole force can also be represented by a potential $\Phi_b = \mu B$. If the magnetic moment is constant this implies that the particles will undergo more total acceleration the lower the magnetic field strength, as shown in the simulations. If collisions are ignored, the ion velocities should be the same at the same final magnetic field strength.

Future simulations should study the inclusion of magnetic mirrors at the edges of the heating regime. These mirrors could lead to very interesting physics due to them acting as a filter for the types of electrons which are allowed to escape the heating region. The effects of these magnetic field maxima could have interesting implications on the formation of potential structures. These structures could result in production of the different particle groups (trapped and free electrons and ions) typically seen in double layer formation.[134, 75, 64, 74] If inclusion of these structures results in a more dramatic potential drop, this could be a good indication of how to drive double-layer formation. There may also be a significant effect on the electron temperatures

(a) Electron density

(b) Ion density

(c) Potential

(d) Mean ion velocity
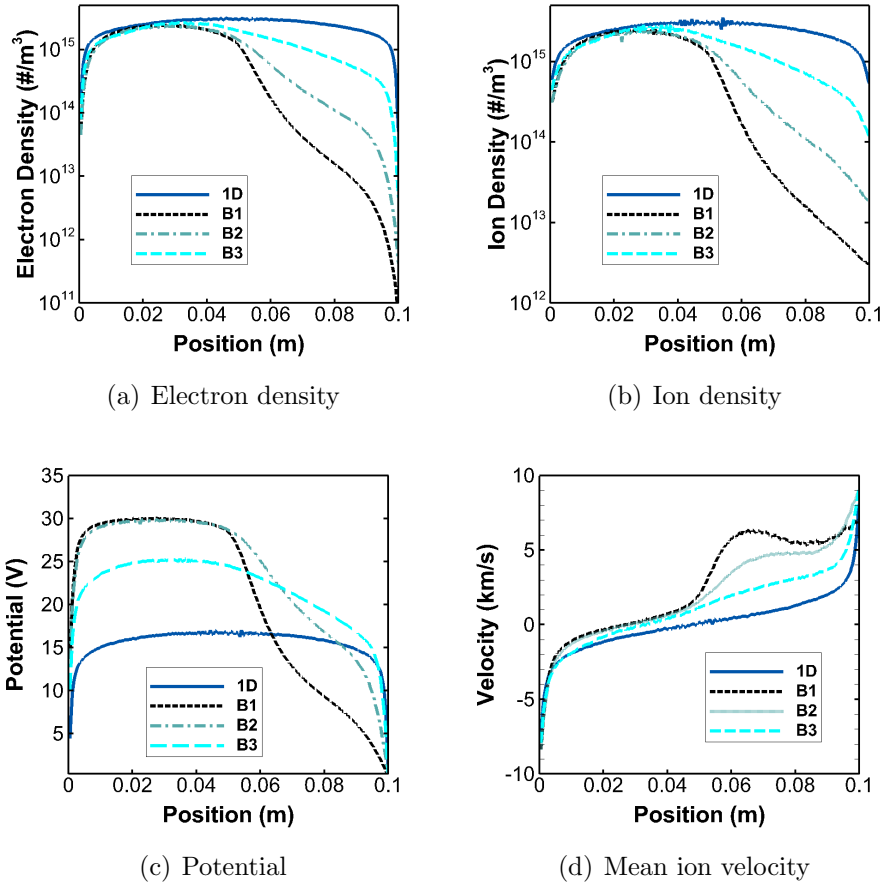
Figure 7.17: Effects of magnetic field topology on Q1D simulation results. B1 is most rapidly decreasing magnetic field while B3 is the slowest varying magnetic field.

and the positioning of the heating zone relative to the magnetic field structure could be very important.

7.7 Xenon Simulations

Simulations were also performed using xenon as the working gas. Xenon has a higher mass and lower ionization potential compared to argon. As such, it was expected that for the same source parameters the xenon velocities should be lower since it requires more energy to accelerate the heavy particles. However, the xenon densities should be higher because it requires less energy to ionize. The results of

these simulations is shown in Figure 7.18. Xenon ion densities are higher than the argon densities in all the simulations due to the lower ionization potential of xenon. The maximum potential in the heating region is also lower which results in a smaller potential drop. The lower potential drop combined with the higher mass of the ions leads to a much lower ion velocity overall for xenon.

(a) Ion density

(b) Potential

(c) Mean ion velocity

(d) Electron density
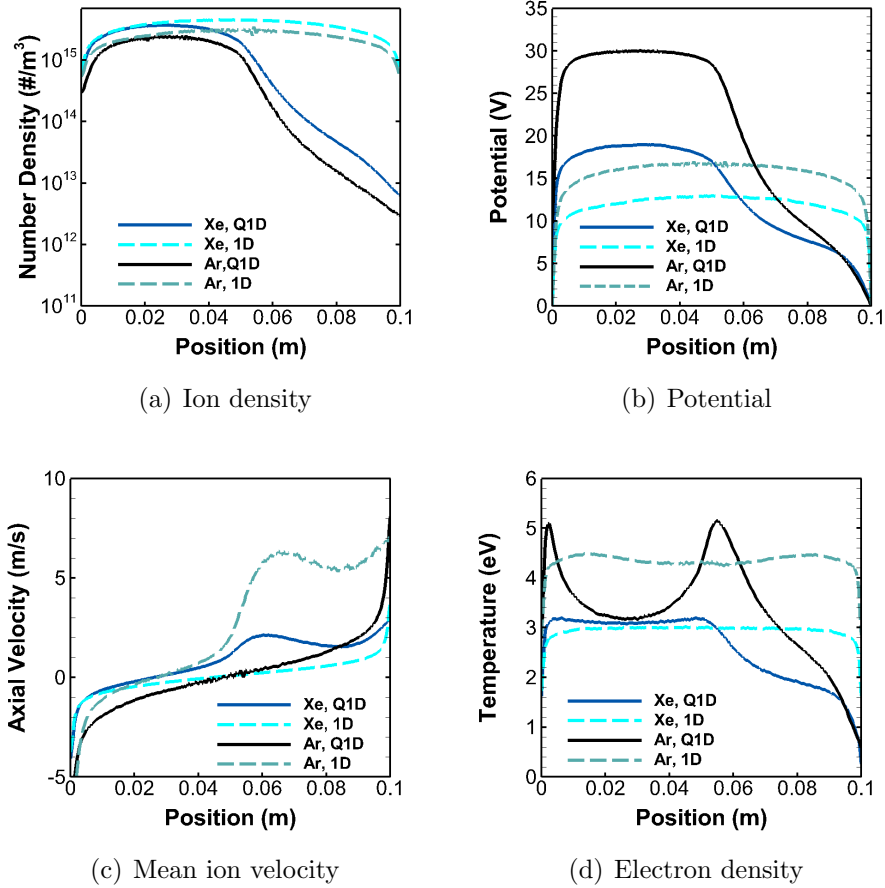
Figure 7.18: Q1D and 1D simulations comparing Xenon and Argon results.

The electron temperatures are also affected by the choice of neutral gas. The xenon simulations have consistently lower temperatures except near the sheaths. This is not a surprise because the equilibrium temperatures are highly dependent on the collisional behavior. Since xenon has a lower ionization potential the electrons will require less energy to begin to have ionization collisions. This lower threshold leads to more collisions, higher ion densities, and more energy loss from the electrons to the ion-

184

ization resulting in an overall lower electron temperature. The electron temperature peaks seen in the xenon simulations are not nearly as dramatic as those seen in the argon simulations which may be a result of the more gentle potential structure.

CHAPTER VIII

Analysis of Test Problem Physics

8.1 Introduction

This chapter will present further analysis of the results from the magnetic nozzle test problem. Data from the test problem simulations will be compared with kinetic theory, fluid theory, and thermodynamic relations. Simple techniques will also be used to illustrate ways to estimate thruster performance from simulation results. First some theory will be presented which will be used in this analysis. The theory will then be applied to the test problem results. Finally, thruster considerations are presented.

8.2 Plasmadynamics in Strong Magnetic Fields

In this section the dynamics of a plasma in a strong magnetic field will be discussed. [135] The treatment of the plasmadynamics presented in this section has been used to study a range of problems from gyration dominated space plasmas to magnetic nozzle plasma expansions. [48, 94, 64, 77, 135, 136, 137] The continuum equations of motion for plasmas can be significantly simplified in strong magnetic fields by assuming that the gyro-motion of the particles is a dominant feature in the dynamics and binds particles to a magnetic field line.[37, 68, 137, 138, 37, 135, 136]

This section summarizes these simplified equations and discusses their origin.

8.2.1 Kinetic Theory

Continuum equations are derived from the Vlasov equation with collisions shown below:

$$\frac{\partial f_\sigma}{\partial t} + \mathbf{c} \cdot \nabla f_\sigma + \frac{q}{m}(\mathbf{E} + \mathbf{v} \times \mathbf{B}) \cdot \nabla_c f_\sigma = \left(\frac{\partial f}{\partial t}\right)_{col} \tag{8.1}$$

In this equation f is the velocity distribution function, $\boldsymbol{c}$ is the velocity space, and the right hand side represents changes due to collisions. Moments $(1, c, c^2, ..)$ of this equation are taken over all velocity space to obtain the continuum conservation equations for properties such as the density $(n = \iiint f d\boldsymbol{c})$ and the mean velocity $\mathbf{u} = \iiint \mathbf{c} f d\boldsymbol{c}$.

All the equations shown in this section are derived from this kinetic perspective, implying that in the correct limit the quasi-1D kinetic model should reproduce the continuum equations. The continuum conservation equations are summarized below.

8.2.2 Continuity

Generally the conservation of mass equation can be written in the following form for each species (σ):

$$\frac{\partial n_\sigma}{\partial t} + \nabla \cdot (n_\sigma \mathbf{u}_\sigma) = \left.\frac{\partial n_\sigma}{\partial t}\right|_\sigma \tag{8.2}$$

In this equation n is the number density, u is the continuum mean velocity, and the right hand side represents the density change due to a source such as ionization collisions.

This equation can be integrated and simplified using Gauss' law to the following form:

$$\iiint \frac{\partial n_\sigma}{\partial t} dV + \oint (n_\sigma \mathbf{u}_\sigma) \cdot d\mathbf{A} = \iiint \frac{\partial n_\sigma}{\partial t} \Big|_\sigma dV \tag{8.3}$$

For plasma flow along a magnetic field this equation can be significantly simplified by assuming the plasma is constrained to a magnetic flux-tube. It is further assumed that the flow is symmetric in directions perpendicular to the magnetic field, eliminating changes to mass density due to flux perpendicular to the magnetic field line. This results in the following form in which A is the cross-sectional area of the flux-tube and s is the length along the field line.

$$\iiint \frac{\partial n_\sigma}{\partial t} dA ds + \oint n_\sigma u_{s,\sigma} dA = \iiint \frac{\partial n_\sigma}{\partial t} \Big|_\sigma dA ds \tag{8.4}$$

If it is further assumed that properties are constant over the cross section, the following form arises:

$$\int \frac{\partial n_\sigma}{\partial t} A ds + n_\sigma u_{s,\sigma} A \Big|_{s_1}^{s_2} = \int \frac{\partial n_\sigma}{\partial t} \Big|_\sigma A ds \tag{8.5}$$

The cross sectional area can also be replaced by the magnetic field strength knowing that $BA = constant$ leading to:

$$\int \frac{\partial n_\sigma}{\partial t} \frac{1}{B} ds + \frac{n_\sigma u_{s,\sigma}}{B} \Big|_{s_1}^{s_2} = \int \frac{\partial n_\sigma}{\partial t} \Big|_\sigma \frac{1}{B} ds \tag{8.6}$$

At steady state this equation implies that the mass flux in and out of a flux tube must be balanced by the source term. Furthermore, when there is no source term and the problem is at steady state the mass flux through a source tube is constant:

$$\frac{n_\sigma u_{s,\sigma}}{B} = constant \tag{8.7}$$

188

8.2.3 Momentum

The momentum equation can be written as:

$$n_\sigma m_\sigma \frac{D\mathbf{u}_\sigma}{Dt} = n_\sigma q_\sigma (\mathbf{E} + \mathbf{u}_\sigma \times \mathbf{B}) - \nabla \cdot \Pi_\sigma + R_\sigma \tag{8.8}$$

In this equation $\frac{D}{Dt} = \frac{\partial}{\partial t} + \mathbf{u} \cdot \nabla$ is the substantiative derivative, Π_σ is the pressure tensor, and R_σ is the collision tensor. The pressure tensor is defined below based on is the perturbation or random velocity (c').

$$\Pi_\sigma = m_\sigma \int \mathbf{c}'\mathbf{c}' f_\sigma d\mathbf{c}' \tag{8.9}$$

Typically it is assumed that the velocity distribution is Maxwellian and isotropic in all directions. This simplifies the pressure tensor by removing the off diagonal terms and simplifying the diagonal terms of the pressure tensor to the following form: $p = nkT$. For magnetized flow along a magnetic field line the pressure tensor may not be isotropic in all directions because the plasma can have different temperatures in the parallel and perpendicular magnetic field directions. This results in a pressure tensor of the following form: [135, 136]

$$\Pi_{jk} = p_\perp \delta_{ij} + (p_\parallel - p_\perp)\hat{B}_j\hat{B}_k \tag{8.10}$$

Substitution of this equation into the momentum equation leads to the following form for the direction along the magnetic field:

$$n_\sigma m_\sigma \frac{D\mathbf{u}_{\parallel\sigma}}{Dt} = n_\sigma q_\sigma (\mathbf{E}_\parallel) - \nabla_\parallel p_\parallel + \left(\frac{p_\parallel - p_\perp}{B}\right)\nabla_\parallel B + R_\sigma \tag{8.11}$$

The above expression looks like the typical one-dimensional momentum equation except with an extra term on the right hand side. The additional pressure term arises from permitting the flow to have anisotropic pressures relative to the magnetic field.

This pressure force accounts for the magnetic mirror force in a continuum description.
[68]

8.2.4 Energy Equation

Energy conservation is a more complex problem because it involves an additional moment of the distribution function. However a number of simplifications can be made to these equations. The simplest of these assumptions is that the gas is isothermal which implies that $T_\sigma = constant$, this is the case for a gas with infinite thermal conductivity. A more complex assumption is that of adiabaticity, or no heat flow in the plasma. This leads to following expression:

$$\frac{d}{dt}\left(\frac{p_\sigma}{n_\sigma^\gamma}\right) = 0 \tag{8.12}$$

In this equation γ is the ratio of the specific heats which is defined as $\gamma = \frac{N+2}{N}$ where N is the number of degrees of freedom in the plasma. A more general description is using a polytropic equation, in which γ is an arbitrary quantity.

For a collisionless plasma bound to a magnetic field line with the anisotropic pressure tensor defined in the previous section this adiabatic law changes to what is known as the double adiabatic law.[136, 135, 137] In the parallel direction the new adiabatic constraint becomes the following:

$$\frac{p_\parallel B^2}{\rho^3} = constant \tag{8.13}$$

And in the perpendicular direction becomes:

$$\frac{p_\perp}{\rho B} = constant \tag{8.14}$$

If none of these assumptions can be made the full energy equation must be considered which is shown below:

$$\frac{\partial}{\partial t}\left(\frac{Np_\sigma}{2}+\frac{m_\sigma n_\sigma u_\sigma^2}{2}\right)+\nabla\cdot\left(\mathbf{Q}_\sigma+\frac{2+N}{2}p_\sigma\mathbf{u}_\sigma+\frac{m_\sigma n_\sigma u_\sigma^2}{2}\mathbf{u}_\sigma\right)-q_\sigma n_\sigma\mathbf{u}_\sigma\cdot\mathbf{E}=-\left(\frac{\partial W}{\partial t}\right)_{E\sigma\alpha}$$

$$(8.15)$$

In the above equation N represents the dimension of random velocity. The velocity has been decomposed into mean u and random c' velocity according to $c = u + c'$. The heat flux Q used in this equation is defined below.

$$\mathbf{Q}_\sigma = \int \frac{m_\sigma \mathbf{c'}^2}{2}\mathbf{c'}f_\sigma d\mathbf{c'} \qquad (8.16)$$

The expression for the heat flux is typically closed by making an assumption about the physics.

8.3 Mass Flow in Simulations

The mass flow and its relation to the continuity equation gives interesting insight into the test problem. Mass flow rates were calculated with Equation 8.7 using RF cycle averaged data after the test problem had reached steady state for the Q1D test problem simulations. These simulations are independent of the cross section size (depend only on ratio of cross-sections), and for the simulation used the inlet cross section (which the rest of the areas are based on) was arbitrarily chosen to have an area of 1 m^2. Therefore, the flow rates presented herein are for a heating region with a cross-section of 1 m^2 and can be scaled to the desired cross-section. The only parameters which would have to scale with this in an actual simulation are the current density and macroparticle weight.

The resulting particle flow rates are shown in Figure 8.1 for the standard Q1D test problem and the problem with decreased neutral background density in the expansion region (DD). Both these simulations show a very interesting result of a constant slope
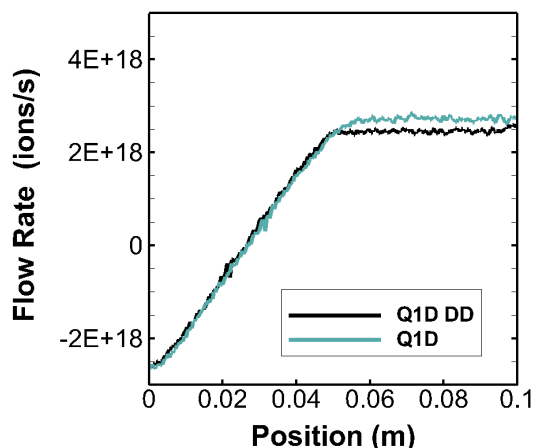
Figure 8.1: Flow rate calculations for simulation with constant background neutral density (Q1D) and decreased neutral density in the plume (Q1D,DD).

for the change of the mass flow rate in the heating region. The constant slope implies that $nvA|_1^2 = \int \frac{\partial n}{\partial t}|_s A dx = constant$. Therefore the source rate in the heating region is constant since in the heating region the area is a constant value. The resulting source rate is $\frac{\partial n}{\partial t}|_s \approx 10^{19} \frac{\#}{m^3 s}$.

In the expansion region the ion flow rate is constant for the case with reduced background density (Q1D DD), as expected, because there are few if any ionization collisions producing new particles. The case with constant background density (Q1D) shows a slight increase in the flow rate as the expansion begins due to energetic particles from the heating region moving outside the heating region and colliding with the high density neutral population. This soon levels off because there is no additional energy driving further collisions.

Analysis of the mass flow rate in the shortened heating region (Q1D,J) was also performed. The resulting flow rate compared to the longer heating region is shown in Figure 8.2. The shortened heating region shows a greater flow rate which agrees with the macroscopic properties shown in the previous chapter where the densities in the heating region were essentially the same, but the mean ion velocities were

192
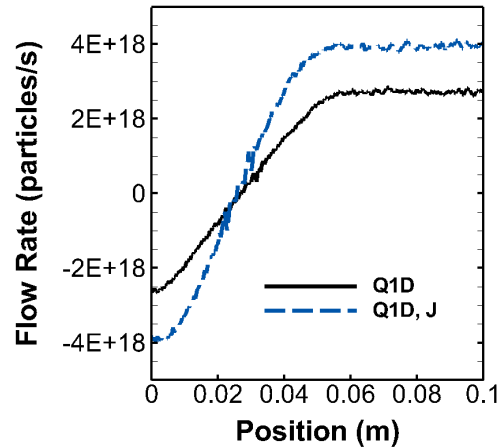
Figure 8.2: Mass flow rate calculations comparing normal length heating region (Q1D) and short heating region (Q1D,J)

higher. The implications of these results is peculiar because for this to occur a higher volumetric source rate is required for the shorter heating region even though the current density stays the same. This implies that the heating is more efficient for the shorter heating region. More efficient heating is also confirmed in the temperature plots of the previous chapter where higher temperatures are seen in the center of the heating region when the heating region is shorter. The shorter heating region had a constant, high temperature and showed no drastic decrease in temperature as was seen in the cases with a longer heating region. The presence of the higher temperature electrons may lead to more ionization. The increases in efficiency may also be attributed to isolating the heating region from the potential drops which occur at the wall sheath and at the beginning of the plasma expansion.

8.4 Ion Acceleration in Simulations

A simple analysis of the ion acceleration can be performed to determine what mechanism is accelerating the ions. The section illustrating the effects of the Q1D model already showed that inclusion of the magnetic field forces on the electrons is the
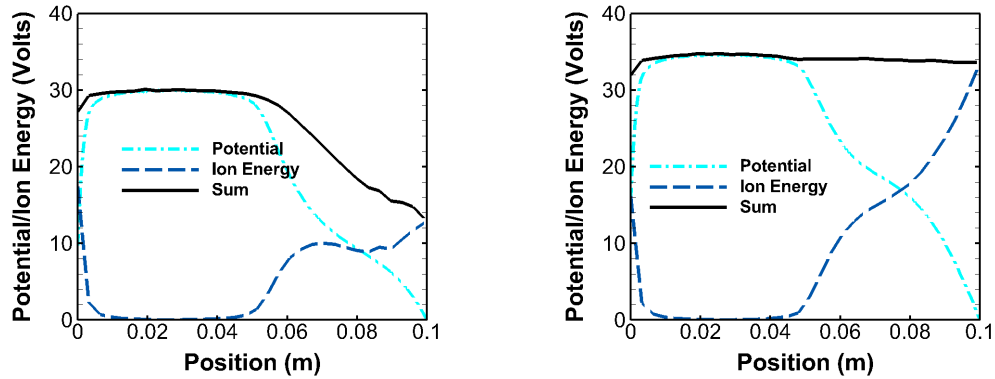
(a) Standard Q1D simulation.

(b) Decreased neutral density Q1D simulation.

Figure 8.3: Potential, ion energy, and summed total energy.

catalyst for generating a potential drop and ion acceleration in these low temperature plasmas. Here it will be shown that in fact the potential structure is the main mechanism accelerating the ions. Other mechanisms which could accelerate the ions include the direct acceleration due to the magnetic field forces. These magnetic field forces however are small for the cold ions. Figure 8.3 shows plots of the potential, ion energy, and sum of these values for the standard Q1D simulation as well as the decreased density Q1D simulations. The sum of the ion energy and potential should be constant in the case of a flow that is purely accelerated by the potential due to energy conservation.

The constant neutral background density simulations show generally that the ions are accelerated as the potential drops, but the ion energy and field energy do not follow each other directly as is shown in the decreasing total energy, implying there is another mechanism affecting the ion energies. The simulation with a decreased neutral density in the expansion region however shows a very strong correlation between the ion energy and the potential. The total energy stays nearly constant, implying that from the energy conservation standpoint the ions are just falling down the potential structure with other mechanisms only marginally affecting the ion dynamics. The

reason the constant neutral density simulation does not show this direct correlation is due to the energy losses that occur from charge exchange collisions with the high density neutral background.

The analysis in this section confirms that the main mechanism accelerating the ions in these low ion temperature and high electron temperature plasmas is the potential structure that is established in the plume as a results of the electron dynamics.

8.5 Electron Dynamics

8.5.1 Electron Random Energy

Evaluation of the electron dynamics was performed using simulations with a shortened heating region and a domain that is twice as long as the typical domain. This is done to better evaluate the electron dynamics in the expansion region and alleviate the effects of the heating region and wall sheaths on the expansion. Simulations with a constant neutral background density and a decreased neutral background density (DD) were performed.

The simplest assumption about the electron dynamics is to treat the electrons as isothermal. In these simulations it was found that this is not the case as shown in Figure 8.4. Non-isothermal electrons implies that the simple Boltzmann relation can not be used. For simulations with a constant neutral background density the temperature is nearly isotropic due to the electron neutral collisions redistributing the electron random energy as the plasma expands. The perpendicular temperature is slightly higher due to the heating in that direction. For the simulations with a decreased background neutral density it is found that the electron temperature is not isotropic. The perpendicular electron temperature decreases rapidly, followed by a slight increase in the far field as collisions begin to redistribute the electron energy. Non-equilibrium effects are clearly important in simulations with a low background
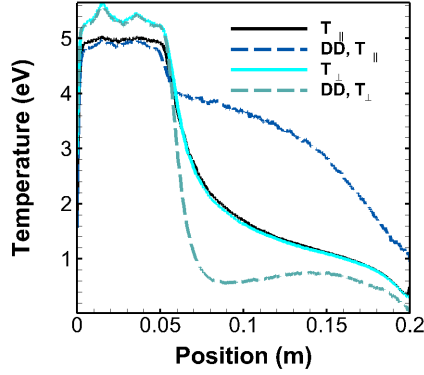
Figure 8.4: Electron temperature variation.

neutral density.

8.5.2 Electron Momentum Equation

In the study of plasmas, assumptions are often made about the electron dynamics to simplify the description of the plasma. These assumptions include ignoring the electron inertia or assuming that the electron motion is fast, resulting in the electrons essentially being in equilibrium. Either of these assumptions results in the left hand side of Equation 8.11 being ignored. The right hand side can then be solved for the electric field and serves as an Ohm's law for the plasma. The resulting equation is shown below.

$$E_\parallel = -\frac{\nabla_\parallel p_\parallel}{n_e e} + \frac{\left(\frac{p_\parallel - p_\perp}{B}\right)\nabla_\parallel B}{n_e e} + \frac{R_\sigma}{n_e e} \qquad (8.17)$$

Ignoring the collisional term, Equation 8.17 gives a simple expression for calculating the electric field required for electron equilibrium based on the electron density, electron temperatures, and magnetic field topology. This expression was evaluated using the continuum properties from the simulation results and compared to the electric field outputs. The results are shown in Figure 8.5.

The first figure (a) shows the analytically calculated electric field as well as the
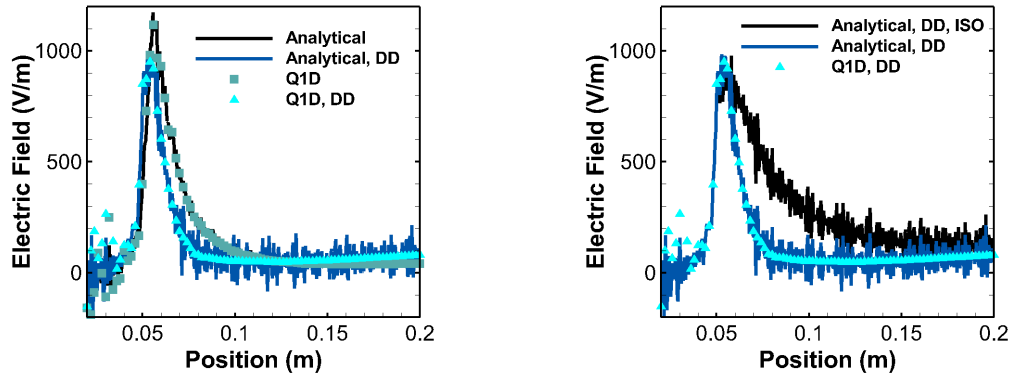
(a) Standard Q1D simulation and decreased plume neutral density simulation (Q1D DD) results

(b) Comparison between isotropic and non-isotropic (pressure) calculation for electric field.

Figure 8.5: Electric field calculated from Ohm's law.

electric field from the simulations for two test cases: the constant neutral density (Q1D) and a decreased background neutral density in the plume (Q1D DD). Both of these results show excellent agreement between the analytical and simulation electric field. The second figure (b) shows a comparison between the electric field calculated from assuming an anisotropic and isotropic (ISO) pressure for the test case with a decreased neutral background density. It is clear from this comparison that the effect of the anisotropic pressure is important in the problem with few collisions in the expansion region. For the standard problem with no density decrease the effects of this term become negligible because the pressure is nearly isotropic due to collisions.

This section reveals a very important result. The electron dynamics can be significantly simplified. In the case of a flow with few collisions in the expansion region anisotropic pressure effects must be included. This conclusion agrees with earlier experimental results. [139]

An important point to stress about the analysis in this section is that the temperatures and pressures used in this analysis were not found by assuming Maxwellian distributions, they were found by using the kinetic description where the pressure represents the flux due to random motion while the temperature represents the mean
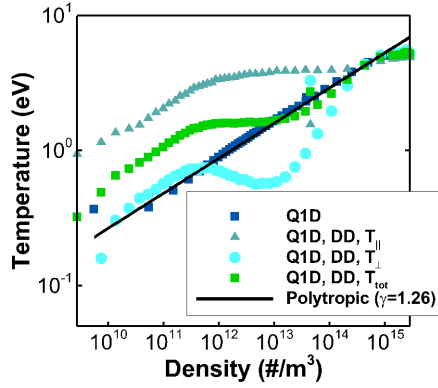
Figure 8.6: Evaluation of adiabatic and polytropic equations.

random kinetic energy.

8.5.3 Electron Energy Equation

The energy equation can be analyzed by studying the electron thermodynamics. Thermodynamics assumes that the plasma is in equilibrium locally, which in the previous chapter was shown may not be a good assumption for the electrons in the magnetic nozzle expansion region. This is evidenced in the non-Maxwellian and potentially bi-Maxwellian velocity distributions seen for the electrons in the expansion region. This section however will attempt to use existing theories which assume equilibrium for the electrons in order to get simple relationships for the electron temperature as the plasma expands. This is essential to closing the equations needed so solve for the ion motion.

The electron thermodynamics was evaluated by first investigating if the adiabatic or polytropic conditions were satisfied. This was investigated by examining the relationship between the density and temperature of the electrons as shown in Figure 8.6. Results are plotted for the constant and decreased neutral density simulations. The axes are plotted on a logarithmic scale. If the polytropic relationship from Equation 8.12 is satisfied, regions of a constant slope equal to $\gamma - 1$ should appear on this plot.

For the case of a constant neutral background density, the polytropic equation with $\gamma = 1.26$ shows good agreement for the bulk of the expansion. This exponent implies a non-adiabatic plasma expansion. The reason the adiabatic condition may not hold in these simulations is because of the presence of heat flux in the axial direction for both parallel and perpendicular kinetic energy. The heat flux was evaluated in the simulations and non-negligible values were found.

The results for cases with a decreased background neutral density (DD) show complex behavior. A constant slope for the entire domain can not be found, although there are interesting regions where the slope appears to be nearly constant. Regions with similar slopes are seen for the parallel and perpendicular temperatures.

An additional simulation was performed with a more slowly decreasing magnetic field (B3 from the previous chapter) to investigate whether the polytropic coefficient found in the constant neutral background density simulation depends explicitly on the magnetic field profile. Interestingly, it was found that the polytropic coefficient had approximately the same value ($\gamma = 1.26$).

Evaluation of the double adiabatic conditions were also performed. These conditions were not found to be satisfied in either of the simulation test cases. The reason for this is because of the presence of both collisions and heat flux in the axial direction in the plume. Equivalent polytropic laws should be considered to replace the double adiabatic laws and may have more success.

8.5.4 Electron Velocity and Energy Distribution Functions

The electron velocity and energy distribution functions were determined to evaluate the non-equilibrium nature of the plasma. The axial variation of the distribution functions for the constant neutral background density simulations are shown in Figure 8.7. For these simulations the axial and transverse velocity distribution functions show very similar behavior due to the presence of a high neutral background density
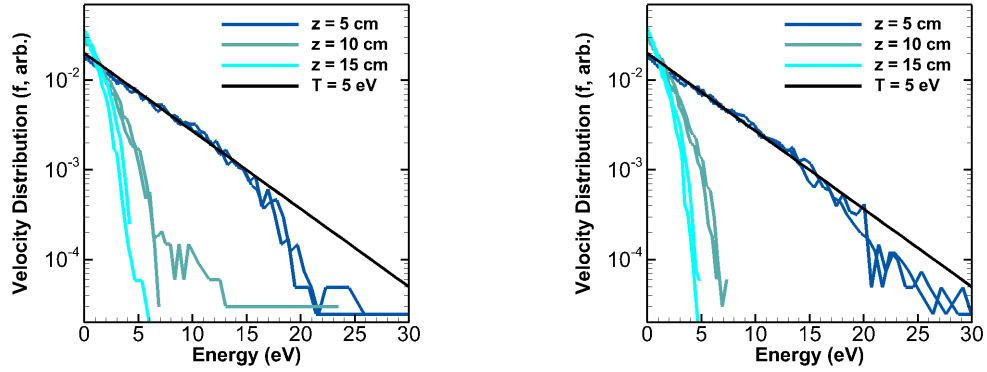
(a) Axial velocity distribution functions.

(b) Transverse ($\hat{x}$) velocity distribution functions.
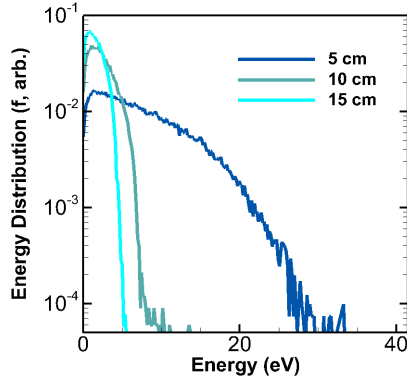
(c) Energy distribution function.

Figure 8.7: Variation of electron distribution function spatially for constant neutral background density.

with which the electrons collide, leading to an isotropic distribution. At the edge of the heating region (5 cm) the distribution is nearly Maxwellian (linear with a single slope) with temperature around 5 eV in both directions. As the plasma expands the energy of the electrons is reduced and the distribution becomes more non-Maxwellian implying that single slope can not be used to characterize the velocity distribution. The energy distribution shows similar behavior. The electron energy is reduced as the plasma expands and the electrons are slowed down by the potential drop.

The distribution functions for the simulations with a reduced neutral background density in the expansion are shown in Figure 8.8. The axial velocity velocity distri-

bution (a) is nearly Maxwellian with a temperature of 5 eV at the edge of the heating region (5 cm). As the plasma expands the low energy particles remain characteristic of a 5 eV distribution while the high energy particles are lost. The distribution in the transverse direction shows a much different structure. The distribution at the edge of the heating region is characteristic of a 5 eV Maxwellian. The distribution changes drastically as the plasma expands. A large population of particles is seen at very low energies (sharp peak at low energy), this is followed by a distribution that is appears nearly Maxwellian with a temperature of 1.75 eV. The distribution remains nearly constant between 10 cm and 15 cm. The energy distribution function shows that the energy is reduced overall as the plasma expands and falls down the potential drop.

8.6   Predictions of Thruster Performance Parameters

The results from this study can be used to estimate some basic thruster performance parameters such as specific impulse and thrust using the test problem as an example.

8.6.1   Specific Impulse

Specific impulse (I_{sp}) can be estimated by looking at the maximum velocity the ions achieve before they reach the edge of the boundary sheath. The resulting velocities for the standard test problem and the test problem with reduced neutral density in the plume are $v_{ex} = 6.25 \ km/s$ and $v_{ex} = 8.12 \ km/s$ respectively. These correspond to specific impulses of 640 seconds and 830 seconds respectively. The reduced specific impulse for the high background density case is explained by losses due to collisions with the neutrals highlighting a potential loss mechanism for these devices. These specific impulses are reasonable considering the current predictions for devices which use this type of electron-driven ion acceleration. [30, 28, 22, 140]
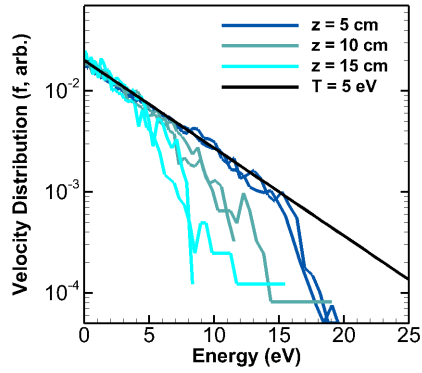
(a) Axial velocity distribution
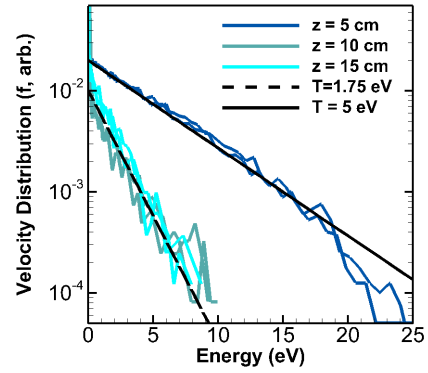
(b) Transverse ($\hat{x}$) velocity distirbution
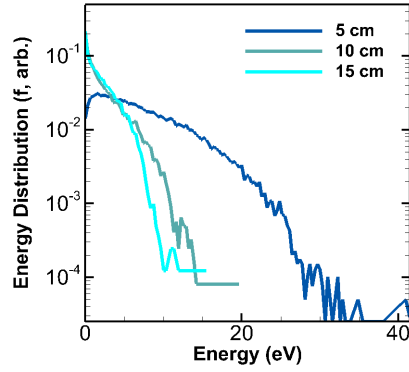
(c) Energy distribution

Figure 8.8: Variation of electron distribution function for decreased neutral background density in the expansion region.

8.6.2 Thrust

The mass flow rate was calculated in this chapter and was shown to be constant in the expansion region. This mass flow rate can be used along with the exhaust velocity of the section above to determine a prediction for thrust ($T = \dot{m}v_{ex}$). As outlined in the mass flow rate section, the numbers given were for a heating section with an area of 1 m^2. These simulation results are independent of cross-section area and can be scaled to the area of a desired device.

For a hypothetical device with a plasma cross section of 10 cm^2 the flow rate in Figure 8.1 scales to 2.5×10^{17} $particles/s$ or a mass flow rate of 0.0165 mg/s. This results in a thrust of 0.103 mN and 0.134 mN which are reasonable numbers for a device with such low densities in the heating region. Many current devices strive for densities a few orders of magnitude above those reported in the test problem.

An important point to make in this section is that the thrust in this device is generated by the magnetic force on the electrons which drives the ion acceleration. Forces on the magnetic dipole moments of the electrons are balanced by forces on the magnets of the devices.

8.6.3 Validity of Predictions

The predictions of specific impulse and thrust in this section are very much a simplification of the effects in an actual thruster. The long range forces due to the magnetic field make this a more complex issue to tackle because ion acceleration occurs until the particles are no longer affected by the magnetic field. In the case of Q1D simulations the particles are always affected by the field so the maximum, or asymptote of the velocity makes the most sense to use as a parameter. Predictions of specific impulse are further complicated by the losses which occur due to collisions in the plume. When these collisions occur the specific impulse can be defined by either the beam velocity or the mean velocity. Efficiency losses due to plume divergence are

also not taken into account. Therefore, these estimates can serve as an upper bound
for the predicted performance.

CHAPTER IX

Device Simulations

9.1 Introduction

In this section simulations are compared with a current helicon thruster, the HDLT.[3] Basic operating parameters for this device are summarized in Table 9.1 below.[30]

Table 9.1: Characteristic parameters for helicon double layer thruster.

Parameter	Value
Source Tube Length	≈ 28 cm
Antenna Length	≈ 18 cm
Maximum Magnetic field	≈ 138 Gauss
Maximum Density	$\approx 2 \times 10^{17}$ #/m^3
Electron Temperature	5.5 eV
Heating Frequency	13.56 MHz
Background Neutral Pressure	53.3 mPa
Gas	Argon

Simulations were performed to strive to recreate these parameters and the physics seen in the HDLT plume. Some simplifications to the problem were made to ease the computation. The simulation setup is outlined in the next section, followed by the results, and then a discussion.

9.2 Simulation Setup

The simulation was performed over a $0.6\ m$ long domain with grounded boundary conditions. The heating region is 12 cm long (slightly shorter than the antenna length) and is applied from $z = [0.065, 0.185]\ m$. The heating region was shortened compared to the antenna to eliminate some interaction of the heating region with the wall sheath and the expansion region. The magnetic field is constant from $z = [0.0, 0.25]\ m$ after which it begins to decrease with a profile similar to that in the experiments. The domain is initially seeded with a population of ions and electrons ($n_{init} = 8 \times 10^{15}\ \#/m^3$) in the constant magnetic field strength region to enable the discharge to start. The simulation parameters are summarized in the Table 9.2 below.

Table 9.2: Parameters for helicon double layer thruster simulation.

Parameter	Value
Domain Length	0.6 m
Number of Cells	$9,000$
Heating region length	12 cm
Heating Current	$800\ A/m^2$
Heating Frequency	13.56 MHz
Time Step	2.5×10^{-11} seconds
Total Time	8×10^{-5} seconds
Background Neutral Pressure	40.4 mPa
Gas	Argon
Particle Weight	10^9 Particles/macro-particle

The magnetic field used in the simulation is shown in Figure 9.1. The simulation magnetic field in the expansion region is applied using a current loop and the magnetic field is assumed to be constant in the heating region for simplicity.
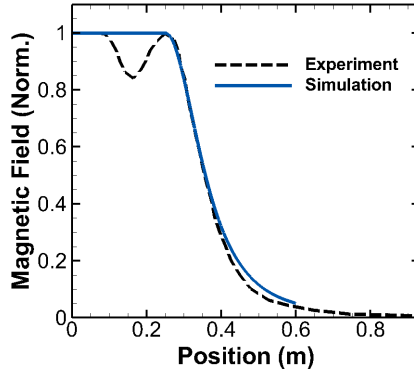
Figure 9.1: Magnetic field in simulation and experiment. Normalized by maximum magnetic field.

9.3   Results

9.3.1   Continuum Properties

HDLT simulation results are presented in this section. The results for the electron number density are shown in Figure 9.2. The simulation results are still a factor of five below the experimental results. Higher densities can be achieved by increasing the current in the heating region. The additional increase in density however comes at a much higher computational cost. The simulation results presented herein ran for 48 hours on 200 processors (9600 CPU-hours). The additional cost for scaling to the appropriate densities can be estimated by considering that at least twice as many grid points, half the time step, and five times as many particles will be required, resulting in at least a factor of 10 increase in computational cost. It is important to stress that the computational costs are the limiting factor not the methodology, future simulations with additional simulation resources can scale up to the densities required for the full thruster simulations.

Normalized density profiles are also shown in Figure 9.2 to compare the profiles. The normalized densities show excellent agreement until about 0.4 m after which the simulation results continue to decrease while the experimental results level off. The
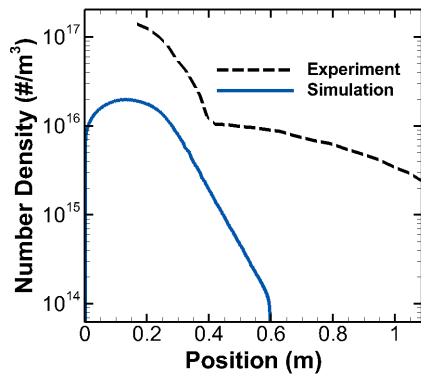
(a) Electron number density in simulation and experiment on a lograithmic plot.

(b) Normalized electron number density in simulations and experiment on a logarithmic plot.
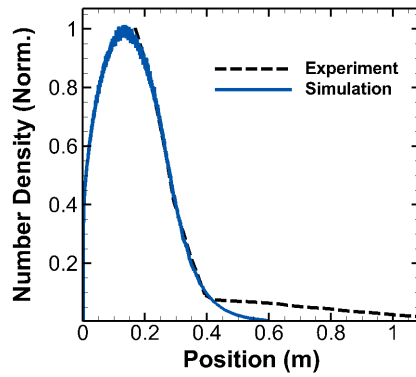
(c) Normalized electron number density in simulations and experiment.

Figure 9.2: Comparison of electron density profiles with experiments.
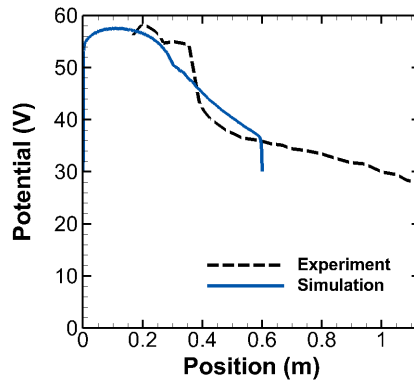
Figure 9.3: Potential in simulations and experiments.

leveling off of the density in the experiment might be attributed to plasma beginning to interact with the chamber walls or the violation of the magnetization assumptions (caused by detachment) made in the Q1D model .

The simulation results for the potential are shown in Figure 9.3. The simulation potential maximum is made to coincide with the experimental maximum. This is necessary because the potential is referenced from different values in the simulation and experiment. Simulation results do not show a sharp potential structure similar to a double layer which was seen in the experiment and instead show a gradual decrease in the potential more characteristic of an ambipolar field. The total potential drop however is very similar at 0.6 m. This difference may be attributed to the different magnetic field profiles used. Incorporation of a magnetic mirror in the heating region could have a profound effect on the potential structure.

The mean ion velocity and temperature profiles obtained in the simulation are shown in Figure 9.4. These profiles are similar to those seen in the test problems of the previous sections and the ion velocity shows a gradual increase over the long potential drop. The maximum mean ion velocity from the simulations was found to be around 5 km/s. The maximum electron temperature in the simulations was found to be around 5 eV which decreases as the plasma expands. The maximum simulation

(a) Mean ion velocity   (b) Electron temperature
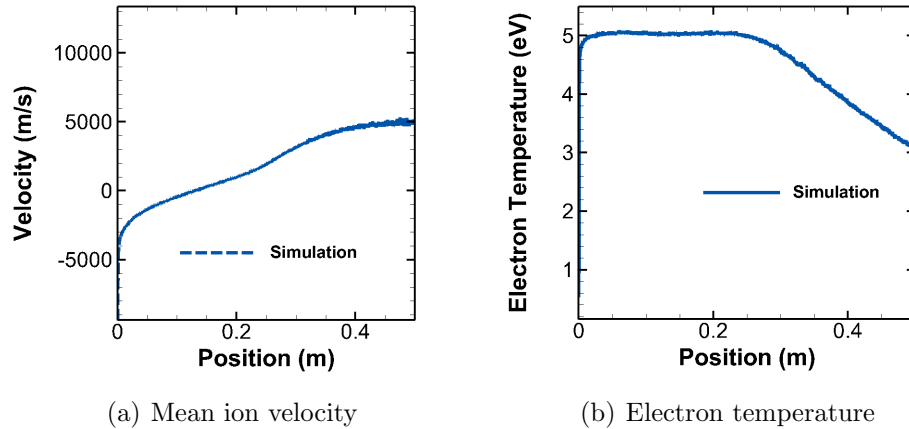
Figure 9.4: Mean ion velocity and electron temperature in simulations.

temperature is similar to the experimental result of 5.2 eV.[30] However, West et al. suggest that the electron temperature is constant throughout the domain, which is contrary to the simulations results. No explicit temperature profiles are shown in the experimental results.

9.3.2   Thermodynamic Considerations

The polytropic relation was evaluated in the HDLT expansion region to see if similar results are found to those seen for the magnetic nozzle test problem with a constant neutral background density. The variation of the electron temperature with the electron number density is shown in Figure 9.5. A linear region is seen on the log-log plot which agrees with a polytropic coefficient of $\gamma = 1.17$. This polytropic coefficient is very similar to that found by Little [48] but is different from that found in the magnetic nozzle test problem ($\gamma = 1.26$).

9.3.3   Velocity and Energy Distribution Functions

The ion and electron velocity and energy distributions were evaluated for further insight into the problem. The results for the ion velocity distribution function at 42 cm are compared to those of the experiment in Figure 9.6. The simulation distribution
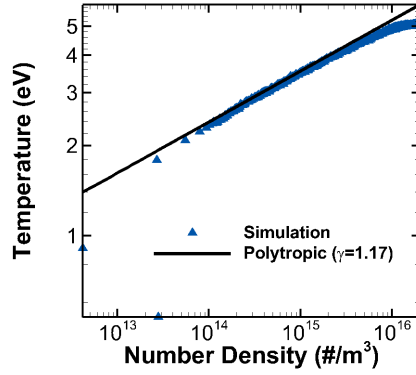
Figure 9.5: Variation of electron temperature with electron number density and comparison with polytropic law.
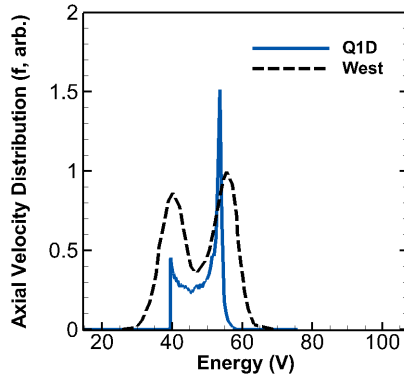
Figure 9.6: Ion axial velocity distribution in simulations and experiments.

function is shown with energy units and is offset by the plasma potential measured in the experiments to compare results.

The ion velocity distribution results show similar trends. The peaks of the beam are near the same value and a large low energy peak of charge exchange particles is seen. The simulation results are sharper and the charge exchange peak smaller. This may indicate that larger neutral densities should be used in part of the simulation domain to broaden the peaks and increase the fraction of low energy particles. The maximum beam velocity was around 10 km/s (at 54 cm) in the simulations. The maximum mean ion velocity and the maximum beam velocity are consistent with the results found in the experiment.
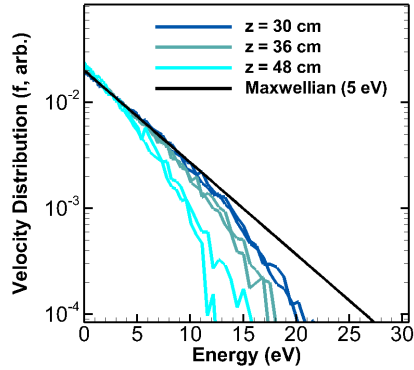
(a) Axial velocity distribution.
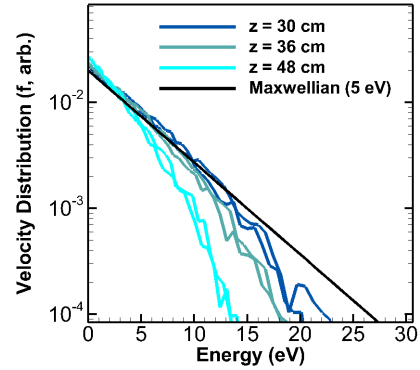
(b) Transverse ($\hat{x}$) velocity distribution.
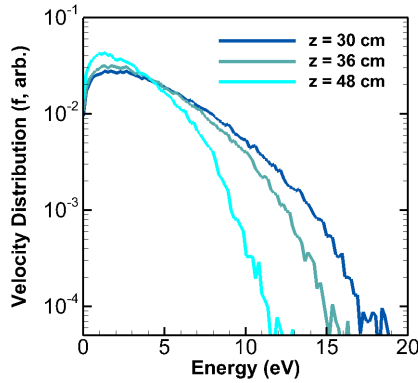
(c) Energy distribution.

Figure 9.7: Comparison of electron velocity and energy probability distribution.

The spatial variation of the electron energy and velocity distribution functions are shown in Figure 9.7. For reference, the point $z = 30$ cm is just outside the constant magnetic field region. The axial and transverse velocity distributions show similar behavior due to the effects of collisions with the high density neutral background. These collisions cause the distribution to be nearly isotropic and redistribute the electron energy as the plasma expands. The velocity distributions also show characteristics of non-Maxwellian distributions as the plasma expands. The energy distribution shows the decrease in the electron energy as the plasma expands and falls down the potential structure. These results are similar to those seen in HDLT experiments which measure the electron energy distribution functions. [141, 142]

9.4 Discussion

Results from the HDLT device simulations are encouraging and show promise of yielding useful insight into the physics. Computational costs are currently limiting further study to higher densities. Simulations presented in this chapter ran for approximately 48 hours on 200 processors (9600 CPU-hours). Tweaking of the parameters used in the simulation are also under way to better match the experiments. Some parameters, such as the neutral density profile in the simulation are unknown and can have profound effects on the simulation results.s

CHAPTER X

Conclusion

10.1 Summary of Work

This work has made contributions to the study of magnetic nozzle physics and more generally the study of magnetic field guided plasma expansions in a number of ways. A thorough study of the operating regimes of current magnetic nozzle thrusters was performed as well as a review of the important physical processes in these devices. The physics for the thrust generation process in magnetic nozzles was outlined and summarized.

A novel quasi-one-dimensional technique for the simulation of magnetic field guided plasma expansions was developed in order to study these important processes in a magnetic nozzle. Two-dimensional effects due to the magnetic field were incorporated in a conventional PIC scheme. This technique was added to a new, parallel PIC code with Monte-Carlo collisions to self-consistently model a magnetic nozzle device from the source region to the expansion.

The Q1D formulation was verified with a newly developed set of test cases which include simple problems to compare with theory (two particle motion and magnetic mirrors) and direct comparison with fully two-dimensional simulations. These test problems will be valuable for verifying future implementations of the model. Furthermore, the Q1D method showed that it is capable of consistently capturing two-

dimensional physics making it a powerful tool for future kinetic simulation of magnetized plasmas without incurring the costs of fully two dimensional simulations.

A test problem of an RF discharge with a magnetic nozzle was also studied. The Q1D model results were compared to purely one dimensional results to illustrate the importance of the two-dimensional effects. Studies on the effects of varying the heating region, magnetic field topology, gas species, and background neutral density were performed to determine the effects on ion acceleration and electron dynamics. Results from these simulations give valuable insight on magnetic nozzle plasmadynamics in the Q1D limit. Simple analyses were performed to make rough estimates of thruster performance parameters in the magnetic nozzle test problem. Insights into magnetic nozzle physics for low-density, low temperature plasmas were gained. Ion acceleration was shown to be caused by induced electric fields. The induced electric fields form in response to the magnetic field forces which accelerate the hot electrons away from the magnetic nozzle throat. These induced electric fields were found to be consistent with theory which takes into account anisotropies in the electron pressure tensor. When few collisions are present in the plume the electron temperature was shown to be highly anisotropic. A decreasing perpendicular temperature occurs due to the magnetic field forces re-directing the perpendicular electron energy into the parallel direction as the electrons expand. The thermal energy lost by the electrons is ultimately gained by the ions through the potential structure which is formed. These simulation results illustrated the need for kinetic simulations of these devices. The presence of bi-Maxwellian or non-Maxwellian distributions as well as anisotropic temperatures were seen in the magnetic nozzle expansions with low background neutral densities. Simulations with high background densities had isotropic temperatures, but still showed bi-Maxwellian or non-Maxwellian distributions. Non-equilibrium effects were clearly shown to be important.

Simulations were performed of the HDLT device which show encouraging results

for using this code to study full devices in the future. These simulations were limited to lower densities than those in the actual device (by factor of 5) due to computational costs. Results from these simulations were consist with many of the data from experiments.

10.2 Future Work

Continuing work on these methods and the study of magnetic nozzle physics is summarized in this section. The areas which will be highlighted are method improvements, additional test problems, and future device simulations.

10.2.1 Model Improvements

A number of improvements can be made to the methods used in this thesis. The first recommendation would be to investigate additional RF heating mechanisms. While the mechanism used in this method worked well it is not adapted well to an axisymmetric problem. Additional effects of heating mechanism on the simulation results can also be investigated, such as including an oscillating field in both of the perpendicular directions, not just one. The scheme presently implemented averages the currents over the whole heating region. Additional tests can be performed with currents that are evaluated cell by cell instead to better capture local heating.

Further improvements to the code in general include the use of implicit schemes for the the particle movers. This would enable significantly larger time steps and cells to be used which would reduce the computational cost.[111] The challenge with this is incorporating the Q1D method in the currently existing implicit schemes. Non-uniform mesh algorithms can also be implemented to take advantage of the decreased densities in the plume by increasing the grid size as the Debye length increases.

The code can also be improved by time centering of the velocities of loaded particles. An algorithm for loading and injection of general distributions should also be

implemented using acceptance-rejection sampling.

Generally the code should be optimized further to improve performance using profiling software and eliminating some of the inefficiencies in the code. There is significant room for improvement in this area.

10.2.2 Additional Test Problems

Simple test problems further investing the physical implications of this model should be performed. One of the first tests which should be performed is an RF source including magnetic mirrors at the edge of the heating region. This can have significant implications on the device performance as some particles are trapped in the heating region. The mirrors also limit the flux of some particles, which will have implications on the potential structures which form. These simulations were attempted in this work, but satisfactory results were not obtained. The heating region was a particular problem here because it was not adapted well to the cylindrical geometry.

Coulomb collisions were also incorporated in this model, but for many of the simulations investigated they were not important. Future work at higher densities should investigate the effects of Coulomb collisions further. Different Coulomb collision algorithms should also be considered.[132, 133] The algorithm chosen for the code used in this work was selected because it depended on the grid and did not require particles to be paired in cells. This decision was made based on the synergy with the parallelization scheme.

10.2.3 Device Simulations

Further device simulations should be investigated to validate the model. Simulations of the HDLT were ambitious due to the size of the device ($\approx 1\ m$) and the large disparity in densities in the problem. This made this problem extremely computationally intensive and did not allow for as much iteration as necessary. Smaller

217

device simulations such as the CubeSat Ambipolar Thruster or the PHDLT may serve as a better platform to validate this model. [22, 28] Simulations of gyration dominated plasma in astrophysics could also serve as an application for this model and allow for validation. There may also be data from the semi-conductor industry of low temperature plasmas guided by magnetic field which can be used for validation.

APPENDICES

APPENDIX A

Magnetic Nozzle Parameters

A.1 Magnetic Nozzle Relevant Parameters

The non-dimensional numbers for the important physical mechanisms in magnetic nozzles are highlighted in the Table A.1 below. The regimes in which they are important are highlighted by the given inequality. The parameters should be placed on the left hand side of the inequalities of the table. It is important to note that many of the non-dimensional numbers are based on arbitrary characteristic lengths of the system which is why some of the ratios do not have a numerical value associated with them and should be used qualitatively instead. For example, increasing R_m will decrease the effects of resistive diffusion on detachment. All conditions presented are necessary, but not sufficient conditions for these mechanisms to be relevant.

A.2 Magnetic Nozzle Experiments

Table A.2 below shows a compilation of experiments which have studied magnetic nozzles. This table is not an exhaustive list, but outlines the general parameter regimes in which some typical magnetic nozzle experiments operate. The parameters

Table: Ion Acceleration Mechanisms and Currents

	Dipole	Magnetic Reynolds	Pressure Ratio	Thermal Velocity Ratio	Ion Collision Hall Parameter	Electron Collision Hall Parameter	Ion Fluid Hall Parameter	Electron Fluid Hall Parameter
	$r_L\|\nabla B\|/\|B\|$	$R_m = UL/\eta$	$\beta_p = \frac{nk_BT}{B^2/2\mu_0}$	$\frac{v_{th,e}}{v_{th,i}} = \sqrt{\frac{T_e m_i}{T_i m_e}}$	$\Omega_{col,i} = \frac{\omega_{ci}}{\nu_i}$	$\Omega_{col,e} = \frac{\omega_{ce}}{\nu_e}$	$\Omega_{f,i} = \frac{\omega_{ci}}{\omega_f}$	$\Omega_{f,e} = \frac{\omega_{ce}}{\omega_f}$
Magnetization	≤ 1	-	-	-	≥ 1	≥ 1	≥ 1	≥ 1
Directing Thermal Energy	-	$\gg 1$	≤ 1 & $\gtrsim 10^{-3}$	-	-	-	-	-
Hall Effect	-	-	-	-	≤ 1	≥ 1	≤ 1	≥ 1
Thermoelectric	-	-	-	≥ 1	-	-	-	-

Table: Detachment Mechanisms

	Demagnetization	Magnetic Reynolds	Recombination & Fluid Frequency Ratio	Alfvén Mach and Kinetic β	Lundquist Number	Hybrid r_L Mass	Hybrid r_L Magnetization
	$r_L\|\nabla B/B\|$	$R_m = UL/\eta$	ν_{ei}/ω_f	$M_A^2 = \frac{U^2}{V_A^2}$, $\beta_f = \frac{\rho u^2/2}{(B^2/2\mu_0)}$	$S = \frac{V_A L}{\eta} = \frac{BL}{\eta\sqrt{\mu_0\rho}}$	$G^{-1/2}\|\nabla B/B\|$	$r_{L,h}\|\nabla B/B\|$
Resistive Diffusion	-	$\lesssim 1$	-	-	-	-	-
Recombination	-	-	≥ 1	-	-	-	-
Adiabaticity	≥ 1	-	-	-	-	-	-
Inertial	-	-	-	-	-	≥ 1	≥ 1
Induced Field	-	$\gtrsim 1$	-	≥ 1	-	-	-
Current Closure	-	-	-	-	-	-	-
Magnetic Reconnection	-	$\lesssim$	-	-	$\lesssim$	-	-

Table A.1: Top: Relevant regimes for energy conversion mechanisms. Bottom: Relevant regimes for detachment mechanisms.

shown are calculated using equations from the Naval Research Lab formulary[130] and the work of Braginskii.[143] Intermediate field strength length scales are found by $\sqrt{r_L\lambda_{mfp}}$ where λ_{mfp} is the mean free path. The values shown are found from a single measurement point nearest the nozzle throat on the centerline with some of the quantities approximated. The parameters can vary by an order of magnitude or more through the rest of the plume. Brief comments about each experiment are given in the following below:

1. **Super-sonic plasma wind tunnel:** Experiment by Andersen which first demonstrated the generation of a supersonic flow with a converging-diverging magnetic nozzle.[18]

2. **Variable Specific Impulse Magnetoplasma Rocket:** The VASIMR experiment heats ions by Ion Cyclotron Resonance Heating (ICRH) which then enter a magnetic nozzle. Energy conversion by the conservation of the adiabatic invariant and ambipolar acceleration has been shown for Helicon only mode. [25, 32, 66, 33, 144] Evidence of detachment has been observed and the responsible mechanism is currently being determined. [61]

3. **CubeSat Ambipolar Thruster:** CAT is an electrodeless thruster which incorporates a magnetic nozzle being developed at PEPL. [22] This device is in

the early stages of testing, but shows great promise for being the first flown magnetic nozzle thruster.

4. **Helicon Double Layer Thruster:** The Helicon Double Layer Thruster (HDLT) produces plasma by a helicon source which expands into a magnetic nozzle configuration. [3, 26, 30] Energy is transfered to the ions by the formation of a current-free double layer. Detachment is predicted due to ion demagnetization.

5. **Permanent Magnet Helicon Double Layer Thruster:** The Permanent Magnet Helicon Double Layer Thruster (PM-HDLT) generates plasma through a helicon source and the expansion is controlled by a permanent magnetic magnetic nozzle.[27, 28, 141, 84] Energy is transfered to the ions through the thermoelectric effect. This experiment separately measures the total force on the propulsion device and the force on the permanent magnets thereby quantifying the thrust due to electromagnetic effects.

6. **Kuriki Arc Heater:** The Kuriki Arc Heater (KAH) experiment studies the flow of an arc heated plasma in a converging-diverging magnetic nozzle.[19] The plasma is shown to be significantly accelerated by both thermoelectric field forces and thermal energy directionalization. An energy equation is suggested that couples ion and electron energies through the electric potential. Detachment is not significantly addressed.

7. **York Θ-Pinch:** The York Θ-Pinch experiment studies the flow of a Θ-pinch plasma with a magnetic nozzle configuration.[41] A converging-diverging configuration was studied which generates supersonic velocities and demonstrates choking. Measurements of electron temperature, flow velocity, and electron density are made. Plasma confinement is achieved by the magnetic pressure and non-isentropic expansion of the plasma is shown. Classical transport phenomenon were shown to be correct, with the exception of the electron thermal

conduction.

8. **Magnetoplasmadynamic Arcjet:** The MagnetoPlasmaDynamic Arcjet (MPDA) experiment studies the flow MPD exhaust under the influence of a magnetic nozzle.[21, 80] Results suggest energy conversion governed by isentropic expansion processes and not conservation of the magnetic moment. Plasma flow velocity and Mach number increase downstream as the ion temperature decreases.

9. **Detachment Demonstration Experiment:** The Detachment Demonstration EXperiment (DDEX) studied plasma produced by a pulsed plasma washer gun under the influence of a magnetic nozzle.[96, 97, 98] Detachment is demonstrated, suggesting super-Alfvénic detachment as the driving mechanism. Super-Alfvénic flow, $\beta_f > 1$, is shown at the detachment location, but field line stretching is not measured.

10. **High Power Helicon:** The High Power Helicon (HPH) is an experiment performed by Winglee et al.[31] in which a plasma produced by a helicon source flows through a magnetic nozzle. This experiment showed both collimation of the plasma plume by a magnetic nozzle and self-collimation due to super-Alfvénic flow. The acceleration of the plasma in the nozzle is attributed to directionalizing of thermal energy.

11. **Princeton Experiment:** This experiment investigated the conditions necessary for plasma confinement in a magnetic nozzle and thoroughly characterized of the plasma plume. [145, 49, 48] Electron cooling is seen in the plume which follows a polytropic law. The plasma is found to become unconfined in the far field when a ion confining plasma potential is no longer present. This loss of confinement was found to coincide with electron demagnetization.

12. **Additional Experiments:** For the sake of brevity not all magnetic nozzle

experiments have not been included. Discussion of additional experiments that have been important to the development of this field have been done in previous reviews. [60] Among these experiments are the HYPER-I experiment [102], the Magnetic Nozzle Experiment (MNX) [69], and an ECR thruster.[146]

	Experiments							
	VASIMR	KAH	Θ-pinch	MPDA	DDEX	HPH	HDLT	PM-HDLT
Inputs								
Gas	Argon	Argon	Deuterium	Helium	Helium	Argon	Argon	Argon
# Density ($\#/cm^3$)	1E+13	5E+13	3E+16	1E+14	4E+12	1E+13	1E+11	2E+12
T_i (eV)	1E+02	1E-01	2E+01	1E+01	1E+00	3E+00	2E-01	1E-01
T_e (eV)	6E+00	6E-01	2E+01	5E+00	1E+00	1E+01	6E+00	6E+00
Flow Velocity (m/s)	4E+04	1E+03	5E+04	3E+04	2E+04	5E+03	1E+04	1E+04
Characteristic Length (m)	6E-01	3E-02	4E-03	3E-02	2E-01	7E-02	2E-01	7E-02
B (Gauss)	6E+02	1E+03	2E+04	1E+03	7E+02	3E+02	1E+02	2E+02
Plasma Parameters								
Debye Length (m)	6E-06	8E-07	2E-07	2E-06	5E-06	7E-06	6E-05	1E-05
Particles in Debye Sphere	2E+03	3E+01	2E+02	5E+02	4E+02	4E+03	2E+04	4E+03
Velocities								
Ion Thermal (m/s)	2E+04	6E+02	3E+04	2E+04	6E+03	3E+03	7E+02	5E+02
Electron Thermal (m/s)	1E+06	3E+05	2E+06	9E+05	5E+05	1E+06	1E+06	1E+06
Alfvén (m/s)	6E+04	5E+04	2E+05	1E+05	4E+05	3E+04	2E+05	6E+04
Ion Sound (m/s)	5E+03	2E+03	4E+04	1E+04	8E+03	6E+03	5E+03	5E+03
Characteristic Frequencies and Times								
Ion Cyclotron ($1/s$)	1E+05	2E+05	1E+08	2E+06	2E+06	7E+04	3E+04	5E+04
Electron Cyclotron ($1/s$)	1E+10	2E+10	4E+11	2E+10	1E+10	5E+09	2E+09	4E+09
Ion Collision ($1/s$)	1E+03	3E+07	1E+08	8E+05	4E+05	1E+05	6E+04	2E+06
Electron Collision ($1/s$)	2E+07	2E+09	8E+09	2E+08	6E+07	1E+07	3E+05	4E+06
Residence Time (s)	2E-05	3E-05	8E-08	1E-06	1E-05	1E-05	2E-05	7E-06
Characteristic Lengths								
Ion Mean Free Path (m)	1E+01	2E-05	3E-04	2E-02	1E-02	3E-02	1E-02	3E-04
Electron Mean Free Path (m)	5E-02	2E-04	2E-04	4E-03	9E-03	1E-01	3E+00	3E-01
Ion r_L (m)	1E-01	2E-03	3E-04	6E-03	3E-03	4E-02	2E-02	1E-02
Electron r_L (m)	1E-04	2E-05	5E-06	5E-05	4E-05	3E-04	4E-04	3E-04
Ion Intermediate (Braginskii) (m)	1E+00	2E-04	3E-04	1E-02	7E-03	3E-02	2E-02	2E-03
Electron Intermediate (Braginskii) (m)	2E-03	5E-05	3E-05	5E-04	6E-04	6E-03	4E-02	8E-03
Non-Dimensional Numbers								
Reynolds Number	1E-01	3E+03	3E+01	2E+00	4E+01	5E+00	2E+02	5E+03
Magnetic Reynolds Number	7E+02	5E-02	5E+01	2E+01	1E+01	2E+01	4E+01	2E+01
Alfvén Mach	6E-01	2E-02	2E-01	2E-01	4E-02	2E-01	7E-02	2E-01
Mach	7E+00	6E-01	1E+00	2E+00	2E+00	8E-01	2E+00	2E+00
Kinetic β	8E-01	1E-01	5E-01	5E-01	2E-01	4E-01	3E-01	4E-01
Pressure β	1E-01	3E-04	4E-02	4E-02	4E-04	2E-02	4E-05	2E-04
Hall, Collision, and Residence Frequency Ratios								
Ion Hall	1E+02	8E-03	1E+00	3E+00	4E+00	6E-01	5E-01	3E-02
Electron Hall	5E+02	9E+00	5E+01	7E+01	2E+02	5E+02	8E+03	9E+02
Ion Cyclotron/Residence	2E+00	7E+00	9E+00	3E+00	2E+01	1E+00	5E-01	3E-01
Electron Cyclotron/Residence	2E+05	5E+05	3E+04	2E+04	2E+05	7E+04	4E+04	2E+04
Ion Residence/Collision	5E+01	1E-03	1E-01	1E+00	2E-01	6E-01	1E+00	8E-02
Electron Residence/Collision	3E-03	2E-05	2E-03	3E-03	1E-03	7E-03	2E-01	4E-02
Knudsen Numbers								
Ion Weak Field	2E+01	7E-04	6E-02	7E-01	7E-02	4E-01	7E-02	4E-03
Electron Weak Field	8E-02	5E-03	6E-02	1E-01	5E-02	2E+00	2E+01	4E+00
Ion Intermediate (Braginskii).	2E+00	7E-03	6E-02	4E-01	4E-02	5E-01	1E-01	3E-02
Electron Intermediate (Braginskii).	4E-03	2E-03	8E-03	2E-02	3E-03	8E-02	2E-01	1E-01
Ion Strong Field	2E-01	8E-02	7E-02	2E-01	7E-02	6E-01	1E-01	2E-01
Electron Strong Field	2E-04	6E-04	1E-03	2E-03	2E-04	4E-03	3E-03	4E-03
Transport Properties								
Dynamic Viscosity ($\frac{kg}{(ms)}$)	1E-01	4E-08	7E-04	2E-04	2E-06	5E-05	5E-08	1E-08
Electrical Conductivity ($\frac{S}{m}$)	3E+04	1E+03	2E+05	2E+04	3E+03	5E+04	2E+04	2E+04
Thermal Conductivity ($\frac{W}{mK}$)	1E+00	2E+01	6E+02	1E+01	6E-02	4E+00	3E-03	3E-01

Table A.2: Magnetic nozzle experiments

APPENDIX B

Trapped Particles in a Magnetic Bottle

B.1 Fraction of Trapped Particles

In this Appendix the process for calculating the fraction of trapped particles in the magnetic mirror simulations is presented. Particles are seeded in the domain according to an isotropic Maxwellian distribution:

$$f = \left(\frac{\kappa}{\pi}\right)^{3/2} \exp\left(-\kappa v^2\right) \tag{B.1}$$

Particles trapped by only the effects due to the magnetic field forces are subject to the simple condition that shown below in which $R = \frac{B_{max}}{B_{min}}$:

$$\frac{v_{\perp,0}^2}{v_{\parallel,0}^2 + v_{\perp,0}^2} > \frac{1}{R} \tag{B.2}$$

This can be used to create a loss cone in velocity space with the angle $\alpha = \sin^{-1}(\sqrt{1/R})$. An image of this loss cone (blue) is shown in Figure B.1.

The number of lost particles is found by integrating the Maxwellian distribution over this loss cone. If the initial velocity distribution is isotropic and the loss cone is the simple conical shape, the fraction of particles lost is equal to the fraction of
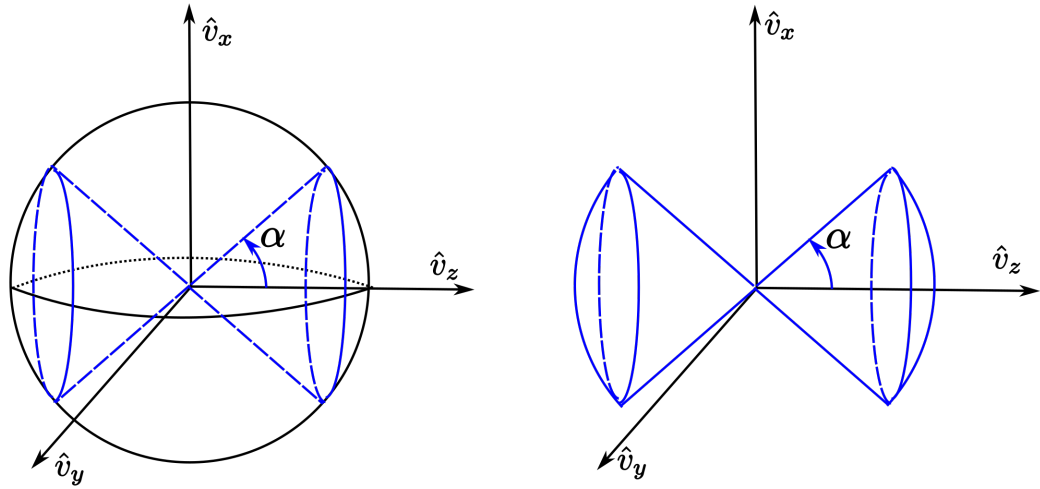
Figure B.1: Illustration of cross-section variation effects.

the total volume in the loss cone. This analysis gives the following relation for the trapped particle fraction:

$$\Gamma = \sqrt{1 - \frac{1}{R}} \tag{B.3}$$

This analysis becomes significantly more complex if an electric field is applied and no simple analytical solution exists. For a non-confining electric field the loss volume
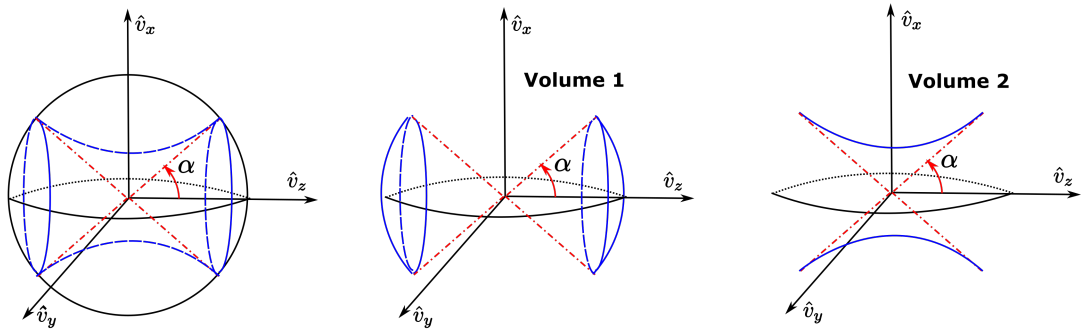
Figure B.2: Loss volumes for non-confining electric field.

grows and more particles are lost. Figure B.2 shows the new expanded loss volume. This loss volume is no longer a simple cone shape, which enabled a simple volume comparison to be made to find the fraction of trapped and/or lost particles. Finding the fraction of particles lost requires explicit integration of the distribution function over the loss volume in velocity space. This is simplified by dividing the loss volume into two volumes shown in Figure B.2. Volume 1 consists of the cone below the angle α while Volume 2 is from α to the blue line which defines the new loss volume. The *fraction of lost particles* is found by integrating the distribution below:

$$Volume\ 1 + Volume\ 2 = \int_0^{\pi/2} \int_0^{v_{max}} 4\pi \left(\frac{\kappa}{\pi}\right)^{3/2} v^2 \exp(-\kappa v^2) \sin(\phi) dv d\phi \quad \text{(B.4)}$$

First the expression is integrated with respect to velocity to an arbitrary value v_{max}:

$$\int_0^v 4\pi \left(\frac{\kappa}{\pi}\right)^{3/2} u^2 \exp(-\kappa u^2) \sin(\phi) du = \left(\frac{\sqrt{\pi}\,\text{erf}(\sqrt{\kappa}v)}{4\kappa^{3/2}} - \frac{v\exp(-\kappa v^2)}{2\kappa}\right) \Big|_0^{v_{max}} \quad \text{(B.5)}$$

The above expression is substituted into the full integral to yield the following expression for Volume 1:

$$Volume\ 1 = \int_0^\alpha \left(\frac{\sqrt{\pi}\,\text{erf}(\sqrt{\kappa}v)}{4\kappa^{3/2}} - \frac{v\exp(-\kappa v^2)}{2\kappa}\right) \Big|_0^\infty \sin(\phi) 4\pi \left(\frac{\kappa}{\pi}\right) |^{3/2} d\phi \quad \text{(B.6)}$$

$$= 1 - \cos(\alpha) \quad \text{(B.7)}$$

Integration over Volume 1 leads to just the traditional loss cone up to the angle α.

The remainder of the loss cone is in Volume 2. This volume is bounded by α and the expression below for v_{max}:

227
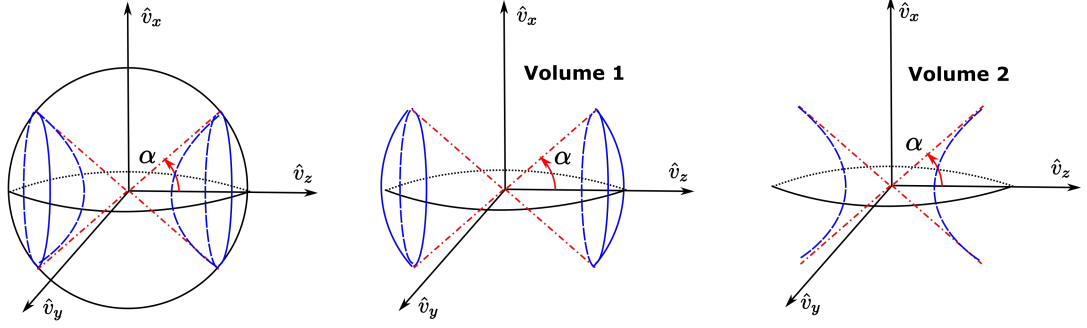
Figure B.3: Loss volumes for confining electric field.

$$v_{max} = \sqrt{\frac{\Phi}{1 - R\sin^2\phi}} \tag{B.8}$$

This is all substituted into the full expression to yield the expression below:

$$
\begin{aligned}
Volume\ 2 &= \int_{\alpha}^{\pi/2} \left(\frac{\sqrt{\pi}\,\mathrm{erf}(\sqrt{\kappa}v)}{4\kappa^{3/2}} - \frac{v\exp(-\kappa v^2)}{2\kappa} \right) \Big|_0^\infty \sin(\phi)4\pi\left(\frac{\kappa}{\pi}\right)|^{3/2}d\phi \\
&= \int_{\alpha}^{\pi/2} \left[erf\left(\sqrt{\frac{\kappa\Phi}{1 - R\sin^2\phi}} \right) - 2\sqrt{\frac{\kappa\Phi}{\pi(1 - R\sin^2(\phi))}}\exp\left(\frac{-\kappa\Phi}{1 - R\sin^2(\phi)} \right) \right] d\phi
\end{aligned}
\tag{B.9}
$$

The above expression is then evaluated numerically and added to the fraction for Volume 1 to get the total combined fraction of lost particles.

A similar process is used to calculate the fraction of particles trapped for a confining field. The loss volume is shrunk in this case. The new volumes are shown in Figure B.3.

For this problem it is easier to calculate the *fraction of particles trapped* and then use this to find the fraction of lost particles. First the volume is integrated from the usual loss cone to $\pi/2$ to get the fraction of particles trapped in Volume 1:

$$Volume\ 1 = \int_{\alpha}^{\phi/2} \left(\frac{\sqrt{\pi}\,\mathrm{erf}(\sqrt{\kappa}v)}{4\kappa^{3/2}} - \frac{v\exp(-\kappa v^2)}{2\kappa} \right) \Big|_0^{\infty} \sin(\phi)4\pi \left(\frac{\kappa}{\pi}\right) |^{3/2}d\phi \quad \text{(B.10)}$$

$$= \cos(\alpha) \quad \text{(B.11)}$$

The particles trapped in Volume 2 is then found by numerically integrating the expression below:

$$Volume\ 2 = \int_{0}^{\alpha} \left(\frac{\sqrt{\pi}\,\mathrm{erf}(\sqrt{\kappa}v)}{4\kappa^{3/2}} - \frac{v\exp(-\kappa v^2)}{2\kappa} \right) \Big|_0^{\infty} \sin(\phi)4\pi \left(\frac{\kappa}{\pi}\right) |^{3/2}d\phi$$

$$\text{(B.12)}$$

$$= \int_{\alpha}^{\pi/2} \left[erf\left(\sqrt{\frac{\kappa\Phi}{1-Rsin^2\phi}} \right) - 2\sqrt{\frac{\kappa\Phi}{\pi(1-R\sin^2(\phi))}} \exp\left(\frac{-\kappa\Phi}{1-R\sin^2(\phi)} \right) \right] d\phi$$

$$\text{(B.13)}$$

The resulting factions are then added to get the total fraction of trapped particles.

APPENDIX C

Maxwellian Source and Collector in a Diverging Magnetic Field Simulation Parameters

C.1   Table of Simulation Parameters

Below is a summary of the parameters used in the verification simulations of a Maxwellian plasma source guided by a diverging magnetic field into a collecting boundary. The inputs to the solver are summarized in Table C.1 while parameters used to compare the simulations (such as Larmor radii) are shown in Table C.1. The first column summarizes the simulation by showing the parameters which were altered compared to the default case. For instance, **Xe,10B,Te=50eV** refers to a case with Xenon as the gas, ten times the applied field strength, and electrons at a temperature of 50 eV. Larmor radii with the subscript a are calculated using the ion acoustic speed as the input perpendicular velocity to consider the affects of the ion inertia which may be gained by the presence of a sheath. Source densities are chosen so that the total flux of electrons is constant for all simulations (at a given domain size). This is done to insure that the source sheath structure is consistent with respect to the electrons and the Debye length in the domain is similar across simulations. Simulations of a domain which is ten times smaller (Mini) are performed to check scaling to a different

	B_{max}	B_{min}	∇B	$L_{\nabla B}$	m_i	n	T_i	T_e
Default	2.7E-02	3.2E-03	1.5E-02	1.3E-01	1.7E-27	1.0E+15	3.0E+02	5.8E+04
10B	2.7E-01	3.2E-02	1.5E-01	1.3E-01	1.7E-27	1.0E+15	3.0E+02	5.8E+04
100B	2.7E+00	3.2E-01	1.5E+00	1.3E-01	1.7E-27	1.0E+15	3.0E+02	5.8E+04
0.1B	2.7E-03	3.2E-04	1.5E-03	1.3E-01	1.7E-27	1.0E+15	3.0E+02	5.8E+04
0.01B	2.7E-04	3.2E-05	1.5E-04	1.3E-01	1.7E-27	1.0E+15	3.0E+02	5.8E+04
0.2B	5.4E-03	6.5E-04	3.0E-03	1.3E-01	1.7E-27	1.0E+15	3.0E+02	5.8E+04
He	2.7E-02	3.2E-03	1.5E-02	1.3E-01	6.6E-27	1.0E+15	3.0E+02	5.8E+04
Ar	2.7E-02	3.2E-03	1.5E-02	1.3E-01	6.6E-26	1.0E+15	3.0E+02	5.8E+04
Ar,10B	2.7E-01	3.2E-02	1.5E-01	1.3E-01	6.6E-26	1.0E+15	3.0E+02	5.8E+04
Xe	2.7E-02	3.2E-03	1.5E-02	1.3E-01	2.2E-25	1.0E+15	3.0E+02	5.8E+04
Xe,10B	2.7E-01	3.2E-02	1.5E-01	1.3E-01	2.2E-25	1.0E+15	3.0E+02	5.8E+04
Te=1eV	2.7E-02	3.2E-03	1.5E-02	1.3E-01	1.7E-27	1.0E+15	3.0E+02	1.2E+04
Te=10eV	2.7E-02	3.2E-03	1.5E-02	1.3E-01	1.7E-27	2.0E+14	3.0E+02	1.2E+05
Te=10eV,Ti=10eV	2.7E-02	3.2E-03	1.5E-02	1.3E-01	1.7E-27	2.0E+15	1.2E+05	1.2E+05
Te=20eV	2.7E-02	3.2E-03	1.5E-02	1.3E-01	1.7E-27	4.0E+15	3.0E+02	2.3E+05
Te=50eV	2.7E-02	3.2E-03	1.5E-02	1.3E-01	1.7E-27	1.0E+16	3.0E+02	5.8E+05
Te=50eV,10B	2.7E-01	3.2E-02	1.5E-01	1.3E-01	1.7E-27	1.0E+16	3.0E+02	5.8E+05
Te=50eV,0.1B	2.7E-03	3.2E-04	1.5E-03	1.3E-01	1.7E-27	1.0E+16	3.0E+02	5.8E+05
Te=50eV,Ti=0.25eV	2.7E-02	3.2E-03	1.5E-02	1.3E-01	1.7E-27	1.0E+16	2.9E+03	5.8E+05
Te=50eV,Ti=0.25eV,0.2B	5.4E-03	6.5E-04	3.0E-03	1.3E-01	1.7E-27	1.0E+16	2.9E+03	5.8E+05
Ar,Te=50eV,Ti=0.25eV	2.7E-02	3.2E-03	1.5E-02	1.3E-01	6.6E-26	1.0E+16	2.9E+03	5.8E+05
Ar,Te=50eV,Ti=0.25eV,0.2B	5.4E-03	6.5E-04	3.0E-03	1.3E-01	6.6E-26	1.0E+16	2.9E+03	5.8E+05
Ar,Ti=5	2.7E-02	3.2E-03	1.5E-02	1.2E-01	1.3E-01	1.0E+16	5.8E+04	5.8E+04
Ti=0.25eV	2.7E-02	3.2E-03	1.5E-02	1.3E-01	1.7E-27	1.0E+15	2.9E+03	5.8E+04
Ti=0.25eV,10B	2.7E-01	3.2E-02	1.5E-01	1.3E-01	1.7E-27	1.0E+15	2.9E+03	5.8E+04
Ti=1eV	2.7E-02	3.2E-03	1.5E-02	1.3E-01	1.7E-27	1.0E+15	1.2E+04	5.8E+04
Ti=1eV,10B	2.7E-01	3.2E-02	1.5E-01	1.3E-01	1.7E-27	1.0E+15	1.2E+04	5.8E+04
Ti=1eV,100B	2.7E+00	3.2E-01	1.5E+00	1.3E-01	1.7E-27	1.0E+15	1.2E+04	5.8E+04
Ti=5eV	2.7E-02	3.2E-03	1.5E-02	1.3E-01	1.7E-27	1.0E+15	5.8E+04	5.8E+04
Mini	2.7E-02	3.2E-03	1.5E-02	1.3E-02	1.7E-27	1.0E+17	3.0E+02	5.8E+04
Mini,10B	2.7E-01	3.2E-02	1.5E-01	1.3E-02	1.7E-27	1.0E+17	3.0E+02	5.8E+04
Mini,100B	2.7E+00	3.2E-01	1.5E+00	1.3E-02	1.7E-27	1.0E+17	3.0E+02	5.8E+04
Mini,0.1B	2.7E-03	3.2E-04	1.5E-03	1.3E-02	1.7E-27	1.0E+17	3.0E+02	5.8E+04
Mini,2B	5.4E-02	6.5E-03	3.0E-02	1.3E-02	1.7E-27	1.0E+17	3.0E+02	5.8E+04

Table C.1: Plasma source with diverging magnetic field simulation parameters.

physical length. For the smaller domain simulations the source densities were chosen to insure the Debye length remained the same fraction of the domain length.

	$r_{L,i}$	$r_{L,e}$	$r_{L,a}$	$\sqrt{r_{L,i}r_{L,e}}$	$r_{L,inertial}$	$r_{L,i}+r_{L,e}$	$\sqrt{r_{L,a}r_{L,e}}$	$r_{L,inertial,a}$	$r_{L,a}+r_{L,e}$
Default	8.6E-03	2.8E-03	1.2E-01	4.9E-03	2.8E-03	1.1E-02	1.8E-02	5.6E-03	1.2E-01
10B	8.6E-04	2.8E-04	1.2E-02	4.9E-04	2.8E-04	1.1E-03	1.8E-03	5.6E-04	1.2E-02
100B	8.6E-05	2.8E-05	1.2E-03	4.9E-05	2.8E-05	1.1E-04	1.8E-04	5.6E-05	1.2E-03
0.1B	8.6E-02	2.8E-02	1.2E+00	4.9E-02	2.8E-02	1.1E-01	1.8E-01	5.6E-02	1.2E+00
0.01B	8.6E-01	2.8E-01	1.2E+01	4.9E-01	2.8E-01	1.1E+00	1.8E+00	5.6E-01	1.2E+01
0.2B	4.3E-02	1.4E-02	6.0E-01	2.4E-02	1.4E-02	5.7E-02	9.1E-02	2.8E-02	6.1E-01
He	1.7E-02	2.8E-03	2.4E-01	6.9E-03	2.8E-03	2.0E-02	2.6E-02	5.6E-03	2.4E-01
Ar	5.4E-02	2.8E-03	7.5E-01	1.2E-02	2.8E-03	5.7E-02	4.6E-02	5.6E-03	7.5E-01
Ar,10B	5.4E-03	2.8E-04	7.5E-02	1.2E-03	2.8E-04	5.7E-03	4.6E-03	5.6E-04	7.5E-02
Xe	9.8E-02	2.8E-03	1.4E+00	1.7E-02	2.8E-03	1.0E-01	6.2E-02	5.6E-03	1.4E+00
Xe,10B	9.8E-03	2.8E-04	1.4E-01	1.7E-03	2.8E-04	1.0E-02	6.2E-03	5.6E-04	1.4E-01
Te=1eV	8.6E-03	1.2E-03	5.4E-02	3.3E-03	1.3E-03	9.8E-03	8.2E-03	2.5E-03	5.5E-02
Te=10eV	8.6E-03	3.9E-03	1.7E-01	5.8E-03	4.0E-03	1.3E-02	2.6E-02	7.9E-03	1.7E-01
Te=10eV,Ti=10eV	1.7E-01	3.9E-03	2.4E-01	2.6E-02	7.9E-03	1.7E-01	3.1E-02	1.2E-02	2.4E-01
Te=20eV	8.6E-03	5.6E-03	2.4E-01	6.9E-03	5.6E-03	1.4E-02	3.6E-02	1.1E-02	2.4E-01
Te=50eV	8.6E-03	8.8E-03	3.8E-01	8.7E-03	8.8E-03	1.7E-02	5.8E-02	1.8E-02	3.9E-01
Te=50eV,10B	8.6E-04	8.8E-04	3.8E-02	8.7E-04	8.8E-04	1.7E-03	5.8E-03	1.8E-03	3.9E-02
Te=50eV,0.1B	8.6E-02	8.8E-02	3.8E+00	8.7E-02	8.8E-02	1.7E-01	5.8E-01	1.8E-01	3.9E+00
Te=50eV,Ti=0.25eV	2.7E-02	8.8E-03	3.8E-01	1.5E-02	8.9E-03	3.5E-02	5.8E-02	1.8E-02	3.9E-01
Te=50eV,Ti=0.25eV,0.2B	1.3E-01	4.4E-02	1.9E+00	7.7E-02	4.4E-02	1.8E-01	2.9E-01	8.8E-02	1.9E+00
Ar,Te=50eV,Ti=0.25eV	1.7E-01	8.8E-03	2.4E+00	3.8E-02	8.9E-03	1.8E-01	1.4E-01	1.8E-02	2.4E+00
Ar,Te=50eV,Ti=0.25eV,0.2B	8.4E-01	4.4E-02	1.2E+01	1.9E-01	4.4E-02	8.8E-01	7.2E-01	8.8E-02	1.2E+01
Ar, Ti=5	7.5E-01	2.8E-03	1.1E+00	4.6E-02	5.6E-03	7.5E-01	5.4E-02	8.4E-03	1.1E+00
Ti=0.25eV	2.7E-02	2.8E-03	1.2E-01	8.6E-03	2.9E-03	2.9E-02	1.8E-02	5.7E-03	1.3E-01
Ti=0.25eV,10B	2.7E-03	2.8E-04	1.2E-02	8.6E-04	2.9E-04	2.9E-03	1.8E-03	5.7E-04	1.3E-02
Ti=1eV	5.3E-02	2.8E-03	1.3E-01	1.2E-02	3.3E-03	5.6E-02	1.9E-02	6.1E-03	1.3E-01
Ti=1eV,10B	5.3E-03	2.8E-04	1.3E-02	1.2E-03	3.3E-04	5.6E-03	1.9E-03	6.1E-04	1.3E-02
Ti=1eV,100B	5.3E-04	2.8E-05	1.3E-03	1.2E-04	3.3E-05	5.6E-04	1.9E-04	6.1E-05	1.3E-03
Ti=5eV	1.2E-01	2.8E-03	1.7E-01	1.8E-02	5.6E-03	1.2E-01	2.2E-02	8.4E-03	1.7E-01
Mini	8.6E-02	2.8E-02	1.2E+00	4.9E-02	2.8E-02	1.1E-01	1.8E-01	5.6E-02	1.2E+00
Mini,10B	8.6E-03	2.8E-03	1.2E-01	4.9E-03	2.8E-03	1.1E-02	1.8E-02	5.6E-03	1.2E-01
Mini,100B	8.6E-04	2.8E-04	1.2E-02	4.9E-04	2.8E-04	1.1E-03	1.8E-03	5.6E-04	1.2E-02
Mini,0.1B	8.6E-01	2.8E-01	1.2E+01	4.9E-01	2.8E-01	1.1E+00	1.8E+00	5.6E-01	1.2E+01
Mini,2B	4.3E-02	1.4E-02	6.0E-01	2.4E-02	1.4E-02	5.7E-02	9.1E-02	2.8E-02	6.1E-01

Table C.2: Plasma source with diverging magnetic field non-dimensional numbers.

APPENDIX D

Plasma Source in a Converging Diverging Magnetic Field Simulation Parameters

D.1 Table of Simulation Parameters

Below is a summary of the parameters used in the verification simulations of a plasma source located in a converging diverging magnetic field. The inputs to the solver are summarized in Table D.1 while parameters used to compare the simulations (such as Larmor radii) are shown in Table D.1. The first column of these tables summarized how each simulation is different from the default simulation. For instance, **Xe,10B,Te=50eV** refers to a case with Xenon as the gas, ten times the applied field strength, and electrons at a temperature of 50 eV. Larmor radii with the subscript a are calculated using the ion acoustic speed as the input perpendicular velocity to consider the affects of the ion inertia which may be gained by the presence of a sheath.

	B_{max}	B_{min}	∇B	$L_{\nabla B}$	m_i	T_i	T_e
Default	2.5E-02	1.4E-02	1.1E-01	1.8E-01	1.7E-27	3.0E+02	5.8E+04
10B	2.5E-01	1.4E-01	1.1E+00	1.8E-01	1.7E-27	3.0E+02	5.8E+04
0.1B	2.5E-03	1.4E-03	1.1E-02	1.8E-01	1.7E-27	3.0E+02	5.8E+04
0.2B	5.1E-03	2.9E-03	2.2E-02	1.8E-01	1.7E-27	3.0E+02	5.8E+04
0.01B	2.5E-04	1.4E-04	1.1E-03	1.8E-01	1.7E-27	3.0E+02	5.8E+04
Te=20eV	2.5E-02	1.4E-02	1.1E-01	1.8E-01	1.7E-27	3.0E+02	2.3E+05
Te=50eV	2.5E-02	1.4E-02	1.1E-01	1.8E-01	1.7E-27	3.0E+02	5.8E+05
Te=50eV,10B	2.5E-01	1.4E-01	1.1E+00	1.8E-01	1.7E-27	3.0E+02	5.8E+05
Te=50eV,0.1B	2.5E-03	1.4E-03	1.1E-02	1.8E-01	1.7E-27	3.0E+02	5.8E+05
Ti=1eV	2.5E-02	1.4E-02	1.1E-01	1.8E-01	1.7E-27	1.2E+04	5.8E+04
Ti=5eV	2.5E-02	1.4E-02	1.1E-01	1.8E-01	1.7E-27	5.8E+04	5.8E+04
Ti=5eV,10B	2.5E-01	1.4E-01	1.1E+00	1.8E-01	1.7E-27	5.8E+04	5.8E+04
Ti=10eV,Te=10eV	2.5E-02	1.4E-02	1.1E-01	1.8E-01	1.7E-27	1.2E+05	1.2E+05
Ti=10eV,Te=10eV,10B	2.5E-01	1.4E-01	1.1E+00	1.8E-01	1.7E-27	1.2E+05	1.2E+05
He,Ti=0.1eV	2.5E-02	1.4E-02	1.1E-01	1.8E-01	6.6E-27	1.2E+03	5.8E+04
He,Ti=0.1eV,10B	2.5E-01	1.4E-01	1.1E+00	1.8E-01	6.6E-27	1.2E+03	5.8E+04
He,Ti=0.1eV,0.1B	2.5E-03	1.4E-03	1.1E-02	1.8E-01	6.6E-27	1.2E+03	5.8E+04
He,Ti=1eV	2.5E-02	1.4E-02	1.1E-01	1.8E-01	6.6E-27	1.2E+04	5.8E+04
He,Ti=1eV,10B	2.5E-01	1.4E-01	1.1E+00	1.8E-01	6.6E-27	1.2E+04	5.8E+04
Ar,Ti=1eV	2.5E-02	1.4E-02	1.1E-01	1.8E-01	6.6E-26	1.2E+04	5.8E+04
Ar,Ti=1eV,10B	2.5E-01	1.4E-01	1.1E+00	1.8E-01	6.6E-26	1.2E+04	5.8E+04
Ar,Ti=1eV,0.1B	2.5E-03	1.4E-03	1.1E-02	1.8E-01	6.6E-26	1.2E+04	5.8E+04
Ar,Ti=5eV	2.5E-02	1.4E-02	1.1E-01	1.8E-01	6.6E-26	5.8E+04	5.8E+04
Mini	2.5E-02	1.4E-02	1.1E+00	1.8E-02	1.7E-27	3.0E+02	5.8E+04
Mini,10B	2.5E-01	1.4E-01	1.1E+01	1.8E-02	1.7E-27	3.0E+02	5.8E+04
Mini,100B	2.5E+00	1.4E+00	1.1E+02	1.8E-02	1.7E-27	3.0E+02	5.8E+04
Mini,2B	5.1E-02	2.9E-02	2.2E+00	1.8E-02	1.7E-27	3.0E+02	5.8E+04

Table D.1: Source with converging-diverging magnetic field simulation parameters.

	$r_{L,i}$	$r_{L,e}$	$r_{L,a}$	$\sqrt{r_{L,i}r_{L,e}}$	$r_{L,inertial}$	$r_{L,i}+r_{L,e}$	$\sqrt{r_{L,a}r_{L,e}}$	$r_{L,inertial,a}$	$r_{L,a}+r_{L,e}$
Default	4.5E-03	1.5E-03	6.3E-02	2.6E-03	1.5E-03	6.0E-03	9.7E-03	3.0E-03	6.5E-02
10B	4.5E-04	1.5E-04	6.3E-03	2.6E-04	1.5E-04	6.0E-04	9.7E-04	3.0E-04	6.5E-03
0.1B	4.5E-02	1.5E-02	6.3E-01	2.6E-02	1.5E-02	6.0E-02	9.7E-02	3.0E-02	6.5E-01
0.2B	2.3E-02	7.4E-03	3.2E-01	1.3E-02	7.4E-03	3.0E-02	4.8E-02	1.5E-02	3.2E-01
0.01B	4.5E-01	1.5E-01	6.3E+00	2.6E-01	1.5E-01	6.0E-01	9.7E-01	3.0E-01	6.5E+00
Te=20eV	4.5E-03	3.0E-03	1.3E-01	3.7E-03	3.0E-03	7.5E-03	1.9E-02	5.9E-03	1.3E-01
Te=50eV	4.5E-03	4.7E-03	2.0E-01	4.6E-03	4.7E-03	9.2E-03	3.1E-02	9.3E-03	2.0E-01
Te=50eV,10B	4.5E-04	4.7E-04	2.0E-02	4.6E-04	4.7E-04	9.2E-04	3.1E-03	9.3E-04	2.0E-02
Te=50eV,0.1B	4.5E-02	4.7E-02	2.0E+00	4.6E-02	4.7E-02	9.2E-02	3.1E-01	9.3E-02	2.0E+00
Ti=1eV	2.8E-02	1.5E-03	6.9E-02	6.5E-03	1.8E-03	3.0E-02	1.0E-02	3.2E-03	7.1E-02
Ti=5eV	6.3E-02	1.5E-03	8.9E-02	9.7E-03	3.0E-03	6.5E-02	1.1E-02	4.4E-03	9.1E-02
Ti=5eV,10B	6.3E-03	1.5E-04	8.9E-03	9.7E-04	3.0E-04	6.5E-03	1.1E-03	4.4E-04	9.1E-03
Ti=10eV,Te=10eV	8.9E-02	2.1E-03	1.3E-01	1.4E-02	4.2E-03	9.1E-02	1.6E-02	6.3E-03	1.3E-01
Ti=10eV,Te=10eV,10B	8.9E-03	2.1E-04	1.3E-02	1.4E-03	4.2E-04	9.1E-03	1.6E-03	6.3E-04	1.3E-02
He,Ti=0.1eV	1.8E-02	1.5E-03	1.3E-01	5.1E-03	1.5E-03	1.9E-02	1.4E-02	3.0E-03	1.3E-01
He,Ti=0.1eV,10B	1.8E-03	1.5E-04	1.3E-02	5.1E-04	1.5E-04	1.9E-03	1.4E-03	3.0E-04	1.3E-02
He,Ti=0.1eV,0.1B	1.8E-01	1.5E-02	1.3E+00	5.1E-02	1.5E-02	1.9E-01	1.4E-01	3.0E-02	1.3E+00
He,Ti=1eV	5.6E-02	1.5E-03	1.4E-01	9.1E-03	1.8E-03	5.8E-02	1.4E-02	3.2E-03	1.4E-01
He,Ti=1eV,10B	5.6E-03	1.5E-04	1.4E-02	9.1E-04	1.8E-04	5.8E-03	1.4E-03	3.2E-04	1.4E-02
Ar,Ti=1eV	1.8E-01	1.5E-03	4.4E-01	1.6E-02	1.8E-03	1.8E-01	2.5E-02	3.2E-03	4.4E-01
Ar,Ti=1eV,10B	1.8E-02	1.5E-04	4.4E-02	1.6E-03	1.8E-04	1.8E-02	2.5E-03	3.2E-04	4.4E-02
Ar,Ti=1eV,0.1B	1.8E+00	1.5E-02	4.4E+00	1.6E-01	1.8E-02	1.8E+00	2.5E-01	3.2E-02	4.4E+00
Ar,Ti=5eV	4.0E-01	1.5E-03	5.6E-01	2.4E-02	3.0E-03	4.0E-01	2.9E-02	4.4E-03	5.6E-01
Mini	4.5E-02	1.5E-02	6.3E-01	2.6E-02	1.5E-02	6.0E-02	9.7E-02	3.0E-02	6.5E-01
Mini,10B	4.5E-03	1.5E-03	6.3E-02	2.6E-03	1.5E-03	6.0E-03	9.7E-03	3.0E-03	6.5E-02
Mini,100B	4.5E-04	1.5E-04	6.3E-03	2.6E-04	1.5E-04	6.0E-04	9.7E-04	3.0E-04	6.5E-03
Mini,2B	2.3E-02	7.4E-03	3.2E-01	1.3E-02	7.4E-03	3.0E-02	4.8E-02	1.5E-02	3.2E-01

Table D.2: Source with converging-diverging magnetic field non-dimensional parameters.

APPENDIX E

Retarding Potential Analyzer for Ion Energy Analysis

E.1   Introduction

The University of Michigan Plasmadynamics and Electric Propulsion Laboratory is currently developing the CubeSat Ambipolar Thruster which utilizes a magnetic nozzle. Work was performed to support the efforts of the experimentalists working on CAT, particularly the setup of a a retarding potential analyzer (RPA) critical to studying the CAT plume ion energetics.

E.2   Retarding Potential Analyzer Basics

Retarding Potential Analyzers (RPA) are diagnostics used to measure ion energy distribution functions in a plasma. [116] Ion temperature and drift velocity can then be determined from the ion energy distribution function. The probe consists of a series of grids which act as a filter only allowing ions above a threshold energy to be measured at a collecting electrode. The measured collector current and applied

235
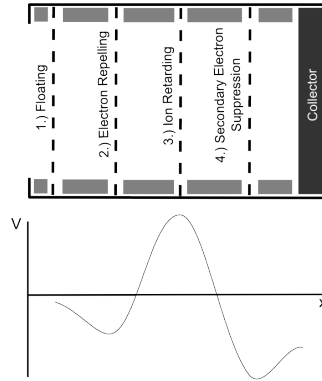
Figure E.1: Schematic of four grid RPA. Typical potential profile is shown.

filter voltage are used to determine ion energy distributions. RPA's are a valuable diagnostic for determining thruster performance and ion energy distribution functions.

A schematic of a typical RPA is shown in Figure E.1. The number of grids in an RPA depends on the specific design, but a typical arrangement includes the grids shown. These grids are separated from one another by insulators (e.g. MACOR/glass-mica), typically in the form of a washer. An insulator (e.g. phenolic) sleeve holds the assembly which is then placed inside a metallic body (e.g. stainless steel). The grids are made of a conducting material (e.g. stainless steel, molybdenum) as well as the collector (e.g. copper, tungsten coated stainless steel). Typical assemblies are held together by compression, but the design is not limited to this approach.

The first grid is electrically floating to minimize the perturbation of the plasma by the probe and attenuate the amount of plasma flowing into the RPA, an important consideration which will be discussed later. The second grid is biased negatively to repel all electrons from the plasma. The third grid potential is swept over a range of voltages and is used to filter ions. The fourth grid is biased negatively to suppress any electrons which are generated inside the RPA due to secondary electron emission.
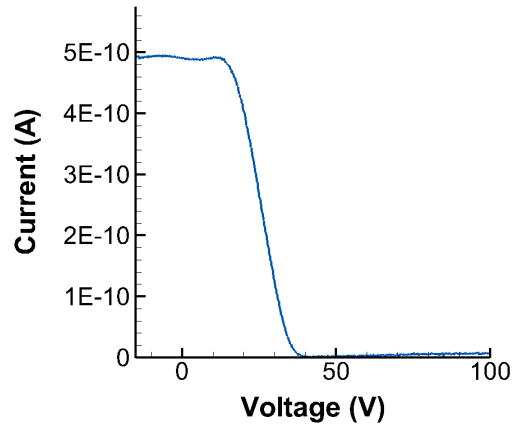
Figure E.2: Example RPA current-voltage trace.

Finally the collector is biased negatively (not as negatively as suppression grid) to insure good current collection. An example of the voltage profile in a four grid RPA is shown in Figure E.1. Additional grids may be added to the RPA, an example of this is adding additional grids on the plasma side of the floating grid in order to further attenuate the plasma.

An example of a good current(collector)-voltage(ion retarding) trace for an RPA is shown in Figure E.2. The current should start with zero slope and then begin to decrease at values near the plasma potential and/or beam energy. All voltages are referenced to ground, which results in all the ion current being collected initially as the ions are accelerated from the plasma potential to ground (if the plasma potential is positive). Since all voltages are applied referenced to ground, the beam energy is found by subtracting the plasma potential (measured by an emissive or Langmuir probe) from the beam energy.

The current-voltage trace can be used to determine the ion energy distribution function. The current collected by the probe (I) is found by the following expression based on the flux of particles into the probe. [116, 147]

$$I = qA \int_{\sqrt{|2eV_{i,rep}/m|}}^{\infty} f(v)v \, dv \qquad \text{(E.1)}$$

The derivative of this expression with respect to the ion repulsion voltage $(V_{i,rep})$ then gives the following relation between the current and the distribution function in which $v = \sqrt{2eV_{i,rep}/m}$.

$$\frac{dI}{dV_{i,rep}} \propto -f(v) \qquad \text{(E.2)}$$

Therefore, the ion energy distribution function is found by simply taking the derivative of the current-voltage trace.

E.2.1 Design Considerations

The important design considerations for an RPA include the grid spacing, grid orifice size, grid transparency, and materials used.

E.2.1.1 Grid Spacing

An RPA works by rejecting all the electrons and only allowing ions to pass through the grids resulting in a non-neutral gas in the diagnostic. If the density of the plasma is too high, space-charge limitations become important because the voltages applied by the grids can be shielded by the high density of ions. When this occurs the grids do not effectively filter the ions. A simple analysis by Hutchison suggests that the grid spacing is constrained by the following equation: [116]

$$\Delta x_{grid} < 1.02\lambda_D \left(\frac{e\Delta V}{T_e(eV)}\right)^{3/4} \qquad \text{(E.3)}$$

The spacing (Δx_{grid}) is limited by the smallest voltage difference applied between the grids (assuming the same spacing between all grids). Physically, when the voltage is small it is easier for the space charge to shield out the applied voltage. The smallest

voltage difference typically occurs between the electron repelling grid and the ion retarding grid when the ion retarding voltage is zero and no ions are filtered out. The lowest voltage between the electron and ion repelling grids is typically a few times the electron temperature, resulting in the general rule of thumb that $\Delta x_{grid} \leq 4\lambda_D$. Since the Debye length scales with $1/\sqrt{n}$, the grid gap size can become prohibitively small for very high density plasmas.

The Debye length used in these calculations is typically the Debye length of the ambient plasma. However, a more accurate approach is to use the density of the plasma which is attenuated by the grids (only a fraction of the plasma flux makes it through the grid). Adding additional attenuating grids with low transparency will lead to a lower density of plasma in the RPA, relaxing the restrictions on the grid spacing. This, however, adds additional uncertainties by adding more surfaces with which the plasma interacts.

E.2.1.2 Orifice Size

The size of the orifice or the mesh used for the grids is an important parameter because it determines whether or not plasma can enter into RPA. The effect of the grids are only felt on a distance of $\approx \lambda_D$ due to charge shielding, therefore, plasma will typically start to enter the RPA unaffected by the grids if the orifice size is larger than the Debye length. The design criteria for the orifice size requires that the orifice size be $< 2\lambda_D$. [147]

The effects of lensing on the particles passing through the grids is also an important consideration. Lensing occurs when the electric field on either side of a grids is different. [147] The electric field must be continuous through the orifice, resulting in curved equipotential lines. These curved lines results in non-axial electric field which can divert particles from the axial direction causing them to collide with other grids resulting in a loss of flux. This effect is considered negligible if the grids are close to

one another. The primary effect of lensing is flux losses.

Lastly, the inlet of the RPA must also be the smallest aperture of the system in order to avoid transverse momentum in the device. [147] A discussion on the resolution of these devices is given by Bohm et al. [147]

E.2.1.3 Grid Transparency

The transparency of the grids is an important parameter for determining the amount of current seen by the collector. The required transparency is determined by the device used to measure current at the collector and the plasma properties. The maximum amount of current arriving at the collector can be estimated by assuming the ions flux into the RPA inlet with the Bohm velocity. This flux is then attenuated by the transparency (η_a). This results in the following expression for the approximate collected current.

$$I_{col} = \eta_a e A_{inlet} n \sqrt{\frac{kT_e}{m_i}} \tag{E.4}$$

The overall diagnostic transparency as well as the device used to collect correct must be designed so that desired current resolution is achieved for the device.

E.2.1.4 Materials

There are a few general considerations that must be taken into account for the materials used in the RPA. Low outgassing materials should be used for the insulator to prevent the build up of neutrals in the RPA. Large neutral densities in the RPA can results in collisions which remove energy from the ions, leading to errors in the measurement. An important resource for this can be found from NASA. [148] Examples of good materials for the insulators and or washers/insulators are MACOR and glass-mica.

Generally the conductors used for the grids and collector should be materials

with low secondary electron emission and low sputtering yields for the energies considered in the plasma. Both of these parameters are important because they affect the amount of charge in the system, but is particularly important for the collector where they change the current collected. Although the material choice is dependent on the operating conditions, generally materials such as stainless steel, nickel, and molybdenum are used.

E.2.2   Operational Considerations

E.2.2.1   Grid Voltages

The choice of the magnitude of the grid voltages has an important effect on the performance of the RPA. The electron repelling grid is typically set to a few times the electron temperature to repel all the electrons.

The ion grid is swept over the desired range of voltages were the ion energies will be filtered. Typically this starts at zero for the grid and extends to some multiple of the maximum ion energy. A negative voltage may also be used as the starting point to verify that the slope of the current is zero initially as required.

The secondary electron suppression grid voltage should be set as the lowest voltage in the RPA. This insures that any secondary electrons created by the other grids in the RPA will be accelerated out toward the plasma while secondaries created by the collector will be accelerated back to the collector (resulting in no net current due to secondaries). [147] If this is not the lowest voltage in the system electrons can get trapped between the secondary electron suppression grid and the electron repelling grid. These electrons can then collide with neutrals and create additional ions.

Lastly, the collector voltage should be few volts greater (still negative) than the suppression grid voltage. This insures accurate current collection and forces secondaries which are emitted from the collector back to the collector by applying a negative voltage between the collector and the secondary electron suppression grid.

All voltages are applied with respect to the facility ground which means that ion energies measured are with respect to the ground as well. The plasma potential must be known as well to find the ion kinetic energy in the plasma.

E.2.2.2 Effects of Magnetic Fields

A strong magnetic field may have an effect on the RPA measurements which becomes an issue if the magnetic field is not aligned with the axis of the RPA. A transverse field may result in sheath effects at the inlet which results in the ions having a fractional energy gain due to the pre-sheath. [116] If the transverse magnetic field is strong enough for a significant fraction of ions to be magnetized, it can significantly affect the measurements by limiting the flow of the lower energy, magnetized ions. Generally in a transverse magnetic field, the ion Larmor radius should be much greater than the dimensions of the RPA to avoid these effects

E.2.2.3 Effects of Neutral Collisions

The presence of neutrals can be detrimental to the measurements of the RPA. If a significant number of neutrals are inside the RPA ion scattering will decrease the energy of the ions and also limit the flux of ions. This results in the ions no longer being representative of the plasma from which they originated. The RPA dimensions should be much smaller than the ion-neutral mean free path.

Neutrals in the device can also result in additional ionization if electrons are generated in the device due to secondary electron emission or imperfect repulsion from the electron repelling grid. Again this new plasma is not representative of the plasma which is being measured outside the RPA and will result in measurement errors. This effect can be mitigated by insuring the the secondary electron repulsion grid is the lowest voltage in the system as discussed previously. A rigorous analysis can be performed by consulting the Paschen curve and considering maximum electric
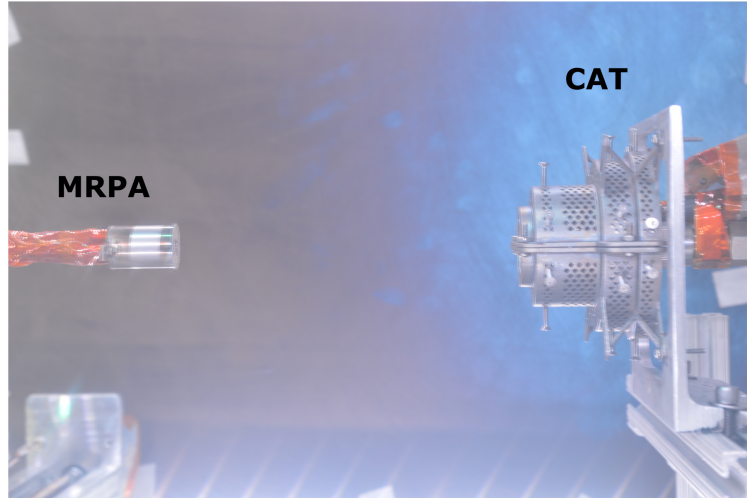
Figure E.3: Micro RPA in vacuum chamber. RPA is on the left, CAT is on the right.

field $(\Delta V/\Delta x)$ in the system.

E.2.2.4 Diagnosing errors

Bohm et. al give a great outline for diagnosing errors in RPA traces which should be referenced for help. [147] Some of these errors include non-zero currents as the ion repelling voltage increases and initial increases in current near zero volts. These effects can occur for incorrectly chosen grid voltages or large neutral densities.

E.3 RPA Setup

The RPA used for these measurements is known as the micro RPA (MRPA). The MRPA is a four grid RPA which was designed to measure ion energies in another helicon source at PEPL.[149] An image of this RPA in the vacuum chamber is shown in Figure E.3.

The MRPA had a 19-mm diameter stainless steel casing and a macor sleeve which is inserted in the casing. The grids were placed in the macor sleeve and are separated by macor washers which are approximately 0.5 mm thick. The grids were made out of stainless steel which was photochemically etched. The collector is a nickel plate.

The assembly of grids, washer, and collector were pressure fit inside the macor sleeve by a spring.

The voltages to the grids were applied with respect to ground using laboratory power supplies. The electron repelling and electron suppression grids were applied with Instek GPR-30H-10D power supplies. The ion retarding and collector biases were Keithley 2410 and 2400 sources respectively. Currents were collected using a Keithley 6485 picoammeter.

E.4   Validation

The RPA was tested with a Commonwealth ion source to validate its accuracy and has since been used to diagnose the CAT plume at a variety of operating conditions. [140]

E.4.1   Ion Source Setup

The ion source used for validation was a 3 cm diameter Commonwealth Ion Source. A schematic of the electrical connections used is shown in Figure E.4. The ion source requires five power supplies: the internal cathode, discharge, beam, acceleration grid, and neutralizer cathode supplies. The power supplies used are summarized in Table E.1. The neutralizer cathode was made by coiling thoriated tungsten. The exact internal cathode material was unknown, but was likely also a type of tungsten wire. The DC power supplies were used for the cathodes in this setup, but typically AC power supplies are used to allow the beam to be visible.

E.4.2   Results

The ion source settings used for the validation are summarized in the Table E.2. These values were read from the dials on the power supply so they may not be as accurate as desired and were not independently measured as they should be.
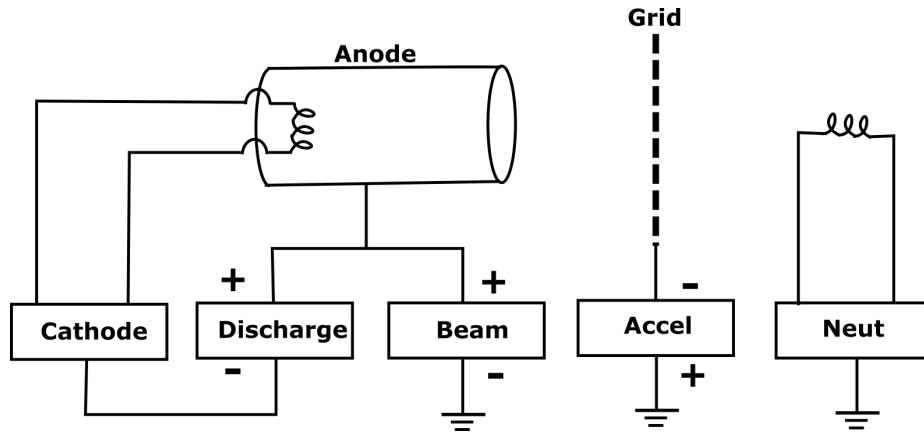
Figure E.4: Schematic of ion source electrical setup for RPA testing.

Table E.1: Summary of ion source power supplies.

Internal Cathode	Sorenson DCS 33-33
Discharge	Sorensen DCS 600-1.7
Beam	Sorensen DCS 600-1.7E
Acceleration Grid	Sorensen DCS 600-1.7E
Neutralizer Cathode	Sorensen DCS 40-25

Table E.2: Ion source power supplies settings for RPA testing.

	8 SCCM		12 SCCM	
	Voltage (V)	Current (A)	Voltage (V)	Current (A)
Internal Cathode	4.9	4.6	5.0	4.6
Discharge	51	0.017	55	0.018
Beam	300	0.004	300	0.004
Acceleration Grid	20	0.002	20	0.004
Neutralizer Cathode	29.1	4.4	29.3	4.4

Figure E.5 below shows the ion energy distributions measured using the RPA positioned 50 cm downstream from the Commonwealth ion source. The ion source was run with argon. As shown in Table E.2, the beam voltage was set to 300 V, which is clearly seen in the 8 SCCM operating condition for the ion source, validating this diagnostic. The high flow-rate case had high background pressures, which resulted in the lower energy plasma potential peak as well as the overall noise of the data. The energy of this peak was confirmed to be the plasma potential by an independent emissive probe measurement. A plasma potential peak is expected in conditions where there are sufficient neutral collisions which both spread out the beam and also result in the formation of low-energy charge exchange ions with energies equal to the local plasma potential. The background pressures for 8 SCCM and 12 SCCM were 1.78×-5 and 2.69×10^{-5} Torr respectively when testing started at each flow rate setting. The pressures while running at 12 SCCM may have been higher because the pressures began creeping up during the 12 SCCM test and eventually saturated the cryo-pumps. The pressure for 12 SCCM may have been nearer to 4.67×10^{-4} Torr. The charge exchange mean free path for the two pressures 2.69×10^{-5} Torr and 4.67×10^{-4} Torr are around 5.9 m and 0.34 m (less than the distance from the source to the RPA) respectively. The appearance of the plasma potential peak would suggest that there is a high presence of neutrals and that at the time of the measurement the background density was at the higher.

E.5 Results and Future Work

This diagnostic has been extensively used for studying the CubeSat Ambipolar Thruster plasma plume. [140] An example of some of these plots is show in Figure E.6. In this figure measurements are shown of two CAT operating conditions. In the diffuse mode no beam is seen and only a plasma potential peak is measured. In the "blue" mode a beam as well as a plasma potential peak is measured. This diagnostic
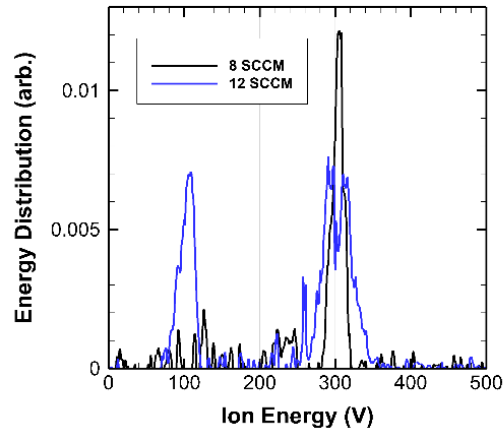
Figure E.5: Ion energy distributions measured for ion source with a beam voltage of 300 V.

confirmed the presence of ion acceleration in the CAT plume through the formation of a high energy beam. Plasma potential peaks were also independently verified with emissive probe measurements.

This diagnostic has been and will be extensively used in the future to diagnose the ion energetics and operating conditions. It will be used to spatially map the ion acceleration characteristics in the plume. [140] This data will be compared with the simulation results of the Q1D code to determine the physics behind the ion acceleration and also validate the outputs of the code. Development of an even smaller nano RPA was initiated to enable measurements closer to the thruster without perturbing the plasma. This will be completed in the future.
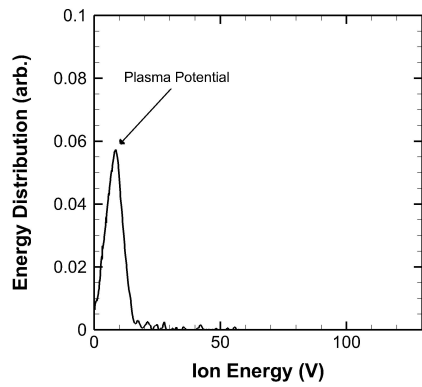
(a) Measurement in diffuse mode with no beam.
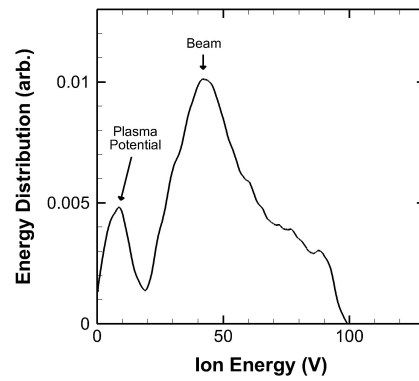
(b) Measurement in blue mode with beam.

Figure E.6: Ion energy measurements in the CAT plume demonstrating beam formation.

BIBLIOGRAPHY

BIBLIOGRAPHY

[1] R.G. Jahn and W. von Jaskowsky. *Physics of Electric Propulsion*, volume 288. McGraw-Hill, New York, 1968.

[2] D.M. Goebel and I. Katz. *Fundamentals of Electric Propulsion: Ion and Hall Thrusters*, volume 1. John Wiley & Sons, 2008.

[3] C. Charles. Plasmas for Spacecraft Propulsion. *Journal of Physics D: Applied Physics*, 42(16):163001, 2009.

[4] George C. Soulas. The Impact of Back-Sputtered Carbon on the Accelerator Grid Wear Rates of the NEXT and NSTAR Ion Thrusters. 2013.

[5] Rohit Shastry, Daniel A. Herman, George C. Soulas, and Michael J. Patterson. Status of NASA's Evolutionary Xenon Thruster (NEXT) Long-Duration Test as of 50,000 h and 900 kg Throughput. 2013.

[6] John R. Brophy, Michael G. Marcucci, Gani B. Ganapathi, Charles E. Garner, Michael D. Henry, Barry Nakazono, and Don Noon. The ion propulsion system for Dawn. *AIAA Paper*, 4542, 2003.

[7] C. T. Russell and C. A. Raymond. The dawn mission to Vesta and Ceres. In *The Dawn Mission to Minor Planets 4 Vesta and 1 Ceres*, pages 3–23. Springer, 2011.

[8] C. T. Russell, M. A. Barucci, R. P. Binzel, M. T. Capria, U. Christensen, A. Coradini, M. C. De Sanctis, W. C. Feldman, R. Jaumann, H. U. Keller, and others. Exploring the asteroid belt with ion propulsion: Dawn mission history, status and plans. *Advances in Space Research*, 40(2):193–201, 2007.

[9] I.G. Mikellides, I. Katz, R.R. Hofer, D.M. Goebel, K. de Grys, and A. Mathers. Magnetic Shielding of the Channel Walls in a Hall Plasma Accelerator. *Physics of Plasmas (1994-present)*, 18(3):033501, 2011.

[10] NASA: Climate Change and Global Warming.

[11] NASA's Earth Observing System.

[12] World Population Prospects - Population Division - United Nations.

[13] International Energy Statistics - EIA.

[14] NASA Spinoff. NASA Spinoff.

[15] Walter Edward Hammond. *Space transportation: A systems approach to analysis and design.* Aiaa, 1999.

[16] W. H. Robbins and H. B. Finger. An historical perspective of the NERVA nuclear rocket engine technology program. 1991.

[17] Stanley Gunn. Nuclear propulsiona historical perspective. *Space Policy*, 17(4):291–298, 2001.

[18] S.A. Andersen, V.O. Jensen, P. Nielsen, and N. D'Angelo. Continuous Supersonic Plasma Wind Tunnel. *Physics of Fluids*, 12(3):557–560, 1969.

[19] K. Kuriki and O. Okada. Experimental Study of a Plasma Flow in a Magnetic Nozzle. *Physics of Fluids*, 13:2262, 1970.

[20] H. Tobari, A. Ando, M. Inutake, and K. Hattori. Direct Measurement of Lorentz Forces in an Applied-Field MPD Thruster. In *Proceedings of the 29th International Electric Propulsion Conference*, 2005.

[21] M. Inutake, A. Ando, K. Hattori, H. Tobari, and T. Yagai. Characteristics Of a Supersonic Plasma Flow in a Magnetic NOZZle. *J. Plasma Fusion Res.*, 78:1352–1360, 2002.

[22] J.P. Sheehan, T. Collard, B.W. Longmier, and I. Goglio. New Low-Power Plasma Thruster for Nanosatellites. AIAA-2014-3914. 50th AIAA/ASME/SAE/ASEE Joint Propulsion Conference, 2014.

[23] H.G. Kosmahl. Three-Dimensional Plasma Acceleration Through Axissymmetric Divergine Magnetic Fields Based on Dipole Moment Approximation. Technical report, National Aeronautics and Space Administration,Lewis Research Center, Cleveland, OH, 1967.

[24] J.C. Sercel. Simple Model of Plasma Acceleration in a Magnetic Nozzle. In *AIAA, DGLR, and JSASS, 21st International Electric Propulsion Conference*, volume 1, 1990.

[25] F.R. Chang-Diaz. The VASIMR rocket. *Scientific American*, 283(5):90–97, 2000.

[26] C. Charles, R.W. Boswell, and M.A. Lieberman. Xenon Ion Beam Characterization in a Helicon Double Layer Thruster. *Applied physics letters*, 89(26):261503–261503, 2006.

[27] K. Takahashi, T. Lafleur, C. Charles, P. Alexander, and R. W. Boswell. Axial Force Imparted by a Current-free Magnetically Expanding Plasma. *Physics of Plasmas*, 19(8):083509, 2012.

[28] K. Takahashi, T. Lafleur, C. Charles, P. Alexander, R. W. Boswell, M. Perren, R. Laine, S. Pottinger, V. Lappas, T. Harle, and D. Lamprou. Direct thrust measurement of a permanent magnet helicon double layer thruster. *Applied Physics Letters*, 98(14):141503, April 2011.

[29] Kazunori Takahashi, Trevor Lafleur, Christine Charles, Peter Alexander, and Rod W. Boswell. Electron Diamagnetic Effect on Axial Force in an Expanding Plasma: Experiments and Theory. *Physical Review Letters*, 107(23):235001, November 2011.

[30] Michael D. West, Christine Charles, and Rod W. Boswell. Testing a helicon double layer thruster immersed in a space-simulation chamber. *Journal of Propulsion and Power*, 24(1):134–141, 2008.

[31] R. Winglee, T. Ziemba, L. Giersch, J. Prager, J. Carscadden, and BR Roberson. Simulation and Laboratory Validation of Magnetic Nozzle Effects for the High Power Helicon Thruster. *Physics of Plasmas*, 14:063501, 2007.

[32] A.V. Arefiev and B.N. Breizman. Theoretical Components of the VASIMR Plasma Propulsion Concept. *Physics of Plasmas*, 11:2942, 2004.

[33] J.P. Squire, C.S. Olsen, F.R. Chang-Daz, L.D. Cassady, B.W. Longmier, M.G. Ballenger, M.D. Carter, T.W. Glover, and G.E. McCaskill. VASIMR VX-200 Operation at 200 kW and Plume Measurements: Future Plans and an ISS EP Test Platform. 2011.

[34] R.A. Gerwin, G.J. Marklin, A.G. Sgro, , and A.H. Glasser. Characterization of Plasma Flow through Magnetic Nozzles. Technical report, DTIC Document, 1990.

[35] R. Gerwin. Integrity of the Plasma Magnetic Nozzle. 2009.

[36] I.G. Mikellides, P.G. Mikellides, P.J. Turchi, and T.M. York. Theoretical Design of a Magnetic-Nozzle Acceleration System for Fusion Propulsion. AIAA-2000-3367, Huntsville, AL, 2000.

[37] L. Spitzer. Physics of Fully Ionized Gases. *Interscience Tracts on Physics and Astronomy, New York: Interscience Publication, 1965, 2nd rev. ed.*, 1, 1965.

[38] P.A. Davidson. *An Introduction to Magnetohydrodynamics*, volume 25. Cambridge University Press, Cambridge, 2001.

[39] A.V. Arefiev and B.N. Breizman. Magnetohydrodynamic Scenario of Plasma Detachment in a Magnetic Nozzle. *Physics of Plasmas*, 12:043504, 2005.

[40] H. Lorzel and P.G. Mikellides. Three-Dimensional Modeling of Magnetic Nozzle Processes. *AIAA Journal*, 48(7):1494–1503, 2010.

[41] T.M. York, P. Mikellides, and B.A. Jacoby. Plasma Flow Processes within Magnetic Nozzle Configurations. AIAA-89-2711, Monterey,CA, 1989.

[42] P.J. Turchi, P.G. Mikellides, P. Gessini, and R.A. Gerwin. Numerical Simulation of Magnetic Nozzle Flow for Nuclear Fusion Space Propulsion. AIAA-99-2701, Los Angeles, CA, 1999.

[43] J.T. Cassibry. Theoretical Performance of an MHD Nozzle Using Super-Alfvenic Detachment. *AIAA*, 2006.

[44] F.H. Ebersohn. *Gas Kinetic Study of Magnetic Field Effects on Plasma Plumes.* PhD thesis, Texas A&M University, 2012.

[45] F.H. Ebersohn, S.S. Sharath, D. Staack, J.V. Shebalin, B.W. Longmier, and C. Olsen. Magnetic Nozzle Plasma Plume: Review of Crucial Physical Phenomena. AIAA-2012-4274, Atlanta, GA, July 2012. 47th AIAA/ASME/SAE/ASEE Joint Propulsion Conference.

[46] E. Ahedo and M. Merino. On Plasma Detachment in Propulsive Magnetic Nozzles. *Physics of Plasmas*, 18:053504, 2011.

[47] E. Ahedo and M. Merino. Preliminary Assessment of Detachment in a Plasma Thruster Magnetic Nozzle. AIAA-2010-6613. 45th AIAA/ASME/SAE/ASEE Joint Propulsion Conference, July 2010.

[48] Justin Little. Performance Scaling of Magnetic Nozzles for Electric Propulsion. 2015.

[49] J.M. Little and E.Y. Choueiri. Thrust and Efficiency Model for Electron-driven Magnetic Nozzles. *Physics of Plasmas (1994-present)*, 20(10):103501, 2013.

[50] A.V. Ilin, F.R. Chang Diaz, J.P. Squire, A.G. Tarditi, B.N. Breizman, and M.D. Carter. Simulations of Plasma Detachment in VASIMR. AIAA-2002-0346, Reno, NV, January 2002.

[51] A. Meige, R.W. Boswell, C. Charles, J.-P. Boeuf, G. Hagelaar, and M.M. Turner. One-dimensional simulation of an ion beam generated by a current-free double-Layer. *IEEE Transactions on Plasma Science*, 33(2):334–335, April 2005.

[52] Adam B. Sefkow and Samuel A. Cohen. Particle-in-cell modeling of magnetized argon plasma flow through small mechanical apertures. *Physics of Plasmas (1994-present)*, 16(5):053501, 2009.

[53] E.B. Hooper. Plasma Detachment from a Magnetic Nozzle. *Journal of Propulsion and Power*, 9(5):757–763, 1993.

[54] S.D. Baalrud, T. Lafleur, R.W. Boswell, and C. Charles. Particle-In-Cell Simulations of a Current-Free Double Layer. *Physics of Plasmas (1994-present)*, 18(6):063502, 2011.

[55] Sathyanarayan Rao and Nagendra Singh. Numerical simulation of current-free double layers created in a helicon plasma device. *Physics of Plasmas (1994-present)*, 19(9):093507, September 2012.

[56] J.V. Shebalin. Strmer Regions for Axisymmetric Magnetic Multipole Fields. *Physics of Plasmas*, 11:3472, 2004.

[57] F.N. Gesto, B.D. Blackwell, C. Charles, and R.W. Boswell. Ion Detachment in the Helicon Double-Layer Thruster Exhaust Beam. *Journal of Propulsion and Power*, 22(1):24–30, 2006.

[58] Kentaro Hara, Michael J. Sekerak, Iain D. Boyd, and Alec D. Gallimore. Mode transition of a Hall thruster discharge plasma. *Journal of Applied Physics*, 115(20):203304, 2014.

[59] Kentaro Hara, Iain D. Boyd, and Vladimir I. Kolobov. One-dimensional hybrid-direct kinetic simulation of the discharge plasma in a Hall thruster. *Physics of Plasmas (1994-present)*, 19(11):113508, 2012.

[60] J.M. Little, A.S. Rubin, and E.Y. Choueiri. Similarity Parameter Evolution within a Magnetic Nozzle with Applications to Laboratory Plasmas. IEPC-2011-229, Wiesbaden, Germany, September 2011. 30th International Electric Propulsion Conference.

[61] C.S. Olsen. *Experimental Characterization of Plasma Detachment from Magnetic Nozzles*. PhD thesis, Rice University: U.S.A., 2013.

[62] J.D. Jackson. *Classical electrodynamics*. Wiley, 1999.

[63] H. Kosmahl and P. Ramins. NASA TECHNICAL.

[64] F.F. Chen. *Introduction to Plasma Physics and Controlled Fusion*, volume 1. Plenum Press, New York, 1984.

[65] Alexey V. Arefiev and Boris N. Breizman. Ambipolar acceleration of ions in a magnetic nozzle. *Physics of Plasmas (1994-present)*, 15(4):042109, April 2008.

[66] Benjamin W. Longmier, Edgar A. Bering III, Mark D. Carter, Leonard D. Cassady, William J. Chancery, Franklin R. Chang Daz, Tim W. Glover, Noah Hershkowitz, Andrew V. Ilin, Greg E. McCaskill, Chris S. Olsen, and Jared P. Squire. Ambipolar ion acceleration in an expanding magnetic nozzle. *Plasma Sources Science and Technology*, 20(1):015007, 2011.

[67] M. Nagatomo. Plasma Acceleration by High Frequency Electromagnetic Wave in Static Magnetic Field Gradient. AIAA-67-660, Colorado Springs, CO, September 1976.

[68] R. Comfort. The Magnetic Mirror Force in Plasma Fluid Models. *Modeling magnetospheric plasma*, 1988.

[69] Siefert N.S. Stange S. Boivin R.F. Scime E.E. Cohen, S.A. and F.M. Levinton. Ion acceleration in plasmas emerging from a helicon-heated magnetic-mirror device. *Physics of Plasmas*, 10:2593, 2003.

[70] A. Fruchtman, K. Takahashi, C. Charles, and R.W. Boswell. A Magnetic Nozzle Calculation of the Force on a Plasma. *Physics of Plasmas*, 19:033507, 2012.

[71] Michael A. Raadu. The physics of double layers and their role in astrophysics. *Physics reports*, 178(2):25–97, 1989.

[72] G. Hairapetian and R. L. Stenzel. Particle dynamics and currentfree double layers in an expanding, collisionless, twoelectronpopulation plasma. *Physics of Fluids B: Plasma Physics (1989-1993)*, 3(4):899–914, April 1991.

[73] C. Charles. A review of recent laboratory double layer experiments. *Plasma Sources Science and Technology*, 16(4):R1, 2007.

[74] M. A. Lieberman, C. Charles, and R. W. Boswell. A theory for formation of a low pressure, current-free double layer. *Journal of Physics D: Applied Physics*, 39(15):3294, 2006.

[75] Eduardo Ahedo and Manuel Martnez Snchez. Theory of a Stationary Current-Free Double Layer in a Collisionless Plasma. *Physical Review Letters*, 103(13):135002, September 2009.

[76] Francis F. Chen. Physical mechanism of current-free double layers. *Physics of Plasmas (1994-present)*, 13(3):034502, 2006.

[77] J. P. Sheehan, B. W. Longmier, E. A. Bering, C. S. Olsen, J. P. Squire, M. G. Ballenger, M. D. Carter, L. D. Cassady, F. R. Chang Daz, T. W. Glover, and A. V. Ilin. Temperature gradients due to adiabatic plasma expansion in a magnetic nozzle. *Plasma Sources Science and Technology*, 23(4):045014, 2014.

[78] M. Coletti. Simple Thrust Formula for an MPD Thruster with Applied-magnetic field from Magnetic Stress Tensor. July 2007.

[79] H. Tobari, A. Ando, M. Inutake, and K. Hattori. Characteristics of Electro-magnetically Accelerated Plasma Flow in an Externally Applied Magnetic Field. *Physics of plasmas*, 14:093507, 2007.

[80] M. Inutake, K. Hattori, A. Ando, F. Hori, T. Sugirnura, K. Fukushi, T. Ochiai, M. Yamamoto, T. Yagai, and A. Imasaki. Supersonic Plasma Flow in a Magnetic Nozzle. Proc. of the 26th IEPC, 1999.

[81] J.M. Little and E.Y. Choueiri. Divergence of a Propulsive Plasma Flow Expanding through a Magnetic Nozzle. In *31st International Electric Propulsion inproceedings*, 2009.

[82] J.M. Little and E.Y. Choueiri. The Influence of Induced Currents on Magnetic Nozzle Acceleration and Plasma Detachment. AIAA-2010-6615, Nashville, TN, July 2010. 45th AIAA/ASME/SAE/ASEE Joint Propulsion Conference.

[83] J.M. Little and E.Y. Choueiri. Plasma Detachment and Momentum Transfer in Magnetic Nozzles. AIAA-2011-6001, San Diego, CA, July 2011. 46th AIAA/ASME/SAE/ASEE Joint Propulsion Conference.

[84] K. Takahashi, T. Lafleur, C. Charles, P. Alexander, and R.W. Boswell. Electron Diamagnetic Effect on Axial Force in an Expanding Plasma: Experiments and Theory. *Physical Review Letters*, 107(23):235001, 2011.

[85] B.R. Roberson, R. Winglee, and J. Prager. Enhanced Diamagnetic Perturbations and Electric Currents Observed Downstream of the High Power Helicon. *Physics of Plasmas*, 18:053505, 2011.

[86] A. Sasoh and Y. Arakawa. Electromagnetic Effects in an Applied-field Magnetoplasmadynamic Thruster. *Journal of Propulsion and Power*, 8(1):98–102, 1992.

[87] A. Sasoh. Generalized Hall Acceleration. *Journal of Propulsion and Power*, 10:251–254, 1994.

[88] A. Sasoh and Y. Arakawa. Thrust Formula for Applied-field Magnetoplasmadynamic Thrusters Derived from Energy Conservation Equation. *Journal of Propulsion and Power*, 11(2):351–356, 1995.

[89] D.B. Fradkin, A.W. Blackstock, K.W. Liewer, D.J. Roehling, T.F. Stratton, and M. Williams. Experiments using a 25-kw Hollow Cathode Lithium Vapor MPD Arcjet. *AIAA Journal*, 8(5), 2012.

[90] A. Sasoh. Simple Formulation of Magnetoplasmadynamic Acceleration. *Physics of Plasmas*, 1(3):464–469, 1994.

[91] D.A. Kaufman, D.G. Goodwin, and J.C. Sercel. Plasma Separation from Magnetic Field Lines in a Magnetic Nozzle. volume 1 of *31st AIAA Aerospace Sciences Meeting and Exhibit*, 1993.

[92] P.F. Schmit and N.J. Fisch. Magnetic Detachment and Plume Control in Escaping Magnetized Plasma. *Journal of Plasma Physics*, 75(03):359–371, 2009.

[93] M. Merino and E. Ahedo. Plasma Detachment Mechanisms in a Magnetic Nozzle. AIAA-2011-5999. 46th AIAA/ASME/SAE/ASEE Joint Propulsion Conference, July 2011.

[94] E. Ahedo and M. Merino. Two-dimensional Supersonic Plasma Acceleration in a Magnetic Nozzle. *Physics of Plasmas*, 17:073501, 2010.

[95] B.N. Breizman, M.R. Tushentsov, and A.V. Arefiev. Magnetic Nozzle and Plasma Detachment Model for a Steady-State Flow. *Physics of Plasmas*, 15:057103, 2008.

[96] C. Deline, G. Chavers, and B. Gilchrist. Physics of Plasma Detachment in a Magnetic Nozzle. AIAA-2006-4653, Sacramento, CA, July 2006.

[97] C. Deline, B. Gilchrist, R. Bengtson, J. Jones, G. Chavers, and C. Dobson. Simulation and Measurement of High-Beta Plasma in a Magnetic Nozzle. AIAA-2007-5259, Cincinnati, OH, July 2007.

[98] C.A. Deline, R.D. Bengtson, B.N. Breizman, M.R. Tushentsov, J.E. Jones, D.G. Chavers, C.C. Dobson, and B.M. Schuettpelz. Plume Detachment from a Magnetic Nozzle. *Physics of Plasmas*, 16:033502, 2009.

[99] George Schmidt. Plasma Motion Across Magnetic Fields. *Physics of Fluids (1958-1988)*, 3(6):961–965, November 1960.

[100] Lennart Lindberg. Plasma flow in a curved magnetic field. *Astrophysics and Space Science*, 55(1):203–225, May 1978.

[101] N. Brenning, T. Hurtig, and M.A. Raadu. Conditions for Plasmoid Penetration Across Abrupt Magnetic Barriers. *Physics of Plasmas*, 12:012309, 2005.

[102] K. Terasaka, S. Yoshimura, K. Ogiwara, M. Aramaki, and M. Y. Tanaka. Experimental studies on ion acceleration and stream line detachment in a diverging magnetic field. *Physics of Plasmas (1994-present)*, 17(7):072106, 2010.

[103] R.W. Moses, R.A. Gerwin, and K.F. Schoenberg. Resistive Plasma Detachment in Nozzle Based Coaxial Thrusters. In *AIP Conference Proceedings*, volume 246, page 1293, 1992.

[104] K. Schoenberg, R. Gerwin, C. Barnes, I. Henins, R. Mayo, and R. Moses. Coaxial Plasma Thrusters for High Specific Impulse Propulsion. In *AIAA, NASA, and OAI, inproceedings on Advanced SEI Technologies, Cleveland, OH*, page 1991, 1991.

[105] GI Dimov and S.Y. Taskaev. Simulation of a Supersonic Plasma Jet with Recombination in a Magnetic Nozzle. 27th European Physical Society Conference on Controlled Fusion and Plasma Physics, Budapest, June 2000.

[106] S.A. Cohen and M.A. Paluszek. The Grand Challenge- A New Plasma Thruster. *Launchspace*, 3(6):46, 1998.

[107] R.P. Hoyt, J.T. Scheuer, K.F. Schoenberg, R.A. Gerwin, R.W. Moses Jr, and I. Henins. Magnetic Nozzle Design for Coaxial Plasma Accelerators. *IEEE Transactions on Plasma Science*, 23(3):481–494, 1995.

[108] R.A. Kopp and G.W. Pneuman. Magnetic Reconnection in the Corona and the Loop Prominence Phenomenon. *Solar Physics*, 50(1):85–98, 1976.

[109] D. Biskamp. *Magnetic Reconnection in Plasmas*, volume 3. Cambridge University Press, 2005.

[110] R. Kawabuchi, N. Matsuda, Y. Kajimura, H. Nakashima, and Y. P. Zakharov. Numerical simulation of plasma detachment from a magnetic nozzle by using fully Particle-In-Cell code. *Journal of Physics: Conference Series*, 112(4):042082, 2008.

[111] C.K. Birdsall. Particle-in-cell charged-particle simulations, plus Monte Carlo collisions with neutral atoms, PIC-MCC. *IEEE Transactions on Plasma Science*, 19(2):65–85, April 1991.

[112] C.K. Birdsall and A.B. Langdon. *Plasma Physics via Computer Simulation*. CRC Press, 2004.

[113] J.P. Verboncoeur, A.B. Langdon, and N.T. Gladd. An Object-Oriented Electromagnetic PIC Code. *Computer Physics Communications*, 87(1):199–211, 1995.

[114] J.P. Verboncoeur. Particle Simulation of Plasmas: Review and Advances. *Plasma Physics and Controlled Fusion*, 47(5A):A231, 2005.

[115] J. P. Verboncoeur, M. V. Alves, V. Vahedi, and C. K. Birdsall. Simultaneous Potential and Circuit Solution for 1d Bounded Plasma Particle Simulation Codes. *Journal of Computational Physics*, 104(2):321–328, February 1993.

[116] I.H. Hutchinson. *Principles of Plasma Diagnostics*. Cambridge university press, 2005.

[117] V. Vahedi and M. Surendra. A Monte Carlo Collision Model for the Particle-In-Cell Method: Applications to Argon and Oxygen Discharges. *Computer Physics Communications*, 87(1):179–198, 1995.

[118] D. Sydorenko. *Particle-In-Cell Simulations of Electron Dynamics in Low Pressure Discharges With Magnetic Fields*. PhD thesis, University of Saskatchewan Saskatoon, 2006.

[119] M.E. Jones, D.S. Lemons, R.J. Mason, V.A. Thomas, and D. Winske. A Grid-Based Coulomb Collision Model for PIC Codes. *Journal of Computational Physics*, 123(1):169–181, 1996.

[120] J.P. Boris. Relativistic Plasma Simulation-Optimization of a Hybrid Code. In *Proc. Fourth Conf. Num. Sim. Plasmas, Naval Res. Lab, Wash. DC*, pages 3–67, 1970.

[121] J.P. Cartwright, K.L.and Verboncoeur and C.K. Birdsall. Loading and Injection of Maxwellian Distributions in Particle Simulations. *Journal of Computational Physics*, 162(2):483–513, 2000.

[122] J. Denavit and J.M. Walsh. Nonrandom Initializations of Particle Codes. *Comments Plasma Phys. Control. Fusion*, 6:209–223, 1981.

[123] L.A. Schwager and C.K. Birdsall. Collector and Source Sheaths of a Finite Ion Temperature Plasma. *Physics of Fluids B: Plasma Physics (1989-1993)*, 2(5):1057–1068, 1990.

[124] A.V. Phelps. The Application of Scattering Cross Sections to Ion Flux Models in Discharge Sheaths. *Journal of applied physics*, 76(2):747–753, 1994. Phelps database, www.lxcat.net, retrieved on March 10, 2015.

[125] D. Piscitelli, A.V. Phelps, J. de Urquijo, E. Basurto, and L.C. Pitchford. Ion Mobilities in Xe/Ne and Other Rare-gas Mixtures. *Physical Review E*, 68(4):046408, 2003. Phelps database, www.lxcat.net, retrieved on March 10, 2015.

[126] L.C. Pitchford. *Swarm Studies and Inelasitc Electron-Molecule Collisions: proceedings of the meeting of the Fourth International Swarm Seminar and the Inelastic Electron-Molecule Collisions Symposium*. Springer Verlag, 1987. Hayashi database, www.lxcat.net, retrieved on February 24, 2015.

[127] V. Vahedi, C. K. Birdsall, M. A. Lieberman, G. DiPeso, and T. D. Ronhlien. Capacitive RF discharges modelled by particle-in-cell Monte Carlo simulation. II. Comparisons with laboratory measurements of electron energy distribution functions. *Plasma Sources Science and Technology*, 2(4):273, 1993.

[128] V. Vahedi, C. K. Birdsall, M. A. Lieberman, G. DiPeso, and T. D. Ronhlien. Capacitive RF discharges modelled by particle-in-cell Monte Carlo simulation. II. Comparisons with laboratory measurements of electron energy distribution functions. *Plasma Sources Science and Technology*, 2(4):273, 1993.

[129] V. Vahedi, G. DiPeso, C. K. Birdsall, M. A. Lieberman, and T. D. Rognlien. Capacitive RF discharges modelled by particle-in-cell Monte Carlo simulation. I. Analysis of numerical techniques. *Plasma Sources Science and Technology*, 2(4):261, 1993.

[130] J.D. Huba. NRL: plasma formulary. Technical report, DTIC Document, 2004.

[131] P. W. Rambo and R. J. Procassini. A comparison of kinetic and multifluid simulations of laserproduced colliding plasmas. *Physics of Plasmas (1994-present)*, 2(8):3130–3145, August 1995.

[132] Wallace M. Manheimer, Martin Lampe, and Glenn Joyce. Langevin Representation of Coulomb Collisions in PIC Simulations. *Journal of Computational Physics*, 138(2):563–584, December 1997.

[133] Tomonor Takizuka and Hirotada Abe. A binary collision model for plasma simulation with a particle code. *Journal of Computational Physics*, 25(3):205–219, 1977.

[134] Nagendra Singh. Current-free double layers: A review. *Physics of Plasmas (1994-present)*, 18(12):122105, December 2011.

[135] P.M. Bellan. *Fundamentals of Plasma Physics*. Cambridge University Press, Cambridge, 2006.

[136] G. F. Chew, M. L. Goldberger, and F. E. Low. The Boltzmann Equation and the One-Fluid Hydromagnetic Equations in the Absence of Particle Collisions. *Proceedings of the Royal Society A: Mathematical, Physical and Engineering Sciences*, 236(1204):112–118, July 1956.

[137] Tamas I. Gombosi and Craig E. Rasmussen. Transport of gyration-dominated space plasmas of thermal origin: 1. Generalized transport equations. *Journal of Geophysical Research: Space Physics*, 96(A5):7759–7778, 1991.

[138] B. O. Lehnert. *Dynamics of charged particles*. North-Holland Pub. Co., 1964.

[139] Yunchao Zhang, Christine Charles, and Rod Boswell. Thermodynamic Study on Plasma Expansion along a Divergent Magnetic Field. *Physical Review Letters*, 116(2):025001, January 2016.

[140] J. P. Sheehan, Timothy A. Collard, Frans H. Ebersohn, and Benjamin W. Longmier. Initial Operation of the CubeSat Ambipolar Thruster. 2015.

[141] K. Takahashi, C. Charles, R. W. Boswell, T. Kaneko, and R. Hatakeyama. Measurement of the energy distribution of trapped and free electrons in a current-free double layer. *Physics of Plasmas (1994-present)*, 14(11):114503, November 2007.

[142] Rod W. Boswell, Kazunori Takahashi, Christine Charles, and Igor D. Kaganovich. Non-local electron energy probability function in a plasma expanding along a magnetic nozzle. *Frontiers in Physics*, 3:14, 2015.

[143] S.I. Braginskii. Transport Processes in a Plasma. *Reviews of Plasma Physics*, 1:205, 1965.

[144] B.W. Longmier, L.D. Cassady, M.G. Ballenger, M.D. Carter, F.R. Chang-Diaz, T.W. Glover, A.V. Ilin, G.E. McCaskill, C.S. Olsen, and J.P. Squire. VX-200 Magnetoplasma Thruster Performance Results Exceeding Fifty-Percent Thruster Efficiency. *Journal of Propulsion and Power*, 27(4):915, 2011.

[145] J.M. Little and E.Y. Choueiri. Critical Condition for Plasma Confinement in the Source of a Magnetic Nozzle Flow. *IEEE Transactions on Plasma Science*, 43(1):277–286, January 2015.

[146] Julien Jarrige, Paul-Quentin Elias, Flix Cannat, and Denis Packan. Performance Comparison of an ECR Plasma Thruster using Argon and Xenon as Propellant Gas. In *Proceedings of the 33rd International Electric Propulsion Conference*, pages 2013–420, 2013.

[147] C. Bhm and J. Perrin. Retarding-Field Analyzer for Measurements of Ion Energy Distributions and Secondary Electron Emission Coefficients in Low-Pressure Radio Frequency Discharges. *Review of scientific instruments*, 64(1):31–44, 1993.

[148] W. A. Campbell and J. J. Scialdone. Outgassing Data for Selecting Spacecraft Materials, NASA RP-1124, Rev. 2, 1990; data is available online at outgassing. nasa. gov. *Quantities quoted are Total Mass Loss (% TML) and Collected Volatile Condensable Materials (% CVCM).*

[149] K.M. Lemmer. *Use of a Helicon Source for Development of a Re-entry Blackout Amelioration System.* PhD thesis, The University of Michigan, 2009.